Stationary and Quasi-Stationary Waves in Even-Order Dissipative Systems

M. V. Averiyanov, M. S. Basova, and V. A. Khokhlova

Moscow State University, Vorob'evy gory, Moscow, 119899 Russia
e-mail: vera@acs366.phys.msu.su
Received May 5, 2004

Abstract—A new equation was recently suggested by Rudenko and Robsman [1] for describing the nonlinear wave propagation in scattering media that are characterized by weak sound signal attenuation proportional to the fourth power of frequency. General self-similar properties of the solutions to this equation were studied. It was shown that stationary solutions to this equation in the form of a shock wave exhibit unusual oscillations around the shock front, as distinct from the classical Burgers equation. Here, similar solutions are studied in detail for nonlinear waves in even-order dissipative media; namely, the solutions are compared for the media with absorption proportional to the second, fourth, and sixth powers of frequency. Based on the numerical results and the self-similar properties of the solutions, the fine structure of the shock front of stationary waves is studied for different absorption laws and magnitudes. It is shown that the amplitude and number of oscillations appearing in the stationary wave profile increase with increasing power of the frequency-dependent absorption term. For initial disturbances in the form of a harmonic wave and a pulse, quasi-stationary solutions are obtained at the stage of fully developed discontinuities and the evolution of the profile and width of the shock wave front is studied. It is shown that the smoothening of the shock front in the course of wave propagation is more pronounced when the absorption law is quadratic in frequency. © 2005 Pleiades Publishing, Inc.

Nonlinear effects arising in acoustic wave propagation depend in many respects on the frequency-dependent behavior of absorption in the medium. In classical liquids, the absorption of acoustic waves is caused by viscosity and thermal conductivity and depends on frequency according to a quadratic law [2, 3]. In media like biological tissues, the absorption law is nearly linear [4, 5]. Higher powers of frequency are characteristic of the absorption laws of scattering media and media with complex small-scale structure [1]. In addition, numerical algorithms of simulating nonlinear shock wave propagation often use fictitious absorption rapidly increasing with frequency according to different laws to artificially smooth out discontinuous solutions and ensure their stability [6].

Rudenko and Robsman [1] recently suggested a new equation (the RR equation) that describes the propagation of nonlinear waves in scattering media with absorption proportional to the fourth power of frequency. In the context of the nonlinear evolution equation of an acoustic wave, this frequency-dependent law corresponds to the absorption operator in the form of the fourth derivative with respect to time. Rudenko and Robsman [1] studied the general self-similar properties of the solutions to the RR equation and showed that strongly decaying oscillations appear in the wave profile around the shock, which is in contrast to the monotonic stationary solution to the Burgers equation. At the same time, the acoustic energy loss at the shock front of the stationary wave is independent of the absorption

magnitude; it is proportional to the third power of the shock wave amplitude and coincides with the absorption described by the Burgers equation and the equation of simple waves [2, 3]. Nevertheless, the problems on nonlinear wave propagation in media with absorption rapidly increasing with frequency are far from being exhaustively investigated. Moreover, an extension of the existing solutions to media with still faster power laws of frequency-dependent absorption (for example, proportional to the sixth power of frequency, which is characteristic of media with a complex small-scale structure) is also of undoubted interest.

It should be noted that the effect of frequency-dependent dissipative properties of a medium on nonlinear wave propagation and the fine structure of the shock front has been studied much better for absorption terms increasing with frequency according to nearly linear and slower laws, which are characteristic of such media as biological tissues and relaxation media [7, 8]. As is known, the shock front of a wave is formed due to the simultaneous action of two competing processes: one of them is the acoustic nonlinearity that steepens the leading edge of the wave and the other is the dissipation that smoothes the shock front. Depending on the absorption behavior, the jump at the shock front can be described by either a finite front width or by a mathematical discontinuity [2, 3]. Exact analytical solutions for strongly distorted nonlinear waves can be derived only for certain simple cases, such as a nonabsorptive medium (the equation of simple waves), viscous

medium with quadratic absorption (the Burgers equation) [2, 3] and frequency-independent absorption [9], and relaxation media [8]. In the general case, the study of nonlinear waves with shock fronts requires resorting to either asymptotic constructions or numerical procedures [6, 7, 9–12]. It was shown [9] that the solution for the wave profile can contain a stable shock front in the form of a mathematical discontinuity if the high-frequency absorption behavior is described by a function increasing slower than the linear one. Characteristic examples are the discontinuous solutions for relaxation media [8, 11], media with frequency-independent absorption [9], and media with selective absorption for certain frequencies [12]. If the absorption increases with frequency according to a law faster than the linear law, the shock front will have a finite width.

In this paper, we investigate in detail and compare the features of nonlinear wave propagation in dissipative media of even orders, where the absorption is proportional to the second (the Burgers equation), fourth (the RR equation), and sixth powers of frequency. We consider the evolution of wave profiles and parameters to the corresponding stationary values and analyze the parameters of the shock fronts of stationary and quasi-stationary solutions.

Consider the nonlinear evolution equation with absorption proportional to an arbitrary even power of frequency:

$$\frac{\partial p}{\partial x} - \frac{\varepsilon}{\rho_0 c_0^3} p \frac{\partial p}{\partial \tau} = (-1)^{\frac{\eta-2}{2}} \beta \frac{\partial^\eta p}{\partial \tau^\eta}. \tag{1}$$

Here, p is the sound pressure; x is the coordinate along which the wave propagates; $\tau = t - x/c_0$ is the time in the moving coordinate system; c_0 is the phase velocity of sound; ε is the coefficient of nonlinearity of the medium; β is the absorption coefficient; and parameter η takes on the values of 2, 4, and 6.

For further calculations, it is convenient to rewrite Eq. (1) in terms of dimensionless variables:

$$\frac{\partial V}{\partial z} - V \frac{\partial V}{\partial \theta} = (-1)^{\frac{\eta-2}{2}} \Gamma \frac{\partial^\eta V}{\partial \theta^\eta}, \tag{2}$$

where

$$V = \frac{p}{p_0}, \quad \theta = \omega_0 \tau,$$

$$z = \frac{x}{x_s} = \frac{\varepsilon p_0 \omega_0}{\rho_0 c_0^3} x, \quad \Gamma = \frac{\beta \omega_0^{\eta-1} c_0^3 \rho_0}{\varepsilon p_0}. \tag{3}$$

Here, V is the sound pressure normalized by a certain characteristic amplitude p_0, x_s is the distance to the point of discontinuity formation in the harmonic wave of frequency ω_0 in the absence of absorption, θ is dimensionless time, and Γ is the dimensionless absorption parameter similar in physical meaning to the inverse Reynolds number in the Burgers equation [2].

We note that the solutions to Eq. (2) for arbitrary $\eta = 2$, 4, and 6 are of a self-similar character, which allows one to construct a whole class of new solutions from a single known solution. One can easily show that, if the function $V_0 V(\theta_0, z_0)$ is a solution to Eq. (2) in the coordinates θ_0 and z_0 for some absorption Γ_0 and characteristic amplitude V_0, then the function $V_1 V(\theta_1, z_1)$ of transformed arguments

$$\theta_1 = \theta_0 \sqrt[\eta-1]{\frac{\Gamma_0 V_1}{\Gamma_1 V_0}}, \quad z_1 = z_0 \frac{V_1}{V_0} \sqrt[\eta-1]{\frac{\Gamma_0 V_1}{\Gamma_1 V_0}} \tag{4}$$

is also a solution to Eq. (2) for other arbitrary absorption Γ_1 and amplitude V_1.

Let us investigate the class of stationary solutions to Eq. (2) in the form of a pressure jump using the self-similarity property (4). For this purpose, we require a single stationary solution for some preset parameter Γ_0 and amplitude V_0. Let us set, for example, $\Gamma_0 = 1$ and $V_0 = V(\theta \longrightarrow \infty) = |V(\theta \longrightarrow -\infty)| = 1$, which corresponds to the discontinuity amplitude (pressure jump at the front) $A_s = 2$. For a numerical study of the stationary solution formation and shock front dynamics, we select the initial condition in the form of the hyperbolic tangent

$$V(z = 0, \theta) = \tanh(\theta/2G), \tag{5}$$

where $2G$ is the initial front width. The solution to Eq. (2) is determined successively for the nodes of a grid along the z coordinate with grid spacing h_z by the finite-difference algorithm:

$$V_n(z + hz) = V_n(hz)$$
$$+ \frac{h_z}{4h_\theta}[V_{n+1}^2(hz) - V_{n-1}^2(hz)] + (-1)^{\frac{\eta-2}{2}} h_z L_\eta(V), \tag{6}$$

which is conservative in the nonlinear operator, first-order in z, and second-order in the time coordinate θ. Here, h_θ is the grid spacing in θ, n is the number of the nodes of the temporal grid, and $L_\eta(V)$ is the operator of the corresponding higher derivative with respect to variable θ for $\eta = 2$, 4, and 6 [13]. In order to determine the optimum values of the grid spacing that ensure the stability and a given accuracy (0.3%) of the solution, we carried out calculations for different values of the grid spacing, different widths of the initial front G, and different disturbances of the initial smooth profile (5). To avoid reflections from the grid boundaries, we used a sufficiently wide temporal window.
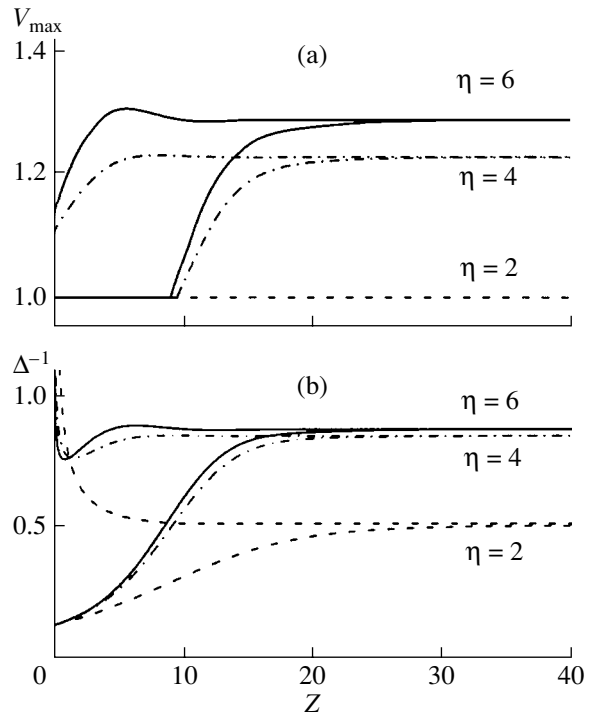
Figure 1 shows the calculated evolution of initial disturbances (a flat disturbance with $G = 4.0$ and a steep disturbance with $G = 0.05$) to a stationary shock profile for different $\eta = 2$, 4, and 6. As may be seen, in the classical case of a viscous liquid ($\eta = 2$), the resulting stationary wave has a smooth shock front of a finite width [2]. The stationary solution to the modified Burgers-type equation with $\eta = 4$ and 6 also behaves as a shock wave; however, the structure of the shock front is essen-
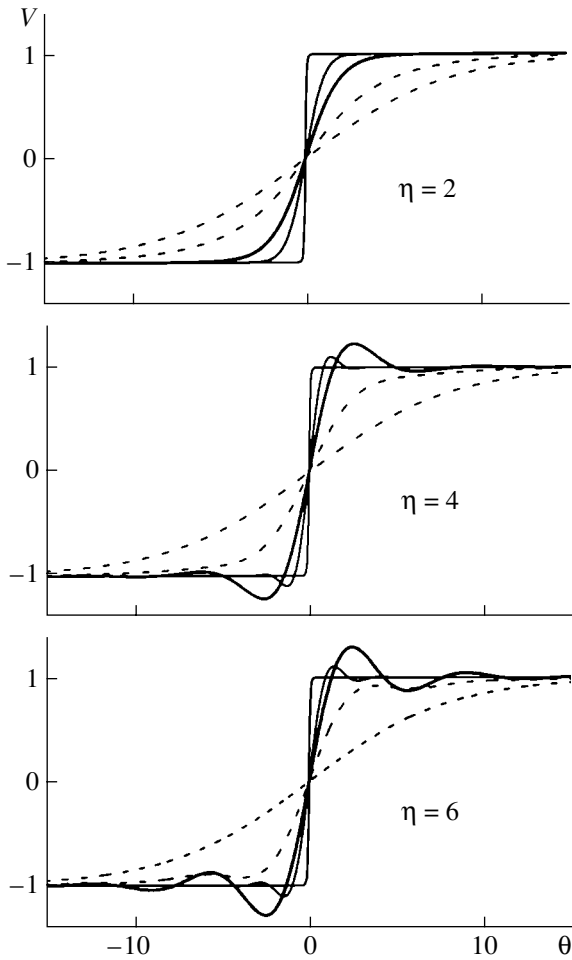
Fig. 1. Nonlinear evolution of the initial disturbances ($G = 4.0$ and $G = 0.05$) to the stationary solution for different absorption laws $\eta = 2$, 4, and 6. The bold line shows the stationary solution.


Fig. 2. Evolution of (a) the peak value $V_{\max}$ of the shock wave profile and (b) the shock front steepness $\Delta^{-1} = \partial V/\partial\theta(\theta = 0)$ to the stationary values for steep ($G = 0.05$) and flat ($G = 4.0$) initial disturbances and different absorption laws $\eta = 2$, 4, and 6. The curves are obtained for the absorption parameter $\Gamma = 1.0$ and the pressure drop at the front $A_s = 2$.

tially different: decaying oscillations appear on both sides of the front. The oscillation period ($T = 6.4$ at $\eta = 6$ and $T = 7.0$ at $\eta = 4$) is comparable to the width of the shock front of the stationary solution, and the number and amplitude of oscillations are the greater, the higher the derivative used in the absorption description.

Figure 2 shows the evolution of the peak value of the wave profile $V_{\max}(z) = \max_\theta(|V(z, \theta)|)$ and the maximum steepness of the shock front to the stationary values for the same initial profiles (5) with front widths obviously greater ($G = 4.0$) and smaller ($G = 0.05$) than the front width of the stationary wave. The steepness (the inverse width) of the shock front Δ^{-1} was determined as the derivative $\Delta^{-1} = \partial V/\partial\theta$ at the front center $\theta = 0$. It is seen from these curves that, in the case of the law quadratic in frequency $\eta = 2$, the profile peak values do not vary with distance, $V_{\max} = 1$, and the front steepness tends monotonically to the stationary value $\Delta^{-1} = 0.5$. For $\eta = 4$ and 6, the steepness of the initially flat front also monotonically increases with the distance travelled by

the wave. The peak value of the wave profile remains intact at the beginning of the propagation process. The oscillations appear and the peak value begins monotonically increasing to the stationary value only when the wave front becomes noticeably steeper. For an initially steep disturbance, oscillations in the wave profile appear from the very beginning; in this case, the peak value sharply increases, the front steepness decreases, and a further evolution of the parameters exhibits a nonmonotonic oscillating behavior. The stationary values of the wave parameters for the considered cases of $\eta = 2$, 4, and 6 are $\Delta_\eta^{-1} = 0.5$, 0.84, and 0.87 and $V_{\max, \eta} = 1$, 1.23, and 1.29, respectively.

Using the self-similarity property (4) and the stationary solutions determined numerically for $\Gamma_0 = 1.0$ and $V_0 = 1.0$, we consider the basic features of stationary solutions as functions of absorption Γ and derivative order η for a fixed amplitude of the shock front. Setting $\Gamma_0 = 1.0$ and $V_0 = V_1 = 1.0$ ($A_s = 2$) in Eqs. (4), we obtain an expression for the shock front steepness for an arbitrary Γ:

$$\Delta^{-1}(\Gamma) = \Gamma^{-\frac{1}{\eta-1}}\Delta^{-1}(\Gamma = 1). \qquad (7)$$
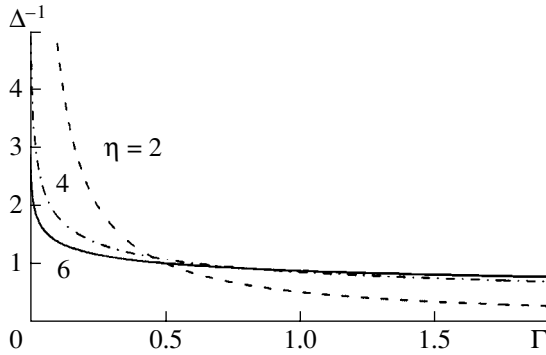
Fig. 3. Shock front steepness $\Delta^{-1} = \partial V/\partial\theta(\theta = 0)$ as a function of the absorption parameter Γ for different $\eta = 2$, 4, and 6. The pressure drop at the front is $A_p = 2$.

Figure 3 shows the shock front steepness versus the quantity Γ for different types of absorption. As can be seen, the front steepness always monotonically decreases with increasing Γ. The curves meet in the region $\Gamma = 0.5$–0.8, where the front steepness approaches unity. If the absorption is weak ($\Gamma < 0.5$), a steeper shock front is formed for the absorption that increases slower with frequency. In the case of a strong absorption ($\Gamma > 0.8$), an opposite relationship between the front steepness and the absorption law occurs in the region after the intersection point of the curves.

Figure 4 shows the stationary solutions to Eq. (2) and their first and second derivatives for different η at $\Gamma = 0.5$. For $\eta = 4$ (the RR equation), the curves obtained correspond to the results obtained in [1]. As is seen from the curves, the oscillations accompanying the establishment of the stationary solution and derivatives are more prominent for the higher derivative describing the absorption law ($\eta = 6$). The oscillation period-to-front width ratio depends on the derivative order only slightly ($T\Delta^{-1}/V_0 = 6.0$ at $\eta = 4$ and $T\Delta^{-1}/V_0 = 5.6$ at $\eta = 6$) and, in view of the self-similar property of the solution, is a quantity invariant with respect to parameter Γ and discontinuity amplitude $A_s = 2V_0$.

Consider now the features of the quasi-stationary solutions to Eq. (2) that occur for small Γ by the examples of an initially harmonic wave and a Gaussian pulse. As is known, at $\eta = 2$, the smooth segments of the wave profile at the stage of fully developed discontinuities are adequately described by the solution to the equation of simple waves, and the structure of the shock front nearly coincides with the stationary solution for the corresponding discontinuity amplitude (the Khokhlov solution to the Burgers equation [2]). One would expect that the oscillating front structure observed for $\eta = 4$ and 6 will nearly coincide with the structure of stationary waves of the corresponding amplitude. However, the steepness of the fronts corresponding to different absorption laws will exhibit different dependences on the distance-dependent discontinuity amplitude $A_s(z)$, which can be unambiguously determined from
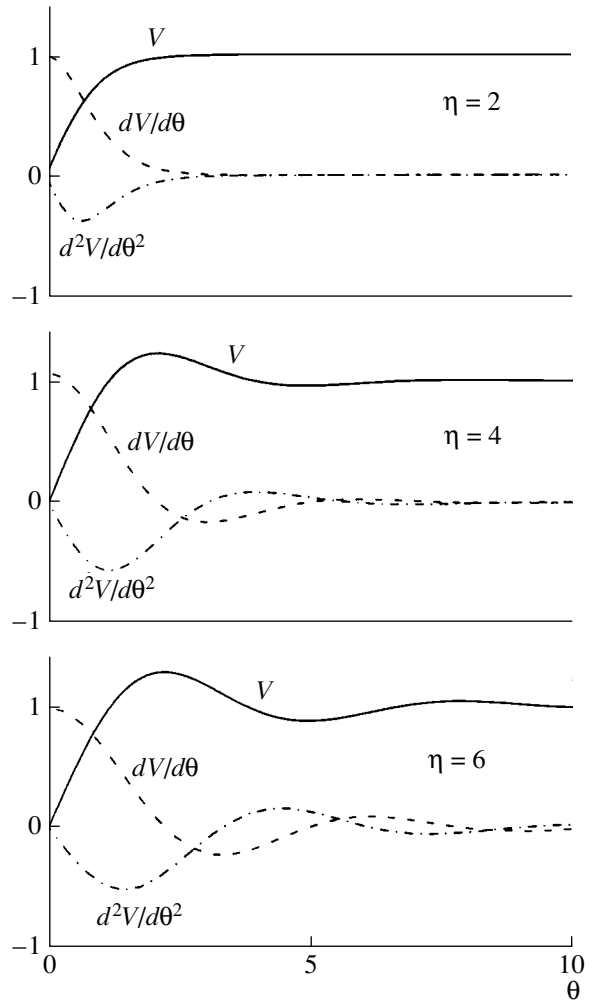
Fig. 4. Nonlinear stationary wave profiles and their first and second derivatives for different absorption laws $\eta = 2$, 4, and 6 at $\Gamma = 0.5$.

the exact solution to the equation of simple waves for an arbitrary initial profile.

Depending on the frequency-dependent absorption law $\eta = 2$, 4, and 6, we select the values of parameter Γ to satisfy the requirement that the shock front steepnesses be identical, say $\Delta_0^{-1} = 5$, at the point where the wave profile has the dimensionless discontinuity amplitude $A_0 = 1$. The corresponding absorption parameters Γ_η are easily determined from the self-similarity property (4) of the resulting stationary solutions whose front steepness Δ_η^{-1} at $\Gamma = 1$ and $A_s = 2$ is known (see Figs. 1 and 2):

$$\Gamma_\eta = \Gamma\left(\frac{A_0}{A_s}\right)^\eta\left(\frac{\Delta_\eta^{-1}}{\Delta_0^{-1}}\right)^{\eta-1}, \qquad (8)$$

which yields $\Gamma_2 = 2.5 \times 10^{-2}$, $\Gamma_4 = 3 \times 10^{-4}$, and $\Gamma_6 = 2.45 \times 10^{-6}$. Figure 5 shows the shock front steep-

ness as a function of distance z and the distance-dependent evolution of the profile of an initially harmonic wave $V(z = 0, \theta) = \sin(\theta)$; all data were calculated numerically on the basis of Eq. (2) for the above parameters Γ_η and $\eta = 2$, 4, and 6. The simulation was carried out in the spectral representation using 100 harmonics of the reference frequency [7]. One can see that the front steepnesses actually coincide for all absorption laws at the distance $z = 5.3$, where the discontinuity amplitude is $A_s = 1$ in accordance with the exact solution to the equation of simple waves. The maximum front steepness is achieved at the maximal value of discontinuity $A_s = 2$ ($z = \pi/2$), and the greatest value of the maximum corresponds to the quadratic law of frequency-dependent absorption $\eta = 2$. The fastest decrease in the front steepness with distance (the maximum smoothing of the shock front) occurs at $\eta = 2$. For $\eta = 4$ and 6, oscillations appear in the profile behind the front; the oscillation amplitude decreases and duration increases as the discontinuity amplitude decreases, in accordance with properties of stationary solutions.

Figure 6 shows similar results of a numerical simulation by Eq. (2) for the same parameters Γ_η, but for the initial disturbance in the form of a Gaussian pulse $V(z = 0, \theta) = 2.0\exp(-\theta^2/1.7^2)$. The pulse amplitude and duration are set in a way that ensures that the distance to the point of discontinuity formation and the maximum discontinuity amplitude are the same as in the case of the above harmonic wave: $z = 1$ and $A_s = 2$. In this case, the shock front steepnesses become equal at greater distances z, because the nonlinear attenuation of the shock pulse $A_s \sim (1 + z)^{-1/2}$ is slower than the attenuation of the symmetric saw-tooth wave $A_s \sim (1 + z)^{-1}$ [2, 3]. The pulse profiles corresponding to different absorption laws nearly coincide for equal distances on smooth segments; however, the front structure is noticeably different and basically reproduces the behavior of the stationary solutions.

It is clear that the degree of closeness of the shock front structure at the stage of fully developed discontinuities to the stationary solution depends on the magnitude of the parameter Γ and on the absorption law η. Figure 7 illustrates the difference between the shock front steepness calculated from Eq. (2) for the initially harmonic wave (the solid curves) and the stationary solution steepness obtained from the discontinuity amplitude of the solution to the equation of simple waves for given parameters Γ and η (the dashed lines). The calculations were carried out for the parameters Γ_η belonging to two sets, every of which corresponded to a certain maximum front steepness (at $z = \pi/2$) for all absorption laws η. It is seen that, for weak absorption (upper curves, the right-hand Δ^{-1} axis) and $\eta = 4$ and 6, the stationary solution adequately describes the shock front steepness beginning almost from the point of discontinuity formation. For quadratic frequency-dependent absorption $\eta = 2$, the differences are more prominent and the shock front approaches the stationary solution at distances of several lengths of discontinuity
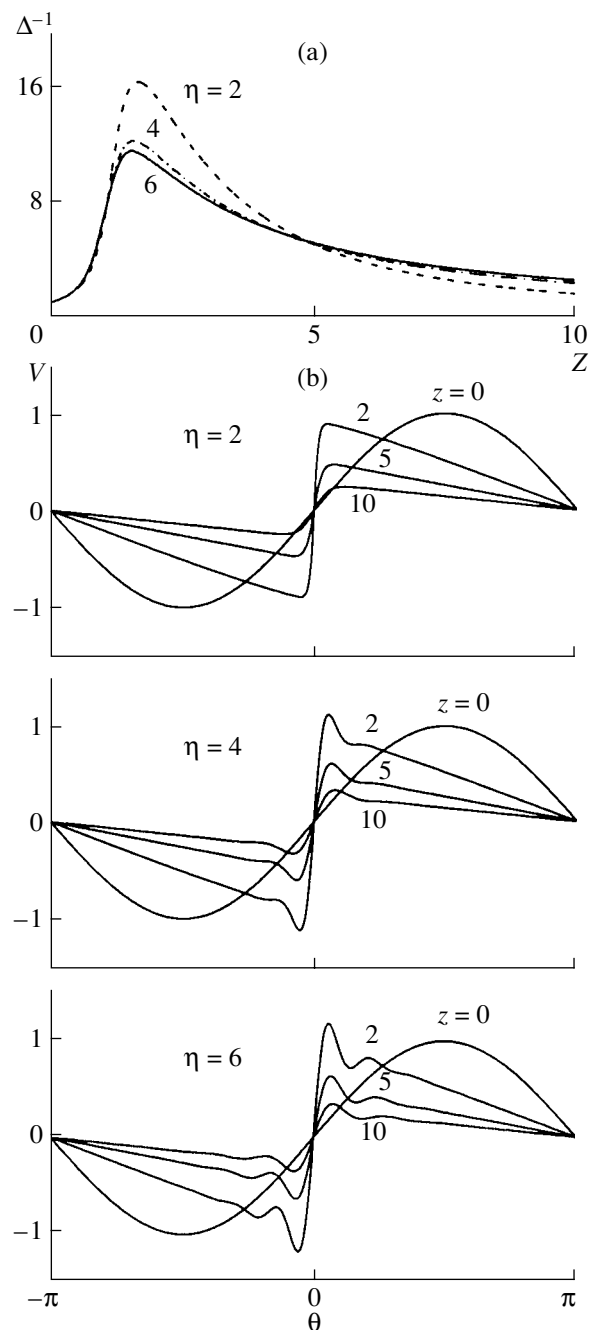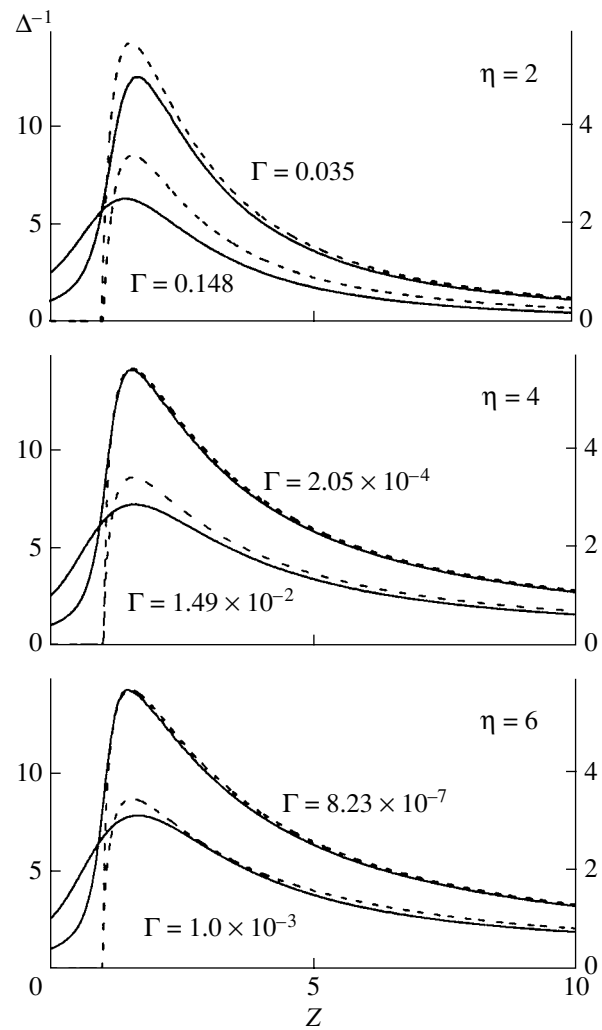

Fig. 5. (a) Shock front steepness as a function of distance and (b) the evolution of the profile of the initially harmonic wave for different absorption laws $\eta = 2$, 4, and 6 and the corresponding absorption parameters $\Gamma_2 = 2.5 \times 10^{-2}$, $\Gamma_4 = 3 \times 10^{-4}$, and $\Gamma_6 = 2.45 \times 10^{-6}$.

formation. For greater values of parameter Γ (lower curves, the left-hand Δ^{-1} axis), the structure of the shock front approaches the stationary solution for greater distances, the front is more spread than in the stationary solution, and these differences are again more prominent for the quadratic absorption law. In the simulations of heavily distorted nonlinear signals, these
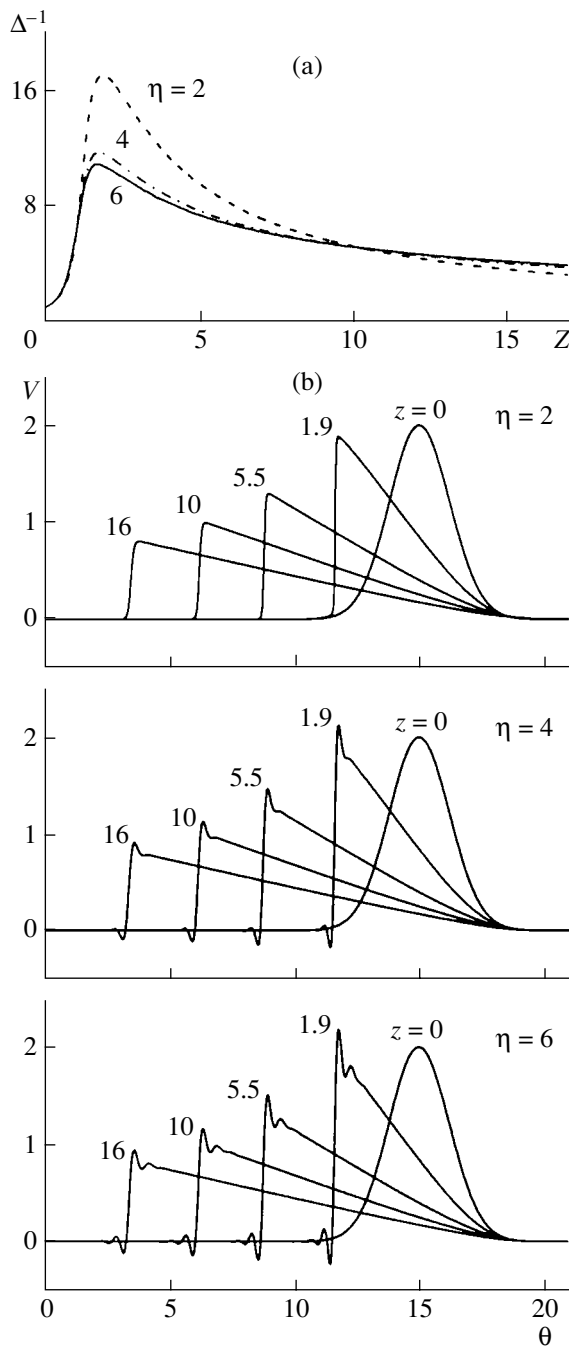
Fig. 6. (a) Shock front steepness as a function of distance and (b) the evolution of the profile of the initially Gaussian pulse for different absorption laws $\eta = 2$, 4, and 6 and the corresponding absorption parameters $\Gamma_2 = 2.5 \times 10^{-2}$, $\Gamma_4 = 3 \times 10^{-4}$, and $\Gamma_6 = 2.45 \times 10^{-6}$.

Fig. 7. Shock front steepness of the initially harmonic wave as a function of distance for different absorption laws $\eta = 2$, 4, and 6 and different absorption parameters Γ. The solid curves are obtained from the numerical solution, and the dashed curves, from the exact solution to the equation of simple waves by replacing the mathematical discontinuity with the corresponding stationary solution.

features play a significant role. It is the front steepness that determines either the temporal spacing of the grid or, in the spectral approach, the required number of harmonics. As a result, for fixed parameters of the numerical scheme, the use of an invented absorption rapidly increasing in the high-frequency region results in smaller distortions of the solution structure in compar-

ison with the discontinuous solution in a lossless medium, in which the mathematical discontinuity is replaced with the corresponding stationary solution. In this case, wave energy absorption will also nearly coincide with the absorption caused by discontinuities in the stationary wave.

As is known, the wave energy absorbed at an infinitely narrow (discontinuous) front is proportional to the third power of the discontinuity amplitude [3]. In dissipative media with $\eta = 2$ and 4, the absorption at the shock front of a finite width is independent of linear loss Γ and coincides with the absorption at an infinitely narrow discontinuity if the shock front width is small in comparison with other wave scales [1, 2]. One can easily show that this situation holds for $\eta = 6$ and any other even η. Assume that the solution V has a narrow shock

front and sufficiently smoothly tends to zero behind the front. As in [1], we multiply Eq. (2) by $Vd\theta$ and integrate the result in infinite limits. Then, using notation $R = (-1)^{\frac{\eta-2}{2}} \Gamma$, for the energy $E = \int_{-\infty}^{\infty} V^2 d\theta$ we obtain the equation

$$\frac{dE}{dz} = 2R \int\limits_{-\infty}^{\infty} V \frac{\partial^\eta V}{\partial\theta^\eta} d\theta, \qquad (9)$$

or, after integration by parts,

$$\frac{dE}{dz} = 2RV \frac{\partial^{\eta-1} V}{\partial\theta^{\eta-1}} \bigg|_{-\infty}^{+\infty} - 2R \int\limits_{-\infty}^{\infty} \frac{\partial^{\eta-1} V}{\partial\theta^{\eta-1}} \frac{\partial V}{\partial\theta} d\theta. \qquad (10)$$

The first term on the right-hand side of Eq. (10) vanishes in view of the condition $V|_{\theta \to \pm\infty} = 0$. Derivatives $\partial^{\eta-1} V/\partial\theta^{\eta-1}$ in the second term behave as narrow peaks near the shock front and rapidly vanishing smooth functions at a distance from the front, so that the absorption mainly occurs at the shock front. Then, assuming that the front profile in the integration region nearly coincides with the stationary wave profile (i.e., setting $\partial V^2/\partial\theta = -2R\partial^\eta V/\partial\theta^\eta$) and integrating over θ in view of $|V|_{\theta \to \pm\infty} = V_0$, we obtain

$$-2R \partial^{\eta-1} V/\partial\theta^{\eta-1} = (V^2 - V_0^2). \qquad (11)$$

Substituting Eq. (11) into Eq. (10), we obtain the desired expression for the wave energy absorption:

$$\frac{dE}{dz} = \int\limits_{-V_0}^{V_0} (V^2 - V_0^2) dV = -\frac{4}{3} V_0^3 = -\frac{1}{6} A_s^3, \qquad (12)$$

where A_p is the amplitude of pressure discontinuity.

Thus, the self-similar property of the solutions to Eq. (2) and the stationary solutions (Fig. 1) obtained numerically in this paper for certain fixed discontinuity amplitude and absorption parameter allow one to obtain the whole class of stationary solutions to Eq. (2) for different absorption laws with even powers of frequency, an arbitrary absorption magnitude, and an arbitrary discontinuity amplitude. As the power η in the frequency-dependent absorption law increases, the amplitude and number of oscillations appearing in the stationary wave profile increase (for $\eta = 4$ and 6). In the case of harmonic and pulsed initial signals, the structure of the shock front of a finite width formed in a weakly absorbing medium at the stage of fully developed discontinuities reproduces the structure of the stationary wave front; moreover, the absorption at the shock front coincides with the absorption at an infinitely narrow discontinuity of the same amplitude. The smoothing of the front in the course of propagation is more prominent for the absorption quadratic in frequency; for this reason, the use of invented absorption rapidly increasing in the high-frequency region is worthwhile in the simulations of discontinuous waves: it minimizes the shock wave spreading and yields a more accurate description of the smooth segments of the wave profile and the wave energy absorption. However, this invented absorption causes oscillations around the shock front, so that the shape of the profile near the front, as well as the peak values of the wave, will be distorted.

REFERENCES

1. O. V. Rudenko and V. A. Robsman, Dokl. Akad. Nauk **384** (6), 31 (2002) [Dokl. Phys. **47**, 443 (2002)].

2. O. V. Rudenko and S. I. Soluyan, *Theoretical Foundations of Nonlinear Acoustics* (Nauka, Moscow, 1975; Plenum, New York, 1977).

3. A. D. Pierce, *Acoustics* (Am. Inst. of Physics, New York, 1991).

4. *Physical Principles of Medical Ultrasound*, Ed. by C. R. Hill (Ellis Horwood, New York, 1986; Mir, Moscow, 1989).

5. M. R. Bailey, V. A. Khokhlova, O. A. Sapozhnikov, *et al.*, Akust. Zh. **49**, 437 (2003) [Acoust. Phys. **49**, 369 (2003)].

6. P. T. Christopher and K. J. Parker, J. Acoust. Soc. Am. **90**, 488 (1991).

7. E. A. Filonenko and V. A. Khokhlova, Akust. Zh. **47**, 541 (2001) [Acoust. Phys. **47**, 468 (2001)].

8. A. L. Polyakova, S. I. Soluyan, and R. V. Khokhlov, Akust. Zh. **8**, 107 (1962) [Sov. Phys. Acoust. **8**, 78 (1962)].

9. O. A. Vasil'eva, A. A. Karabutov, E. A. Lapshin, and O. V. Rudenko, *Interaction of One-Dimensional Waves in Dispersionless Media* (Mosk. Gos. Univ., Moscow, 1983) [in Russian].

10. S. S. Kashcheeva, O. A. Sapozhnikov, V. A. Khokhlova, *et al.*, Akust. Zh. **46**, 211 (2000) [Acoust. Phys. **46**, 170 (2000)].

11. V. G. Andreev, Yu. A. Pishchal'nikov, O. A. Sapozhnikov, *et al.*, Akust. Zh. **45**, 13 (1999) [Acoust. Phys. **45**, 8 (1999)].

12. V. A. Khohlova and S. S. Kashcheeva, in *Proceedings of Seminar of Prof. V.A. Krasil'nikov Scientific School on Physical and Nonlinear Acoustics* (Moscow, 2002), p. 161.

13. W. H. Press, S. A. Teukolsky, W. T. Vetterling, and B. P. Flannery, *Numerical Recipes in FORTRAN* (Cambridge Univ. Press, New York, 1992).

Translated by A. Vinogradov

Image Quality Improvement in Ultrasonic Nondestructive Testing by the Maximum Entropy Method

A. E. Bazulin and E. G. Bazulin

OOO Ekho+ Research and Production Center, Russian Research Center Kurchatov Institute,
pl. Kurchatova 1, Moscow, 123182 Russia
e-mail: bazulin@echoplus.ru; baz-a@mail.ru
Received March 11, 2004

Abstract—We consider the possibility of solving the inverse scattering problem in the linear approximation (in the form of a convolution equation) by reducing it to a system of linear algebraic equations and minimizing the residual. Since the problem is an ill-posed one, the Tikhonov regularization proves useful. The possibility of using the entropy of the image estimate as a stabilizing functional is considered, which is the key idea of the maximum entropy method. The single-frequency and multifrequency versions of the method are realized. The advantage of the maximum entropy method over the conventional linear methods of solving the inverse scattering problem is shown. The superresolution and sidelobe suppression abilities of the maximum entropy method are demonstrated. The method is shown to be stable to measurement noise and multiplicative interference in the form of aperture decimation. Examples of the image reconstruction by the maximum entropy method from model and experimental data are presented. © 2005 Pleiades Publishing, Inc.

INTRODUCTION

Obtaining information on the internal structure of such different optically opaque objects as the ocean, human body, welds in pipelines, etc., is a topical problem belonging to the class of inverse scattering problems. The inverse scattering problem consists in determining the quantitative characteristics of inhomogeneities from observations of the field scattered by them. Different types of incident field are used: electromagnetic, X-ray, acoustic, etc.

A widespread type of inverse scattering problems in nondestructive testing are those concerned with ultrasonic sounding of optically opaque objects and structures. The purpose of sounding is to find internal defects (cavities, cracks, etc.) and determine their size. An important issue in ultrasonic nondestructive testing is how to classify the defects found and how to generate an expert evaluation of whether the object is suitable for use.

To obtain sufficiently high-resolution images of the defects, systems that coherently process the measured echo signals are employed. In Russia, the Avgur-4.2 system [1] is used to test pipeline welds at nuclear power plants. Abroad, the Masera system from Technoatom and the μ+ system from Sonomatic are used to check performance-critical structures. Such industrial systems obtain images of the scatterers by algorithms that solve the scalar inverse scattering problem in the Born approximation. Among the algorithms of this class, there are the SAFT method [2, 3], the angular spectrum method [4], and the

method of projection in the spectral space [5, 6]. The latter method is especially efficient, because it takes a small time to reconstruct the scatterer images from a set of echo signals measured in the combined mode, when the ultrasonic pulses are transmitted and received by the same transducer.

The underside of simplicity of these algorithms is that images of the defects are far from always being of a sufficiently high quality. They exhibit a high level of spurious images produced by multiply scattered pulses and pulses generated in wave transformations accompanying the scattering from the inhomogeneities. Also, it is not always possible to uniquely identify the defect's shape, because the image is reconstructed only for the part of its boundary from which the echo pulses are recorded at the reception site. The problem of improving the resolution and reducing the speckle noise is topical in nondestructive ultrasonic testing.

To obtain images whose resolution is higher than the Rayleigh limit, i.e., superresolution images, algorithms that extrapolate frequency and angular signal spectra are used. For example, the Gershberg–Papoulis iteration algorithm [7–10, 22] or the algorithm that extrapolates the spectrum of echo signals through constructing their autoregressive (AR) model [11–14]. The Gershberg–Papoulis algorithm is used to extrapolate the echo signal spectrum, which enhances the range resolution, as well as to extrapolate the complex image spectrum, which enhances both the range resolution and the lateral resolution. Because the Gershberg–Papoulis method applies thresholding at a level of about 30% of

the maximum value, it neglects information about small-amplitude scatterers. Extrapolation of the echo signal spectrum in terms of its AR model improves only the range resolution rather than the lateral resolution.

Among various methods for solving such problems, one may distinguish the so-called maximum entropy method (MEM). It was substantiated, and the first practical results were obtained in the 1950s by Jaynes, who demonstrated that Shannon's entropy can be used in fuzzy decision problems. Shannon's entropy of a set of discrete independent random quantities is defined as follows:

$$H = -\sum_{i=1}^{N} p_i \ln p_i.$$

In 1972, Freiden showed that entropy can be used as a stabilizing functional in the Tikhonov regularization method [20]. It was demonstrated that superresolution can be achieved in an imaging system (a one-dimensional noncoherent object and a diffraction-limited forming system) [15]. The image pixel intensity was associated with probabilities. The study has shown that the MEM is efficient for reconstructing images in tomography [16], radio astronomy [17], nuclear magnetic resonance (NMR) [18], and ultrasonic testing [19]. Conferences under the title *Bayesian Framework and Maximum Entropy* are held on a regular basis, and capabilities of the MEM are extended from year to year.

In this paper, we consider the possibility of applying the MEM in ultrasonic testing to enhance the scatterer image quality.

MATRIX MODEL OF THE SCATTERING PROBLEM

Following [19], let us write the formula that describes the scattering and reception of ultrasound at a frequency ω:

$$U(r_{RCV}, \omega) = \pm 2jk \int_S \theta(r, \omega) \tag{1}$$
$$\times g(r_{RCV} - r, \omega) U_0(r, \omega) f(r) dr + n(r_{RCV}, \omega).$$

Here, $r \in S_{DEF} \subset R^2$ is the position vector of a point in the scattering region (shown in Fig. 1 in gray), $r_{RCV} \in S_{RCV} \subset R^1$ is the position vector of a point on the linear receiving aperture, j is the imaginary unit, k is the wave number, $g(r, \omega)$ is the Green's function of the Helmholtz equation at the frequency ω, $\theta(r, \omega)$ is the receiver pattern, $f(r)$ is the scattering potential (independent of frequency), $U_0(r, \omega)$ is the primary illumination field, and $n(r_{RCV}, \omega)$ is the additive measurement noise.

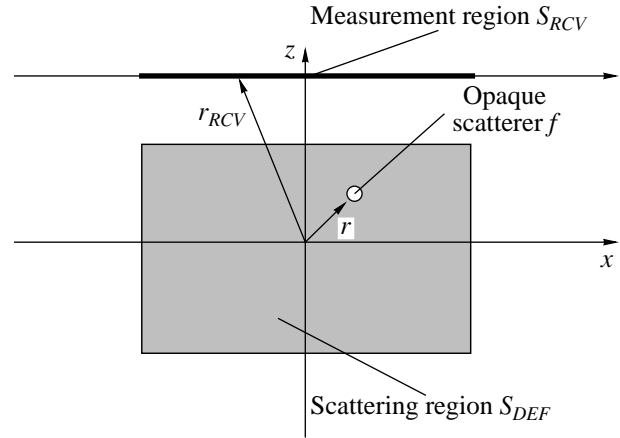The plus and minus signs before the integral in Eq. (1) refer to boundary problems I and II, respec-

Fig. 1. Schematic diagram of the scattered field measurements in the combined mode.

tively. Boundary problem I models acoustically soft scatterers; boundary problem II, acoustically hard scatterers and is typical of ultrasonic nondestructive testing applications.

The system that creates holograms $U(r_{RCV}, \omega)$ is assumed to be linear, and the linear model is constructed in terms of the Kirchhoff approximation (physical optics approximation) for opaque scatterers. Equation (1) was derived under the following assumptions:

(i) only the first-order scattering from the scatterers is taken into account (multiple scattering is ignored);

(ii) the mode transformation is ignored;

(iii) the scatterer boundary is smooth;

(iv) the field in the scatterer's shadow is zero;

(v) the field gradients and the Green's function are calculated under the assumption that only plane waves propagate in the medium and the wave reflected by the scatterer's face propagates along the normal to the face; and

(vi) only the I- and II-kind boundary conditions are modeled.

In spite of these assumptions, there are many methods for solving the inverse scattering problem in the linear approximation that provide images whose quality is sufficiently high for the majority of applications. Systems that successfully realize these algorithms in practice were mentioned in the Introduction.

The above model allows us to simulate various sounding techniques by choosing the corresponding function $U_0(r, \omega)$. In particular, to simulate monostatic measurements, in which the transmitter and receiver are collocated, we use $U_0(r, \omega)$ in the form of the same Green's function $g(r, \omega)$ and, without loss of generality, the monostatic measurement model alone is considered below.

To solve the direct and inverse scattering problems on a computer, a discrete model of ultrasonic scattering and reception must be constructed. Equation (1) is sampled on a uniform grid in Cartesian coordinates xz. The same grid is used for the unknown solution f to the equation.

Below, we use the following notations: N and M are the x- and y-axis dimensions of the grid in the image reconstruction region, respectively; Δx and Δz are the grid step sizes in the x and z axes, respectively; A is the number of points on the linear aperture (the distance between the samples is also Δx); f is the lexicographically ordered $NM \times 1$ vector, which is a discrete representation of the scattering potential in the image reconstruction region

$$\text{(i.e., we write } f = \begin{pmatrix} f_{11} \\ f_{12} \\ \vdots \\ f_{1N} \\ f_{21} \\ f_{22} \\ \vdots \\ f_{2N} \\ \vdots \\ f_{M1} \\ f_{M2} \\ \vdots \\ f_{MN} \end{pmatrix} \text{ instead of } f = \begin{pmatrix} f_{11} & f_{12} & \cdots & f_{1N} \\ f_{21} & f_{22} & \cdots & f_{2N} \\ \vdots & \vdots & \ddots & \vdots \\ f_{M1} & f_{M2} & \cdots & f_{MN} \end{pmatrix},$$

where f_{ij} is the value of function $f(r)$ at the point r_{ij}); h_ω is the $A \times 1$ vector, which represents the ultrasonic field $U(r_{RCV}, \omega)$ measured on the receiving aperture at the frequency ω (in the single-frequency case, we omit the subscript); we will also call h_ω a hologram at the frequency ω; and $h_\omega^i = U(r_{RCV_i}, \omega)$, where r_{RCV_i} is the distance to the ith point of the receiving aperture. In practicing nondestructive testing, numbers of samples N, M, and A may be as high as about 1000.

The wave propagation to the receiving aperture is taken into account by the $A \times NM$ circulant matrix[1] G_ω, which is a discrete representation of the squared Green's function in the image reconstruction region with allowance for the pattern:

[1] The term circulant matrix refers to the matrix of the following structure: $Q = \begin{pmatrix} q_{11} & q_{12} & \cdots & q_{1N} \\ q_{21} & q_{22} & \cdots & q_{2N-1} \\ \vdots & \vdots & \ddots & \vdots \\ q_{12} & q_{13} & \cdots & q_{11} \end{pmatrix}$, i.e., each subsequent row of the matrix is equal to the preceding row shifted one place to the right.

$$G_\omega = \begin{pmatrix} g_{1,1} & g_{1,2} & \cdots & g_{1,NM} \\ g_{2,1} & g_{2,2} & \cdots & g_{2,NM} \\ \vdots & \vdots & \ddots & \vdots \\ g_{A,1} & g_{A,2} & \cdots & g_{A,NM} \end{pmatrix}.$$

Here, the row of number i is a discrete representation of the squared Green's function, with which the scattering potential must be convolved to obtain the field at the ith point of the receiving aperture:

$$g_{i,nm} = \pm 2jk\theta^2(r_{nm})g^2(r_{RCV_i} - r_{nm}, \omega)/\Delta x,$$

where r_{RCV_i} is the distance to the ith point of the receiving aperture and r_{nm} is the distance to the point in the image reconstruction region, at which the sample of number n, m on the X and Z axes, respectively, is taken. This model can also describe the effect of a multiplicative interference on the hologram. The multiplicative interference is represented by multiplying the hologram by a random function. In the discrete formulation, it is convenient to represent the effect of the multiplicative interference by multiplying the hologram by a diagonal matrix.

It is of interest in image reconstruction when S is a decimation operator, which models the loss of a portion of data on the receiving aperture. In the harmonic case, to solve the direct scattering problem, i.e., to calculate the field on the receiving aperture, one can perform the following matrix operations:

(i) multiply the matrix of the operator G of the direct problem by f (which corresponds to the calculation of the convolution integral in Eq. (1) by the method of rectangles);

(ii) add the vector of the discrete complex zero-mean Gaussian white noise with the variance σ^2, i.e., $n_\omega = (n_1 \ n_2 \ \dots \ n_A)^T$, where $\mathrm{Re} n_i \sim N(0, \sigma^2)$ and $\mathrm{Im} n_i \sim N(0, \sigma^2)$; and

(iii) apply the matrix S of the multiplicative interference for the aperture decimation case, which sets the field measured at particular nodes equal to zero in order to allow for the data loss on the receiving aperture.

Ultimately, the direct scattering problem at the frequency ω is formulated as follows:

$$h_\omega = S(G_\omega f + n_\omega). \tag{2}$$

In practice, holograms are usually calculated at K frequencies within the range $(\omega_{min}; \omega_{max})$ and processed simultaneously:

$$h = (h_{\omega min} \ \dots \ h_{\omega max})^T$$

$$= \begin{pmatrix} S_{\omega min} & \dots & 0 \\ \vdots & \ddots & \vdots \\ 0 & \dots & S_{\omega max} \end{pmatrix} \begin{pmatrix} G_{\omega min} \\ \vdots \\ G_{\omega max} \end{pmatrix} f + \begin{pmatrix} n_{\omega min} \\ \vdots \\ n_{\omega max} \end{pmatrix}. \tag{3}$$

This model can be modified in order to allow, for example, for multiple scattering of the field by the inhomogeneities and for wave transformation. It may also be possible to allow for the geometry and smooth variation of the velocity of sound in the object under testing by constructing an appropriate Green's function, which is in general a separate and very complex problem. The more accurately the direct scattering problem is described, the more reliable the solutions obtained by minimizing the residual of the direct problem are.

As the quality criterion of the reconstructed image, we use the squared residual (written for a single frequency below):

$$\chi^2(f) = \rho^2(SGf, h) = \|SGf - h\|^2$$
$$= (SGf - h)^T(SGf - h). \tag{4}$$

That is, the reconstructed image is a solution to the unconstrained minimization problem (solution in terms of the least squares method):

$$\hat{f} = \arg \min_{f \in R^{MN}} (\chi^2(f)). \tag{5}$$

Within the terminology used in [20], a solution to degenerate system (2) that provides the minimum error χ^2 is called a pseudosolution. There are an infinite number of such pseudosolutions, and such parameters as resolution and level of speckle noise are in general far from ideal values.

Since the digital acoustic holography uses complex numbers, the dimension of all variables becomes twice as large and both the real and imaginary parts of the image must be reconstructed, which is required by the optimization problem with a complex criterion. In the calculations, the vectors and matrices are written in the form:

$$f \equiv \begin{pmatrix} f^{\mathrm{Re}} \\ f^{\mathrm{Im}} \end{pmatrix}, \quad G \equiv \begin{pmatrix} G^{\mathrm{Re}} & -G^{\mathrm{Im}} \\ G^{\mathrm{Im}} & G^{\mathrm{Re}} \end{pmatrix}. \tag{6}$$

The gradient and Hessian of the criterion are calculated as follows (using differentiation rules for matrix equations):

$$\nabla \chi^2(f) = 2G^T(SGf - h), \tag{7}$$

$$\nabla \nabla \chi^2(f) = 2G^T SG. \tag{8}$$

The formal solution in terms of the necessary condition for the first-order extremum (the gradient of the criterion must be zero) yields [19, 20]

$$\hat{f} = W^T \mathrm{diag}\left[\frac{1}{\lambda_1}, \frac{1}{\lambda_2} \dots \frac{1}{\lambda_{NM}}\right] WG^T Sh, \tag{9}$$

where the singular value decomposition (SVD) of the degenerate matrix is used:

$$G^T SG = W \mathrm{diag}[\lambda_1, \lambda_2, \dots \lambda_{NM}] W^T.$$

The superscript T means matrix transposition. An analog of expression (9) is the inverse filter. If zero values of λ_i or values close to zero appear in the denominator in Eq. (9), it becomes impossible to find a unique solution. The least-squares method is extremely unstable to measurement noise. The noise component soon starts dominating over the useful part of the solution due to the large number of zero-valued λ_i. At the same time, the property that the Hessian is positively semidefinite guarantees the necessary conditions for the second-order minimum to exist in the optimization problem (5).

The fundamental importance of the approach based on the least-squares method consists in the freedom of choosing the point spread function G. To determine the point spread function, one can solve the problem for the Green's function of half-space, layer, or more complex geometry or use an experimentally measured point spread function. At the same time, this approach places demanding requirements on computer resources. In particular, to reconstruct an $M \times N = 256 \times 256$ image

measured on an aperture consisting of $A = 128$ samples, it is necessary to store a 256×32768 matrix G and multiply it by the vector f consisting of 256 rows. Since the matrix G is circulant, there exists the possibility of considerably reducing the memory required (only one row can be stored) and the time necessary to calculate the product Gf by using the property that the circulant matrix can be transformed to a diagonal matrix by the discrete Fourier transform [19]. The use of the fast Fourier transform (FFT) algorithm reduces the computational complexity of calculating the product Gf from about N^3 to $N\log N$; however, in this case, it is necessary to use a regular grid in the discrete model.

THE MAXIMUM ENTROPY METHOD AS A PARTICULAR CASE OF THE REGULARIZATION METHOD

Tikhonov developed a method for solving ill-posed problems called the regularization method [20]. For the Hadamard ill-posed problem written in the operator form

$$Af = h,$$

the variational principle of solution selection (construction of the regularization operator) can be formulated as the optimization problem

$$\hat{f}_\alpha = \arg\min_{f \in R^{MN}} (\chi^2(f) + \alpha\Omega(f)), \qquad (10)$$

where f is the solution, $\chi^2(f)$ is the squared residual of the solution in the metric determined by the specific problem, and $\Omega(f)$ is the stabilizing functional intended to reduce the domain of solutions. An ill-posed inverse convolution problem can be solved as follows:

(i) we transform the convolution equation to a system of linear equations with a degenerate matrix (2), (3);

(ii) choose a stabilizing functional $\Omega(f)$;

(iii) formulate the optimization problem to minimize the discrete analog of the functional $\Omega(f)$ and the residual of the solution to system (4); and

(iv) solve the optimization problem and the problem of choosing the optimal regularization parameter α.

Thus, instead of solving the original problem given by Eq. (5), we solve problem (10), which is stable to small variations in the input data h.

As the stabilizing functional, the optimization problem can use functionals of different classes. The purpose of using the stabilizing functionals is to allow for certain prior information on the solution of the ill-posed problem and thereby reduce the solution domain. The prior information can vary from the simplest constraint that the solution be nonnegative or its certain norm be minimal to constraints imposed on the known autocorrelation function, spectrum structure, and so on.

In [19], an algorithm is presented for the ultrasonic image reconstruction by the maximum entropy method, in which the optimization problem uses entropy of the image estimate as the stabilizing functional:

$$\hat{f} = \arg\min_{f \in R^{MN}} (\chi^2 - \alpha H(f)).$$

Here, H is either the entropy of a set of independent discrete random variables defined (for nonnegative real f_i) as

$$H(f) = -\sum_{i=1}^{NM} f_i \ln f_i = -\Omega(f), \qquad (11)$$

where NM is the number of pixels in the image being reconstructed or the cross entropy, also called Kullback–Leibler distance [21]:

$$H(f) = -\sum_{i=1}^{NM} f_i \ln \frac{f_i}{m_i}. \qquad (12)$$

Here, m is the prior model or estimate of the form of solution f. As the simplest model, a constant value $e\mu$ was used, where μ represented the estimate of the average intensity of the image background. This formulation circumvents one of the problems associated with the maximum entropy criterion. The point is that, when part of the image pixel intensities approach zero, the logarithm in the expression for the entropy becomes too large, which hampers the convergence to images with a zero background level. In this case, the components of the entropy gradient will be close to zero for intensities close to μ. An additional difficulty of using entropy in form (12) is that the parameter μ must be estimated; however, it has been shown that identical results are observed in reconstructing from model and experimental data with values of μ that differ by several orders of magnitude. The question of using not so trivial image models is the subject of further research. We expect that the amount of artefacts in the images being reconstructed may be reduced through the use of nontrivial prior image models. The maximum entropy criterion is known to enhance the contrast regions of the image (point scatterers, boundaries). Due to this feature, the MEM has found wide application in radio astronomy and may be used in ultrasonic testing.

Since the algorithm is nonlinear, superresolution can be achieved in the image reconstruction, because the components that are produced not only by incomplete source information appear in the spectrum of $f(r)$.

The fact that the logarithm automatically allows for the constraint that the image be nonnegative was recognized in [22, 23] as the main advantage of the maximum entropy method in the form of Eq. (11). However,

to correctly reconstruct the image of f in the coherent case (ultrasonic nondestructive testing, NMR), it must be reconstructed as a complex function and its real and/or imaginary parts may take negative values. Various approaches exist that circumvent this problem [19]. For example, the image can be decomposed into four subimages whose phases are shifted so that the real part of each subimage is nonnegative. Thus, one has to solve four independent reconstruction problems, shift their phases back, and combine the subimages into a single result.

In this paper, we generalize the MEM to complex calculations by using the entropy of the absolute value of the complex image. For vectors (6) with complex-valued components, we can write

$$z_i = |f_i| = \sqrt{(f_i^{Re})^2 + (f_i^{Im})^2},$$

$$H = -\sum_{i=1}^{NM} z_i \ln \frac{z_i}{e\mu}.$$

In this case, the components of the gradient and Hessian of the entropy have the form

$$\frac{\partial H}{\partial f_i^{Re}} = \frac{f_i^{Re} \ln\left(\frac{z_i}{\mu}\right)}{z_i}; \quad \frac{\partial H}{\partial f_i^{Im}} = \frac{f_i^{Im} \ln\left(\frac{z_i}{\mu}\right)}{z_i};$$

$$\frac{\partial^2 H(f_i)}{\partial (f_i^{Re})^2} - \frac{-f_i^{Re} - f_i^{Im} \ln\left(\frac{z_i}{\mu}\right)}{z_i^3};$$

$$\frac{\partial^2 H(f_i)}{\partial (f_i^{Im})^2} = \frac{-f_i^{Im} - f_i^{Re} \ln\left(\frac{z_i}{\mu}\right)}{z_i^3};$$

$$\frac{\partial^2 H(f_i)}{\partial f_i^{Re} \partial f_i^{Im}} = \frac{\partial^2 H(f_i)}{\partial f_i^{Im} \partial f_i^{Re}} = \frac{f_i^{Im} f_i^{Re}\left(\ln\left(\frac{z_i}{\mu}\right) - 1\right)}{z_i^3}.$$

Thus, the optimization problem can be solved by the first-order methods and by the second-order methods as well. First-order methods of the gradient-descent type have been applied with partial success. Since the entropy function is nonlinear, the convergence is extremely slow [24]. The second-order methods, which require the inversion of the Hessian, cannot be applied in practice, because the dimension of the Hessian is too large.

To solve the optimization problem with the entropy as the regularizing functional, a high-performance fast and robust Cambridge algorithm was developed by a research team headed by Skilling [25]. An important property of this algorithm is that it does not invert the Hessian (whose dimension may by quite large), while the convergence is provided by projecting the gradient and the Hessian onto a specially constructed subspace. Circulant matrices are multiplied by vectors with the help of the FFT, which dramatically saves memory, because only one row (or column) of the matrix rather than the whole matrix can be stored. The convergence rate is also increased by changing the metric of the space in such a way that components of the metric tensor become dependent on the entropy's Hessian at the current step of the optimization process. The Cambridge algorithm was extended to the case of complex calculations [19]. Another advantage of this algorithm is that it offers a better estimate of the regularization parameter α. Apparently, the effective practical implementation of the MEM should employ the Cambridge algorithm.

Results reported below were obtained by the high-dimension quasi-Newton algorithm based on the projection onto a two-dimensional space [26].

One of the main problems in implementing regularization methods is the choice of the regularization parameter α, which plays the role of the Lagrange multiplier in constrained optimization problems. The purpose of α is to reconcile the necessity of obtaining an exact solution to the ill-posed problem with the constraint imposed by the stabilizing functional.

There exist many methods for estimating the optimum regularization parameter α^*, which require prior information on the source data precision and/or high computer resources [20]. As a result of the comparative analysis of these methods, we decided to use our proprietary empirical MEM algorithm. Its choice of the optimal regularization parameter relies on an adaptive estimate. The estimate α^* can be calculated from the requirement that the norm of the residual's gradient be equal to the norm of the regularization functional at each step of the optimization process:

$$\alpha_{i+1}^* = -\frac{\|\nabla \chi^2(\hat{f}_i)\|}{\|\nabla H(\hat{f}_i)\|}. \tag{13}$$

This choice of the regularization parameter provides equal norms of the gradient components (necessary conditions for the first-order extremum) and the convergence to a high-quality solution. Since α^* is updated at each step, the choice method given by Eq. (13) is called the adaptive regularization parameter estimator. Its main advantage is that it estimates α^* without any information about the additive measurement noise and about the structure of the decimated aperture. This method also works about ten times faster than some other methods, because it does not solve the same problem many times.

This method showed very good results in the reconstruction of model and experimental data. The image
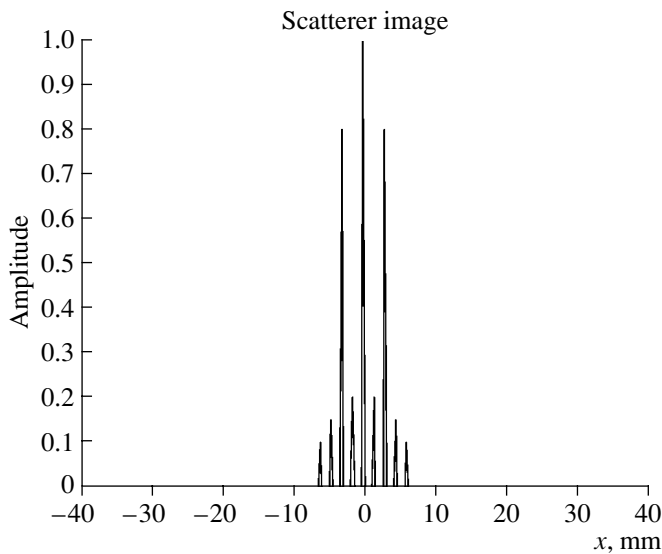
Scatterer image

**Fig. 2.** Image of nine point scatterers used to solve the direct scattering problem.

reconstruction results reported in this paper were obtained using the adaptive regularization parameter estimator.

MODEL NUMERICAL EXPERIMENT

Consider the model of defects in the form of nine point scatterers placed at a depth of 40 mm and spaced 1.5 mm apart (six readings of 1.2λ, where λ is the wavelength at the central frequency of 2.5 MHz) in a sample with a sound velocity of 6.26 mm/μs. The scattering coefficients of the model defects differ by a factor of 10. A 2.5-MHz transducer transmitted and received longi-

tudinal waves. The spatial aperture consisted of 256 readings taken at 0.25-mm-long intervals. The perfect image of the defects is shown in Fig. 2. All figures presented below represent the x coordinate on their abscissas and the magnitude of the complex scattering coefficient on their ordinates. The image reconstructed by the angular spectrum method (ASM) from the measurements taken at five frequencies in the range from 1.0 to 4.0 MHz is shown in Fig. 3a. The Rayleigh resolution at the central frequency of 2.5 MHz is 2.0 mm. The low-amplitude scatterers cannot be distinguished in the reconstructed image in the presence of sidelobes of high-amplitude scatterers. The superresolution provided by the maximum entropy method allows us to reliably determine the number of scatterers and their scattering coefficients (Fig. 3b). It should be noted that amplitudes of the scatterers on the left and on the right of the central scatterer are estimated as 0.26 instead of the true value of 0.2; i.e., the error is 30%.

Figure 4a shows the image of the same defects reconstructed by the angular spectrum method from the data taken on the same spatial aperture but at five frequencies from 2.0 to 3.0 MHz. The image quality also fails to correctly estimate the number of scatterers and their amplitudes, because the quality is such that one can conclude that the number of scatterers is five. The maximum entropy method (Fig. 4b) reliably retrieves the number of scatterers; however, their amplitudes are reconstructed not as reliably as in Fig. 3b because of the insufficient lateral resolution. And, finally, due to the high sidelobes, the measurements taken at a single frequency of 2.5 MHz fail to reliably detect the defects whose amplitudes are 20% lower than the maximum amplitude (Fig. 5).
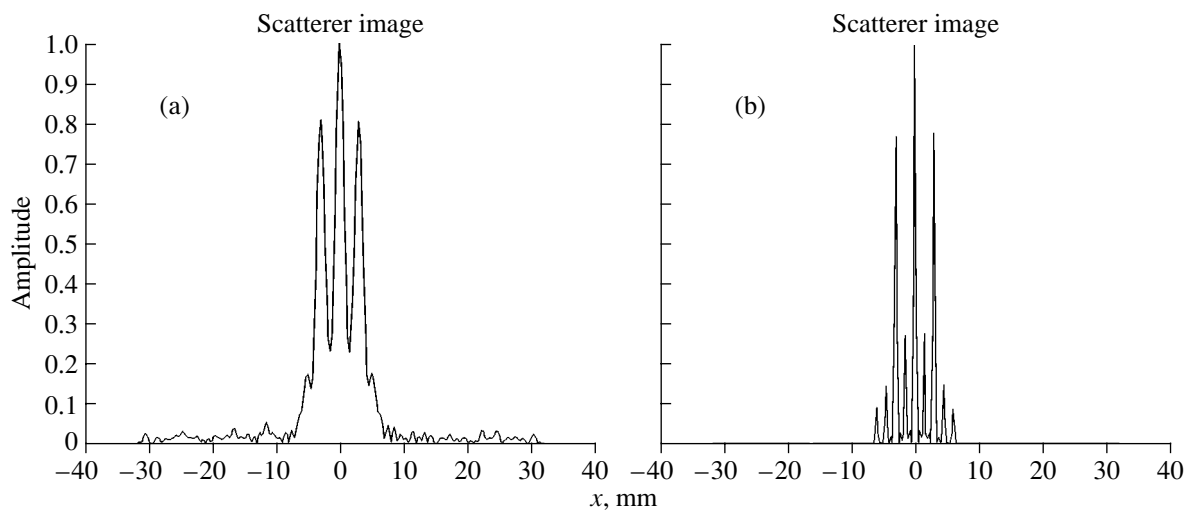
Fig. 3. Image of nine scatterers reconstructed by the (a) ASM and (b) MEM from holograms recorded over the frequency range of 1.0 to 4.0 MHz.
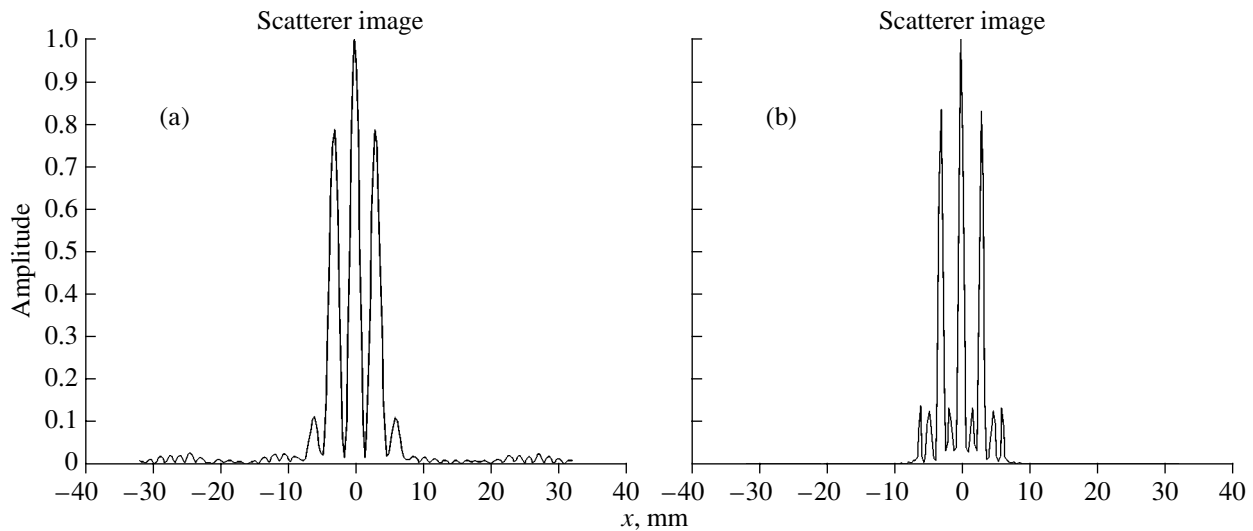
Fig. 4. Image of nine scatterers reconstructed by the (a) ASM and (b) MEM from holograms recorded over the frequency range of 2.0 to 3.0 MHz.
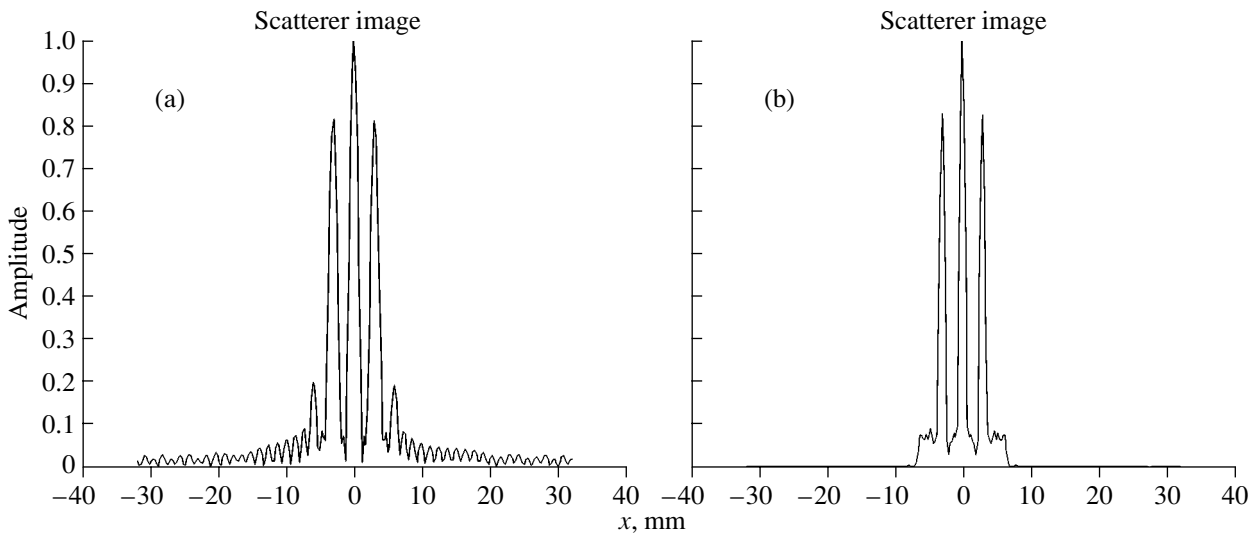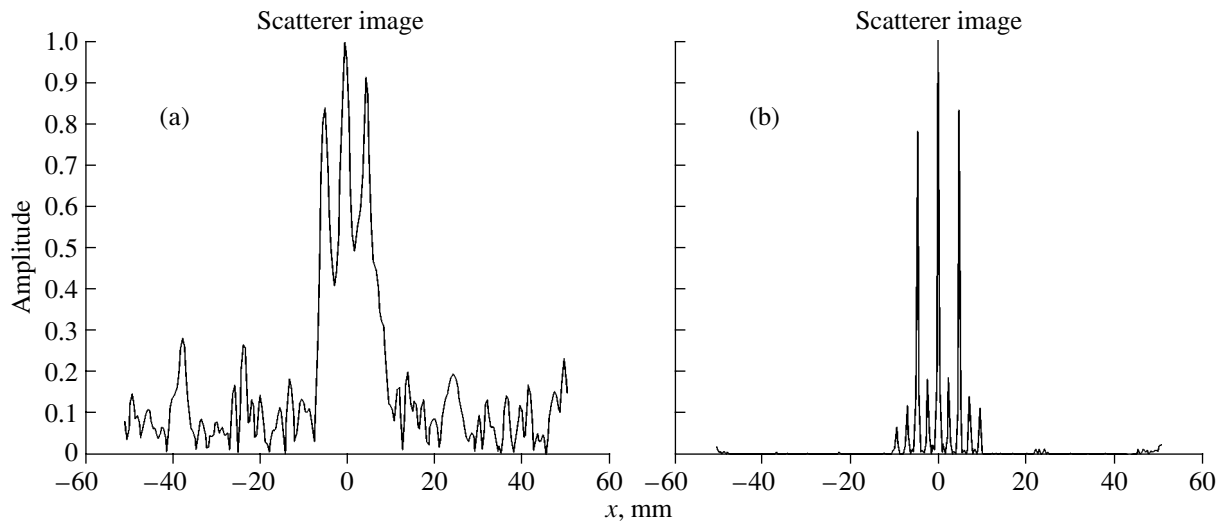

Fig. 5. Image of nine scatterers reconstructed by the (a) ASM and (b) MEM from holograms recorded at a frequency of 2.5 MHz.

The MEM demonstrates the stability to aperture decimation. Figure 6 shows the images reconstructed by the (a) ASM and (b) MEM from holograms measured on 20% of the aperture, the readings being taken at random. The rest of the modeling conditions were the same as in the case illustrated in Fig. 2. A decimation of the aperture by a factor of five exerts almost no effect on the image reconstructed by the MEM, whereas the quality of the image obtained by the ASM noticeably degrades. Figure 7 shows the results of the reconstruction from holograms of Fig. 3 contaminated by an additive Gaussian noise with an intensity σ^2 equal to 0.4 of

the maximum amplitude of the useful signal. The MEM is seen to be quite stable to additive noise.

MODEL EXPERIMENT

The object used in our experiments was a duraluminum sample with six grooves 50 μm wide and 65 mm deep. The distances between the grooves were 1.0, 2.0, 3.5, 5.0, and 7.5 mm. The measurements were taken by a transducer with a flare angle of 60°, central frequency of 2.5 MHz, and frequency band measured between 0.25-power points of 1.8 to 3.2 MHz. The longitudinal wave velocity was $c = 6.26$ mm/μs. The receiving aper-

Fig. 6. Image of nine scatterers reconstructed by the (a) ASM and (b) MEM from holograms recorded over the frequency range of 1.0 to 4.0 MHz with the aperture decimated in a random manner to 20%.
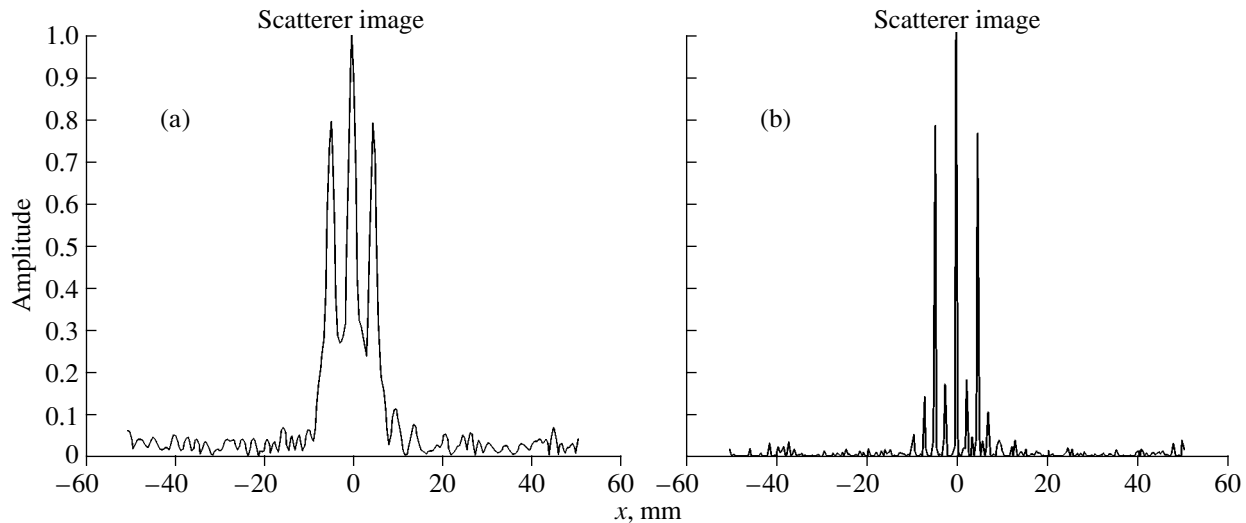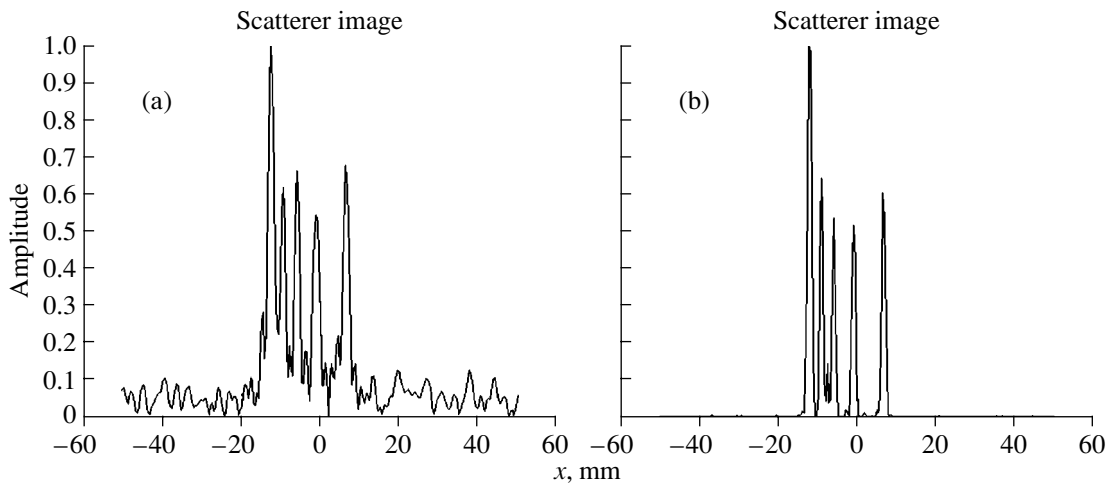

Fig. 7. Image of nine scatterers reconstructed by the (a) ASM and (b) MEM from holograms recorded over the frequency range of 1.0 to 4.0 MHz contaminated with Gaussian noise.

ture consisted of 256 points spaced at 0.394 mm. The tips of the grooves, which are typical point scatterers, were the only objects that could be reconstructed. In order to equalize the frequency and spatial spectra, the inverse frequency and spatial filtering was preliminarily performed.

Figure 8 shows the images reconstructed from a hologram taken at 2.602 MHz by the (a) ASM and (b) MEM. Figures 9 and 10 are the images reconstructed from the data taken at five frequencies in the range from 2.368 to 2.680 MHz by the (a) ASM and (b) MEM, respectively, without aperture decimation and with the aperture decimated by a factor of 2.

The MEM demonstrates its advantage in reconstructing from experimental data. The sidelobe level is lower, and the resolution is a little better than those shown by the ASM. The superresolution ability of the MEM was found to be insufficient to discriminate between the nearest two sidelobes.

It is clear that, in practice, it is necessary to reconstruct two-dimensional and three-dimensional images. To realize an algorithm capable of reconstructing large images, it is necessary to use the FFT to multiply circulant matrices and, perhaps, employ special-purpose optimization algorithms (like the Cambridge algorithm).

Fig. 8. Image of scatterers reconstructed by the (a) ASM and (b) MEM from holograms measured experimentally at 2.602 MHz.
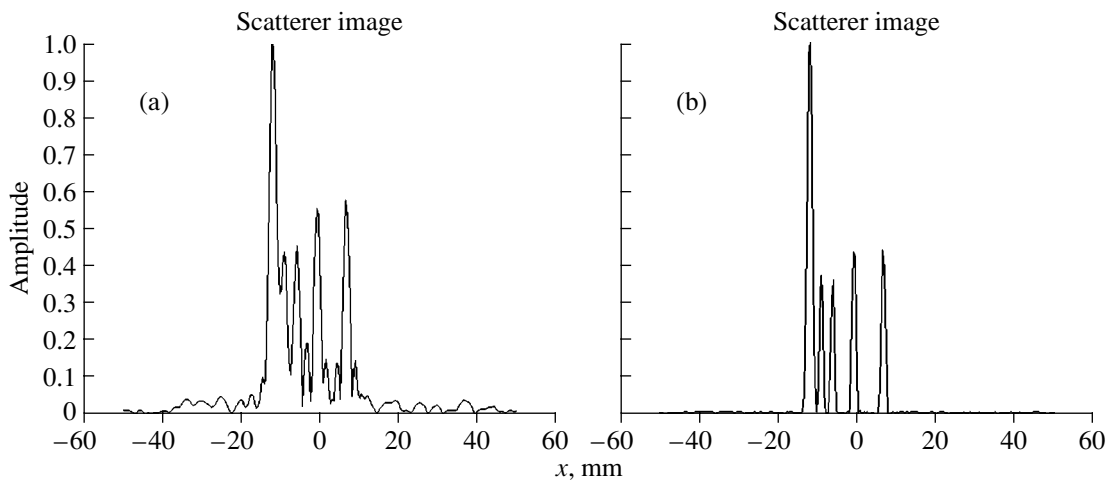
Fig. 9. Image of scatterers reconstructed by the (a) ASM and (b) MEM from holograms measured experimentally at five frequencies in the range from 2.368 to 2.680 MHz.
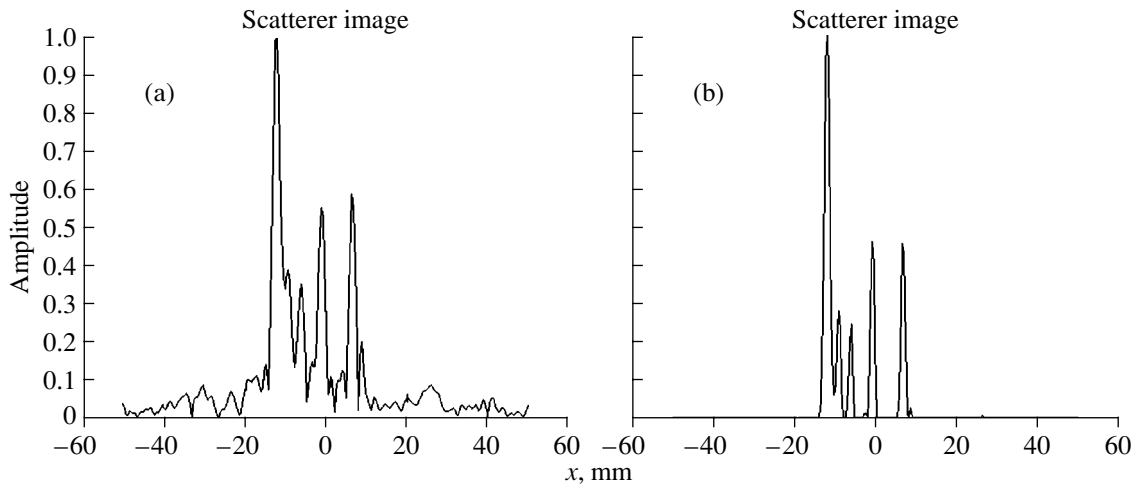
Fig. 10. Image of scatterers reconstructed by the (a) ASM and (b) MEM from holograms measured experimentally at five frequencies in the range from 2.368 to 2.680 MHz on the aperture decimated by a factor of 2.

CONCLUSIONS

A new class of algorithms for reconstructing the images of defects by the nondestructive ultrasonic testing technique is studied. Possibilities of using the maximum entropy method in the image reconstruction from single-frequency and multifrequency holograms are investigated. An efficient method for estimating the regularization parameter is proposed.

The MEM is capable of providing a superresolution and reducing the speckle noise. It is also stable to additive and multiplicative (in the form of decimation) measurement noise. The possibility of using a decimated aperture reduces the amount of measured data, in particular, in three-dimensional holography.

The approach based on the minimization of residual in the solution to the direct problem in combination with various problem-specific constraints holds much promise for wide practical applications, which is demonstrated by model examples. Until recently, the comparatively high demand on computer resources hampered the use of such methods, but the advances in computers has made it possible. The fundamental importance of this approach lies in its ability to solve a wide range of problems of ultrasonic nondestructive testing by choosing an appropriate point spread function (PSF) G. To determine the PSF, one can solve the Green's function problem for a half-space, layer, or more complex structure or use a PSF measured experimentally.

REFERENCES

1. V. G. Badalyan and A. Kh. Vopilkin, Diagnostika **9**, 35 (2000).
2. T. E. Hall, S. R. Doctor, L. D. Reid, *et al.*, Acoust. Imaging **15**, 253 (1987).
3. A. Erhard, B. Lucht, E. Schulz, *et al.*, J. Nondestruct. Test. Ultrason. **5** (9) (2000).
4. J. W. Goodman, *Introduction to Fourier Optics* (McGraw-Hill, New York, 1968; Mir, Moscow, 1970).
5. K. Mayer, R. Markelein, K. J. Langenberg, and T. Kreutter, Ultrasonics **28**, 241 (1990).
6. V. G. Badalyan and E. G. Bazulin, Akust. Zh. **34**, 222 (1988) [Sov. Phys. Acoust. **34**, 132 (1988)].
7. R. W. Gershberg, Opt. Acta **21**, 709 (1974).
8. P. Lasaygues and J.-P. Lefebvre, in *Proceedings of 7th European Conference on Nondestructive Testing, Copenhagen, 1998* (Copenhagen, 1998), p. 3001.
9. A. Papoulis and D. Chamras, IEEE Trans. Acoust., Speech, Signal Process. **25**, 492 (1979).
10. E. G. Bazulin, Akust. Zh. **37**, 8 (1991) [Sov. Phys. Acoust. **37**, 3 (1991)].
11. S. L. Marple, Jr., *Digital Spectral Analysis with Aplication* (Prentice-Hall, Englewood Cliffs, N.J., 1987; Mir, Moscow, 1990).
12. M. Faur, P. Morisseau, and L. Poradis, in *Proceedings of 7th European Conference on Nondestructive Testing, Copenhagen, 1998* (Copenhagen, 1998), p. 2429.
13. G. E. P. Box, G. M. Jenkins, and G. C. Reinsel, *Time Series Analysis. Forecasting and Control* (Prentice Hall, Englewood Cliffs, 1994).
14. E. G. Bazulin, Akust. Zh. **39**, 213 (1993) [Acoust. Phys. **39**, 113 (1993)].
15. B. R. Freiden, J. Opt. Soc. Am. **62**, 511 (1972).
16. C. T. Mottershead, in *Maximum Entropy and Bayesian Methods* (Kluwer, Dordrecht, 1996), pp. 425–436.
17. S. J. Wernecke and L. R. D'Addario, IEEE Trans. Comput. **26**, 351 (1977).
18. P. J. Hore, in *Maximum Entropy in Action* (Clarendon, Oxford, 1991), pp. 41–72.
19. D. J. Battle, *Maximum Entropy Regularization Applied to Ultrasonic Image Restoration* (Univ. Sydney, Sydney, 1999).
20. A. N. Tikhonov and V. Ya. Arsenin, *Methods for Solving Ill-Posed Problems* (Nauka, Moscow, 1986) [in Russian].
21. S. Kullback, *Information Theory and Statistics* (New York, 1968).
22. G. I. Vasilenko and A. M. Taratorin, *Reconstruction of Images* (Radio i Svyaz', Moscow, 1986) [in Russian].
23. A. A. Goryunov and A. V. Saskovets, *Inverse Problems in Acoustics* (Izd. MGU, Moscow, 1989).
24. J. Skilling and R. K. Bryan, Royal Astron. Soc. **211**, 111 (1984).
25. J. Skilling, in *Maximum Entropy and Bayesian Methods in Applied Statistics* (Cambridge University Press, Cambridge, 1986), pp. 179–193.
26. T. F. Coleman and Y. Li, SIAM J. Optim. **6**, 418 (1996).

Translated by A. Khzmalyan

Ocean Acoustic Tomography with a Nonstandard Representation of Refractive Inhomogeneities

V. A. Burov, A. Yu. Popov, S. N. Sergeev, and A. S. Shurup

Faculty of Physics, Moscow State University, Vorob'evy gory, Moscow, 119992 Russia
e-mail: burov@phys.msu.ru
Received July 14, 2004

Abstract—The two-dimensional tomography problem of reconstructing a refractive inhomogeneity in the ocean is considered. A distinction of this paper is the expansion of the inhomogeneity under investigation in a nonstandard (nonorthogonal and overfull) basis. This basis makes it possible to overcome some problems inherent in the conventional schemes dividing the ocean into squares, triangles, and other figures with corners. In addition, the perturbation matrix can be easily constructed in such a basis. The proposed approach can be used in its present form for reconstructing flows and solving combined refractive-kinetic problems. The solution of the tomography problem with the use of the proposed basis is carried out in both ray and wave representations. © 2005 Pleiades Publishing, Inc.

MOSAIC BASIS

In solving the problem of oceanic inhomogeneity reconstruction, one must choose the basis elements that should be used to expand the desired hydrological parameters, such as refractive inhomogeneities, flows, and eddies. In two-dimensional problems, the basis elements usually are plane figures, e.g., squares or triangles, covering the water area of interest [1–3] so that, within every single figure, the parameters remain constant; or, the water area is covered with a grid, at the nodes of which the parameters are specified and the values for intermediate points are calculated by interpolation algorithms [4–7]. However, such an approach to the choice of the basis elements causes technical difficulties even at the stage of solving the direct problem, which precedes the tomographic reconstruction of the desired inhomogeneities. Indeed, after setting the initial approximation for the hydrological parameters and positioning the source–receiver pairs, the standard procedure searches (in the ray approximation) for sound propagation paths (ray trajectories or modes) connecting the elements of such pairs using, for example, the bracket method. In this process, either some rays unavoidably fall in the corners of the basis figures, which makes it impossible to apply Snell's law for calculating their further trajectories, or, in the case of the wave approximation, the grid corners cause false diffraction effects. How to overcome these difficulties is unclear, although it is evident that they are of model origin rather than physical.

In this paper, by analogy with [8], we suggest another approach to the choice of the basis elements. This approach rests upon the expansion of inhomogeneities in the so-called nonstandard bases (Fig. 1), which can be conditionally called mosaic bases. An example of such a basis is the strip basis, i.e., a set of parallel strips rotated in the interval from 0 to π at a uniform angular step. This procedure creates a two-parameter set of strips, where one parameter is the distance to the strip from the center of the circular region and the other is the angular displacement of the strip relative to the initial position. The use of basis elements in the form of strips makes this method free of the above difficulties inherent in tomography schemes dividing the region of interest into elements containing corners.

It is usually assumed that, in the actual ocean, refractive inhomogeneities are weak, so that a nearly linear relationship occurs between the perturbation of sound velocity in a certain area of the reconstructed region and the variation of time required for a ray to travel through this inhomogeneity from the source to the receiver in the case of the ray approach or the perturbation of acoustic field in the case of the wave approach. The process of reconstruction is as follows. Receiving–transmitting antennas are positioned along the perimeter of the region, so that each antenna can communicate with all other antennas. The reconstruction process starts with setting the background (not necessarily everywhere identical) sound velocity distribution in the region of interest (for example, the season-average distribution). Then, sequentially setting a small reference perturbation of sound velocity in each strip and calculating the corresponding perturbation of the received data (variations of propagation time along rays or field perturbation on the transmitter–receiver path) for each of the possible paths, one can construct the perturbation matrix that is denoted **A** in what follows. The column index of this matrix corresponds to the parameters of the transmitter–receiver pair, and the row index corresponds to the parameters of the basis strips. On the other hand, any inhomogeneity, for which one knows
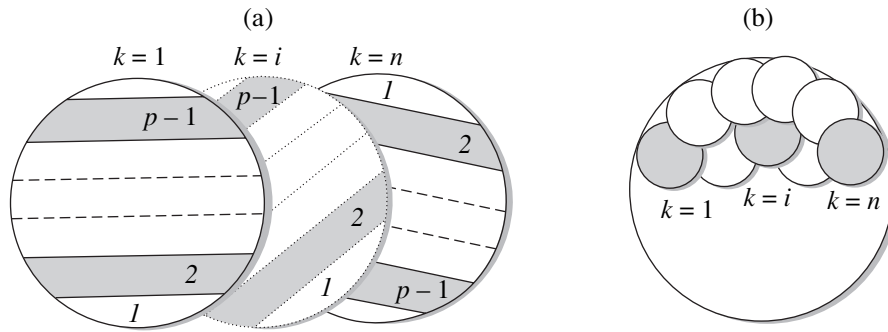
Fig. 1. (a) Strip and (b) cylindrical bases.

only the temporal delays or the field perturbation caused by its insertion in the region of interest, can be expanded in such a strip basis. The expansion coefficients can be found by solving the inhomogeneous system of linear equations

$$\mathbf{AX} = \Delta\mathbf{T}, \qquad (1)$$

where $\mathbf{A}$ is the perturbation matrix; $\Delta\mathbf{T}$ is the received data vector, i.e., the vector of temporal delays or field perturbations caused by the inhomogeneity; and $\mathbf{X}$ is the vector of expansion coefficients of the unknown inhomogeneity in the strip basis, or, in the general case, in another mosaic basis. The least-squares solution of this system has the form

$$\mathbf{X} = (\mathbf{A}^{+}\mathbf{A})^{-1}\mathbf{A}^{+}\Delta\mathbf{T}, \qquad (2)$$

where superscript "+" denotes the Hermitian conjugation. The synthesis and visualization of the reconstructed inhomogeneity is performed by summing the coefficients $\mathbf{X}$ of all strips containing the given spatial point.

The use of the strip basis (and other bases of unconventional expansion) combined with the least-squares solution has a number of useful features. For example, in contrast to the classical tomography scheme based on the Radon transformations, the integrals are taken here over homogeneous basis strips. This fact is important for the ocean tomography problems, where a ray trajectory depends on the inhomogeneity under testing and cannot be considered rectilinear, as in the case of the X-ray tomography. In addition, it appears that the strict requirements usually imposed on a basis, such as completeness and orthogonality, can be slackened. The proposed basis is nonorthogonal and overfull. It is clear that it permits an arbitrary amount of redundancy of the initial data. The nonorthoganility of the basis is of little significance for the problems under consideration, because the reconstruction algorithm includes no scalar product of the basis elements. The presence of overfull data with respect to the basis dimension plays a positive role, because it offers a possibility to increase the number of linear equations of the initial system (1) and, consequently, to enhance the stability of the least-squares

solution. In the context of the problem under consideration, the overfull property implies that the volume of data of all source–receiver pairs considerably exceeds the total number of strips. Naturally, the number of receiving–transmitting transducers I should be reduced to a minimum required value dictated by the resources of an actual experiment. For this reason, one must search for certain combinations of the number of strips and angles to adequately describe the region under investigation. In this process, the number of basis elements must not exceed the number $I(I-1)/2$ of the independent source–receiver pairs.

The use of a priori information through filtering or in the form of regularization procedures can be ascribed to other methods of increasing the stability of the solution. As an example, the receiving–transmitting antennas can be equipped with sound velocity sensors to determine the exact velocity distribution along the perimeter of the region. In the simplest case, the solution can also be regularized by adding the matrix $\mathbf{A}^{+}\mathbf{A}$ with an additional diagonal matrix with small weights, which reduces the degree of singularity of matrix $\mathbf{A}^{+}\mathbf{A}$. Another way to regularize the solution (we use this approach in the numerical simulation of the inhomogeneity reconstruction) consists in imposing certain restrictions on the smoothness of the coefficients of the unknown inhomogeneity expansion in basis elements. Note that the basis used for expanding the inhomogeneity of interest must not necessarily possess a wide degree of completeness. In fact, the degree of completeness should only guarantee the required accuracy of the expansion of the desired distribution. In addition, the additive property of the perturbation effects should be provided (at least approximately).

It should certainly be remembered that this basis is somewhat rough to provide an exact reconstruction of an arbitrary function; however, as we will show below by model examples, it ensures quite acceptable accuracy in the determination of hydrological inhomogeneities. The accuracy can be slightly improved by using the a priori information on the smoothness of the inhomogeneity and performing the corresponding matched filtration, which will be discussed below in the context of numerical simulations.

To illustrate the suggested tomography scheme, we solved the reconstruction problem for different types of inhomogeneities located in the region under consideration in both ray and wave formulations. Computer simulations demonstrated the efficiency of the proposed method.

RECONSTRUCTION OF A REFRACTIVE INHOMOGENEITY IN THE FRAMEWORK OF THE RAY TOMOGRAPHY PROBLEM

The main advantages of the ray theory of wave propagation are the physical clarity and relative simplicity of using the resulting formulas in practical applications. We used the suggested method to investigate the solution of the ray problem taking into consideration the horizontal refraction of rays. With this in view, we considered the eikonal equation whose solution makes it possible to determine the ray trajectories. The presence of inhomogeneity in the region of interest bent the rays and shifted the instants of signal arrival. Varying the positions of the source and receivers, one can obtain the complete pattern of the sounded region and form the vector of relative temporal delays $\Delta\mathbf{T}$.

Solving the inverse problem, we regularized the solution to Eq. (2) according to the simplest procedure $\mathbf{X} = (\mathbf{A}^+\mathbf{A} + \varepsilon\mathbf{E})^{-1}\mathbf{A}^+\Delta\mathbf{T}$, where $\mathbf{E}$ is the unit matrix and ε is the regularizing coefficient.

In numerical simulations, we used the following parameters. We considered a water region 100 km in diameter surrounded by a system of 16 receiving–transmitting transducers. The model distribution of sound velocity over the water region is shown in Fig. 2a. We assumed that the velocity inside the reconstructed inhomogeneity is by 4% smaller than the background velocity everywhere equal to 1500 m/s. In the basis strips, the perturbation corresponded to the decrease in velocity by 1% of the background velocity value. Figure 2b shows the result of reconstruction of a cylindrical inhomogeneity displaced 25 km from the region's center along the negative direction of the abscissa axis. We used the regularizing coefficient $\varepsilon = 0.3$, which is smaller than the maximal eigenvalue of matrix $\mathbf{A}^+\mathbf{A}$ by a factor of about 1000. To improve the quality of reconstruction, we filtered the spatial spectrum of the reconstructed image by cutting off its high-frequency portion (Fig. 2c).

The accuracy of the results was estimated by considering the discrepancies of the solution (n_c) and the right-hand side (n_T) of the system of equations (1). These discrepancies were calculated by the formulas

$$n_c = \sqrt{\frac{\sum_{i,j} |c(x_i, y_j) - \hat{c}(x_i, y_j)|^2}{\sum_{i,j} c^2(x_i, y_j)}},$$

$$n_T = \sqrt{\frac{\sum_m |\Delta T_m - \Delta\hat{T}_m|^2}{\sum_m |\Delta T_m|^2}},$$

where $c(x, y)$ and $\hat{c}(x, y)$ are the actual and reconstructed velocities at a given point (x, y) characterized in discrete form by indices (i, j), $\Delta\hat{\mathbf{T}}$ is the right-hand side of system (1) obtained as a result of the substitution of solution $\mathbf{X}$ into the system, and $\Delta\mathbf{T}$ is the acoustic field perturbation vector corresponding to the actual inhomogeneity (m is the index of elements of this vector). The results of reconstruction seem to be quite satisfactory from the viewpoint that we succeeded in reconstructing the actual velocity value and estimating the radius of the inhomogeneity. We note that the reconstruction quality appears to be satisfactory despite the relatively high values of discrepancies (for example, the discrepancy of the solution measures $n_c \sim 0.5$); namely, the inhomogeneity position, radius, and peaks are reconstructed quite adequately. The point is that the main contribution to the discrepancies is made by fluctuations related to the reconstruction of the background, i.e., the areas where the inhomogeneity is certainly absent; nevertheless, the calculation of discrepancies over the whole water region takes these fluctuations into account.

The use of the nonstandard basis combined with the eikonal equation makes it possible to solve the reconstruction problem using the iteration approach. We introduced iterations as follows. The inhomogeneity reconstructed at the preceding iteration stage was sounded with rays; simultaneously, to this inhomogeneity we successively added additional basis strips characterized by a reference perturbation of sound velocity in the way described earlier, which resulted in a new matrix of perturbations that affects the propagation time at the current iteration. The result of sounding is supposed to be the matrix of relative (i.e., against the background of the unperturbed region) temporal delays of signals propagating through the region occupied by the inhomogeneity. There is no need to solve the eikonal equation at the first iteration (in this case, the background velocity is assumed to be constant for the whole region), because the simplest approach based on Snell's law appears to be adequate for this simple perturbation geometry. However, the construction of perturbation matrix $\mathbf{A}$ at further iterations requires solving the eikonal equation.

Figure 3 shows the results of the iterative reconstruction of an inhomogeneity of radius 20 km located at the center of the water region under test. Figure 3a shows the model distribution of sound velocity over the water region. As earlier, the perturbation of sound velocity in the inhomogeneity was equal to 4% of the background velocity. In the reconstruction, we used the
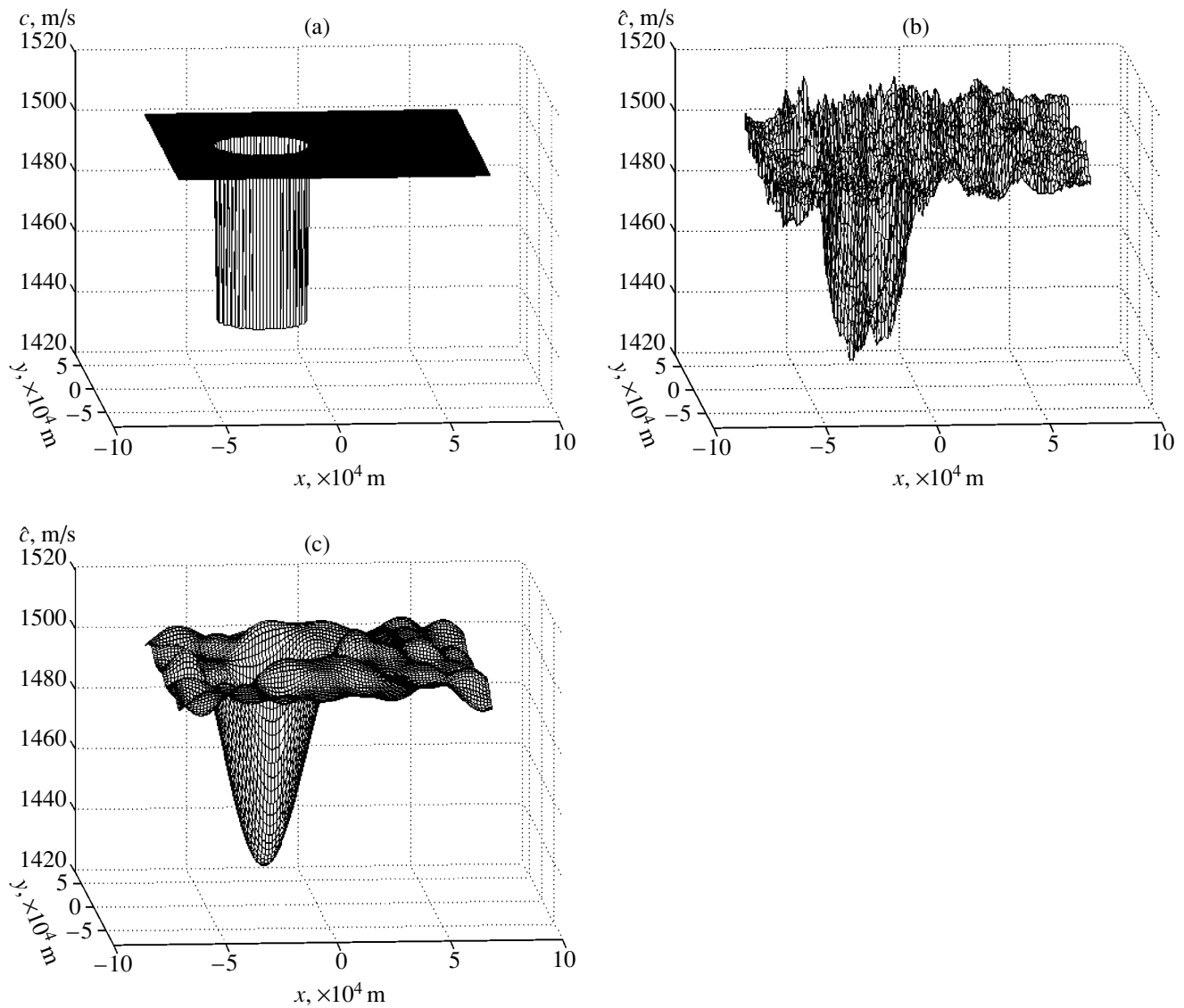
Fig. 2. (a) Model sound velocity distribution over the water region and (b, c) the result of reconstructing this distribution in the ray approximation for the number of receiving–transmitting transducers $I = 16$, the number of basis strips $P = 25$, the number angles of orientation $U = 35$, and the regularizing coefficient $\varepsilon = 0.3$. The estimate (b) before filtration is characterized by the solution discrepancy $n_c = 0.52$ and the right-hand side discrepancy $n_T = 0.28$ and (c) after filtration, by $n_c = 0.45$ and $n_T = 0.27$.

same matrix as in the case shown in Fig. 2. We did not use the high-frequency filtration, because its effect becomes negligible with increasing number of iterations.

From the analysis of the results, we infer that the above iteration process converges to the solution. Indeed, the discrepancies decrease (although slowly) with increasing number of iterations: $n_c = 0.57 \longrightarrow 0.45 \longrightarrow 0.42 \longrightarrow$ .... As earlier, the discrepancies are mainly formed by the noise background of the unperturbed part of the region under investigation, whereas the accuracy of reconstructing the location, size, and peak values of the inhomogeneity is increased, which can be seen from graphical data (see Figs. 3b–3d). Of

course, one must bear in mind that the strip basis used here is a rough basis and the iteration process will improve the solution only to a certain limit.

RECONSTRUCTION OF A REFRACTIVE INHOMOGENEITY IN THE FRAMEWORK OF THE WAVE TOMOGRAPHY PROBLEM

The wave approach is more rigorous and the only one acceptable for working in the low-frequency limit. For solving the direct problem in the wave representation, we had to derive analytical formulas for a cylindrical wave scattered by a basis strip oriented at an arbitrary angle. We solved this problem in two stages. At
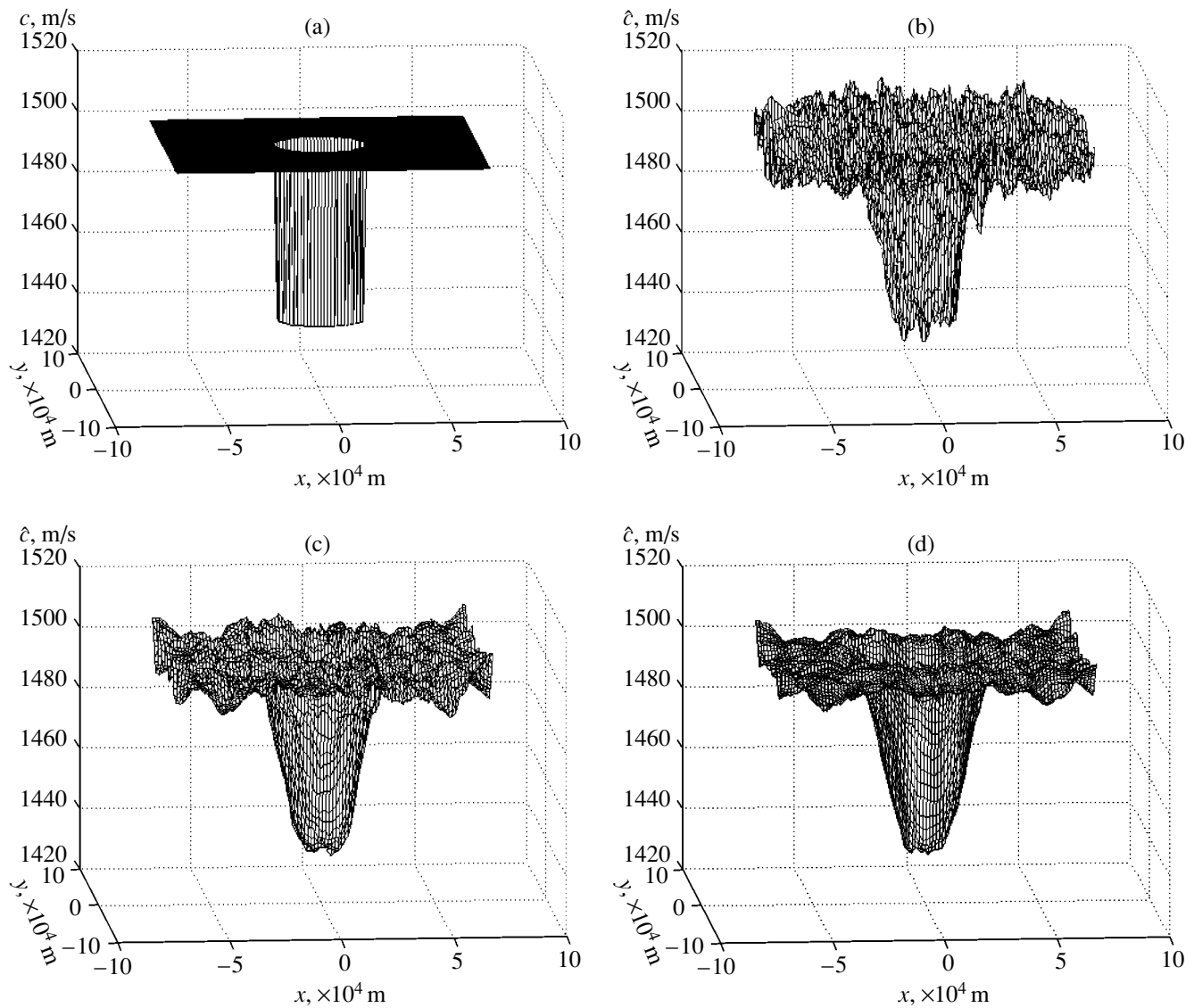
Fig. 3. (a) Model distribution of a cylindrical inhomogeneity at the center of the water region and (b–d) the result of iterative reconstruction of this inhomogeneity in the ray approximation for the number of receiving–transmitting transducers $I = 16$, the number of basis strips $P = 25$, the number of angles of orientation $U = 35$, and the regularizing coefficient $\varepsilon = 0.3$: (b) the first iteration ($n_c = 0.57$, $n_T = 0.26$), (c) the second iteration ($n_c = 0.45$, $n_T = 0.22$), and (d) the third iteration ($n_c = 0.42$, $n_T = 0.14$).

the first stage, we considered the scattering of a cylindrical wave generated by a point source and scattered by a cylindrical refractive inhomogeneity. The problem of the second stage consisted in extending the results to the case of the strip that required a procedure for matching the incident wave with the plane boundary of the scatterer.

Because we assume that the medium is homogeneous in the vertical direction, the problem under consideration is a two-dimensional one. As is known, in the case of a two-dimensional inhomogeneous space containing a cylindrical inhomogeneity characterized by the sound velocity different from that of the background space, the Green's function can be determined

from the system of two Helmholtz equations (one for the external medium and the other for the internal medium) and two boundary conditions reflecting the continuity of the field and its normal derivative at the interface between the media. This procedure allows one to determine an exact expression for the Green's function under consideration; however, it is too cumbersome in the case of the scattering of a cylindrical wave by the basis strip. Here, the main difficulty lies in different symmetry types of the wave and the boundary. The wave has a cylindrical symmetry, whereas the boundary is plane. For this reason, we naturally solve the problem by expanding the incident wave in plane waves, especially due to the fact that the theory of
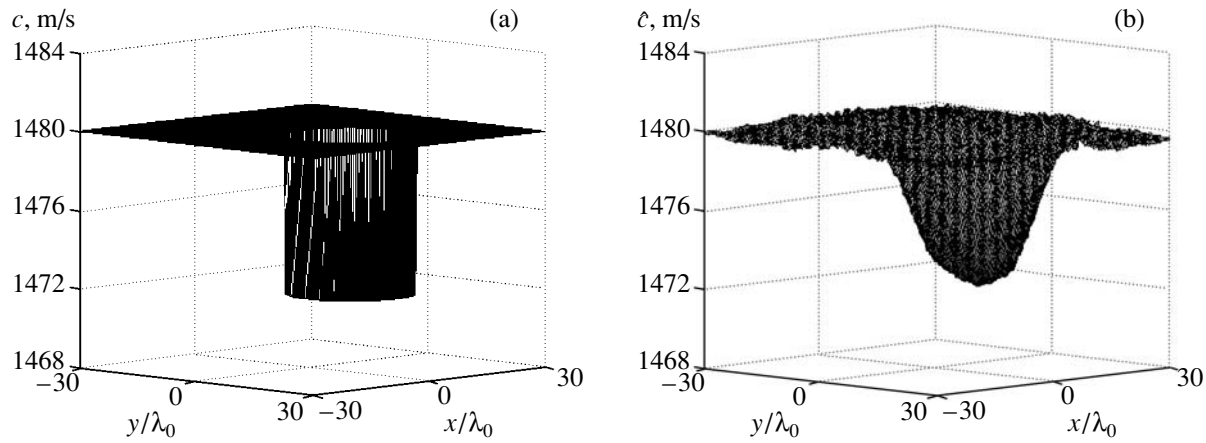
Fig. 4. (a) Model sound velocity distribution over the water region and (b) the result of reconstructing this distribution in the wave representation for the number of receiving–transmitting transducers $I = 22$, the number of basis strips $P = 14$, the number of angles of orientation $U = 21$, and the regularizing coefficient $\mu = 0.05$; the resulting discrepancies are $n_c = 0.43$ and $n_T = 0.43$.

reflection, refraction, and transmission of plane waves is well known. We described the incident field in the form of the integral representation of a two-dimensional Green's function of the homogeneous space with sound velocity c_0 and wave number k_0 ([9], Ch. 27):

$$g(\mathbf{r}|\mathbf{r}_S, \omega) = \int\limits_{-\infty}^{\infty}\int\limits_{-\infty}^{\infty} \frac{e^{-i\mathbf{k}_1(\mathbf{r}-\mathbf{r}_S)}}{k_1^2 - k_0^2}\frac{dk_{1x}dk_{1y}}{4\pi^2},$$

$$\mathbf{k}_1 = \{k_{1x}, k_{1y}\}, \quad k_1 = |\mathbf{k}_1|, \quad k_0 = \frac{\omega}{c_0},$$

where $\mathbf{r}$ and $\mathbf{r}_S$ are the radius-vectors of the receiving point and the point source, respectively.

As was shown in [10] (where the direct problem of the transmission of a cylindrical wave through the strip inhomogeneity is solved in detail), neglect of decaying surrounded waves and the summation of only the plane waves whose wave vectors lie on the Evald sphere yield a sufficiently accurate approximation to the actual Green's function, which supports the idea of calculating the field as the sum of plane waves.

As the initial data, we used the total field received by all antennas positioned along the perimeter of the water region. In simulations, we considered the water region with a radius of $30\lambda_0$ evanescent by a system of 22 receiving–transmitting transducers radiating at a frequency of 30 Hz. We assumed that the velocity inside the reconstructed inhomogeneity is 0.5% smaller than the background velocity of 1480 m/s. Figure 4a shows the inhomogeneity to be reconstructed; it has the shape of a cylinder of radius $r_0 \sim 12\lambda_0$ shifted by $\sim 10\lambda_0$ along the positive direction of the Oy axis. The simulation of reconstruction of a cylindrical inhomogeneity follows from the need to obtain a rigorous solution of the direct problem. In addition, the solution of the problem on the cylindrical wave refraction by a cylindrical inhomogeneity is well known. Thus, we used different procedures for

determining the elements of the perturbation matrix and the terms of the right-hand side of Eq. (1).

We regularized the matrix $\mathbf{A}^+\mathbf{A}$ using a priori information. In the reconstruction process, we used the fact that the objects under consideration had simple shapes, so that the expansion coefficients of adjacent basis elements could not differ widely. This fact offered a possibility of imposing additional conditions on the expansion coefficients of the inhomogeneity in the basis elements. We introduced a regularizing parameter μ that characterized the additional requirement of smoothness for the expansion coefficients (for $\mu = 1$, the reconstructed coefficients must be equal). In the case of simulations shown in Fig. 4b, this parameter was $\mu = 0.05$.

EFFECT OF THE STRIP BASIS PARAMETERS ON THE QUALITY OF RECONSTRUCTION

We estimated the effect of the parameters of the proposed basis (such as the number of strips, the width of strips, and the number of angles) according to the following procedure. We fixed the numbers of transducers, strips, and angles of strip orientation and constructed a perturbation matrix $\mathbf{A}$, after which we evaluated the degree of conditionality of the matrix by the formula $\alpha = \sqrt{\dfrac{\lambda_{max}}{\lambda_{min}}}$, where λ_{max} and λ_{min} are the maximum and minimum eigenvalues of the square matrix $\mathbf{A}^+\mathbf{A}$. The degree of conditionality varied from $\alpha = 213$ for 5 strips, 20 angles, and 16 transducers to $\alpha = 8833$ for 25 strips, 35 angles, and 16 transducers. With an increase in the number of transducers, the degree of conditionality decreased, for example, to $\alpha = 1142$ for 10 strips, 25 angles, and 32 transducers.

In numerical simulations, we modeled the inhomogeneity to be reconstructed as a cylindrically distributed phase velocity perturbation localized in the central

part of the water region of interest. The magnitude of the velocity specifying the perturbation in both basis strips and inhomogeneities to be reconstructed was assumed to be 0.5% smaller than the background velocity and was equal to 1472 m/s. We fixed the number of transducers ($I = 22$) and reconstructed the inhomogeneity of radius $r_0 \sim 15\lambda_0$ (Fig. 5a) for different numbers of basis elements. We considered two cases: in the first case, the number of strips was $P = 12$ and the number of angles of orientation was $U = 7$; in the second case, we used $P = 6$ and $U = 15$. The degrees of conditionality for these cases differed slightly and were $\alpha = 18$ and 32, respectively. Here, we performed no regularization ($\mu = 0$), because our task consisted in estimating precisely the effect of the parameters of the basis on the quality of reconstruction.

Figures 5b and 5c show the results of reconstruction for the basis with the above parameters. It should be noted that the reconstructed expansion coefficients of the unknown inhomogeneity $\mathbf{X}$ have nonzero imaginary parts, which, in turn, causes an error in the form of the imaginary component of the estimated velocity (see curves for Im$\hat{c}$ in Figs. 5b and 5c). This can be used as an additional indicator of the accuracy of the reconstruction algorithm, because the imaginary part tends to zero for the exact reconstruction.

Comparison of Figs. 5b and 5c shows that, although the total amount of information increases with increasing number of basis strips due to the increase in the number of elements that intersect the inhomogeneity, the quality of reconstruction appears to be worse (Fig. 5b). This effect can be explained by an increase in the number of poorly illuminated regions falling within the reconstructed region. Consider the propagating cylindrical wave localized in a certain ray tube of characteristic width $d \sim \sqrt{\dfrac{D\lambda_0}{2}}$, where D is the distance between the source and the receiver and λ_0 is the wavelength. For the problem under consideration, the maximum width of the ray tube measures $d \sim \sqrt{1500 \text{ m} \times 50 \text{ m}} \sim 270$ m, whereas the distance between the adjacent receivers illuminated by the ray tubes of the same transmitter measures ~430 m for $I = 22$. As a result, the region of interest appears to be nonuniformly illuminated. If a strip is sufficiently narrow, its major part may fall in the shadow region and, consequently, fall out of the reconstruction algorithm. One can expect that, with a decrease in the number of strips and an increase in the strip width (for a uniform partition of the water region into strips), one should obtain estimates for the velocity in poorly illuminated regions that will approach the correct values at the expense of the well-illuminated regions. This will improve the whole pattern of reconstruction. In this case, one must increase the number of angles of strip orientation U to enlarge the system describing the region, which can become less informative with decreasing number P.

An additional reasonable requirement that should be imposed on the numbers of strips and angles is the requirement of mutual intersection of the peripheral parts of the basis strips corresponding to the adjacent angles of orientation. For basis strips of width $h = \dfrac{2R_0}{P}$ (R_0 is the radius of water region under investigation), this condition can be written in the form $h \geq R_0 \dfrac{\pi}{U}$, where $\dfrac{\pi}{U}$ is the angle between the adjacent strip orientations. Thus, we obtain the condition on the numbers of basis strips and angles in the form

$$U \geq \frac{\pi}{2} P. \qquad (3)$$

Note that a similar requirement is used in the X-ray transmission tomography for the number of angular samples and the number of samples per projection (see [11], Ch. 4).

As it follows from the results of simulations, a decrease in the strip number by a factor of two and an increase in the number of angles also by a factor of two (in this case, condition (3) is satisfied) results in a considerable improvement of the reconstructed pattern of velocity distribution (Fig. 5c). In addition, the false imaginary part Im$\hat{c}$ decreases, which is also indicative of a higher reconstruction accuracy.

Our next step consisted in decreasing the number of transducers by a factor of two; namely, we used $P = 6$, $U = 15$, and $I = 12$ (see Fig. 5d). Despite the substantial decrease in the amount of data on the region under investigation, the reconstruction quality was reduced only slightly.

Implementing the above algorithm, we revealed an additional possibility of varying the basis so as to affect the reconstruction quality. This possibility arises if we specify no immediate relationship between the strip number and the strip width; i.e., if we consider a nonuniform partition of the region into strips. Assume that some preliminary experiment (with certain possible parameters P, U, and I) showed that an inhomogeneity is located at the center (or near the center) of the region under testing. Then, we can improve the reconstruction accuracy by decreasing the widths of the basis strips with retaining the parameters P, U, and I. In this case, the region is divided into strips nonuniformly; namely, the strips are numerous in the central part of the water region and only few of them are at the periphery. Such an approach only slightly affects the conditionality degree of matrix $\mathbf{A}$ (because the parameters P, U, and I remain intact); however, it can considerably increase the number of strips intersecting the inhomogeneity, which increases the total amount of information provided by the basis. This procedure can be useful, for example, for reconstructing small inhomogeneities that
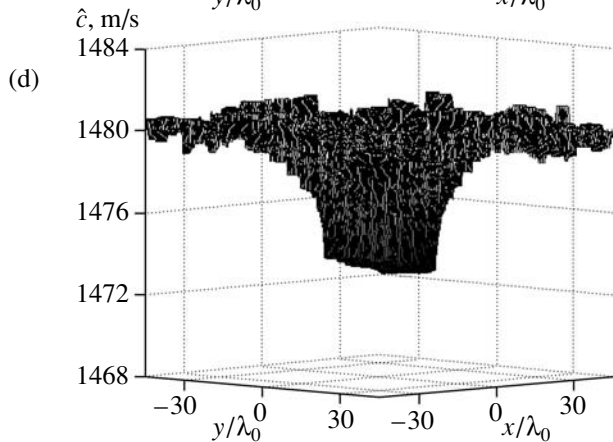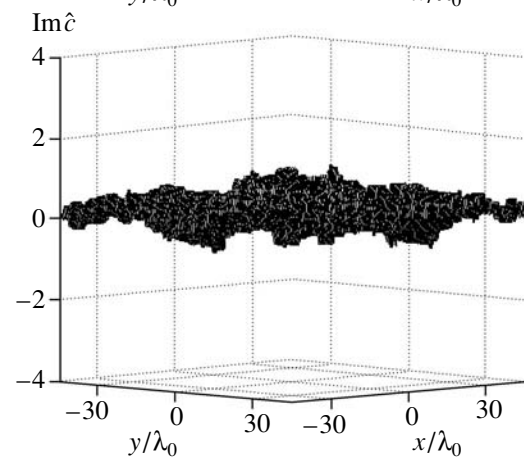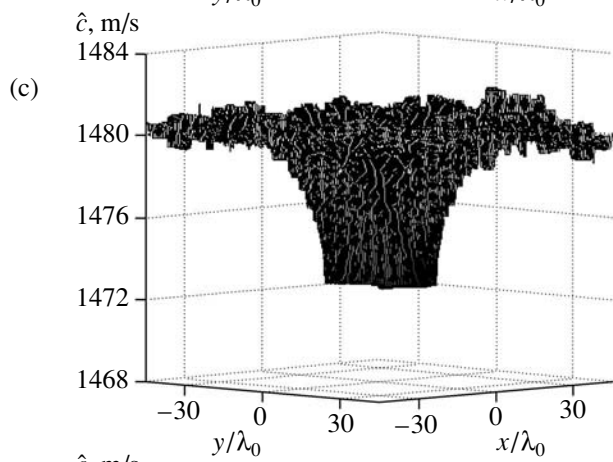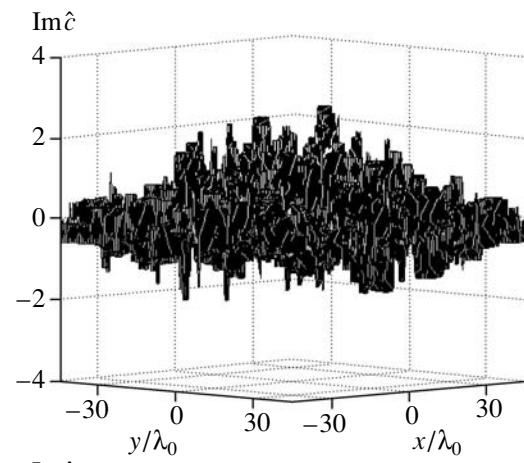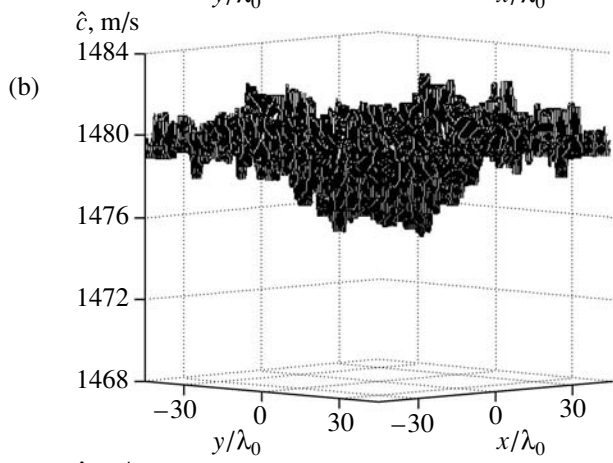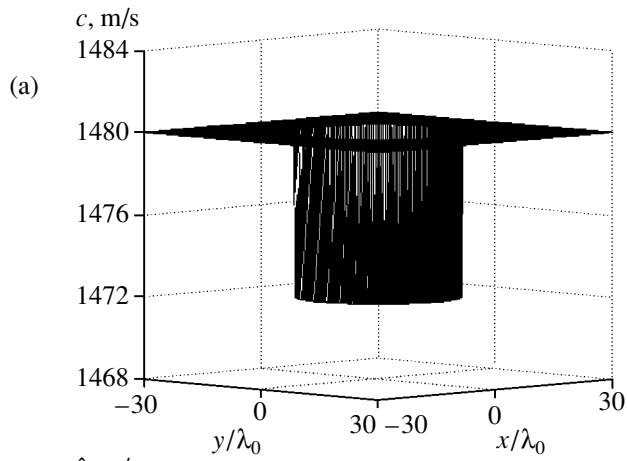
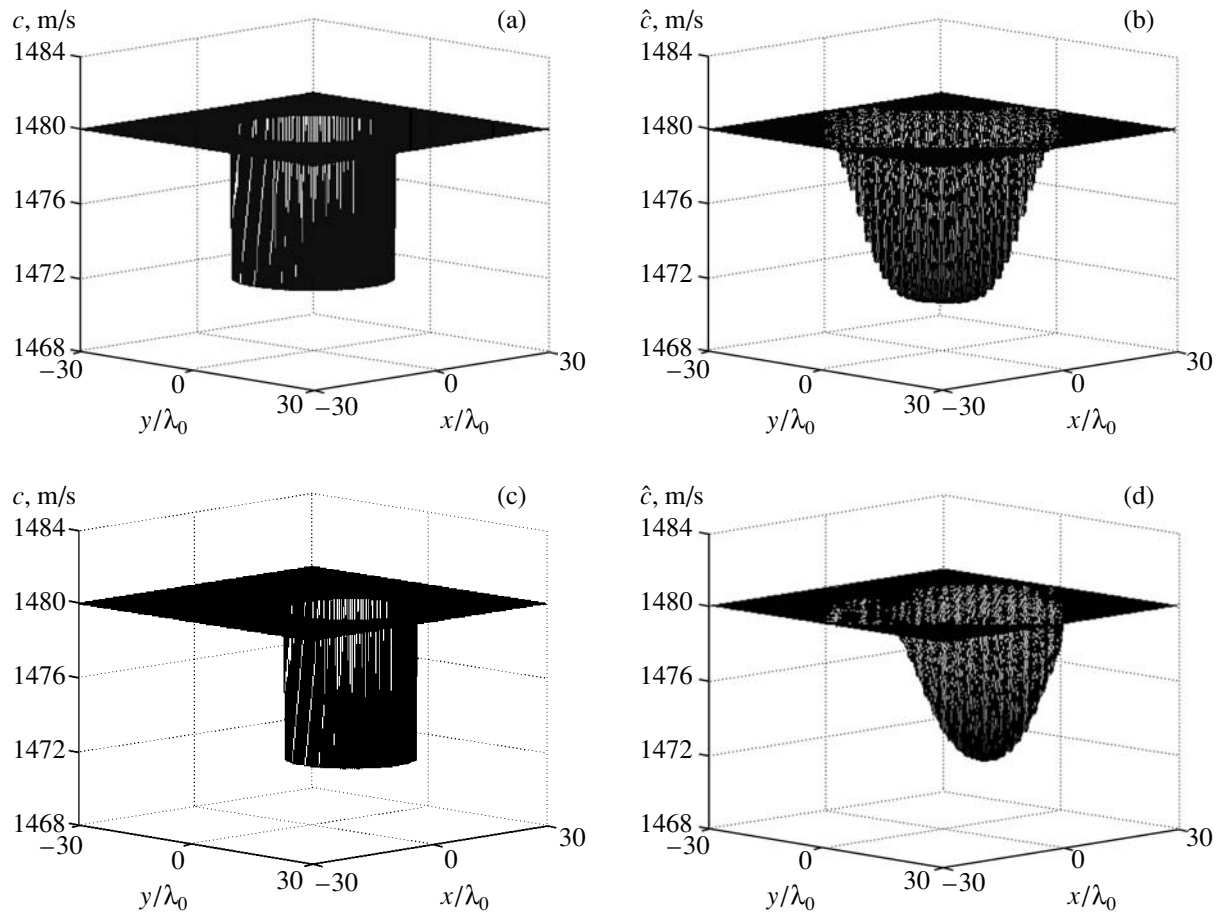**Fig. 5.** (a) Model distribution of a cylindrical inhomogeneity of radius $r_0 \sim 15\lambda_0$ and (b–d) the result of reconstructing this inhomogeneity in the wave representation (with the error estimated as the imaginary velocity component $\text{Im}\hat{c}$) for different numbers of receiving–transmitting transducers I, basis strips P, and angles of orientation U: $P =$ (b) 12 and (c, d) 6; $U =$ (b) 7 and (c, d) 15; $I =$ (b, c) 22 and (d) 12 ($n_c =$ (b) 0.72, (c) 0.53, and (d) 0.56; $n_T =$ (b) 0.46, (c) 0.3, and (d) 0.09).

cannot be adequately reconstructed with the use of wide strips. An adequate reconstruction requires that the diameter of the inhomogeneity measures several strip widths. Instead of increasing the number of strips by decreasing the strip width (as it is the case for the uniform partition), we can use a nonuniform partition. The nonuniform partition offers a possibility to achieve the same effect without such a significant decrease in the conditionality degree of the system as in the case of a uniform partition. For example, to reconstruct the actual velocity inside an inhomogeneity of smaller radius $r_0 \sim 10\lambda_0$ (Fig. 6a) with a uniform partition, we

should use a greater number of basis strips and, hence, reduce the strip width. In accordance with condition (3), a greater number of strip orientations will be used in this case. Figure 6b shows the simulated results for $P = 12$, $U = 31$, and $I = 22$; these parameters correspond to the basis strip width $h \sim 10\lambda_0$. However, in the case of a nonuniform partition, qualitatively similar results can be obtained with a smaller number of basis elements. Figure 6c shows the result of reconstructing this inhomogeneity with the use of a smaller number of narrower strips for $P = 6$, $U = 21$, $I = 22$, and $h \sim 4\lambda_0$.
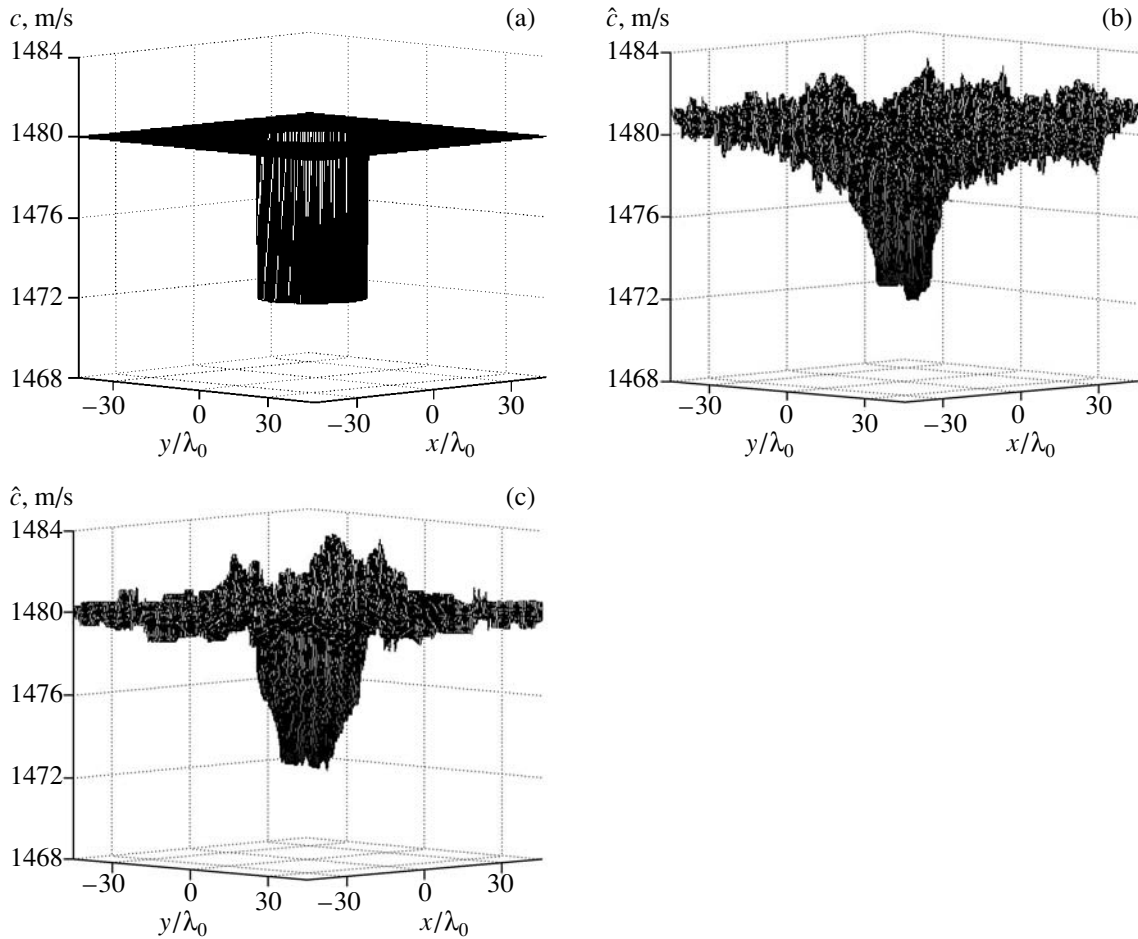
Fig. 6. (a) Model distribution of a cylindrical inhomogeneity of radius $r_0 \sim 10\lambda_0$ and (b, c) the result of reconstructing this inhomogeneity in the wave representation for the number of receiving–transmitting transducers $I = 22$, different numbers of basis strips P and angles of orientation U, and different basis strip widths h: (b) auniform partition of the water region into basis strips with $P = 12$, $U = 31$, and $h \sim 10\lambda_0$ ($n_c = 0.79$, $n_T = 0.1$); (c) a nonuniform partition of the water region with $P = 6$, $U = 21$, and $h \sim 4\lambda_0$ ($n_c = 0.59$, $n_T = 0.36$).

Fig. 7. (a, c) Model distributions of cylindrical inhomogeneities and (b, d) the results of reconstructing these inhomogeneities in the wave representation with the use of the cylindrical basis for the number of receiving–transmitting transducers $I = 22$, the number of circular basis elements 841, and the regularizing coefficient $\mu = 0.03$: (a) for an inhomogeneity of radius $r_0 \sim 15\lambda_0$ at the center of the water region, we have (b) $n_c = 0.45$ and $n_T = 0.2$; (c) for an inhomogeneity of radius $r_0 \sim 12\lambda_0$ shifted along the positive direction of the Oy axis by $\sim 10\lambda_0$, we have (d) $n_c = 0.51$ and $n_T = 0.22$.

USE OF OTHER NONSTANDARD BASES

The above method of constructing the strip basis can be used for constructing other nonstandard bases whose elements will have shapes suitable to either the type of inhomogeneities to be reconstructed or the type of the sound field representation. For example, when dealing with the reconstruction of eddies, it is worthwhile to apply circular bases. In addition, in the context of the wave approach, the use of circles as basis elements offers the possibility for a rigorous construction of the perturbation matrix.

As an example, consider the reconstruction problem with the use of the cylindrical version of the mosaic basis formed by the following procedure (Fig. 1b). The circular region of interest is uniformly covered (with overlapping) with cylinders (circles in the two-dimensional case) as basis elements. Then, matrix **A** is calculated in the same way as in the above procedure for solving the problem with the use of the strip basis, i.e., by a sequential specification of a reference perturba-

tion in each cylinder and the calculation of the corresponding field perturbation. The expansion coefficients of the reconstructed inhomogeneity are determined from Eq. (2).

In simulations, we considered a water region of radius $30\lambda_0$. As earlier, the velocity in the inhomogeneity was assumed to be 0.5% smaller than the background velocity. For the cylindrical inhomogeneities shown in Figs. 7a and 7c, the results of reconstruction are given in Figs. 7b and 7d, respectively. Note that, in this case, the discrepancy n_T appears to be smaller than in the case of the use of the strip basis for reconstructing the inhomogeneities with the same parameters (radius, location relative to the center of the water region, and velocity perturbation) (see Figs. 5c and 4b).

CONCLUSIONS

From the results obtained, we conclude that the requirements on the basis used to expand an inhomogeneity can be considerably slackened if necessary a priori

information is available, which leads to a convenient and efficient expansion of the inhomogeneity under test. The few conditions that should be satisfied by the bases used in tomography problems include its relative completeness (i.e., the basis should be sufficient for describing the inhomogeneity to be reconstructed with the required accuracy) and the additivity of the effects taken into account. The orthogonality requirement is not necessary. In addition, the basis can be overfull.

The proposed strip basis is a convenient structure for constructing the perturbation matrix of the field caused by a refractive inhomogeneity in both ray and wave approaches to the sound field description. An extension of the problems under consideration to media with flows and eddies can be successfully realized.

The problem can be extended to the case of the initial data represented by the phase shifts of the vertical modes in the horizontal rays–vertical modes combined scheme and to more complicated cases with the initial data given as amplitudes and phases of the signals received by a vertical hydroacoustic array.

ACKNOWLEDGMENTS

REFERENCES

1. V. V. Goncharov, V. Yu. Zaĭtsev, V. M. Kurtepov, *et al.*, *Acoustic Tomography of the Ocean* (Novgorod, 1997) [in Russian].

2. S. V. Baykov, V. A. Burov, and S. N. Sergeev, in *Proceedings of the 4th European Conference on Underwater Acoustics* (1998), p. 617.

3. V. Yu. Zaĭtsev, A. G. Nechaev, and L. A. Ostrovskiĭ, in *Acoustics of the Oceanic Medium*, Ed. by L. M. Brekhovskikh and I. B. Andreeva (Nauka, Moscow, 1989) [in Russian].

4. W. Munk and C. Wunsh, Deep-Sea Res. A **26** (2), 123 (1979).

5. W. Munk, P. Worcester, and C. Wunsh, *Ocean Acoustic Tomography* (Cambridge University Press, Cambridge, 1995).

6. V. V. Goncharov and V. M. Kurtepov, in *Acoustics of the Oceanic Medium*, Ed. by L. M. Brekhovskikh and I. B. Andreeva (Nauka, Moscow, 1989) [in Russian].

7. D. L. Aleĭnik, V. V. Goncharov, and Yu. A. Chepurin, in *Proceedings of VIII School-Seminar of Academician L.M. Brekhovskikh on Acoustics of the Ocean* (GEOS, Moscow, 2000), p. 18.

8. V. A. Burov, S. N. Sergeev, and A. S. Shurup, in *Proceedings of X School-Seminar of Academician L.M. Brekhovskikh on Acoustics of the Ocean Combined with XIV Session of the Russian Acoustical Society* (GEOS, Moscow, 2004), p. 193.

9. E. Skudrzyk, *The Foundation of Acoustics: Basic Mathematics and Basic Acoustics* (Spinger, Wien, 1971; Mir, Moscow, 1976), Vol. 2.

10. S. N. Sergeev and A. S. Shurup, Vestn. Mosk. Univ., Ser. 3: Fiz., Astron., No. 6, 34 (2004) (in press).

11. *The Physics of Medical Imaging*, Ed. by S. Webb (IOP Publishing, 1988; Mir, Moscow, 1991), Vol. 2.

Translated by A. Vinogradov

Interaction of a Shear Wave with a Moving Domain Wall in a Ferromagnetic Crystal with Allowance for the External Magnetic Field

E. A. Vilkov

Institute of Radio Engineering and Electronics, Ul'yanovsk Branch, Russian Academy of Sciences,
ul. Goncharova 48, Ul'yanovsk, 432700 Russia
e-mail: vilkov@vens.ru
Received March 25, 2004

Abstract—The boundary-value problem of the magnetoelastic wave interaction with a moving domain wall in a ferromagnetic crystal is solved in the nonexchange magnetostatic approximation with allowance for the external magnetic field. It is shown that the difference introduced by magnetic field between the ferromagnetic resonance frequencies of the domains does not cause any noticeably departure of the refraction characteristics of reflected and transmitted waves from those observed at zero frequency mismatch. By contrast, the magnitudes of the transmission and reflection coefficients strongly depend on the external magnetic field and on the mobility of the domain wall. The dependence of the magnitude of the reflection coefficient on the external magnetic field at a fixed angle of shear wave incidence is found to possess two ferromagnetic resonance peaks. The positions and heights of the peaks may vary depending on the mobility of the domain wall. © 2005 Pleiades Publishing, Inc.

The refractive interaction of a magnetoelastic wave with a moving 180° domain wall (DW) was considered in [1] without taking into account the external magnetic field. The ferromagnetic resonance (FMR) frequencies of domains were assumed to be identical, which can be true only when the anisotropy field of the ferromagnet far exceeds the external field responsible for the motion of the domain wall. However, in sufficiently strong external magnetic fields, the difference arising between the FMR frequencies of the domains (the FMR mismatch) under the effect of the external magnetic field can be significant. Therefore, the results reported in [1] require an additional verification with allowance made for the nonzero difference between the frequencies of uniform spin precession in the domains. For this purpose, the present paper considers the initial equations with allowance for the external magnetic field and calculates the refraction characteristics and amplitude factors of the refracted waves.

The results reported in [1] were obtained using the simplest model of a geometric DW. Let us specify the limitations introduced by this model in connection with the presence of an additional factor, namely, the motion of the DW. It is conventionally assumed that the DW motion initiated by an external control action is not accompanied by any structural changes in the DW if the DW velocity satisfies the condition $V_D = \mu_D H_0 < v_w$, where v_w is the Walker limiting velocity [2], μ_D is the mobility of the DW, and H_0 is the external field. It should be noted that, under steady-state motion condi-

tions, the structural stability of a DW is determined by the equilibrium thermodynamic conditions under which the crystal is studied and by the technological characteristics of the crystal (the presence of defects, impurities, etc.). Therefore, the structural stability of the DW manifests itself in different ways in bulk crystals and films.

The aforementioned limitation imposed on the DW velocity is typical of bulk crystal samples away from the phase transition. Taking into account the inequality that is typical of cubic ferromagnets, namely, $v_w > c_t$, where c_t is the shear wave velocity without considering magnetostriction, in addition to the requirement for the geometricity of the DW on the wavelength scale $k\Delta \ll 1$, we impose a limitation on the DW velocity in the form $V_D < c_t$. With the nonexchange magnetostatic approximation [3] in mind, we assume that $k < k_{max}$ and $k_{max}^2 D \ll H_a$, where D is the exchange constant of the ferromagnet, H_a is the anisotropy field, k is the magnetoelastic wave number not exceeding the threshold value k_{max}, and Δ is the actual thickness of the DW.

Assume that the easy magnetization direction corresponds to the z axis of the $x0yz$ crystallographic coordinate system ($z \parallel [001]$). Then, bringing the 180° DW into coincidence with the (010) plane of the crystal makes sense only for ferromagnets with a positive magnetic anisotropy constant $K_1 > 0$. The case considered below, namely, the refraction of shear waves by a (010)-oriented

DW moving in a cubic ferromagnet, is sufficiently general, because, with the substitution [4]

$$\lambda_{44} \longrightarrow \lambda'_{44} = \frac{1}{3}(\lambda_{11} - \lambda_{12} + \lambda_{44}), \quad \beta \longrightarrow \beta',$$

$$\omega_{0j} = \omega_{01,2} = \gamma(H_a \pm H_0), \quad (1)$$

$$H_a = \frac{2K_1}{M_0} \longrightarrow H'_a = -\frac{4K_1}{3M_0},$$

the equations written for a crystal with $K_1 > 0$ are transformed to the corresponding equations for a crystal with $K_1 < 0$. In the latter case, the easy magnetization direction coincides with the principal diagonal of the unit cell while the shear waves with displacements parallel to the spontaneous magnetizations $\mathbf{M}_0$ propagate in the (111) plane of the crystal. In Eq. (1), b_{11}, b_{12}, and b_{44} are the nonzero components of the magnetoelastic interaction tensor; λ_{11}, λ_{12}, and λ_{44} are the components of the elastic modulus tensor of the cubic crystal; and β is the magnetoelastic coefficient.

Let us assume that shear waves propagate in the (001) plane of an iron garnet crystal with the displacements $\mathbf{u}_j$, which are collinear with the spontaneous magnetizations $\mathbf{M}_0^{(j)}$ in the domains ($\mathbf{M}_0^{(1)} \uparrow\downarrow \mathbf{M}_0^{(2)} \parallel$ [001]; $j = 1, 2$ is the domain order number). The domains are separated in the (010) plane by a geometrically thin structureless DW with the current coordinate $y_D = V_D t$, where t is time. Accordingly, we assume that the spontaneous magnetizations $M_0^{(j)}$ and the internal magnetic fields $H_i^{(j)}$ in the domains have the form

$$M_0^{(j)} = (-1)^{j+1} M_0,$$
$$H_i^{(j)} = (-1)^{j+1}(H_a \pm H_0), \quad (2)$$

where H_a is the anisotropy field, $j = 1$ for $y > y_D$, and $j = 2$ for $y < y_D$. The minus sign before H_0 corresponds to the DW motion along the direction of the [010] axis ($V_D > 0$), and the plus sign, to the motion in the opposite direction ($V_D < 0$).

In describing the propagation of magnetoelastic waves in a ferromagnet, the common practice [5, 6] is to use the equation of motion from the elasticity theory

$$\rho\frac{\partial^2 u_j}{\partial t^2} = \frac{\partial}{\partial x_k}\left[\frac{1+\delta_{ik}}{2}\frac{\partial w}{\partial u_{jk}}\right], \quad (3)$$

the equation of motion for the magnetic moment

$$\rho\frac{\partial \mathbf{M}}{\partial t} = \gamma\left[\frac{\mathbf{M}}{M_s}\frac{\partial w}{\partial(\mathbf{M}/M_s)}\right], \quad (4)$$

and the Maxwell equations. The quantity appearing on the right-hand side of Eq. (3) in square brackets is the stress tensor T_{ik} [7]:

$$T_{ik} = \frac{1+\delta_{ik}}{2}\frac{\partial w}{\partial u_{ik}}. \quad (5)$$

In Eqs. (3) and (4), ρ is the density of the crystal, t is time, $\gamma = 2\mu_b\hbar$ is the gyromagnetic ratio, μ_b is the Bohr magneton, and $\hbar$ is the Plank constant.

In the general case, the energy density of the crystal is expressed as [3]

$$w = w_M + w_H + w_{MU} + w_U, \quad (6)$$

where w_M is the magnetization energy density, w_H is the energy density of magnetic field, w_{MU} is the energy density of magnetoelastic interaction, and w_U is the elastic energy density.

Using Eqs. (3)–(6) and the propagation conditions mentioned above, we obtain the equations that are valid in the nonexchange magnetostatic approximation in the presence of a bias magnetic field:

$$\nabla^2 u_j + (\rho\Omega^2/\lambda_\Omega^*)u_j = 0,$$
$$\nabla^2\varphi_j = (-1)^{j+1}\frac{4\pi\gamma\beta\omega_{0j}}{\Omega^2 - \omega_{kj}^2}\nabla^2 u_j. \quad (7)$$

Here, Ω is the frequency of the incident or refracted wave; ∇ is the Hamiltonian in the $x0y$ plane; φ_j is the magnetostatic potential; $\lambda_\Omega^* = \lambda + \gamma\beta^2\omega_{0j}/[M_0(\Omega^2 - \omega_{kj}^2)]$; and $\omega_{0j} = \gamma(H_a \pm H_0) = \omega_0 \pm \Delta\omega_0$ are the uniform precession frequencies in the domains, where ω_0 is the FMR frequency in the absence of the external magnetic field, $\Delta\omega_0$ is the shift of the FMR frequency ($\omega_{01} > \omega_{02}$ for $V_D < 0$ and $\omega_{01} < \omega_{02}$ for $V_D > 0$), $\omega_{kj} = [\omega_{0j}(\omega_{0j} + \omega_M)]^{1/2}$ is the magnetoacoustic resonance frequency, $\omega_M = 4\pi\gamma M_0$ is the magnetization frequency, and $\lambda = \lambda_{44}$ is the shear modulus.

The first of Eqs. (7) is the Helmholtz equation. The solution to this equation can be represented in the form of plane harmonic waves with the dispersion law

$$k^2 \equiv k^2(\Omega) = \rho\Omega^2/\lambda_\Omega^*. \quad (8)$$

The second of Eqs. (7) yields

$$\varphi_j = (-1)^{j+1}\frac{4\pi\gamma\beta\omega_{0j}}{\Omega^2 - \omega_{kj}^2}u_j + \Phi_j, \quad \nabla^2\Phi_j = 0, \quad (9)$$

where Φ_j is the potential of the scattering field of the magnetic poles [1].

Let us preset the frequency ω and the wave vector of the incident wave $\mathbf{k} = \mathbf{n}k$, where $\mathbf{n} = (\sin\theta, -\cos\theta)$, θ is the angle of incidence, and $k = k(\omega)$ is the wave number determined from Eq. (8) in which Ω is replaced by ω. The waves refracted by the moving DW are characterized by the frequencies ω' and ω'' and by the wave vec-
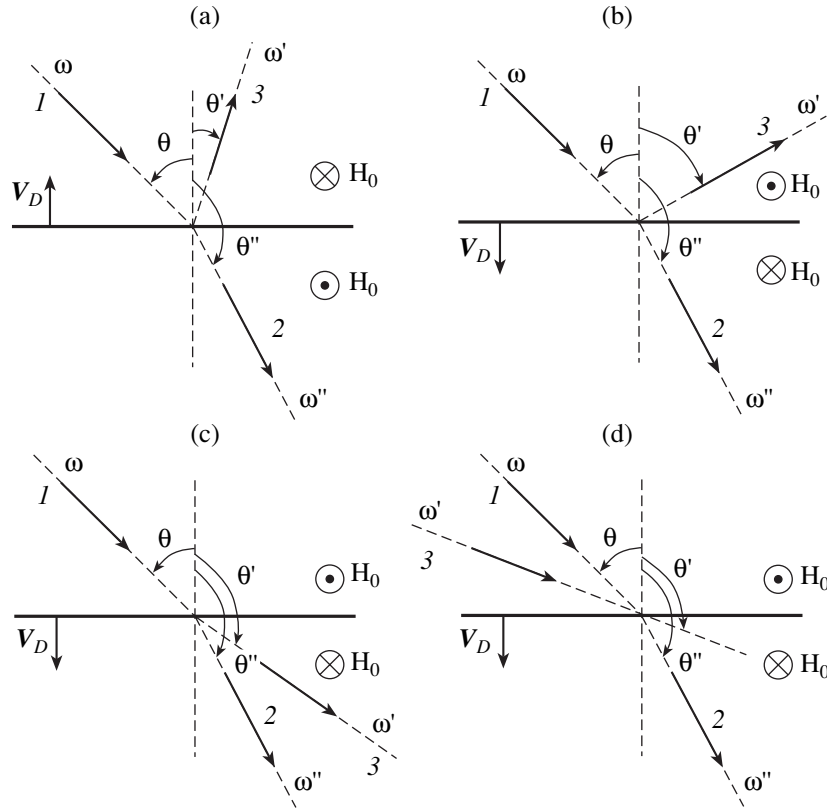
Fig. 1. Refraction diagrams for a shear wave refracted by an (a) oncoming DW and (b–d) a receding DW with (b) acute and (c, d) obtuse angles of refraction: the wave vectors of the (*1*) incident, (*2*) deflected, and (*3*) refracted waves.

tors $\mathbf{k}' = \mathbf{n}'k'$ and $\mathbf{k}'' = \mathbf{n}''k''$ with the wave normals $\mathbf{n}' = (\sin\theta', \cos\theta'')$ and $\mathbf{n} = (\sin\theta'', \cos\theta'')$ and with the wave numbers $k' = k'(\omega')$ and $k'' = k''(\omega'')$, respectively; the latter are obtained from Eq. (8) by replacing Ω with ω' and ω'', respectively. Here, the angles θ' and θ'' are the refraction angles lying within the interval $[0, \pi]$ (Fig. 1).

Because of the difference in the FMR frequencies of the domains, the calculation of the refraction characteristics of refracted waves should be performed with four equations instead of two. The equations express the condition of the conjunction of the wave fields at the DW by the phase invariant method [8]. Namely, the projections of the wave vectors of the incident and refracted waves are equal at $y = y_D$, which yields

$$\frac{\omega}{v}\sin\theta = \frac{\omega'}{v'}\sin\theta', \quad \frac{\omega}{v}\sin\theta = \frac{\omega''}{v''}\sin\theta'' \equiv k_\tau, \quad (10)$$

and the temporal synchronism of the phases of oscillations at the DW yields

$$\omega\left(1 + \frac{V_D}{v}\cos\theta\right) = \omega'\left(1 - \frac{V_D}{v'}\cos\theta'\right),$$

$$\omega\left(1 + \frac{V_D}{v}\cos\theta\right) = \omega''\left(1 - \frac{V_D}{v''}\cos\theta''\right) = \tilde{\omega}. \quad (11)$$

In Eqs. (10) and (11), $v = \omega/k$, $v' = \omega'/k'$, and $v'' = \omega''/k''$ are the phase velocities of waves.

Taking into account Eq. (8), one can prove that Eqs. (10) and (11) are equivalent to the system of equations

$$\sin\theta' + \frac{V_D}{v}\sin(\theta + \theta')$$
$$= \frac{\sin\theta}{v}c_t\left[1 + \frac{\chi_1\omega_{01}^2}{\omega^2 f^2(\theta, \theta') - \omega_{k1}^2}\right]^{1/2}, \quad (12a)$$

$$\sin\theta'' + \frac{V_D}{v}\sin(\theta + \theta'')$$
$$= \frac{\sin\theta}{v}c_t\left[1 + \frac{\chi_2\omega_{02}^2}{\omega^2 f^2(\theta, \theta'') - \omega_{k2}^2}\right]^{1/2}, \quad (12b)$$

$$\frac{\omega'}{\omega} = 1 + \frac{V_D}{v}\frac{\sin(\theta + \theta')}{\sin\theta'} \equiv f(\theta, \theta'),$$
$$\frac{\omega''}{\omega} = 1 + \frac{V_D}{v}\frac{\sin(\theta + \theta'')}{\sin\theta''} \equiv f(\theta, \theta''). \quad (13)$$

The quantities $\chi_1 = \gamma\beta^2/(\lambda M_0\omega_{01})$ and $\chi_2 = \gamma\beta^2/(\lambda M_0\omega_{02})$ are dimensionless (and usually small: $\chi_1 \ll 1$ and $\chi_2 \ll 1$) parameters of magnetoelastic coupling and $c_t = (\lambda/\rho)^{1/2}$.

Since θ, ω, and, hence, $v = v(\omega)$ are known, Eqs. (12) determine θ' and θ'' as the roots of transcendental equations. The corresponding values of ω' and ω'' can be easily calculated by Eqs. (13), which exhibit the presence of Doppler shifts in the refracted waves. Numerically, it was found that, in the general case, the number of the roots of Eqs. (12a) and (12b) is four. However, according to Bolotovskiĭ and Stolyarov [8], in problems with moving boundaries, the causality requirement is only satisfied for waves with a positive projection of their group velocity $\mathbf{V}_g = \partial\tilde{\omega}/\partial\tilde{\mathbf{k}}'$ onto the direction of the energy transfer, irrespective of the type of the energy state of the medium. Here, $\tilde{\omega}$ and k' are the frequency and the wave vector of the refracted wave in the DW frame of reference, $\tilde{x}0\tilde{y}\tilde{z}$, which is related to the laboratory frame of reference, $x0yz$, by the Galilean transformation: $\tilde{x} = x$, $\tilde{y} = y - V_D t$, $z = \tilde{z}$, $\tilde{t} = t$. Thus, the selection criterion is the requirement that the energy transferred by the refracted wave be carried away from the DW:

$$\mathrm{sgn}(\tilde{y})\,\mathrm{sgn}(V'_{gy}) > 0, \qquad (14)$$

where $\mathbf{V}_{gy} = \partial\tilde{\omega}/\partial k'_y$ is the projection of the group velocity of the refracted wave onto the $\tilde{y}$ axis. Here, it is necessary to know the group velocity of the refracted wave, $\mathbf{V}_g$, in the DW frame of reference.

Taking into account Eq. (8), one can show that $\mathbf{k}'^2 c_t^2 = \omega'^2(\omega'^2 - \omega_k^2)[(\omega'^2 - \omega_k^2) + \chi_1\omega_{01}^2]^{-1}$. This equality is a biquadratic equation in ω'. According to the nonexchange approximation condition, the smaller root of this equation determines the low-frequency branch of the magnetoelastic wave spectrum:

$$\omega' = \tilde{\omega} + \mathbf{k}'\mathbf{V}_D$$
$$= \frac{1}{\sqrt{2}}[(\omega_k^2 + \mathbf{k}'^2 c_t^2) - \sqrt{(\omega_k^2 - \mathbf{k}'^2 c_t^2)^2 + 4k'^2 c_t^2\chi_1\omega_{01}^2}]^{1/2}.$$

Deriving $\tilde{\omega} = \tilde{\omega}(\mathbf{k}')$ from this equation and differentiating with respect to $\mathbf{k}'$, we perform some simple transformations to obtain the following formula for verifying condition (14):

$$V'_{gy} = \cos(\theta')v(\omega')\Psi(\omega') - V_D,$$
$$v(\omega') = c_t\sqrt{1 - \chi_1\omega_{01}^2(\omega_{k1}^2 - \omega'^2)^{-1}}. \qquad (15)$$
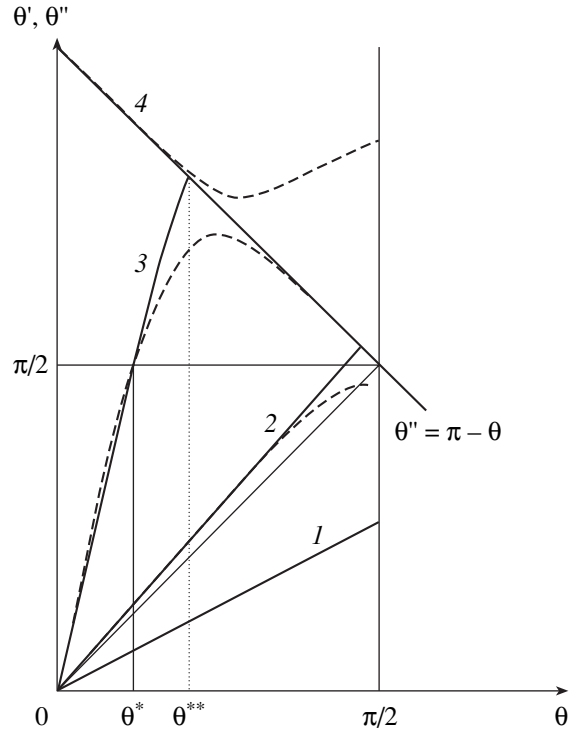
Fig. 2. Typical refraction dependences near the frequency ω_0 (solid curves) and near the frequency $\omega_k = \omega_0(\omega_0 + \omega_M)$ (dashed curves): (*1*) the case of an oncoming DW (the solid and dashed curves coincide, $|V_D| < c_t$), (*2*) the case of a receding DW ($|V_D| < c_t$), (*3*) the refraction dependence $\theta'' = \pi - \theta$ for the directly transmitted wave near the FMR frequency, and (*4*) the deflected wave near the MAR frequency.

Here, according to Eq. (8), $v(\omega')$ is the phase velocity of the refracted wave; the function $\Psi(\omega')$ is determined as

$$\Psi(\omega') = \left(1 - \frac{\chi_1\omega_{01}^2}{\omega_{k1}^2 - \omega'^2}\right)$$
$$\times\left[1 - \frac{\chi_1\omega_{01}^2}{\omega_{k1}^2 - \omega'^2}\left(1 - \frac{\omega'^2}{\omega_{k1}^2 - \omega'^2}\right)\right]^{-1}. \qquad (16)$$

For the wave propagating in the second domain, the substitutions $\omega' \longrightarrow \omega''$, $k' \longrightarrow k''$, $\theta' \longrightarrow \theta''$, $\chi_1 \longrightarrow \chi_2$, $\omega_{01} \longrightarrow \omega_{02}$, and $\omega_{k1} \longrightarrow \omega_{k2}$ should be made in Eqs. (15) and (16).

Equation (12a) describes the refraction angles for the waves propagating in the first domain ($y > y_D$), and, according to the causality requirement, they must have a positive projection of the group velocity onto the y axis. Correspondingly, the solutions to Eq. (12b) determine the waves propagating in the second domain ($y < y_D$), and, by virtue of inequality (14), the projection of their group velocity will be negative.
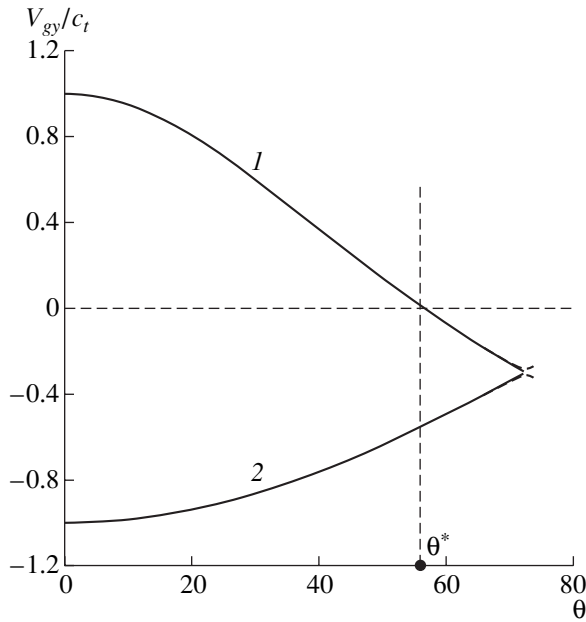
Fig. 3. Dependence of the projection of the group velocity on the angle of incidence of a shear wave for the frequency $\omega = 1.45 \times 10^{10}$ s^{-1} and $V_D/c_t = -0.3$: (*1*) refracted and (*2*) deflected waves; $\Delta\omega_0 = 0$ (solid curves) and 0.57×10^{10} s^{-1} (dashed curves).

The calculation by Eqs. (15), (16) and (12) at a fixed FMR mismatch ($H_0 = $ const) shows that the first of the two solutions to Eq. (12a) only exists for obtuse refraction angles $\theta'_1 = \pi - \theta$ and does not depend on V_D. A wave refracted in this way is characterized by ω, v, and **k** identical to those of the incident wave with $V'_{gy} < 0$. Evidently, this wave does not satisfy the requirement of the energy transfer away from the DW and can be rejected.

For the second root of Eq. (12a), θ'_2, in the case of $V_D > 0$ (the oncoming DW), the projection of the group velocity is always positive and the dependence $\theta'_2(\theta)$ has the form of curves *1* in Fig. 2. A wave with such refraction characteristics is actually the reflected wave shown (in terms of wave vectors) by arrow *3* in the refraction diagram represented in Fig. 1a. When $V_D < 0$ (a receding DW), the projection of the group velocity is positive, $V'_{gy} > 0$, only for the angles of incidence $\theta < \theta^*$ (at $\theta = \theta^*$ $\theta' = \pi/2$).

For the first root of Eq. (12b), θ''_1, the projection of the group velocity is always negative and this root corresponds to the deflected shear wave (arrow *2* in Fig. 1) irrespective of the sign of the DW velocity. In the case of the oncoming DW, the second root of Eq. (12b) gives a positive projection of the group velocity and the parameters of the wave are identical to those of the

reflected wave. Therefore, in the case of $V_D > 0$, this root can be excluded from consideration. When $V_D < 0$, for the second root of Eq. (12b), θ''_2, the projection of the group velocity is negative, $V'_{gy} < 0$, for $\theta > \theta^*$.

Thus, in the case of a receding DW, the refraction angle for $\theta < \theta^*$ should be calculated using the second root of Eq. (12a), whereas its calculation for $\theta > \theta^*$ should be performed using the second root of Eq. (12b). In Fig. 2, the refraction angles calculated in this manner form continuous curves *2* without any discontinuity at $\theta = \theta^*$.

Remember that the angle θ^* is the angle at which the reflective refraction (Fig. 1b) changes to the reflectionless refraction (the double transmission mode) [1] (Fig. 1c, $\theta' > \pi/2$, $V'_{gy} < 0$) or the adjustment-type refraction [8] (Fig. 1d, $\theta' > \pi/2$, $V'_{gy} > 0$). In the case under consideration, only the reflectionless refraction of the magnetoelastic wave is realized. This can be explained as follows. The nonexchange approximation accepted above cuts off the short-wave part, i.e., the spin part, of the low-frequency branch of the spectrum and the acoustic part of the high-frequency branch. This limitation, together with the specific features of the dispersion spectrum of the low-frequency branch, leads to the following results. In the case of a receding DW, according to Eq. (10), the refracted wave has a lower frequency and, hence, a higher group velocity (estimated by the slope of the tangent to the dispersion curve), as compared to the incident wave. This effect is the stronger, the closer the frequency of the incident wave is to the forbidden frequency band. Therefore, when the velocity of the receding DW is relatively low, the wave propagating along a flatter trajectory may have enough time to pass ahead of the DW and get into the second domain.

As one can see from Fig. 2, in the vicinity of the FMR, the transmitted wave is the directly transmitted one whose refraction dependence is represented by line *3* in Fig. 2. On the whole, according to Fig. 2, the inclusion of the external magnetic field does not cause any considerable departure of the dependence $\theta'(\theta)$ from that observed at zero FMR mismatch [1]. A noticeable difference is observed for frequencies ($\omega > \omega_{k1}$ for $V_D > 0$ and $\omega > \omega_{k2}$ for $V_D < 0$) in the vicinity of the magnetoacoustic resonance (MAR). In a narrow angular interval, the directly transmitted wave becomes a deflected wave (curve *4* in Fig. 2). However, it should be noted that a correct calculation in the region of the magnetoelastic wave spectrum is possible with a rigorous consideration for the exchange interaction.

According to the aforementioned selection of the roots of Eqs. (12), Fig. 3 presents the dependence of the projection of the group velocity on the angle of incidence at fixed values of the FMR mismatch ($H_0 = $

const); the dependence was calculated by Eqs. (15) and (16). One can see that, when the reflective refraction ($\theta < \theta^*$) changes to the double transmission mode ($\theta > \theta^*$), the group velocity changes sign (as was mentioned above). The fact that, at $\theta = \theta^*$ and $\theta' = \pi/2$, the projection of the group velocity is equal to zero means that, in the case of the grazing propagation along the DW, the magnetoelastic wave transfers the energy neither toward the DW nor away from it. The condition $\cos(\theta')v(\omega')\Psi(\omega') > -2V_D$, which follows from Eq. (15) and the general limitation $V'_{gy} < 0$, can be represented in the form $\theta < \theta^{**}$, where $\cos\theta^{**} = -2V_D/[v\Psi(\omega)]$; here, θ^{**} is the angle of incidence starting from which the incident wave ceases interacting with the DW and the problem loses its meaning. In Fig. 2, this angle corresponds to the point of intersection of the dependence $\theta'(\theta)$ corresponding to the vicinity of the FMR with curve *3*.

Now, after the determination of the regions of the refracted wave propagation, we can construct two independent solutions to the boundary-value problem of the refractive interaction of a magnetoelastic wave with a moving DW. One of the solutions refers to the case of the reflective refraction with the solution to Eqs. (9) in the form

$$u_1 = U[\exp i(\mathbf{kr} - \omega t) + R\exp i(\mathbf{k'r} - \omega' t)],$$
$$u_2 = UT\exp i(\mathbf{k''r''} - \omega'' t). \tag{17}$$

The other solution refers to the double-transmission refraction:

$$u_1 = U\exp i(\mathbf{kr} - \omega t),$$
$$u_2 = U[T\exp i(\mathbf{k''r''} - \omega'' t) + T'\exp i(\mathbf{k'r} - \omega' t)]. \tag{18}$$

In both cases, the potentials of the fields of the near-boundary magnetostatic oscillations have the same form and, as the solutions to the second of Eqs. (9), are determined with allowance for the limitations given by the equalities

$$\Phi_1 = C\exp[ik_x x - i(\omega - \mathbf{kV}_D)t]\exp[-k_x(y - y_D)],$$

$$(y > y_D);$$
$$\Phi_2 = D\exp[ik_x x - i(\omega - \mathbf{kV}_D)t]\exp[k_x(y - y_D)], \tag{19}$$

$$(y < y_D).$$

Expressions (19) take into account that the near-boundary magnetostatic oscillations are transferred by the moving DW and have a frequency equal to $\tilde{\omega}$.

The boundary conditions of the problem have the standard form [1], but they apply to the DW plane $y = y_D$. Taking into account Eq. (9) and the aforementioned jump of static fields at the DW, the components of both magnetic moment $m_y^{(j)}$ and stress tensor $T_{yz}^{(j)}$ that are required for the substitution can be represented in the form

$$m_y^{(j)} = \frac{\gamma\beta}{\Omega^2 - \omega_{kj}^2}\left[i\Omega\frac{\partial u_j}{\partial x} + (-1)^{j+1}\omega_0\frac{\partial u_j}{\partial y}\right]$$
$$+ \frac{\omega_M}{4\pi(\Omega^2 - \omega_{0j}^2)}\left[\omega_{0j}\frac{\partial\Phi_j}{\partial y} + (-1)^{j+1}i\Omega\frac{\partial\Phi_j}{\partial x}\right], \tag{20}$$

$$T_{yz}^{(j)} = \lambda^*\frac{\partial u_j}{\partial y} + (-1)^{j+1}i\Omega\frac{\gamma\beta_0^2}{M_0(\Omega^2 - \omega_{kj}^2)}\frac{\partial u_j}{\partial x}$$
$$+ \frac{\gamma\beta}{4\pi(\Omega^2 - \omega_{0j}^2)}\left[i\Omega\frac{\partial\Phi_j}{\partial y} + (-1)^{j+1}\omega_{0j}\frac{\partial\Phi_j}{\partial y}\right]. \tag{21}$$

The quantity Ω involved in Eqs. (20) and (21) represents ω or ω', depending on which of the terms u_j appearing in Eqs. (20) and (21) is used for the substitution. The value of λ_Ω^* is chosen with the corresponding frequency.

Omitting the intermediate calculations, we obtain the final result in the form of expressions for the reflection coefficient R, transmission coefficient T, and secondary transmission coefficient T' for a magnetoelastic wave propagating through a moving DW. In the case of reflective refraction, we have

$$1 + R = T,$$

$$R = \frac{-i(\lambda_\omega^*\cot\theta + \lambda_{\omega''}^*\cot\theta'') + \dfrac{\gamma\beta^2}{M_0}\{-G'_-(\omega', \omega'') + G'_+(\omega'', \omega')\}}{i(-\lambda_{\omega'}^*\cot\theta' + \lambda_{\omega''}^*\cot\theta'') + \dfrac{\gamma\beta^2}{M_0}\{G''_-(\omega', \omega'') - G''_+(\omega'', \omega')\}}, \tag{22}$$
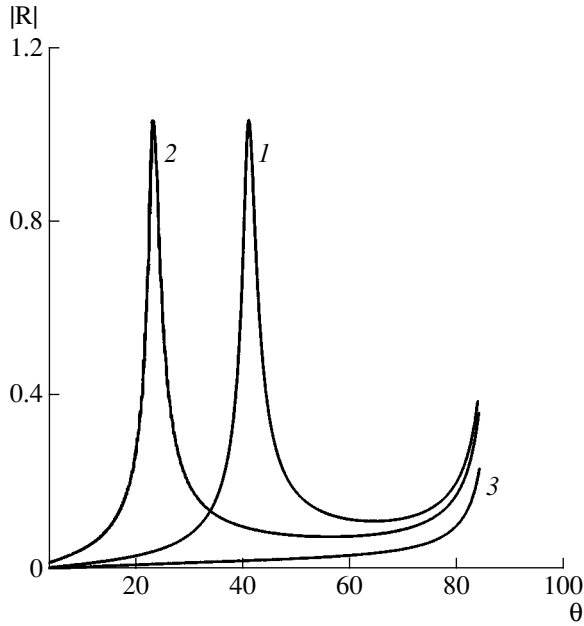
Fig. 4. Dependences $|R(\theta)|$ for the frequency $\omega = 1.45 \times 10^{10}$ s^{-1} and $V_D/c_t = -0.05$: $H_0 = (1)$ 0, (2) 75, and (3) 190 Oe; $\mu_D = (1, 2)$ 250 and (3) 100 cm/s Oe.
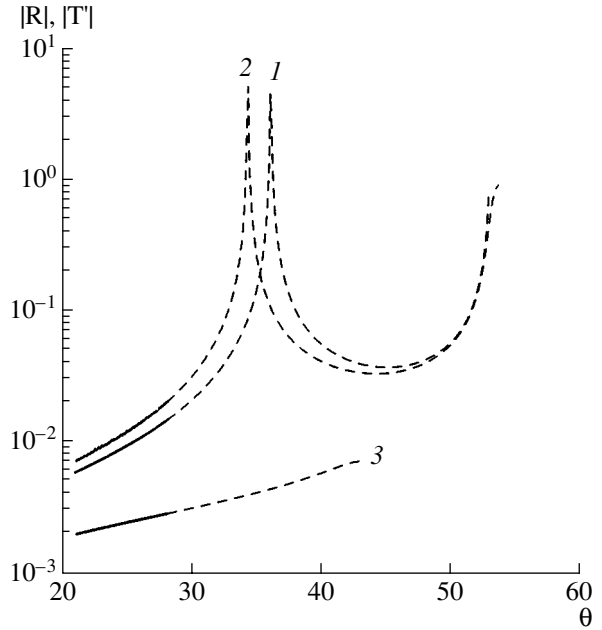
Fig. 5. Dependences $|R(\theta)|$ (solid curves) and $|T'(\theta)|$ (dashed curves) for the frequency $\omega = 1.7 \times 10^{10}$ s^{-1} and $V_D/c_t = -0.6$: $H_0 = (1)$ 0, (2) 100, and (3) 500 Oe; $\mu_D = (1, 2)$ 2880 and (3) 466 cm/s Oe.

where

$$G'_{\mp}(\Omega', \Omega'') = f_2(\Omega')\frac{1}{f_1(\omega') + f_2(\omega'')}$$

$$\times \{F_1(\omega) - F_1(\omega'') \mp f_1(\Omega'')[F_2(\omega'') + F_2(\omega)]\}$$

$$\pm \frac{1}{2}(F_1(\omega) + F_2(\omega'')),$$

$$G''_{\mp}(\Omega', \Omega'') = f_2(\Omega')\frac{1}{f_1(\omega') + f_2(\omega'')} \tag{23}$$

$$\times \{F_1(\omega') - F_1(\omega'') \mp f_1(\Omega'')[F_2(\omega'') + F_2(\omega')]\}$$

$$\pm \frac{1}{2}(F_1(\omega') + F_2(\omega'')),$$

$$f_1(\Omega') = \frac{\Omega'^2 - \omega_{kj}^2 - \omega_M\Omega'}{\Omega'^2 - \omega_{0j}^2}, \quad f_2(\Omega') = \frac{\omega_M}{\Omega' - \omega_{0j}},$$

$$F_1(\Omega') = \frac{\Omega'}{\Omega'^2 - \omega_{kj}^2}, \quad F_1(\Omega') = \frac{-\omega_{0j}}{\Omega'^2 - \omega_{kj}^2}, \tag{24}$$

$$\lambda^*_{\Omega'} = \lambda\left[1 + \frac{\chi_j\omega_{0j}^2}{\Omega'^2 - \omega_{kj}^2}\right], \quad \chi_j = \frac{\gamma\beta^2}{\lambda M_0\omega_{0j}}.$$

If, in Eqs. (22)–(24), $\Omega' = \omega$ or ω', it is necessary to take the FMR and MAR frequencies with subscript 1: ω_{01},

ω_{k1}, χ_1; if $\Omega' = \omega''$, with subscript 2: $\omega_{02}, \omega_{k2}, \chi_2$. In the case of the double-transmission refraction, the formulas for the amplitude factors coincide with formulas (22)–(24) in their structure and are therefore not presented here to save room.

The calculations by Eqs. (22)–(24) were performed for an iron garnet crystal with the parameters $c_t = 3.8 \times 10^5$ m/s, $\omega_M = 3.5 \times 10^{10}$ s^{-1}, $\omega_0 = \gamma H_a = 1.4 \times 10^{10}$ s^{-1}, $M_0 = 140$ G, $\lambda = 7.64 \times 10^{11}$, and $\beta = 7.4 \times 10^6$. In iron garnets at room temperature, the mobility is $\mu_D = 100$–500 cm/s Oe [9]. However, to reveal certain features of the amplitude factor behavior, some calculations were performed with much higher mobility values.

Figure 4 shows the dependence of the reflection coefficient on the angle of incidence of a shear wave for different fixed values of the external magnetic field in the case of a receding DW. One can see that the FMR peak observed in magnetostatic scattering fields at zero FMR mismatch [1] is displaced toward smaller angles of incidence in a relatively weak magnetic field (curve 2) and may disappear in strong magnetic fields (curve 3). This means that the position of the forming FMR maximum and the conditions for its existence are determined by the strength of the external magnetic field H_0. This should be expected, because H_0 determines the mismatch of the uniform spin precession frequencies in the domains, ω_{0j}. The latter frequencies are involved in Eqs. (23) and (24) for the reflection coefficients as the pole singularities, which determine the position of the FMR peak.
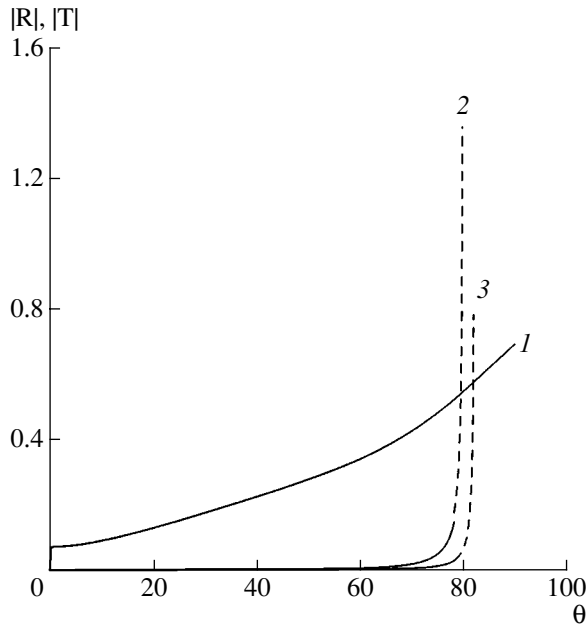
Fig. 6. Dependences $|R(\theta)|$ (solid curves) and $|T'(\theta)|$ (dashed curves) for the frequency $\omega = 2.62 \times 10^{10}$ s^{-1} and $V_D/c_t = -0.1$: $H_0 = (1)$ 0, (2) 50, and (3) 200 Oe; $\mu_D = (1, 2)$ 760 and (3) 190 cm/s Oe.

Fig. 7. Dependence $|R(H_0)|$ for the angle of incidence $\theta = 45°$ and frequency $\omega = 1.45 \times 10^{10}$ s^{-1}: $\mu_D = (1)$ 400, (2) 300, and (3) 200 cm/s Oe.

As shown in Fig. 5, a similar transformation of the FMR peak with varying magnetic field strength also occurs for the amplitude factor of the additionally transmitted wave T'. From Fig. 5 it follows that, when the refraction mode changes, the dependence of the reflection coefficient on the angle of incidence smoothly, without any discontinuities, passes into the angular dependence of the transmission coefficient of the additionally deflected wave. A similar situation takes place for the frequencies in the vicinity of the MAR (Fig. 6). As one can see from Fig. 6, the inclusion of the external magnetic field noticeably affects the angular dependences of the amplitude factors of refracted waves.

Figure 7 shows the dependence of the reflection coefficient on the external field at a fixed angle of incidence for different values of the DW mobility. The external magnetic field is directed so that $V_D < 0$. The angle of incidence corresponds to the FMR peak in Fig. 4 at zero difference between the uniform precession frequencies in the domains. A specific feature of the dependence $R(H_0)$ is the presence of the resonance peak in strong external magnetic fields. Thus, even for a large difference between the FMR frequencies of the domains, conditions for the total reflection of the incident wave from the moving DW can be realized. From Fig. 7, it also follows that the number and height of the FMR peaks and their positions strongly depend on the mobility of the DW.

By choosing the appropriate conditions, it is possible to obtain a change from reflective refraction to double transmission mode for a shear wave incident at a fixed angle (Fig. 8). One can see that, as in the case of
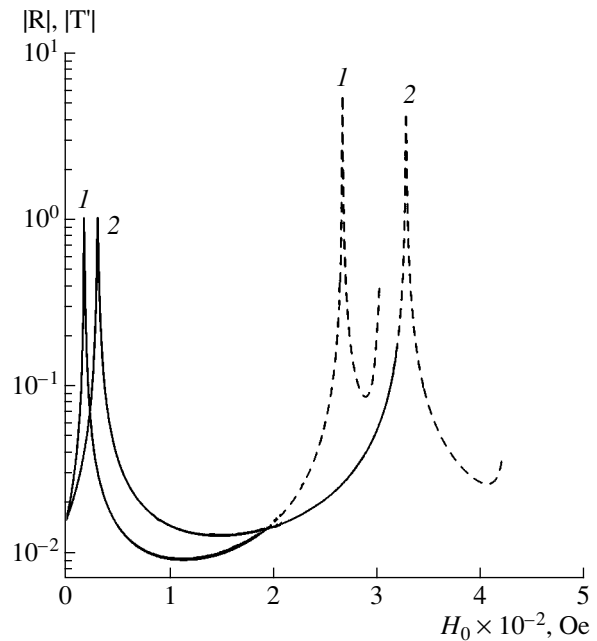
Fig. 8. Dependences $|R(H_0)|$ (solid curves) and $T'(H_0)$ (dashed curves) for the angle of incidence $\theta = 36.5°$ and frequency $\omega = 1.45 \times 10^{10}$ s^{-1}: $\mu_D = (1)$ 1000 and (2) 600 cm/s Oe.

angular dependence, the change in the refraction modes does not cause any discontinuity of the amplitude factors.

ACKNOWLEDGMENTS

REFERENCES

1. E. A. Vilkov, V. G. Shavrov, and N. S. Shevyakhov, Akust. Zh. **47**, 200 (2001) [Acoust. Phys. **47**, 160 (2001)].

2. A. Malozemov and J. Slonczewski, *Domain Walls in Materials with Cylindrical Magnetic Domains* (Mir, Moscow, 1982) [in Russian].

3. A. I. Akhiezer, V. G. Bar'yakhtar, and S. V. Peletminskii, *Spin Waves* (Nauka, Moscow, 1967; North-Holland, Amsterdam, 1968).

4. V. Strauss, in *Physical Acoustics: Principles and Methods*, Ed. by W. P. Mazon (Academic, New York, 1968; Mir, Moscow, 1970), Vol. 4, Part B, pp. 211–268.

5. R. LeCraw and R. Comstock, in *Physical Acoustics: Principles and Methods*, Ed. by W. P. Mazon (Academic, New York, 1965; Mir, Moscow, 1968), Vol. 3, Part B, pp. 127–200.

6. Yu. M. Yakovlev and S. Sh. Gendelev, *Ferrite Single Crystals in Radio Electronics* (Sovetskoe Radio, Moscow, 1975) [in Russian].

7. V. V. Lemanov and G. A. Smolenskiĭ, Usp. Fiz. Nauk **108** (3), 465 (1972) [Sov. Phys. Usp. **15** (6), 708 (1973)].

8. B. M. Bolotovskiĭ and S. N. Stolyarov, Usp. Fiz. Nauk **159** (1), 155 (1989) [Sov. Phys. Usp. **32**, 813 (1989)].

9. G. A. Smolenskiĭ and V. V. Lemanov, *Ferrites and Their Technical Applicaton* (Nauka, Leningrad, 1975) [in Russian].

Translated by E. Golyamina

High-Q Oscillations in a Layered Elastic Medium

O. Yu. Dinariev and V. N. Nikolaevskiĭ

Shmidt United Institute of Physics of the Earth, Russian Academy of Sciences,
ul. Bol'shaya Gruzinskaya 10, Moscow, 123995 Russia
e-mail: dinariev@mail.ru
Received June 23, 2004

Abstract—Conditions of the existence of long-lived acoustic resonances that occur in a layered medium because of its oscillation with low damping factors are considered. A priori theoretical estimates relating the distribution of resonance frequencies in the complex plane to the parameters of inhomogeneity of the layered system are obtained. A scheme of resonance calculations in numerical modeling is described. Examples of geophysical media with long-lived resonances are presented. © *2005 Pleiades Publishing, Inc.*

INTRODUCTION

The problem of oscillations of a finite-size elastic body consists in determining a denumerable set of eigenmodes whose frequencies have a crowding point at infinity. If the body is placed in an unbounded medium with other properties, the eigenfrequency spectrum in the general case is shifted in the complex plane. Simultaneously, the eigenfrequencies acquire imaginary parts, and the corresponding modes of oscillation are called acoustic resonances. The study of the relations between the characteristics of inhomogeneity and the parameters of resonances is the subject of acoustic spectroscopy [1]. It should be noted that the conceptual and mathematical apparatus of this field of science is to a considerable extent borrowed from quantum mechanics [2], where the study of resonances is the most important source of information about quantum systems.

In geophysics, studies of resonances related to a layered elastic medium are of great importance. Such resonances affect the amplitude–frequency characteristic of a system formed by the medium and a ground-based object [3] and, hence, the service conditions of structures and instruments. Long-lived resonances are of special importance, because, according to modern concepts, precisely these resonances determine the efficiency of vibroseismic actions on oil pools [4]. In our previous work [5], we studied the distribution of resonance frequencies in the complex plane for an unbounded layered medium. In the present paper, we consider the conditions of the existence of long-lived resonances in unbounded and semibounded media.

ACOUSTIC RESONANCES IN LAYERED MEDIA

Consider elastic waves (longitudinal or transverse ones) described by the equation

$$\rho \partial_t^2 u - \partial_x (E \partial_x u) = f, \tag{1}$$

where $u = u(t, x)$ is the displacement function, $\rho = \rho(x)$ is the density, $E = E(x)$ is the elastic modulus, and $f = f(t, x)$ is the external force field. We redefine the spatial coordinate according to the differential relation

$$dy = E_0 dx / E(x),$$

where E_0 is a constant with the pressure dimension (the characteristic value of the elastic modulus). Then, Eq. (1) takes the form

$$\kappa^2 \partial_t^2 u - \partial_y^2 u = f_* = E_0^{-2} E f,$$
$$\kappa = (\rho E)^{1/2} E_0^{-1}. \tag{2}$$

Let us discuss the boundary conditions for Eq. (2). We seek the solution to Eq. (2) for the half-space $y > 0$ (Problem 1) and for the unbounded space $-\infty < y < +\infty$ (Problem 2) and interpret this solution as the response of the system to an external force f. In both cases, we assume that the force f is equal to zero outside some finite spatial interval of length L. In addition, the value of κ outside this spatial interval is constant. We can assume that $\kappa = \kappa_-$ for $y < 0$ (Problem 2) and $\kappa = \kappa_+$ for $y > L$ (Problems 1 and 2). At spatial infinity, the radiation conditions are imposed, and at the boundary of the half-space in Problem 1, we impose the condition of zero stress. Hence, we have the following boundary conditions for Problem 1:

$$\partial_y u|_{y=0} = 0, \tag{3}$$

$$(\kappa_+ \partial_t u + \partial_x u) \longrightarrow 0, \quad y \longrightarrow +\infty, \tag{4}$$

and for Problem 2:

$$(\kappa_- \partial_t u - \partial_x u) \longrightarrow 0, \quad y \longrightarrow -\infty, \tag{5}$$

$$(\kappa_+ \partial_t u + \partial_x u) \longrightarrow 0, \quad y \longrightarrow +\infty. \tag{6}$$

Since Eq. (2) and boundary conditions (3)–(6) contain no explicit time dependence, we can apply the Fourier transformation

$$v = v(\omega, y) = \int \exp(-i\omega t)u(t, y)dt.$$

Then, we obtain an ordinary differential equation

$$\partial_y^2 v + \omega^2 \kappa^2 v = F = -\int \exp(-i\omega t)f_*(t, y)dt \quad (7)$$

with the following boundary conditions:

$$\partial_y v\big|_{y=0} = 0 \quad (8)$$

$$(i\omega\kappa_+ v + \partial_x v) \longrightarrow 0, \quad y \longrightarrow +\infty \quad (9)$$

for Problem 1 and

$$(i\omega\kappa_- v - \partial_x v) \longrightarrow 0, \quad y \longrightarrow -\infty, \quad (10)$$

$$(i\omega\kappa_+ v + \partial_x v) \longrightarrow 0, \quad y \longrightarrow +\infty \quad (11)$$

for Problem 2.

For each of the Problems 1 and 2, we introduce two solutions to homogeneous equation (7) (i.e., when $F = 0$), namely, $v_- = v_-(\omega, y)$ and $v_+ = v_+(\omega, y)$, so that they are determined by the following boundary conditions:

$$v_-\big|_{y=0} = 1, \quad \partial_y v_-\big|_{y=0} = 0,$$

$$v_+ \longrightarrow \exp(-i\omega\kappa_+ y), \quad y \longrightarrow +\infty$$

for Problem 1 and

$$v_- \longrightarrow \exp(i\omega\kappa_- y), \quad y \longrightarrow -\infty,$$

$$v_+ \longrightarrow \exp(-i\omega\kappa_+ y), \quad y \longrightarrow +\infty.$$

for Problem 2.

We define the Green's function by the formula

$$G(\omega, y, y_0) = \Delta^{-1}\begin{cases} v_+(\omega, y)v_-(\omega, y_0), & y > y_0, \\ v_-(\omega, y)v_+(\omega, y_0), & y < y_0, \end{cases} (12)$$

$$\Delta = \partial_y v_+(\omega, y_0)v_-(\omega, y_0) - v_+(\omega, y_0)\partial_y v_-(\omega, y_0).$$

Here, Δ is the Wronskian constructed on the basis of two solutions to the homogeneous equation. Therefore, Δ does not depend on the parameter y_0:

$$\Delta = \Delta(\omega).$$

One can easily verify that the following equation is satisfied:

$$(\partial_y^2 + \omega^2\kappa^2(y))G(\omega, y, y_0) = \delta(y - y_0),$$

where the Dirac delta function is on the right-hand side. Therefore, we can write the formal solution to Eq. (7) in the form

$$v(\omega, y) = \int G(\omega, y, y_0)F(\omega, y_0)dy_0. \quad (13)$$

The integration in formula (13) is performed over the half-axis for Problem 1 and over the whole axis for Problem 2. Expression (13) gives the solution to the problems stated above, because the boundary conditions imposed on the functions $v_- = v_-(\omega, y)$ and $v_+ = v_+(\omega, y)$ provide for the fulfillment of boundary conditions (8)–(11).

The functions $v_- = v_-(\omega, y)$ and $v_+ = v_+(\omega, y)$ can be analytically continued to complex values of ω. The functions $\Delta = \Delta(\omega)$ and $G(\omega, y, y_0)$ allow a corresponding continuation. In this case, the Green's function $G(\omega, y, y_0)$ may have poles coinciding with zeroes of function $\Delta = \Delta(\omega)$. If Ω is a root of the equation

$$\Delta(\omega) = 0, \quad (14)$$

the corresponding coordinate functions $v_-(\Omega, y)$ and $v_+(\Omega, y)$ are proportional to

$$v_+(\Omega, y) = C(\Omega)v_-(\Omega, y). \quad (15)$$

The reverse is true as well: from Eq. (15), one obtains Eq. (14).

According to [5], for any of the solutions Ω to Eq. (14), either $\Omega = 0$ or $\text{Im}\,\Omega > 0$. Solutions with a positive imaginary part may be absent, but if they exist, they are identified with the resonance frequencies of the layered system under consideration. At the same time, the corresponding solutions to the problem, namely, $v_- = v_-(\Omega, y)$ (or $v_+ = v_+(\Omega, y)$, which is equivalent by virtue of Eq. (15)), are identified with the resonant modes of oscillation.

This definition is based on the following speculation. Using Eq. (12), we apply the inverse Fourier transformation

$$u(t, y) = (2\pi)^{-1}\int \exp(i\omega t)$$
$$\times G(\omega, y, y_0)F(\omega, y_0)dy_0 d\omega. \quad (16)$$

The integration in Eq. (16) is performed along the straight line $\text{Im}\,\Omega = a$ lying below all singularities of the integrand. As it was shown above, the poles of the Green's function $G(\omega, y, y_0)$ lie in the upper complex half-plane. Let all singularities of the function $F(\omega, y)$ lie above the straight line $\text{Im}\,\Omega = \Lambda > 0$. This assumption corresponds to the condition that the external force $f_*(t, y)$ is equal to zero for $t < t_*$ at a certain t_* (the Paley–Wiener theorem [6]). As for the Green's function $G(\omega, y, y_0)$, in the region $0 \leq \text{Im}\,\Omega < \Lambda$, it may have poles $\Omega_0 = 0, \Omega_1, \Omega_2, \ldots$, where $\text{Im}\,\Omega_n > 0$ for $n > 0$. Shifting the contour of integration in Eq. (16) upwards with bypassing the poles and taking the corresponding residues, we arrive at the formula

$$u(t, y) = i\int dy_0 \text{Res}_{\Omega_0}[G(\omega, y, y_0)F(\omega, y_0)]dy_0$$

$$+ i\sum_{n>0}\int dy_0 \exp(i\Omega_n t)$$

$$\times \text{Res}_{\Omega_n}[G(\omega, y, y_0)F(\omega, y_0)]dy_0 + O(\exp(-\Lambda t)).$$

From this expression, one can see that the total solution contains a sum of damped oscillations (resonances) corresponding to the complex frequencies Ω_n.

In this case, $\alpha_n = \mathrm{Re}\,\Omega_n$ is the oscillation frequency, $\beta_n = \mathrm{Im}\,\Omega_n$ is the damping factor, $T_n = 2\pi/\alpha_n$ is the oscillation period, $\tau_n = 1/\beta_n$ is the lifetime, and $\xi_n = \tau_n/T_n$ is the dimensionless lifetime of a resonance.

Thus, for determining the resonances of a layered system, it is sufficient to have the solution to the homogeneous equation (2). In a small number of cases, such a solution can be obtained in an analytical form [7] and, hence, the parameters of the resonances can be exactly determined. In the general case, the wave equation should be solved numerically for different complex values of ω and, then, a numerical solution to Eq. (13) should be sought for. Note that, to estimate the number N_C of the roots of Eq. (13) in a complex plane region bounded by a piecewise smooth contour C, one can use the formula

$$N_C = (2\pi i)^{-1} \int_C \Delta(\omega)^{-1} (\partial\Delta(\omega)/\partial\omega)\,d\omega,$$

where the right-hand side can be numerically determined for specific media and contours C.

LONG-LIVED RESONANCES

To study the conditions of the existence of long-lived resonances, it is convenient to begin with the simplest models that allow an exact calculation of resonances. We consider Problem 1, in which $\kappa = \kappa_0$ for $0 < y < L$ and $\kappa = \kappa_+$ for $L < y$. Within each of the intervals, the solution to homogeneous equation (2) is determined in the form of a sum of exponentials, which are sewn together according to the continuity conditions for the function v and its derivative. The Wronskian is determined by a direct calculation:

$$\Delta = -2^{-1} i\omega((\kappa_+ - \kappa_0)\exp(i\omega(\kappa_+ - \kappa_0)L)$$
$$+ (\kappa_+ + \kappa_0)\exp(i\omega(\kappa_+ + \kappa_0)L)).$$

Therefore, the equation for the resonances has the form

$$\exp(2i\omega\kappa_0 L) = \gamma, \qquad (17)$$

where $\gamma = (\kappa_0 - \kappa_+)/(\kappa_0 + \kappa_+)$. Depending on the sign of γ, two sets of solutions are possible:

(a) for $\gamma > 0$,

$$A_+ = \{(2\kappa_0 L)^{-1}(2\pi n + i\beta)\,|\,n = 0, \pm1, \pm2, \dots\}; \quad (18)$$

(b) for $\gamma < 0$,

$$A_- = \{(2\kappa_0 L)^{-1}(\pi + 2\pi n + i\beta)\,\big|\,n = 0, \pm1, \pm2, \dots\}. \qquad (19)$$

Here, $\beta = -\ln|\gamma|$. For $\gamma = 0$, Eq. (17) has no solutions. It is evident that long-lived resonances can exist when $|\gamma|$ is close to unity; i.e., when the layers widely differ in acoustic stiffness.

Now, let us consider Problem 2, in which $\kappa = \kappa_-$ for $y < 0$, $\kappa = \kappa_0$ for $0 < y < L$, and $\kappa = \kappa_+$ for $L < y$. The

problem is solved in the same way as Problem 1. The Wronskian is calculated in an explicit form:

$$\Delta = -i\omega(2\kappa_0)^{-1}\exp(-i\omega\kappa_+ L)$$
$$\times ((\kappa_+ - \kappa_0)(-\kappa_- + \kappa_0)\exp(-i\omega\kappa_0 L)$$
$$+ (\kappa_+ + \kappa_0)(\kappa_- + \kappa_0)\exp(i\omega\kappa_0 L)).$$

As in the case of Problem 1, the equation for the resonances has the form of Eq. (17) with solutions (18) and (19), where

$$\gamma = (\kappa_0 - \kappa_-)(\kappa_0 - \kappa_+)/(\kappa_0 + \kappa_+)(\kappa_0 + \kappa_+).$$

Again, long-lived resonances are possible when the acoustic stiffness of the middle layer is much higher or much lower than the acoustic stiffnesses of the outer layers.

Although it is impossible to analytically calculate the resonances for the case of layered media of the general form, it is possible to obtain a priori estimates for their distribution in the complex plane. For this purpose, we calculate the Green's functions for the following auxiliary nonresonance problems.

Problem 1: $\kappa = \kappa_+$ for $0 < y$, and the Green's function $G_*(y, y_0, \omega)$ is calculated by formula (12), where

$$v_- = (\exp(-i\omega\kappa_+ y) + \exp(i\omega\kappa_+ y))/2,$$

$$v_+ = \exp(-i\omega\kappa_+ y),$$

$$\Delta = -i\omega\kappa_+.$$

Problem 2: $\kappa = \kappa$ for $y < 0$, $\kappa = \kappa$ for $0 < y$, and the Green's function $G_*(y, y_0, \omega)$ is calculated by formula (12), where

$$v_- = \begin{cases} \exp(i\omega\kappa_- y), & y < 0, \\ (2\kappa_+)^{-1}((\kappa_+ - \kappa_-)\exp(-i\omega\kappa_+ y) \\ + (\kappa_+ + \kappa_-)\exp(i\omega\kappa_+ y)), & y > 0, \end{cases}$$

$$v_+ = \begin{cases} (2\kappa_-)^{-1}((\kappa_- - \kappa_+)\exp(-i\omega\kappa_- y) \\ + (\kappa_+ + \kappa_-)\exp(i\omega\kappa_- y)), & y < 0, \\ \exp(-i\omega\kappa_+ y), & y > 0, \end{cases}$$

$$\Delta = -i\omega(\kappa_+ + \kappa_-).$$

We seek the solution to Problem 1 or Problem 2 in the form

$$v(\omega, y) = \int G_*(y, y_0, \omega) V(\omega, y_0)\,dy_0 \qquad (20)$$

and define the function

$$\nu(y) = \begin{cases} \kappa(y)^2 - \kappa_-^2, & y < 0 \\ \kappa(y)^2 - \kappa_+^2, & y > 0. \end{cases}$$
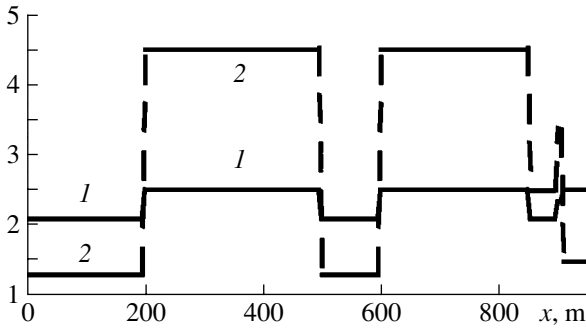
Fig. 1. Problem 1: (*I*) density (t/m³) and (*2*) phase velocity (km/s) distributions in depth.

Fig. 2. Problem 1: resonance frequency distribution in the complex plane.

Substituting Eq. (20) into Eq. (2), we obtain the integral equation

$$V(\omega, y) + \omega^2 v(y)$$
$$\times \int G_*(y, y_0, \omega) V(\omega, y_0) dy_0 = F(\omega, y). \quad (21)$$

Since the external force $F(\omega, y)$ and the function $v(y)$ are equal to zero outside the interval $0 \leq y \leq L$, the function $V(\omega, y)$ is also equal to zero outside this interval. Therefore, Eq. (21) can be interpreted as an integral equation for the functions on the interval $0 \leq y \leq L$. Equation (21) with zero right-hand side serves for the simultaneous determination of resonance modes and resonance frequencies. In the latter case, the problem for resonances can be represented in the operator form

$$(1 + K)V = 0, \quad (22)$$

where K is a linear integral operator appearing on the left-hand side of Eq. (21) and acting in the function space on the segment [0, L]. If, in this space, we introduce an appropriate norm in which operator K is continuous, from Eq. (22) we obtain an estimate for the operator norm:

$$\|K\| \geq 1. \quad (23)$$

The choice of the norm and the function space is not uniquely defined. Therefore, inequality (23) represents a family of a priori estimates for the distribution of resonance frequencies in the co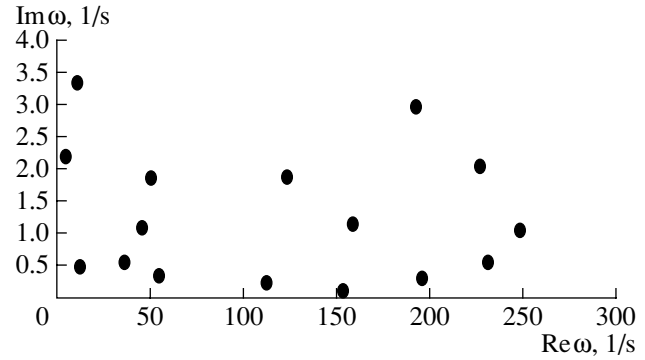mplex plane. For example, if we chose a space of continuous functions with the norm $\max_{0 \leq y \leq L} |V|$, we obtain the estimate

$$|\omega| \kappa_*^{-2} \max_{0 \leq y \leq L} |v(y)| (\mathrm{Im}\,\omega)^{-1}$$
$$\times (\exp(L\kappa_+ \mathrm{Im}\,\omega) - 1) \geq 1, \quad (24)$$
$$\kappa_* = \min(\kappa_-, \kappa_+).$$

Another example: if we chose a space of integrable functions with the norm $\int |V| dy$, we obtain the estimate

$$|\omega| \kappa_*^{-1} \int |v(y)| \exp(y\kappa_+ \mathrm{Im}\,\omega) dy \geq 1. \quad (25)$$

Estimates (24) and (25) show that small values of the function $v(y)$ characterizing the inhomogeneity of the layered system preclude the presence of resonances with large relative lifetimes ξ but still allow the presence of resonances with large absolute lifetimes and large periods. Resonances with large relative lifetimes are only possible in a system with a strong inhomogeneity.

NUMERICAL CALCULATION OF RESONANCES

To study the distribution of resonance frequencies in the complex plane, we performed numerical calculations for different layered media. With a view to geophysical applications, we chose the parameters of media (density ρ, phase velocity of waves $c = (E/\rho)^{1/2}$, and thickness) close to those of actual sediment deposits. Below, we present the results of the numerical modeling of Problems 1 and 2 for the cases where long-lived resonances were obtained.

In Problem 1, we considered an inhomogeneous region with a total size $L = 950$ m. The density and velocity distributions in this range are shown in Fig. 1. Below a depth of 950 m, the density and velocity were assumed to be constant: $\rho = 2.35$ t/m³ and $c = 3.35$ km/s. The distribution of resonances in the complex plane is shown in Fig. 2. The calculated parameters of the resonance with the longest lifetime are $\mathrm{Re}\,\omega = 153.72$ 1/s, $\mathrm{Im}\,\omega = 0.11$ 1/s, and $\xi = 231.51$.

In Problem 2, we considered an inhomogeneous region with a total size $L = 293$ m. The density and velocity distributions in this range are shown in Fig. 3. Outside this region, the density and velocity were assumed to be constant: $\rho = 2.55$ t/m³ and $c = 4.32$ km/s for $x < 0$; $\rho = 2.7$ t/m³ and $c = 4.5$ km/s for $x > L$. The
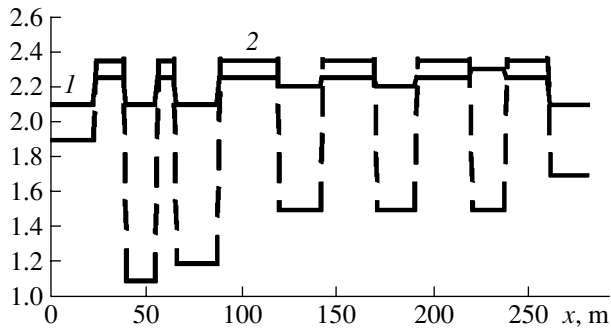
Fig. 3. Problem 2: (*1*) density (t/m^3) and (*2*) phase velocity (km/s) distributions in depth.
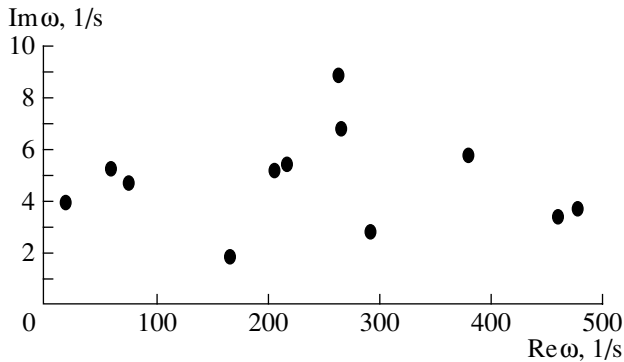
Fig. 4. Problem 2: resonance frequency distribution in the complex plane.

distribution of resonances in the complex plane is shown in Fig. 4. The calculated parameters of the resonance with the longest lifetime are $\mathrm{Re}\,\omega = 165.32$ 1/s, $\mathrm{Im}\,\omega = 1.88$ 1/s, and $\xi = 14.03$.

CONCLUSIONS

The results of numerical modeling demonstrate that the existence of actual geophysical media with acoustic resonances characterized by large relative lifetimes is possible. However, the above theoretical analysis shows that such resonances can only occur in media with strong inhomogeneities of density and elastic modulus. In the wide class of weakly inhomogeneous media, such resonances are impossible while a broad spectrum of resonances with small lifetimes may be present. The method presented in this paper allows a numerical calculation of resonance frequencies and resonance modes.

REFERENCES

1. N. D. Veksler, *Acoustic Spectroscopy* (Valgus, Tallinn, 1989) [in Russian].

2. A. I. Baz', Ya. B. Zel'dovich, and A. M. Perelomov, *Scattering, Responses, and Decays in Quantum Mechanics* (Nauka, Moscow, 1966) [in Russian].

3. *Local Resonances in Layered Media* (OIFZ RAN, Moscow, 2000) [in Russian].

4. M. A. Mokhov, V. A. Sakharov, and Kh. Kh. Khabibullin, Neftepromyslovoe Delo **4**, 24 (2004).

5. O. Yu. Dinariev and V. N. Nikolaevskiĭ, Izv. Ross. Akad. Nauk, Mekh. Tverd. Tela **3**, 88 (2001).

6. L. Hermander, *The Analysis of Linear Partial Differential Operators* (Springer, Berlin, 1983), Vol. 1.

7. L. M. Brekhovskikh and O. A. Godin, *Acoustics of Layered Media* (Nauka, Moscow, 1989; Springer, Berlin, 1990).

Translated by E. Golyamina

Experimental Estimate for the Transformation of Underwater Acoustic Radiation into a Seismoacoustic Wave

G. I. Dolgikh and V. A. Chupin

Il'ichev Pacific Oceanological Institute, Far East Division, Russian Academy of Sciences,
ul. Baltiĭskaya 43, Vladivostok, 690041 Russia
e-mail: dolgikh@poi.dvo.ru
Received May 5, 2004

Abstract—On the basis of experimental data obtained from a non-equal-armed strainmeter with an arm length of 52.5 m in the presence of a low-frequency hydroacoustic source operating in a deep sea and in a shallow sea, an estimate is obtained for the ratio of the energy flux in the Rayleigh wave to the acoustic power emitted by the hydroacoustic source. © *2005 Pleiades Publishing, Inc.*

Experiments on using coast-based strainmeter for recording the oscillations excited in water by low-frequency hydroacoustic sources [1] showed good prospects for strainmeters as instruments for studying the behavior of seismoacoustic and hydroacoustic oscillations and waves at the hydrosphere–lithosphere interface [2]. At the Schulz test site of the Pacific Oceanological Institute, a 52.5-m non-equal-armed stationary strainmeter was installed at a depth of 5–7 m below the earth surface and oriented along the north–south line. The interference units, which include a frequency-stabilized laser, a collimator, and an optical gate (a diaphragm, a polaroid, and a λ/4 plate), of the strainmeter

were placed in a thermally insulated room. The corner reflectors were positioned in individual thermally insulated chambers. The whole path of the laser beam between reflector and interference unit ran through a light guide made of stainless steel pipes.

Figure 1 schematically represents the recording system of the strainmeter. To control the interferometer of the strainmeter, a reference-frequency oscillator (RFO) generates an electric signal with a frequency of 25 kHz, an amplitude of 5 V, and an off-duty ratio of 2. This signal is transformed to a sinusoid and amplified by a power amplifier (PA) to control the piezoceramic element that changes the length of one of the arms of the
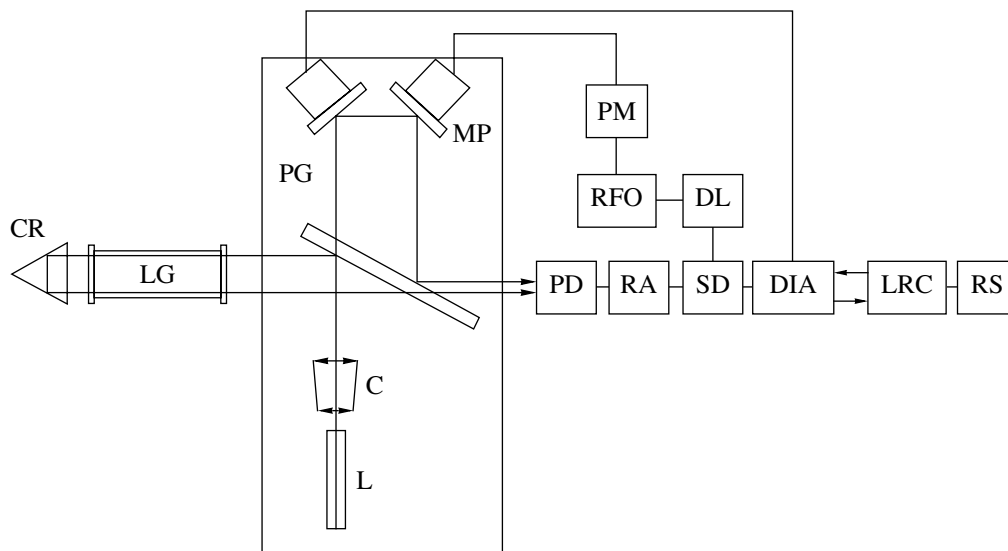
Fig. 1. The optical scheme of the strainmeter with a flow chart of the recording system: (CR) corner reflector, (LG) light guide, (MP) mirrors on piezoceramic elements, (PG) plane-parallel glass plate, (C) collimator, (L) He-Ne frequency-stabilized laser, (PD) photodiode, (RA) resonance amplifier, (SD) synchronous detector, (DIA) differential integral amplifier, (LRC) level-reset circuit, (PA) power amplifier, (RFO) reference-frequency oscillator, (DL) delay line, and (RS) recording system.

2.5 E–03 μm

0

Sept. 17, 2004 17:45:34.00   Sept. 17, 2004 18:45:34.01
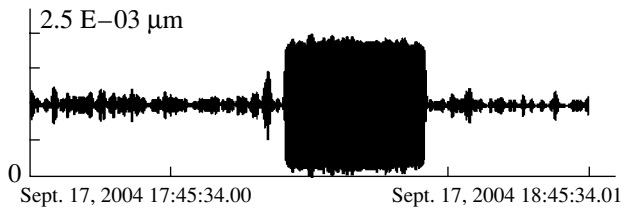
Fig. 2. Filtered part of the strainmeter record obtained in the course of the operation of the low-frequency hydroacoustic source at a frequency of 32.6 Hz.

1.1E–03 μm

1.2E–06 μm; 1.5 Hz   25.7 Hz   50 Hz

Fig. 3. Spectrum of a part of the strainmeter record obtained in the course of the operation of the hydroacoustic source at a frequency of 32.6 Hz.

interferometer by $0.1\lambda/2$ (λ is an He–Ne laser wavelength of 0.63×10^{-6} m). This leads to modulation of the interference pattern intensity incident on the photodiode (PD), from which the signal is supplied to the resonance amplifier (RA). The latter provides an amplification by a factor of 10^4 at a frequency of 25 kHz with a passband of 6 kHz and is made in the form of a separate unit positioned on the optical bench. The resonance amplifier produces a signal that is proportional to the variation in the arm length difference of the interferometer. The signal passes to a synchronous detector (SD), to the second input of which the reference signal passed through a delay line (DL) is supplied. The delay line is used to compensate for the time delay of the signal passing through the interferometer. It allows a phase shift in the output signal by $\pm\pi/2$ with respect to the input signal. The synchronous detector gives an output signal of ± 1 V proportional to the phase of the input signal. Then, the signal is supplied to the differential integral amplifier (DIA). The latter produces a signal of ± 130 V, which controls the second piezoceramic element. This element, displacing the mirror of the interference unit, equalizes the arm difference of the interferometer within $\pm\lambda/2$. To compensate for deformations exceeding the variation $\Delta L = \pm\lambda/2$, a level-reset circuit (LRC) is used. This circuit equalizes the DIA output voltage with the inner reference voltage U_{ref}, and, when the DIA voltage reaches the value of $\pm U_{ref}$, which corresponds to the variation $\Delta L = \pm\lambda/2$, a reset pulse is generated to reset the control voltages at the DIA output from $U_{max} = \pm U_{ref}$ to $U = 0$ within 1 ms. This corresponds to a jump of the interference pattern from one minimum to another, nearest to it. The case of $U_{max} = +U_{ref}$ corresponds to an extension of the deformograph base by $\lambda/2$, and the case of $U_{max} = -U_{ref}$, to a compression of the deformograph base by $\lambda/2$. The recording system (RS) follows the variation of the deformograph base to an accuracy of $10^{-4}\lambda/2$ in the frequency band within 0–1000 Hz. At the analog output, the RS produces the voltage $U_{out} = \pm 5$ V that is proportional to the deformation $\Delta L = \pm\lambda/2$. At the pulse output, the RS produces the reset pulses (Ur^+ and Ur^-) whose sum determines the shift of the deformation in $\lambda/2$ units.

Thus, the strainmeter measures the variation in the length of the deformograph arm between the interfer-

ence unit and the reflector, which are mounted on separate basements. The arm length of the deformograph is 52.5 m. In addition, the deformograph is characterized by the following parameters: a sensitivity of 10^{-10}–10^{-11} ($\Delta L/L$, where ΔL is the displacement of the deformograph base and ΔL is the deformograph length, equal to 52.5 m), the accuracy of microdisplacement measurements within 10^{-9}–10^{-10} m, the operating frequency band 0–1000 Hz, and an unbounded dynamic range.
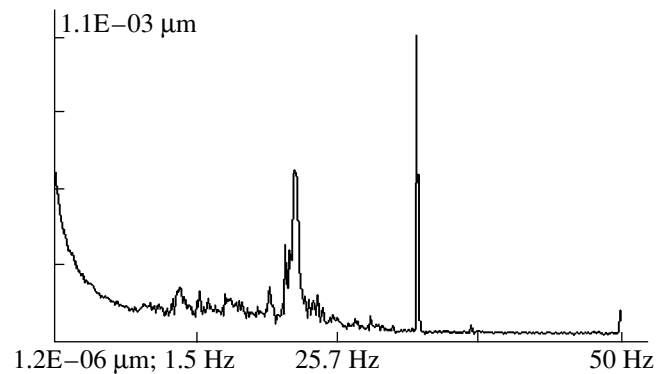
In studying the behavior of seismoacoustic and hydroacoustic oscillations and waves at the hydrosphere–lithosphere interface, it is important to know the amount of hydroacoustic energy transformed into seismoacoustic one and received by the strainmeter. Over a period of many years, in the Sea of Japan and at its coast, the excitation of hydroacoustic oscillations by a low-frequency source and the reception of seismoacoustic oscillations induced by it had been studied with the use of a coast-based strainmeter. The main conclusion derived from all these experimental studies was that the use of a coast-based strainmeter for studying the generation, dynamics, and transformation of hydroacoustic oscillations and waves at the hydrosphere–lithosphere interface is rather promising. Here, it is necessary to note that the strainmeter provides a reliable detection of seismoacoustic oscillations caused by the operation of low-frequency hydroacoustic sources in both shallow and deep water even when the source power is low. As an example (Figs. 2, 3), we present a bandpass-filtered record obtained from the strainmeter and the spectrum of this record. The bandpass filter had the following parameters: cutoff frequencies of 32.5 and 32.7 Hz, a length of 12000, and a Hamming window. Figure 3 shows a part of the spectrum of the unfiltered record obtained from the strainmeter in the course of the operation of the low-frequency hydroacoustic source. The maximum observed at a frequency of about 22 Hz is associated with one of the resonances of the strainmeter system. This experiment was
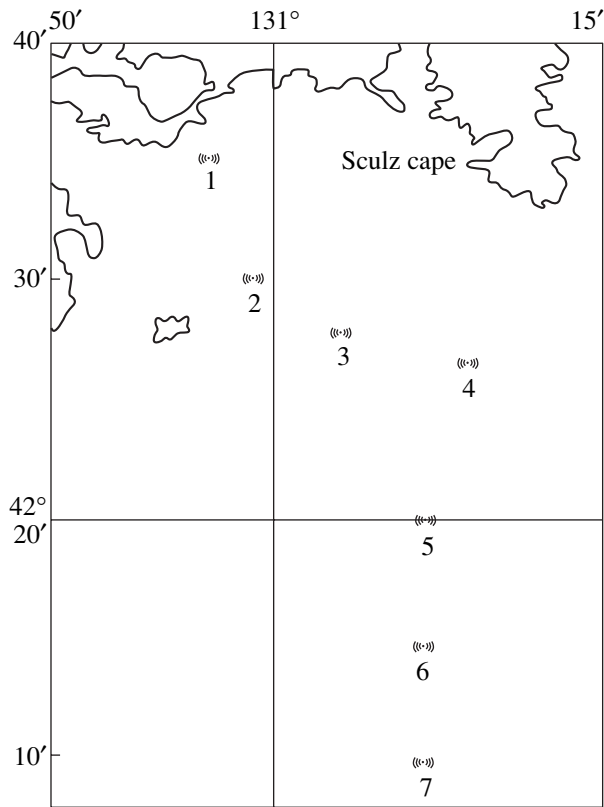
Fig. 4. Positions of the hydroacoustic transmitting stations (station nos. 1–7).

carried out in 2004 in Vityaz' Bay. The source depth was 12 m, the sea depth at the source site was 12.6 m, and the distance from the source to the deformograph, 1.5 km. The pressure referred to the distance of 1 m from the geometrical center of the source was 1.25 kPa.

Data from the 1995 experiment

Station no.	R, km	H, m	h, m	F, Hz	P_m, kPa	A_1, nm
1	16	34	31	32	1.87	0.23
2	16	35	31	32	2.3	0.30
3	16	53	31	32	1.9	0.29
4	16	71	31	32	2.3	1.77
5	25	106	31	32	1.9	0.51
6	34	1300	31	32	1.9	0.61
7	43	2131	31	32	1.75	0.52

Notes: R is the distance from the source to the strainmeter, H is the sea depth at the source site, h is the source depth, P is the pressure referred to the distance of 1 m from the geometrical center of the source, F is the frequency of the emitted signal, and A_1 is the average amplitude of the seismoacoustic signal detected by the non-equal-armed strainmeter with an arm length of 52.5 m in the course of the cw operation of the low-frequency hydroacoustic source.

We believe that the distribution of the pressure field caused by the operation of the low-frequency source in the hydrosphere obeys the same conditions that are valid for the operation of a point source of radiation in an elastic medium [3]. Expressions for the compression waves, shear waves, and Rayleigh waves are given in [3]. In this case, the energy is distributed as follows:

$$W_l \approx 0.0852 \frac{\omega^2 P^2}{\pi \rho c_l^3}; \quad W_t \approx 0.2993 \frac{\omega^2 P^2}{\pi \rho c_l^3};$$

$$W_r \approx 0.822 \frac{\omega^2 P^2}{\pi \rho c_l^3},$$

where P is the amplitude of the total vertical force, c_l is the velocity of the longitudinal wave in the bottom, ρ is the density of water, W_l is the radiation power in the longitudinal wave, W_t is the radiation power in the transverse wave, W_r is the radiation power in the Rayleigh wave, and ω is the cyclic frequency.

From this energy distribution for a point source of radiation, one can see that, in the framework of the given experiment, the radiation power associated with the Rayleigh wave predominates over the radiation powers associated with other types of elastic waves. Therefore, we perform the subsequent calculations under the assumption that the contribution of the Rayleigh wave predominates in the record obtained from the deformograph.

Using the experimental data partially reported in [2], we estimate the ratio of the energy flux carried by the Rayleigh wave to the emitted acoustic power. Figure 4 shows the positions of the emitting stations in the given experiment. The experimental data of [4] are presented in the table. We make our estimates for the data obtained with stations 6 and 7, which correspond to the deep sea conditions ($H \gg \lambda$, where H is the sea depth at the site of the source of radiation and λ is the wavelength of the excited hydroacoustic oscillations).

According to [5], when the source is placed at a small depth h, its field is of a dipole character and the sound pressure amplitude is the lower the smaller the depth h is. Following [5], we can write the power of a near-surface source in the form

$$P_a = \frac{4\pi P_m^2}{\rho c}\left(1 - \frac{\sin(4\pi h/\lambda)}{4\pi h/\lambda}\right), \quad (1)$$

where P_m is the effective acoustic pressure referred to the distance of 1 m from the geometrical center of the source, λ is the acoustic wavelength in water, and c is the sound velocity in water.

Knowing the total energy flux carried by the Rayleigh surface acoustic wave $E(z)$, according to [6], we express the coefficient A through the amplitude $U_x(0)$ of the horizontal displacement component measured by the strainmeter:

$$U_x(z) = Ak_r\left[\exp(-q_r z) - \frac{2q_r s_r}{k_r^2 + s_r^2}\exp(-s_r z)\right],$$

where A is the coefficient calculated from the Rayleigh wave amplitude measured at the surface at the point of observation, k_r is the Rayleigh wave number, k_l is the longitudinal wave number, k_t is the transverse wave number, $q_r = \sqrt{k_r^2 - k_i^2}$, and $s_r = \sqrt{k_r^2 - k_t^2}$.

Then, at the surface ($z = 0$), we obtain

$$A = \frac{U_x(0)(k_r^2 + s_r^2)}{k_r(k_r^2 + s_r^2 - 2q_r s_r)}.$$

The energy flux density in the Rayleigh wave is equal to $E(z)c_r$ [7]. Hence, for the total energy flux Φ_r, we obtain the expression

$$\Phi_r = c_r\int_0^\infty 2\pi RE(z)dz$$

$$= \frac{A^2\rho\omega^4 c_t^2}{2c_r^4}\left(\frac{A_1(\nu)}{2q_r} - \frac{A_2(\nu)}{q_r + s_r} + \frac{A_3(\nu)}{2s_r}\right)2\pi Rc_r,$$

where

$$A_1(\nu) = 4 + \eta_r^2 - 4\eta_r^2\xi^2,$$

$$A_2(\nu) = \frac{2\sqrt{1 - \eta_r^2\xi^2}(\sqrt{1 - \eta_r^2} + \sqrt{1 - \eta_r^2\xi^2})(2 + \eta_r^2 + 2\sqrt{1 - \eta_r^2}\sqrt{1 - \eta_r^2\xi^2})}{2 - \eta_r^2},$$

$$A_3(\nu) = \frac{4(1 - \eta_r^2\xi^2)(4 - 3\eta_r^2)}{(2 - \eta_r^2)^2},$$

$$\eta_r = \frac{0.87 + 1.12\nu}{1 + \nu},$$

$$\xi = \sqrt{\frac{1 - 2\nu}{2(1 - \nu)}},$$

c_r is the Rayleigh wave velocity, c_t is the transverse wave velocity in the bottom, and ν is Poisson's ratio.

Expressing A through $U_x(0)$, we arrive at the formula

$$\Phi_r = \left[\frac{A_1(\nu)}{2q_r} - \frac{A_2(\nu)}{q_r + s_r} + \frac{A_3(\nu)}{2s_r}\right]$$

$$\times \frac{(k_r^2 + s_r^2)^2 U_x^2(0)c_r}{k_r^2(k_r^2 + s_r^2 - 2q_r s_r)^2}\frac{\rho\omega^4 c_t^2}{2c_r^4}2\pi R.$$

This formula can be reduced to a form more convenient for analysis by using the notation for the Rayleigh equation in the polynomial form: $\eta = k_t/k_r = c_r/c_t$ and $\xi = k_l/k_t = c_t/c_l$. In this case, we have

$$\Phi_r = \pi R\rho U_x^2(0)\omega c_t^2$$

$$\times\left[\frac{A_1(\nu)}{2\sqrt{1 - \eta_r^2\xi^2}} - \frac{A_2(\nu)}{\sqrt{1 - \eta_r^2\xi^2} + \sqrt{1 - \eta_r^2}} + \frac{A_3(\nu)}{2\sqrt{1 - \eta_r^2}}\right] \quad (2)$$

$$\times\left(\frac{2 - \eta_r^2}{2 - \eta_r^2 - 2\sqrt{1 - \eta_r^2\xi^2}\sqrt{1 - \eta_r^2}}\right)^2.$$

Using Eqs. (1) and (2), we determine the ratio of the energy flux in the Rayleigh wave Φ_r to the acoustic power emitted by the near-surface source P_a for stations 6 and 7. In the region where the experiment was carried out, samples of the bottom material were taken and analyzed. According to the results of the analysis, the following values were accepted for the elastic constants to calculate the Rayleigh wave parameters: a

Poisson ratio of 0.3, a transverse wave velocity of 3400 m/s, and a bottom rock density of 2600 kg/m^3. Then, using the experimental data from the table, we obtain

for station 6, $\dfrac{\Phi_r}{P_a} = 9.89 \times 10^{-3}$, and

for station 7, $\dfrac{\Phi_r}{P_a} = 11.07 \times 10^{-3}$.

From the estimates presented above, it follows that about 1% of the acoustic energy emitted by the hydroacoustic source is transformed into the energy of Rayleigh elastic waves.

ACKNOWLEDGMENTS

REFERENCES

1. A. V. Davydov, G. I. Dolgikh, and N. F. Kabanov, Akust. Zh. **41**, 235 (1995) [Acoust. Phys. **41**, 201 (1995)].

2. G. I. Dolgikh, Akust. Zh. **44**, 358 (1998) [Acoust. Phys. **44**, 301 (1998)].

3. V. V. Gushchin, V. P. Dokuchaev, Yu. M. Zaslavskiǐ, and I. D. Konyukhova, in *Earth Investigation by Nonexplosive Seismic Sources* (Nauka, Moscow, 1981), pp. 113–118 [in Russian].

4. G. I. Dolgikh, *Investigation of Oceanic Wave Fields and Lithosphere by Laser Interference Methods* (Dal'nauka, Vladivostok, 2000) [in Russian].

5. G. M. Sverdlin, *Applied Hydroacoustics* (Sudostroenie, Leningrad, 1990) [in Russian].

6. I. A. Viktorov, *Surface Acoustic Waves in Solids* (Nauka, Moscow, 1981) [in Russian].

7. V. A. Aleshkevich, L. G. Dedenko, and V. A. Karavaev, *Oscillations and Waves* (Mosk. Gos. Univ., Moscow, 2001) [in Russian].

Translated by E. Golyamina

Experimental Study of Nonlinear Acoustic Effects in a Granular Medium

V. Tournat**, V. Yu. Zaĭtsev*, V. E. Nazarov*, V. É. Gusev**, and B. Castagnéde**

* Institute of Applied Physics, Russian Academy of Sciences,
ul. Ul'yanova 46, Nizhni Novgorod, 603950 Russia
*e-mail: vyuzai@hydro.appl.sci-nnov.ru*
** Université du Maine, Av. O. Messiaen, 72 085, Le Mans, France
Received August 16, 2004

Abstract—Results of a series of experimental studies of nonlinear acoustic effects in a granular medium are presented. Different effects observed in the experiments simultaneously testify that the nonlinearity of granular media is governed by the weakest intergrain contacts. The behavior of the observed dependences suggests that the distribution function of contact forces strongly increases in the range of forces much smaller than the mean force value, which is inaccessible for conventional experimental measuring techniques. For shear waves in a granular medium, the effects of demodulation and second harmonic generation with conversion to longitudinal waves are studied. These effects are caused by the nonlinear dilatancy of the medium, i.e., by the nonlinear law of its volume variation in the shear stress field. With the use of shear waves of different polarizations, the anisotropy of the nonlinearity of the medium is demonstrated. The observation of the cross-modulation effect shows that the nonlinearity-induced modulation components of the probe wave are much more sensitive to weak nonstationary perturbations of the medium, as compared to the linearly propagating fundamental harmonic. The nonlinear effects under study offer promise for diagnostic applications in laboratory measurements and in seismic monitoring systems. © 2005 Pleiades Publishing, Inc.

1. INTRODUCTION

The development of seismoacoustic diagnostic techniques and methods of monitoring geophysical media requires knowledge of the elastic and inelastic, as well as linear and nonlinear, properties of these media and understanding of the relation between these properties and the structure of the medium; i.e., physical models of such media and the corresponding equations of state are necessary. As a rule, the chemical compositions and the physical structures of different kinds of rock are complex and diversified, which determines the wide range of acoustic properties of rocks and, hence, a rich "spectrum" of nonlinear wave processes in them. On the other hand, the variety of rocks can be separated into several classes according to their structural similarity, which determines the similarity of their acoustic properties (even for different chemical compositions). One such important class of geophysical media includes granular materials. Their specificity is primarily determined by the nonlinearity of the contacts between the grains forming a granular medium. This structural feature of granular media makes their acoustic nonlinearity qualitatively different from that of homogeneous (continuous) amorphous and crystalline solids, which makes studying the nonlinear propagation and interaction of elastic waves in granular systems particularly interesting [1]. To describe and predict the macroscopic behavior of a granular medium (with one or another packing) in the field of elastic waves, it is necessary to know the distribution of the forces f acting on the intergrain contacts. The results of both theoretical and experimental studies point to the fact that the distribution function of the contact forces, $P = P(f)$, rapidly decreases when f exceeds a certain characteristic force f_0 related to the strain of the medium [1–7]. On the other hand, there still are no commonly accepted models of the distribution $P = P(f)$ for $f < f_0$. In the literature, one can find arguments in favor of both a decrease [4] and an increase [5–7] in $P(f)$ for $f < f_0$. The existing experimental techniques [1–4] are insufficiently sensitive to allow choosing between the theories describing the distribution of weak forces ($f \ll f_0$). These techniques are based on the study of the prints of grains on a carbon paper, the use of a microbalance for measuring the normal forces acting on individual grains at the boundary of the medium, and the visualization of the deformation of grains with the help of optoelastic effects. All of these methods deal with effects that become stronger as the force f increases, so that the contribution of the most-loaded contacts to the result of measurements is predominant. Hence, it is especially important to study the aforementioned manifestations of granular media by experimental methods in which the response of weak contacts is greater than that of strong contacts. Such methods can be developed on the basis of nonlinear acoustic effects, which are sensitive to the weakest mechanical contacts and defects in the structure of the medium [8–11]. In contrast to the

(a)   (b)
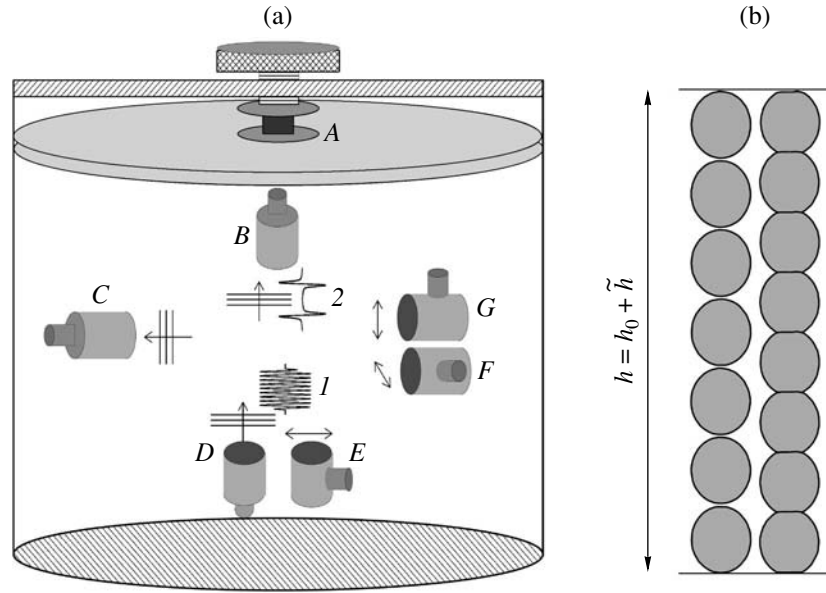
Fig. 1. (a) Experimental setup and (b) a schematic representation of two grain chains of a granular medium with different static compressions: (*A*) control dynamometer, (*B*, *C*) receiving transducers, (*D*) longitudinal wave radiator, and (*E–G*) transverse wave radiators with different wave polarizations.

known approaches [1–4], nonlinear acoustic methods, in principle, allow one to obtain information on the distribution function $P = P(f)$ in the bulk of the medium (rather than at its boundary) for the range of forces $f < 5 \times 10^{-2} f_0$.

In this paper, we combine and discuss from a single point of view the results of a series of experimental studies of the effects associated with the nonlinear propagation and interaction of longitudinal (L) and shear (S) elastic waves in granular media. The intensity of these effects mainly depends on the nonlinearity of weak intergrain contacts, which determine the acoustic nonlinearity of the medium as a whole. We consider demodulation effects, second harmonic generation for high-frequency (HF) pulses, and cross-modulation of a weak (probing) harmonic wave under the effect of an intense amplitude-modulated pump wave.

2. ELASTIC NONLINEARITY OF A GRANULAR MEDIUM

Let us discuss the origin of the high sensitivity of nonlinear acoustic effects in a granular medium to the presence of weak intergrain contacts. As is known, the origin of the strong elastic nonlinearity of a granular medium is the Hertzian nonlinearity of contacts between the grains [12]. For a medium with uniformly loaded contacts, this nonlinearity leads to the following equation of state, i.e., to the dependence $\sigma = \sigma(\varepsilon)$:

$$\sigma(\varepsilon) = bn\varepsilon^{3/2}H(\varepsilon), \quad (1)$$

where σ and ε are the stress and strain, the factor b depends on the elastic moduli of the grain material, n is

the average number of contacts per grain, and $H(\varepsilon)$ is the Heaviside function showing that stress occurs in the medium only when the contacts are under compression ($\sigma, \varepsilon > 0$). An actual granular medium contains contacts with different loads [1–8], which requires a modification of Eq. (1). To reveal the role of different contacts in acoustic manifestations, we assume that a granular medium contains only two fractions of contacts with different static strains. Separating the static (σ_0, ε_0) and dynamic ($\tilde{\sigma}$, $\tilde{\varepsilon}$) components of stress and strain for both fractions, we obtain the following equation from Eq. (1):

$$\sigma_0 + \tilde{\sigma} = bn_1(\varepsilon_0 + \tilde{\varepsilon})^{3/2}H(\varepsilon_0 + \tilde{\varepsilon}) + bn_2(\mu\varepsilon_0 + \tilde{\varepsilon})^{3/2}H(\mu\varepsilon_0 + \tilde{\varepsilon}), \quad (2)$$

where n_1 and n_2 are the average numbers of contacts per grain for the two fractions and μ is the dimensionless parameter characterizing the weak ($\mu \ll 1$) static strain of grains of the second fraction compared to that of the first fraction. Note that the dynamic strain $\tilde{\varepsilon}$ is the same for both fractions. This can be explained by considering the deformation of loaded grain chains shown in Fig. 1. Assume that, under the effect of dynamic stress, the chain length h oscillates around its mean value h_0 ($h = h_0 + \tilde{h}$, $|\tilde{h}| \ll h_0$). Then, the strain of the chain consisting of N grains with a diameter d will be equal to $\varepsilon = (Nd - h_0 - \tilde{h})/Nd$. Consider a chain that has a zero strain in the absence of acoustic load and assume that this chain has a number of grains equal to $N_0 = h_0/d \gg 1$. Taking the number of grains in the ith chain to be $N_i =$

$N_0 + \Delta N_i$, where $\Delta N_i \ll N_0$, we find that the strain ε_i determined as the sum of the static and dynamic components is approximately $\varepsilon_i \cong \Delta N_i/N_0 + \tilde{h}/h_0$. Correspondingly, the dynamic strain component $\tilde{\varepsilon} = \tilde{h}/h_0$ will be the same for all of the grains belonging to different chains. By contrast, the static strains $\varepsilon_0^{(i)} = \Delta N_i/N_0$ ($i = 1, 2$) are different for different chains, because $\Delta N_1 \neq \Delta N_2$. Note that the difference in the static strains $\varepsilon_0^{(i)}$ for these chains can be relatively large even for $\Delta N_i/N_0 \ll 1$. Evidently, the model of the medium presented above is quasi-one-dimensional, and it assumes that the more neavily loaded grain chains relieve other grains from the load. In actual three-dimensional packings, it is possible to single out similar, predominantly loaded, quasi-one-dimensional grain chains, so that, in an actual medium, the dynamic strain can be considered as identical for all contacts to a first approximation. Then, at $n_1 \sim n_2$, we obtain that the first (more strained) fraction in Eq. (1) carries the major part of the static load applied to the medium. For this fraction, the strain $\varepsilon_0^{(1)} = \Delta N_1/N_0$ approximately corresponds to the strain of the medium ε_0. Thus, in terms of the static strains of different contact fractions, the compliance parameter of the ith fraction is determined by the ratio: $\mu^{(i)} = \varepsilon_0^{(i)}/\varepsilon_0$.

For preliminarily compressed contacts and moderate dynamic strains $|\tilde{\varepsilon}| \ll \mu\varepsilon_0$, Eq. (2) can be expanded into a Taylor series with coefficients $d^m\tilde{\sigma}(\varepsilon_0)/d\tilde{\varepsilon}^m$. These coefficients characterize the linear ($m = 1$) and nonlinear ($m = 2, 3, \ldots$) elastic moduli M_m of the medium, which determine the velocity of acoustic wave propagation, the nonlinear correction to it, and the intensity of nonlinear effects of the mth order:

$$M_m \sim \frac{d^m\tilde{\sigma}(\varepsilon_0)}{d\tilde{\varepsilon}^m} \sim bn_1\left(1 + \frac{n_2}{n_1}\mu^{(3/2)-m}\right)\varepsilon_0^{(3/2)-m}. \quad (3)$$

Expression (3) shows that the contribution made by the weak contacts to the linear modulus M_1 is proportional to $\mu^{1/2} \ll 1$ and is negligibly small at $n_1 \sim n_2$. By contrast, the contribution of the weak fraction to the nonlinear moduli M_m ($m = 2, 3, \ldots$) is proportional to $\mu^{(3/2)-m} \gg 1$ and, hence, predominates in the presence of sufficiently small static strains $\mu \le 10^{-1}$–10^{-2}. Such strains correspond to still smaller forces $f/f_0 \le 3 \times 10^{-2}$–$10^{-3} \ll \mu$, which fall beyond the sensitivity range of the known experimental techniques [1–4].

From Eq. (3), it follows that, in the case of the demodulation of weak HF acoustic pulses with an amplitude $\varepsilon_p < \mu\varepsilon_0$, when the power series expansion of Eq. (2) is valid, the amplitude $\in_{det}$ should be quadratic in ε_p: $\in_{det} \sim M_2\varepsilon_p^2$. For higher amplitudes ($\varepsilon_p > \mu\varepsilon_0$), with allowance for the fact that the nonlinearity in

Eq. (2) is governed by the second term, the amplitude $\in_{det}$ is determined by the expression: $\in_{det} \sim \langle\tilde{\varepsilon}^{3/2}H(\tilde{\varepsilon})\rangle \sim \varepsilon_p^{3/2}$. This means that the dependence of $\in_{det}$ on ε_p should exhibit a transition from the square law to the 3/2-power law. Such a transition testifies that weak contacts with $\mu \sim \varepsilon_p/\varepsilon_0 \ll 1$ are present in the medium. Similar speculations are valid for the amplitude dependence of the nonlinear sources producing the second-harmonic wave in the medium.

3. EXPERIMENTAL SETUP

The experimental setup for studying the nonlinear acoustic effects in a granular medium is shown in Fig. 1. The granular medium was composed of glass beads 2 mm in diameter, which filled a cylindrical container with a diameter of 40 cm and a height of 50 cm. The vertical static load was produced by a rigid piston and controlled by an electronic dynamometer. The static stresses and strains could be varied within 10–50 kPa and $(1–5) \times 10^{-4}$, respectively. Piezoelectric transducers were used to excite intense longitudinal and shear waves in the pulsed or continuous modes (the diameter of the transducers was about 4 cm). The receivers of acoustic (strain) waves transmitted through the medium were piezoelectric transducers with a longitudinal polarization (of the same type as those used for the emission of longitudinal waves). The positions and polarization of acoustic radiators and receivers in the container are shown in Fig. 1.

4. DEMODULATION OF A HIGH-FREQUENCY S WAVE WITH A CONVERSION INTO A LOW-FREQUENCY L WAVE

In the first experiment [13], primary HF pulses (with a carrier frequency of 30–80 kHz) with longitudinal and transverse polarizations were excited in the medium. Because of the strong absorption in the granular medium, these pulses rapidly decayed (within a distance of 5 cm). As a result of the demodulation (rectification) of these pulses in the medium because of the Hertzian nonlinearity of the contacts, secondary low-frequency (LF) longitudinal pulses (with a characteristic frequency of 4–6 kHz determined by the steepness of the leading edges of the primary HF pulses) were generated in the medium and propagated through it. In hydroacoustics, devices whose operation is based on this principle are called parametric radiators [14]; in this case, both primary and secondary waves are assumed to be longitudinal. The operation of parametric radiators with a shear pump wave is possible in a granular medium because of its dilatancy [15, 16], i.e., the ability of the granular medium to expand under shear stresses. This leads to a nonlinear transformation of the signal frequency with a simultaneous change of the wave polarization (i.e., an amplitude-modulated HF S pump wave is transformed into a demodulated LF L
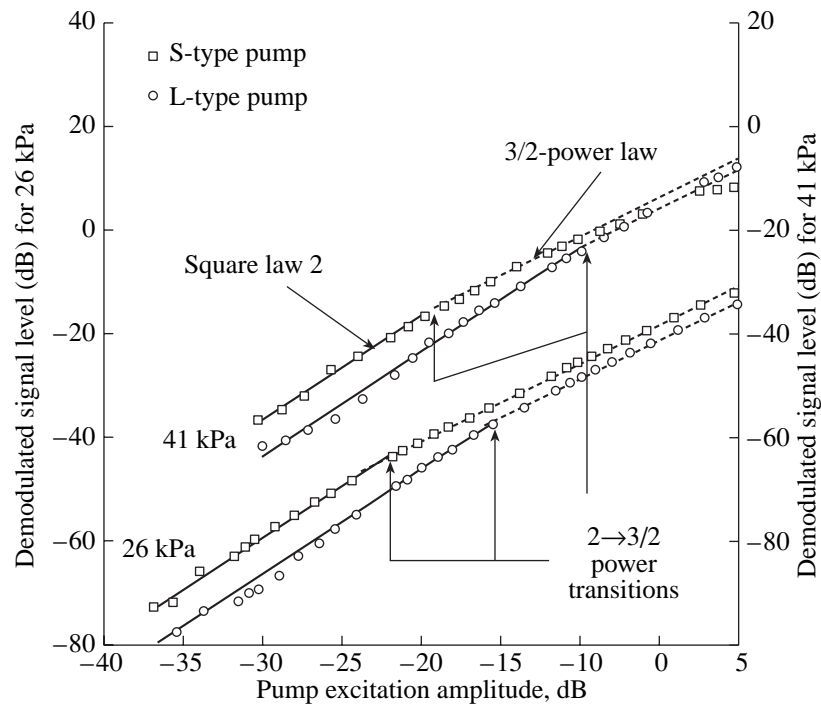
Fig. 2. Demodulated signal amplitude as a function of the excitation amplitude of vertically propagating S and L pump waves for two static pressures.

wave). Generally speaking, the effect of demodulation of HF acoustic pulses with a conversion from S to L waves is also possible in a homogeneous medium with a quadratic elastic nonlinearity [17]. However, because of the noticeable difference in the propagation velocities of the primary S wave and the secondary L wave (when the dissipation in the medium is relatively weak), their interaction will be asynchronous and the amplitude of the demodulated signal will experience spatial beatings.

In the given experiment, relatively long HF pulses with a rectangular envelope were emitted, so that the demodulated LF pulses from the leading and trailing edges of the primary HF pulses did not overlap and could be observed separately. With the chosen parameters of HF pulses and pump transducer dimensions, the demodulation of the signal occurred for a highly directional primary wave [14]. In this case, the shape of the demodulated strain pulses corresponded to the second derivative of the HF pulse envelope with respect to time. Figure 2 shows examples of the dependences of the amplitude $\in_{dem}$ of the demodulated pulses on the amplitude ε_p of the primary L and S pulses (for different values of static pressure). The strain level in the pump wave (in its whole range) remained below the initial static strain of the medium.

From the amplitude dependences obtained for the demodulated pulses (Fig. 2), one can see that their main feature (for both L and S pump pulses) is as follows: for small amplitudes ε_p of the primary pulse, a quadratic

dependence of the amplitude $\in_{dem}$ on ε_p is observed, and for large primary pulse amplitudes, this dependence exhibits a transition to a 3/2-power law, which corresponds to the Hertzian nonlinearity. It should be stressed that this transition occurs when the strain amplitude ε_p is 15–20 dB lower than the static strain ε_0. As it was noted above, the 3/2-power-law amplitude dependence is typical of weak "clapping" contacts, and the predominance of this dependence for $\varepsilon_p \ll \varepsilon_0$ testifies to a considerable growth of the distribution function $P = P(f)$ in the range of small contact forces (below several percent of their mean value f_0). Here, it should be taken into account that, in terms of the introduced notations, the following relation is valid for Hertzian contacts: $f/f_0 \sim \mu^{3/2} \ll 1$. This allows one to relate the distribution function $P = P(f)$ to the contact strain distribution $n = n(\mu)$ or vice versa, by taking into account the relation $P(f)df = n(\mu)d\mu$, so that, if, e.g., $n(\mu) = $ const, one obtains $P(f) \sim f^{-1/3}$. Concerning the behavior of the function $P = P(f)$, many publications argue that the distribution of contact forces for $f < f_0$ has a fairly flat plateau $P(f) \approx $ const [2, 3, 5, 6]. However, it can be easily shown that such an assumption is inconsistent with the observed dependence of $\in_{det}$ on ε_p. Moreover, even assuming that $P(f) \sim f^{-1/3}$, which corresponds to $n(\mu) = $ const in Eq. (2), one can see that the power law $P(f) \sim f^{-1/3}$ (for small f) is insufficient to obtain the transition from power 2 to power 3/2 observed in the dependence of $\in_{dem}$ on ε_p. A calculation showed (see Fig. 3a) that, in the case of a uniform dis-

tribution of contacts in the initial strain $n(\mu) = $ const (i.e., for the distribution of the form $P(f) \sim f^{-1/3}$ in terms of contact forces), despite the discontinuities (clapping) of the weak contacts, the amplitude $\in_{dem}$ almost quadratically depends on ε_p in the whole range of the pump amplitude up to its value equal to the mean static strain of the material, $\varepsilon_p \sim \varepsilon_0$. Indeed, in the case of the distribution $n(\mu) \approx$ const, the number of clapping contacts increases with increasing ε_p. As a result, the amplitude of the demodulated pulse grows faster than $\varepsilon_p^{3/2}$ and the amplitude dependence of this pulse remains close to quadratic one as long as $\varepsilon_p/\varepsilon_0 \le 1$. It is only when $\varepsilon_p/\varepsilon_0 > 1$ that almost all contacts begin clapping and the quadratic dependence passes into $\in_{dem} \sim \varepsilon_p^{3/2}$. Thus, the transition from the 2-power law to the 3/2-power law in the amplitude dependence of the demodulated signal observed in the experiment for $\varepsilon_p/\varepsilon_0 \ll 1$ testifies to the presence of a considerable fraction of weak contacts (with $\mu \sim 10^{-1}$ or less). We stress that, for the realization of the 2 $\longrightarrow$ 3/2 transition in the power law characterizing the amplitude dependence of the demodulated signal, it is necessary to have a sufficiently large total number of clapping contacts with $\mu \ll \varepsilon_p/\varepsilon_0$. Hence, to model the effect of this group of contacts, it is sufficient to complement the smooth function $n(\mu) = $ const with a fraction of weak contacts concentrated in the region $0 \le \mu \le \mu_0 \ll 1$ (see the example in Fig. 3b, where we chose $\mu_0 = 10^{-1}$, while the total number of contacts remained the same as in Fig. 3a). In this case, the change in the power law is evident as early as at $\varepsilon_p/\varepsilon_0 \ll 1$. A similar pronounced 2 $\longrightarrow$ 3/2 transition in the power law of the amplitude dependence (Fig. 3b) can also be obtained when the function $n = n(\mu)$ increases smoothly but fairly rapidly, for example, when $n(\mu) \sim \mu^{1/2}$ for $0 < \mu < 1$. A more detailed reconstruction of the function $n = n(\mu)$ for $\mu \ll 1$ is difficult because of the integral character of its manifestation, but the pronounced 2 $\longrightarrow$ 3/2 power-law transition observed at $\varepsilon_p \sim 10^{-1}\varepsilon_0$ testifies that the growth of the contact force distribution function in the region of $f/f_0 \ll 1$ is substantial and allows one to estimate the fraction of the weak contacts belonging to this region. Note that, for the predicted 2 $\longrightarrow$ 3/2 transition to agree with experimental results, the characteristic value μ_0 (below which a considerable part of weak contacts is concentrated and the distribution function exhibits a sharp growth) should be not too small. Otherwise, for example, at $\mu_0 = 10^{-2}$, the 2 $\longrightarrow$ 3/2 transition would be observed at a much smaller value of ε_p than that obtained from the experiment.

Studying the polarization of the demodulated LF pulses, we found that it was longitudinal for both longitudinal and transverse polarizations of the HF pump wave. In addition, the propagation velocity of these pulses, which was determined from the arrival time,
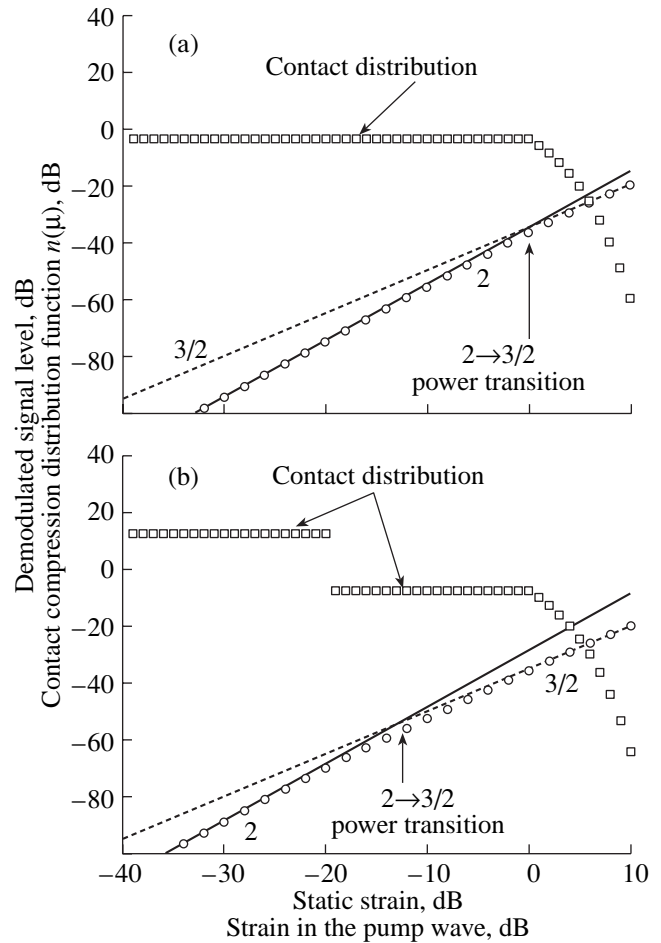
Fig. 3. Demodulated signal level $\in_{dem}$ (circles) modeled as a function of pump amplitude ε_p for different contact compression distribution functions $n(\mu)$ (squares): (a) $n(\mu)$ in the form of a flat plateau, $n(\mu) = $ const, for $0 \le \mu \le 1$; (b) $n(\mu)$ in the form of a plateau with an additional weak contact fraction containing about 50% of the total contact number in the region $0 \le \mu \le \mu_0 = 10^{-1}$. The value of 0 dB on the abscissa axis corresponds to the static strain of contacts with $\mu = 1$, i.e., to the initial static strain of the medium.

was also close to the propagation velocity of the L wave. Figure 4 shows the shapes of the LF pulses for two different frequencies of the S pump wave. When the frequency of the S pump wave was reduced, the decrease in its attenuation caused an increase in the length of the nonlinear interaction region, where the nonlinear source propagated with the velocity of the S wave. This caused a noticeable additional delay of the demodulated pulses and an increase in their duration, which was not observed in the case of L pump pulses.

As noted above, the conversion of a shear wave into a demodulated longitudinal wave occurs owing to the dilatancy phenomenon (an increase in the volume of the medium under the effect of a shear). Therefore, the dependence of the demodulated pulse amplitude $\in_{dem}$ on the shear pump amplitude ε_p provides the information on the character of the dynamic (i.e., caused by the

Amplitude, arb. units
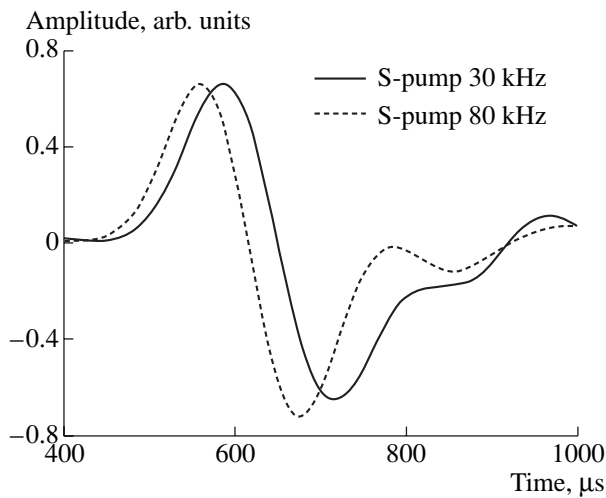
Fig. 4. Examples of the shapes of the received demodulated pulses for the longitudinal mode and two frequencies of the shear pump wave. For a pump frequency of 30 kHz, the additional delay in the first maxima is 26 ± 1 μs and the pulse broadening (between the extrema) is 14 ± 1 μs, as compared to the case of a pump frequency of 80 kHz.

Demodulated signal level, dB

Fig. 5. Demodulated signal amplitude as a function of the amplitude of the S pump wave for the case of its horizontal propagation with (V) vertical and (H) horizontal polarizations (the pressure on the medium is 64 kPa). The characteristic amplitudes corresponding to the 2 ⟶ 3/2 power transition are indicated by arrows.

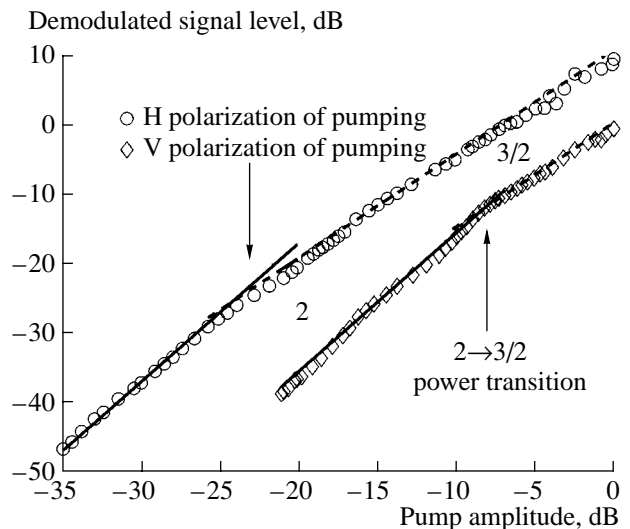shear acoustic wave) dilatancy of the medium. The classical dilatancy of a granular medium (according to Reynolds) can be qualitatively understood from kinematic considerations [15] as the combination of slip and rotation of the initially closely-packed grains with respect to each other, which leads to an increase in the volume of the medium. Both the kinematics of incompressible grains [15, 16] and the linearized hyperplasticity equations [18] predict a volume expansion of a granular medium in direct proportion to the shear stress amplitude. Such a dilatancy law leads to a linear dependence of $\in_{dem}$ on ε_p (note that the stress and strain in an acoustic wave are proportional to each other in the first approximation). However, at small amplitudes, the experimental dependence of $\in_{dem}$ on ε_p is quadratic and, as the pump amplitude increased (up to $\varepsilon_p \sim \varepsilon_0 \sim (1–5) \times 10^{-4}$), passed to the 3/2-power law, which corresponds to the nonlinearity of clapping Hertzian contacts. Thus, in the presence of small (acoustic) strains, the dilatancy of a granular medium noticeably manifests itself and is primarily related to the compressibility of the intergrain contacts rather than to the kinematic effects of a repacking of grains.

The effect of demodulation of shear waves with different polarizations can also be used for determining the anisotropy of the contact nonlinearity of the granular medium and for revealing the force chains preliminarily oriented along the static stress in the medium. Indeed, since the contact nonlinearity is inversely proportional to the static strain (Eq. (3)), a medium with an anisotropy of contact loads should have different nonlinearities for shear waves of different polarizations. Figure 5 shows examples of the amplitude dependences

of demodulated pulses originating from identical horizontally directed S pump radiators with vertical (V) and horizontal (H) polarizations. From these dependences, one can see that, first, in the case of an H-polarized pumping, the demodulated pulse amplitude is approximately 10 dB higher than that in the case of the V-polarized pumping; second, the transition to clapping contacts (2 ⟶ 3/2) for H-polarized pumping is observed at amplitudes 7–12 dB lower than that for V-polarized pumping. These facts testify that the nonlinear elastic parameters of a granular medium are different for the H- and V-polarized shear pump waves; i.e., an anisotropy of nonlinearity occurs in the medium, because the horizontal contacts are loaded less than the vertical ones. In connection with this, we note that the propagation of an HF harmonic S pump wave with a circular polarization of frequency Ω in such a medium may be accompanied by the effect of generation of LF L waves with frequencies $2k\Omega$, where $k = 1, 2, \ldots$. The amplitude dependences and the amplitude ratios of these waves characterize the dynamic dilatancy law and the anisotropy of the acoustic nonlinearity of a granular medium.

5. SECOND HARMONIC GENERATION FOR AN L WAVE UNDER AN S PUMP WAVE

The second harmonic generation is a classical nonlinear effect that is widely used, for example, in optics for the radiation frequency conversion and in nonlinear acoustics for nondestructive testing of materials. The efficiency of the conversion of the fundamental harmonic to the second one depends on the nonlinear

parameters and dispersion of the medium. The latter determines the possibilities for a synchronous accumulation of the nonlinear effect. In dispersive media, the phase velocities of waves with frequencies ω and 2ω differ from each other, and the dependence of the second harmonic amplitude on distance exhibits oscillations (beatings). For acoustic waves, the dispersion is usually weak and only manifests itself in certain specific cases, for example, in acoustic waveguides [19]. Below, we describe the observation of such beatings for the second harmonic generation in a granular medium [20]; however, these beatings are characterized by some distinctive features. First, the lack of synchronism between the primary pump wave and the second harmonic is in this case related not to the dispersion of a single type of waves but to the velocity difference arising with the nonlinear conversion of the S wave of frequency ω into the L wave of frequency 2ω. (In homogeneous solids, such a process is virtually unobservable because of the large difference between the longitudinal and shear wave velocities and because of the small value of the nonlinear parameter.) Second, beatings of the second harmonic amplitude were observed not with an increase in distance but with an increase in the amplitude of the primary S wave, which is related to the nonlinear transformation in the wave interaction region.

In the experiment, the frequency of the horizontally propagating S pump wave was $f = 5.12$ kHz (the wavelength was $\lambda \approx 4$ cm), and its polarization could be either vertical or horizontal. The distance from the radiating transducers to the receiver was $R \approx 16$ cm. For a transducer with a radius of $a \approx 2$ cm, the diffraction length was $L_d \sim \pi a^2/\lambda \sim 3$ cm, so that the second harmonic generation mainly occurred in the region of the spherical divergence of the pump wave. Here, as in the case of demodulation, the generation of the second harmonic for the S wave is accompanied by a conversion to the L wave.

Figure 6 shows examples of the observed dependences of the second harmonic amplitudes received in the longitudinal mode on the amplitudes of a longitudinal pump wave and a V-polarized shear pump wave (at a static pressure of 41 kPa). From Fig. 6a, one can see that, in the amplitude dependence obtained for a longitudinal pump wave, beatings are absent and the behavior of the second harmonic amplitude is similar to the behavior of the amplitude of a demodulated pulse (see Fig. 2); i.e., a $2 \longrightarrow 3/2$ transition is observed in the power-law dependence. For the shear pumping case (Fig. 6b), the behavior of the second harmonic amplitude is qualitatively different: instead of the monotonic $2 \longrightarrow 3/2$ transition, the power law exhibits pronounced beatings. In Fig. 6, the level of 0 dB on the abscissa axis corresponds to the maximum strain amplitude of the pump wave $\varepsilon_p \approx 1.4 \times 10^{-5}$, which is more than an order of magnitude smaller than the static strain of the medium (2.4×10^{-4} at a static pressure of
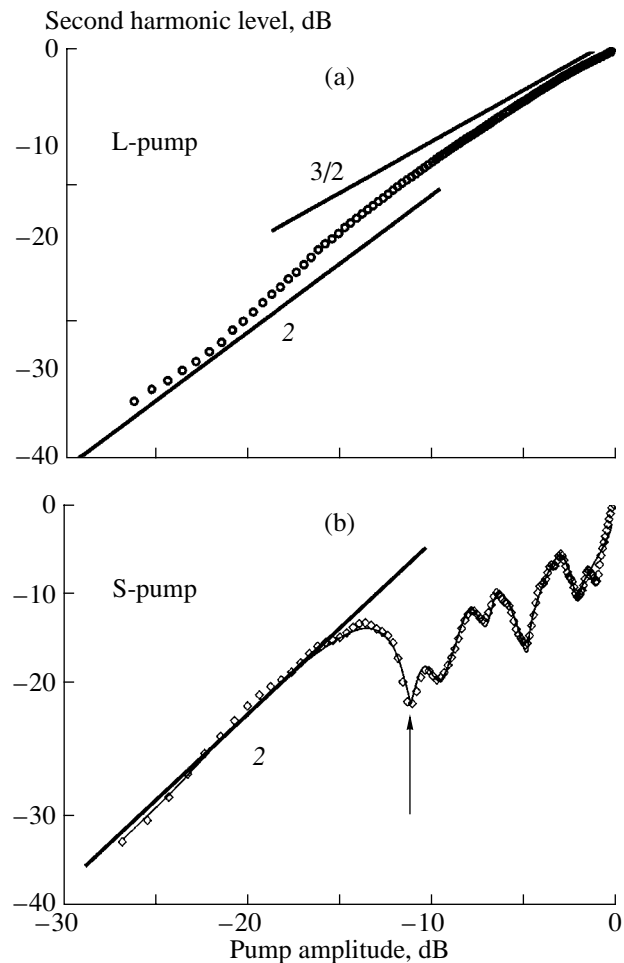
Fig. 6. Examples of the second harmonic level, measured for the longitudinal mode, as a function of the amplitude of the horizontally propagating (a) L pump wave and (b) V-polarized S pump wave. The straight lines represent the square power law and the 3/2 power law (the powers are indicated near the lines).

41 kPa). As the static pressure increases, the position of the first minimum of the second harmonic amplitude (indicated by the arrow in Fig. 6b) is shifted toward higher pump amplitudes.

As in the demodulation experiments described above, the use of shear pump waves of different polarization made it possible to observe the effect of anisotropy of the medium by comparing the dependences of the second harmonic amplitude on the amplitudes of horizontally propagating H- and V-polarized S pump waves. The comparison of these dependences showed that, under the same static pressure, for the H-polarized wave, the second harmonic level was higher (typically, by 5–10 dB) and the beatings began at lower (also by 5–10 dB) pump amplitudes, as compared to those for the V-polarized wave. This result agrees well with analogous observations for the demodulation effect.

The beatings observed with varying amplitude of the S pump wave were related to the fact that, in the
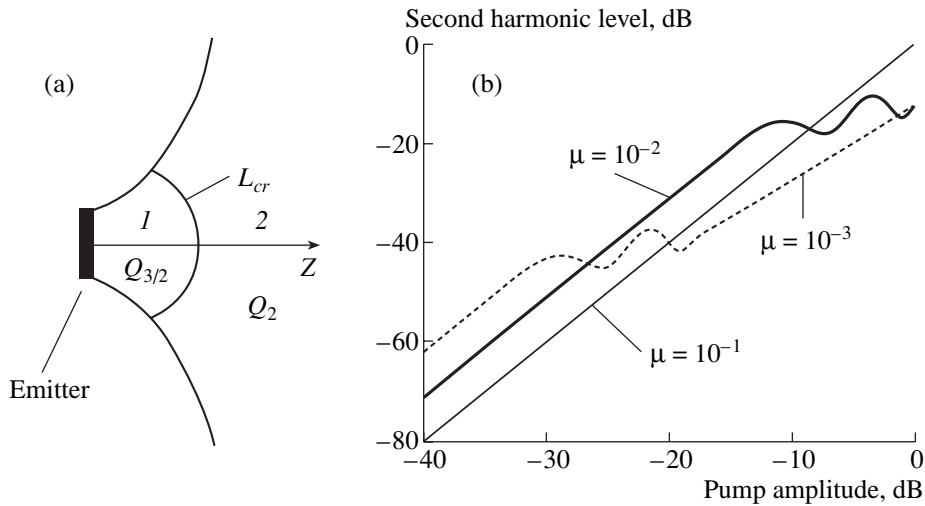
Fig. 7. (a) Schematic representation of the clapping ($Q_{3/2}$) and square-law (Q_2) modes of nonlinear sources in the second harmonic generation region and (b) dependences of the second harmonic amplitude on the pump amplitude modeled on the basis of integral (6) for different values of the compliance parameter μ of the additional weak contact fraction.

region of second harmonic generation, an increase in the pump amplitude was accompanied by a change in the conditions of wave interaction. As we have noted above, the contribution of the unloaded contact fraction to the demodulated signal is predominant, and part of the weak contacts may pass to the clapping mode and make a contribution to the second harmonic so that this contribution proves to be comparable to (or even greater than) the contribution from the contacts that remain closed during the whole period of pump oscillation.

The process of the second harmonic generation in the propagation of a longitudinal harmonic pump wave is described by the integral [14]

$$\sigma^{nl}(\mathbf{r}) = \mathrm{Re}\frac{1}{4\pi}\int Q(\mathbf{r}')\frac{\exp[i\mathbf{k}_{\mathrm{rad}}(\mathbf{r}-\mathbf{r}')]}{|\mathbf{r}-\mathbf{r}'|}d^3\mathbf{r}', \quad (4)$$

where σ^{nl} and k_{rad} are the stress and the wave vector of the secondary wave and the integration is performed over the volume occupied by the nonlinear sources $Q(\mathbf{r}') \equiv Q(x', y', z')$ produced by the primary pump wave; $\mathbf{r}$ represents the coordinates of the observation point. (For a medium with a quadratic nonlinearity, $Q(\mathbf{r}') \sim \mathrm{Re}[(\varepsilon_p/2)\exp(-i\omega t + ikr')]^2$.) A similar integral can describe the generation of an L wave of frequency 2ω in the field of an intense S wave of frequency ω in a granular medium. However, in this case, it is necessary to take into account the velocity difference between the S and L waves and the specific feature of the granular medium, namely, the $2 \longrightarrow 3/2$ transition in the power law characterizing its nonlinearity.

From the study of the demodulation effect, it was found that the nonlinearity of a granular medium is quadratic only for small amplitudes ε_p of the pump wave,

as long as $\varepsilon_p/\varepsilon_0 \ll \mu$; in this case, the source Q in Eq. (4) is also quadratic: $Q = Q_2 \sim (3/16)(\mu\varepsilon_0)^{-1/2}\varepsilon_p^2$. As the pump amplitude increases up to $\varepsilon_p/\varepsilon_0 > \mu$, the Hertzian nonlinearity becomes clapping, which leads to the following expression for the source: $Q = Q_{3/2} \sim (3/4\pi)\varepsilon_p^2$. At some distance L_{cr} from the pump radiator, the amplitudes of these sources coincide at the amplitude value $\varepsilon_p^{cr} \approx 16\mu\varepsilon_0/\pi^2$, which can be considered as the characteristic pump amplitude corresponding to the $2 \longrightarrow 3/2$ transition in the power law. In this approximation, Eq. (4) falls into two integrals corresponding to the square-law and clapping (3/2-power-law) modes of the sources:

$$\varepsilon^{2\omega}(\mathbf{r}) \sim \mathrm{Re}\frac{1}{4\pi}\left\{ \int\limits_{r' < L_{cr}} Q_{3/2}\frac{\exp[i\mathbf{k}_{\mathrm{rad}}(\mathbf{r}-\mathbf{r}')]}{|\mathbf{r}-\mathbf{r}'|}d^3\mathbf{r}' \right.$$

$$\left. + \int\limits_{r' > L_{cr}} Q_2\frac{\exp[i\mathbf{k}_{\mathrm{rad}}(\mathbf{r}-\mathbf{r}')]}{|\mathbf{r}-\mathbf{r}'|}d^3\mathbf{r}' \right\}, \quad (5)$$

where $\varepsilon^{2\omega}$ is the strain in the wave of frequency 2ω. Schematically, these subregions are shown in Fig. 7a. At a small pump amplitude ε_p, the region of clapping sources can still be absent. As the pump amplitude grows, such a region appears near the transducer and then moves into the depth of the medium, so that the distance L_{cr} is determined by the condition of equal amplitudes of the sources in the closed and clapping modes: $\varepsilon_p(r = L_{cr}) = 16\mu\varepsilon_0/\pi^2$. From this equality and from the condition that the pump wave be spherically divergent (i.e., $\varepsilon_p(r) \approx \varepsilon_p(r = 0)L_d/r$) in the major part of the interaction region, we obtain $L_{cr} \approx \pi^2 L_d\varepsilon_p(0)/(16\mu\varepsilon_0)$. Performing the integration across the pumping beam

and assuming that $|r' - r| \sim r$ in the denominator of integral (5), we arrive at the expression

$$\varepsilon^{2\omega}(R) \sim \mathrm{Re}\left\{\frac{\varepsilon_p^{3/2}(0)}{\pi\sqrt{L_d}}\int\limits_{L_d}^{L_{cr}}\frac{\exp(i\Delta kz')}{(z')^{1/2}}dz'\right.$$
$$\left. + \frac{\varepsilon_p^2(0)}{4(\mu\varepsilon_0)^{1/2}}\int\limits_{L_{cr}}^{R}\frac{\exp(i\Delta kz')}{z'}dz'\right\},$$

(6)

where $\Delta k = k - k_{\mathrm{rad}}$.

In Fig. 7b, integral (6) is represented as a function of the pump amplitude $\tilde{\varepsilon}_a$ for several values of the parameter μ characterizing the degree of unloading of the weak contacts and for other parameters corresponding to the experimental conditions (the S and L wave velocities $c_S = 225$ m/s and $c_L = 335$ m/s, respectively; $\Delta k = 95$ m^{-1}). The amplitude $\varepsilon_p^{\max}(0)$ corresponding to the level of 0 dB was chosen to be an order of magnitude smaller than the static strain ε_0. The behavior of the second harmonic amplitude shown in Fig. 7b for the same pump amplitude range as in the experiment strongly depends on the parameter μ characterizing the reduced strain of the weak contact fraction. Specifically, the initial quadratic growth and the subsequent harmonic amplitude oscillations corresponding to $\mu \sim 10^{-2}$ in the calculated plot are close to the behavior observed in the experiment.

The difference in the effective interaction lengths L_{eff} corresponding to the adjacent extrema in the second-harmonic amplitude dependence can be estimated as $\Delta z = \pi/\Delta k \sim 3.3$ cm. As the pump amplitude grows, the boundary L_{cr} of the $2 \longrightarrow 3/2$ transition in the power law describing the amplitude dependence of the demodulated signal is gradually displaced. Hence, at an observation distance of $R \sim 16$ cm, the maximum number of possible extrema can be estimated as $R/\Delta z \sim 4$–5, which agrees well with the experiment. The following increase in the effective length of the antenna array will cause no new extrema, because, within the entire distance from the emitter to the receiver, the nonlinear sources will mainly be in the clapping mode corresponding to the harmonic amplitude dependence $\sim\varepsilon_p^{3/2}$. In Fig. 7b, such a situation is illustrated by the curve corresponding to the choice of $\mu = 10^{-3}$. On the other hand, if the parameter μ is too large ($\mu = 10^{-1}$ in Fig. 7b), in the given range of pump amplitudes, the number of clapping contacts will be small and their contribution (and, hence, the change in the effective length of the array) will be too small, so that the beatings will be absent and the harmonic amplitude dependence will be quadratic. Note that, to simplify the model calculations, we used a simple approximation of the distribution function (the same parameter μ for all unloaded contacts), which already allowed us to illustrate the role of unloaded

contacts in the beating effect. Thus, the nonmonotonic behavior of the second harmonic generated by a shear pump wave proves to be a sensitive indicator of the presence of weak contacts in a granular medium.

6. CROSS-MODULATION EFFECT AND ITS SENSITIVITY TO STRUCTURAL PERTURBATIONS OF THE GRANULAR MEDIUM

In addition to the aforementioned effects related to nonlinear frequency transformations toward higher and lower frequencies, we also performed experimental observations of the nonlinear acoustic response of a granular medium to transient processes induced by short pulsed actions with the use of the less common effect of amplitude modulation transfer from an intense amplitude-modulated pump wave to a probe wave of another frequency [11]. This effect is an acoustical analog of the Luxemburg–Gorki effect [21] observed in the radio wave interaction in the ionosphere. A similar effect of amplitude modulation of a weak seismoacoustic wave under the effect of an intense amplitude-modulated wave was observed in sandy soil [22]. In the model experiments described below, the effects in a granular medium were studied using an experimental setup similar to that shown in Fig. 1. A more detailed description of the experimental technique and the experimental results can be found in [23, 24].

In addition to the results considered in [23, 24], we present another typical example illustrating the great difference between the sensitivity of the fundamental component of the probe wave to the structure of the medium and the corresponding sensitivity of the first- and second-order cross-modulation components arising in the course of its propagation. In the experiment, a monochromatic probe wave with a frequency of 10 kHz and a 100% amplitude-modulated pump wave with a carrier frequency of 7 kHz and a modulation frequency of 30–40 Hz were emitted into the medium. These waves could be either parallel or perpendicular to each other. Their mutual orientation only weakly affected the efficiency of the modulation transfer, because, in contrast to the harmonic generation, the induced changes in the absorption in the medium were important for this effect, so that no spatial synchronism of the interacting waves was necessary. In the experiment, the spectra of the probe wave were recorded at 1-s intervals, which allowed us to compare the variations of the fundamental harmonic and the modulation lobes in time. An additional vibrator immersed in the medium generated short (1–10 ms) shock pulses, which produced perturbations in the medium. Figure 8 shows the time dependences of the amplitude of the fundamental (with the carrier frequency) component of the probe wave and the amplitudes of the induced first- and second-order combination components. In the course of these measurements, several pulses perturbing the medium were emitted (the instants of the pulse generation are indicated by arrows). Figure 8 demonstrates the
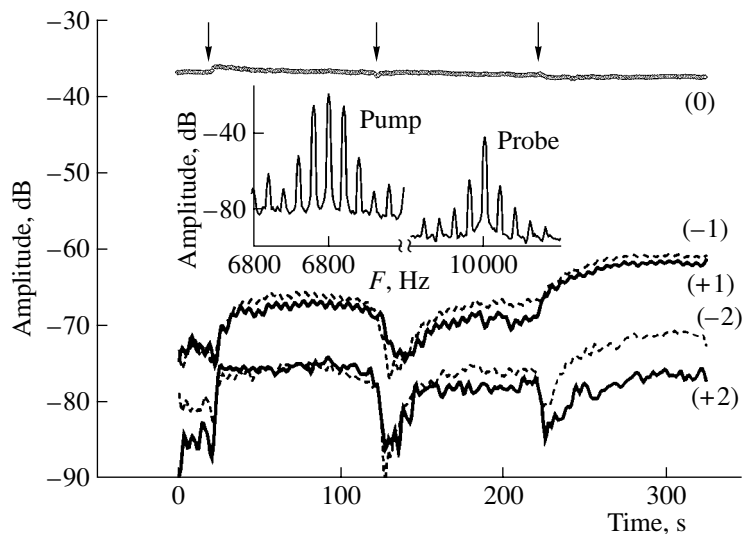
Fig. 8. Time dependences (at a step of 1 s) of the fundamental harmonic amplitude of the probe wave (marked with number 0) and of its right-hand and left-hand first- and second-order modulation lobes (marked with numbers ±1 and ±2). The arrows indicate the instants of "seismic events." The inset shows examples of the spectra of the 100% amplitude-modulated pump wave and the probe wave with induced modulation after their transmission through the medium.

difference in the sensitivity of the level variations for the modulation components and the fundamental harmonic: for the latter, these variations are very small. An important feature of the variations induced by the shock pulses in the cross-modulation components of the probe wave is their transient nature with a pronounced slow dynamics. The dynamics of these variations is determined by the gradual structural relaxation of the material within 1–70 s after the perturbing pulse (see Fig. 8). The inset to Fig. 8 shows the spectra of the pump and probe waves. Note that the higher modulation components appeared in the spectrum of the pump wave as a result of its propagation through the medium, and the shape of the spectrum of the probe wave does not reproduce the shape of the pump spectrum. For example, in the probe wave spectrum, the level of the second-order components may in some cases be equal to the level of the first-order components or even exceed it (as in Fig. 8 after the first perturbing pulse). Thus, the observed high sensitivity of the cross-modulation effects to small structural changes in the granular medium and, especially, to the structural relaxation processes can be effectively used, along with other nonlinear effects, for nondestructive testing of the state of a granular medium.

CONCLUSIONS

The results of the experimental studies described above testify that the nonlinear effects occurring in a granular medium are selectively sensitive to the presence of weak contacts (in contrast to linear elastic characteristics, for which the contribution of strong contacts predominates). The transition from the square law to the 3/2-power law in the amplitude dependence of the demodulated pulse and the beatings of the second harmonic with increasing amplitude of the primary shear wave suggest that the medium contains a considerable fraction of weak contacts (according to estimates, 60–70% of the total number of contacts). These nonlinear effects observed for shear waves made it possible to investigate the law of the dynamic dilatancy using the dependence of the amplitude of the demodulated signal on the shear pump amplitude. The characteristic features of the effects under study testify that the distribution function of intergrain contact forces noticeably increases in the region of small forces, much smaller than the mean contact force. For grains of irregular shape, such an increase near a zero force value is still more pronounced, because, for example, in dry sand, the square-law part of the amplitude dependence of the demodulated signal is practically absent [23]. These conclusions agree qualitatively with the recent results of the three-dimensional modeling of intergrain forces on the basis of the molecular dynamics approach [7]. For unloaded packings with allowance for friction, the modeling revealed a pronounced growth of the function $P = P(f)$ for $f \leq 10^{-1} f_0$. The results obtained should stimulate further theoretical modeling and experimental investigations of the elastic and inelastic behavior of granular materials.

The observed high sensitivity of nonlinear effects to the structure of a granular medium suggests good prospects for diagnostic applications of these effects in laboratory conditions and in seismic monitoring systems (where, in particular, the use of the acoustical analog of the Luxemburg–Gorki cross-modulation effect, which consists in the amplitude modulation transfer from an intense pump wave to a probe harmonic wave, may be of special interest).

ACKNOWLEDGMENTS

REFERENCES

1. H. M. Jaeger, S. R. Nagel, and R. P. Behringer, Rev. Mod. Phys. **68**, 1259 (1996).

2. D. L. Blair *et al.*, Phys. Rev. E **63**, 041304 (2001).

3. G. Løvoll, K. J. Måløy, and E. G. Flekøy, Phys. Rev. E **60**, 5872 (1999).

4. C.-H. Liu *et al.*, Science **269**, 513 (1995).

5. F. Radjai and M. Jean, Phys. Rev. Lett. **77**, 274 (1996).

6. S. Luding, Phys. Rev. E **55**, 4720 (1997).

7. L. E. Silbert, G. S. Grest, and J. W. Laundry, Phys. Rev. E **66**, 061303 (2002).

8. V. Yu. Zaĭtsev, Akust. Zh. **41**, 439 (1995) [Acoust. Phys. **41**, 385 (1995)].

9. I. Yu. Belyaeva and V. Yu. Zaĭtsev, Akust. Zh. **43**, 594 (1997) [Acoust. Phys. **43**, 510 (1997)].

10. V. Yu. Zaĭtsev, A. B. Kolpakov, and V. E. Nazarov, Akust. Zh. **41**, 347 (1999) [Acoust. Phys. **45**, 305 (1999)].

11. V. Zaitsev, V. Gusev, and B. Castagnede, Phys. Rev. Lett. **89**, 105502 (2002).

12. L. D. Landau and E. M. Lifshitz, *Theory of Elasticity*, 4th ed. (Nauka, Moscow, 1986; Pergamon, Oxford, 1986).

13. V. Tournat, V. Zaitsev, V. Gusev, *et al.*, Phys. Rev. Lett. **92**, 085502 (2004).

14. B. K. Novikov, O. V. Rudenko, and V. I. Timoshenko, *Nonlinear Hydroacoustics* (Sudostroenie, Leningrad, 1981) [in Russian].

15. O. Reynolds, Philos. Mag. **20**, 469 (1885).

16. J. D. Goddard and A. K. Didwania, Q. J. Mech. Appl. Math. **51**, 15 (1998).

17. L. K. Zarembo and V. A. Krasil'nikov, *Introduction to Nonlinear Acoustics* (Nauka, Moscow, 1966) [in Russian].

18. D. Kolymbas *et al.*, Int. J. Numer. Anal. Met. Geomech. **19**, 415 (1995).

19. M. F. Hamilton, Yu. A. Ilĭnskii, and E. A. Zabolotskaya, *Nonlinear Acoustics*, Ed. by M. F. Hamilton and D. T. Blackstock (Academic, San Diego, 1997), pp. 151–175.

20. V. Tournat, V. Gusev, V. Zaitsev, and B. Castagnede, Europhys. Lett. **66**, 798 (2004).

21. V. L. Ginzburg, Izv. Akad. Nauk SSSR, Ser. Fiz. **12**, 253 (1948).

22. A. L. Bagmet, V. E. Nazarov, A. V. Nikolaev, *et al.*, Dokl. Ross. Akad. Nauk **346** (3), 390 (1996).

23. V. Zaitsev, V. Nazarov, V. Tournat, *et al.*, in *Proceedings of Joint Congress SFA/DAGA-04* (Strasbourg, 2004), p. 553.

24. V. Zaitsev, V. Nazarov, V. Tournat, *et al.*, Europhys. Lett. **70**, 607 (2005).

Translated by E. Golyamina

Numerical Modeling of the Wave Field in Seismic Profiling of the Seafloor

Yu. M. Zaslavskiĭ, B. V. Kerzhakov, and V. V. Kulinich

Institute of Applied Physics, Russian Academy of Sciences, ul. Ul'yanova 46, Nizhni Novgorod, 603950 Russia
*e-mail: zaslav@hydro.appl.sci-nnov.ru*
Received May 12, 2004

Abstract—The seismoacoustic field produced by an omnidirectional sound source located near the bottom of a shallow-water sea is numerically modeled at frequencies lower than 100 Hz. The main types of waves that are excited and scattered in the fluid and the layered bottom medium are represented in the form of wave hodographs on the distance–arrival time plane. A possibility to solve some problems of acoustic tomography of the bottom is demonstrated, in particular, the problem of determining the thickness of the bottom sediment layers and the velocities of the longitudinal and transverse waves propagating in them. By varying the elastic parameters of the layered bottom model, typical changes in the wave field are analyzed and the possibility to predict the presence of oil-saturated layers in the seafloor is established. © *2005 Pleiades Publishing, Inc.*

The problem of seismic profiling of the seafloor in shelf zones is the important part of ocean acoustics, in particular, the acoustics of bottom strata, including its applications in the exploration of hydrocarbon deposits. Although this problem has been studied since the second half of the last century, the intensity of research in this field remains high. The efforts of the researchers are focused on experimental and technical aspects, as well as on theoretical considerations (see [1–6], for instance). Note that the analytical approach to studying the field of elastic waves encounters considerable difficulties even in the case of a plane-layered medium, because the computations become extremely complex when the number of layers increases. The modern methods of numerical modeling allow one to overcome these difficulties and to take into account a wide variety of the geological and acoustical properties of the seafloor that are characteristic of the natural shelf regions. Modeling offers much more opportunities to the researcher than the analytical approach does. As the sign or indicator of a mineral deposit at a specific horizon, the behavior of the ratio of the attenuation coefficients of the transverse and longitudinal waves is often used, specifically, a sharp increase in this ratio. On the other hand, a fluid-saturated layer can manifest itself as a sharp change in the propagation velocity of elastic waves. The most advantageous method for measuring and monitoring the group velocities of pulsed signals carried by elastic and hydroacoustic waves in the bottom medium and in the fluid consists in plotting the wave hodographs on the range–arrival time plane. Such hodographs identify different types of waves transmitted by the source of oscillations and received by an antenna array, that is, by a linear chain of hydrophones or bottom-moored geophones.

The aforementioned approach is used as the basis for our numerical modeling and analysis of the wave fields produced by the pulsed radiation of an underwater sound source in the frequency band of seismic exploration. The seismoacoustic fields in the seafloor and in the fluid are studied with the use of the OASES software (Version 2) that was also used [7] for modeling the spatial wave structure of the fields generated by tone sources. In the computations, the structure of the seafloor is modeled by three layers, such a structure being typical of a number of shallow-water basins. The first layer, with a very low velocity of shear waves, is directly followed by the second bottom layer, with a higher stiffness and a higher velocity of transverse waves. At the horizons corresponding to the second layer, porous interlayers that contain the hydrocarbon fluid are present. The existence of such interlayers correlates with a decrease in the mean velocity of transverse waves in this region. Thus, the objective of this study is to analyze the qualitative change in the character of the wave field (represented as hodographs on the range–arrival time plane) under the influence of a decrease in the velocity of shear waves in the region of the second bottom layer.

With the model adopted, the seismoacoustic field was calculated for the ranges up to 10 km with an increment of 50 m, and for the depths down to 1.5 km with an increment of 6 m. The frequencies varied from 5 to 70 Hz at a step of 0.05 Hz to model the propagation of broadband pulsed signals with different carrier frequencies.

The model of the layered structure is identical to that used earlier [7]: it consists of the underlying halfspace (the crystalline basement) and the three covering layers, including the upper fluid layer. The parameters
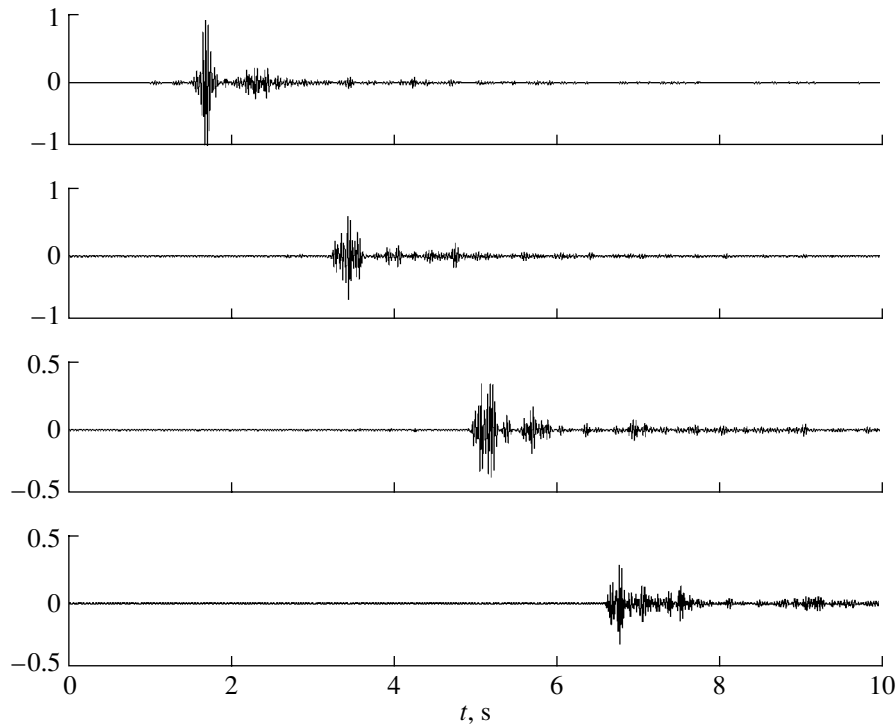
Fig. 1. Oscillograms of the signals at a depth of 246 m for the distances $X = 2.5, 5, 7.5,$ and 10 km. The velocity of the transverse waves in the second bottom layer is $V_S^{(3)} = 1$ km/s, the carrier frequency is $f = 30$ Hz, and the bandwidth is $\Delta f = 25$ Hz.

of these layers are as follows: (1) the isovelocity layer with $h_1 = 50$ m, $\rho_1 = 1$ g/cm^3, and $V_P^{(1)} = 1.5$ km/s; (2) the first bottom layer, i.e., the sediment layer, with $h_2 = 50$ m, $\rho_2 = 1.5$ g/cm^3, $V_P^{(2)} = 1.6$ km/s, $V_S^{(2)} = 0.06$ km/s, $\alpha_P^{(2)} = 0.05$ dB/(m kHz), and $\alpha_S^{(2)} = 0.5$ dB/(m kHz); (3) the second bottom layer with $h_3 = 300$ m, $\rho_3 = 2.1$ g/cm^3, $V_P^{(3)} = 2.5$ km/s, $V_S^{(3)} = $ (I) 1, (II) 0.5, and (III) 0 km/s, $\alpha_P^{(3)} = 0.03$ dB/(m kHz), and $\alpha_S^{(3)} = 0.1$ dB/(m kHz); and (4) the stiff basement with $\rho_4 = 2.5$ g/cm^3, $V_P^{(4)} = 4$ km/s, $V_S^{(4)} = 2.5$ km/s, $\alpha_P^{(4)} = 0.02$ dB/(m kHz), and $\alpha_S^{(4)} = 0.1$ dB/(m kHz). Here, h is the thickness of the layer, ρ is the density, V_P and V_S are the velocities of the longitudinal and transverse waves, and α_P and α_S are the corresponding attenuation coefficients. To analyze the effect of the shear stiffness of the second layer on the wave field characteristics, three values of the velocity $V_S^{(3)}$ of the transverse waves were used for this layer (I, II, and III).

In modeling, the omnidirectional sound source of small wave size was placed into water at 1 m above the bottom. The received pulsed signals were filtered and then used to plot the seismograms. Figure 1 shows the normalized impulse responses of the medium for the depth $Z = 246$ m. These responses are obtained by matched filtering of the sound field at the ranges $X = 2.5, 5, 7.5,$ and 10 km. The maximum of the response at $X = 2.5$ km was used as the normalizing factor.

The full set of seismograms, like that shown in Fig. 1, allows one to visualize the seismoacoustic field produced by the source of the pulses on the range–arrival time plane and, with the known depths of the receivers, to obtain the godograph curves on this plane. In this way, one can identify different types of waves and thereby estimate the structure of the layers, in particular, the depths of the interfaces and the velocities of longitudinal and transverse waves in the bottom layers. The darkening of the pattern indicates the sound pressure level p in the fluid and the zz component of the stress tensor in the three layers of the stiff bottom structure. In principle, the difference in the arrival times of the signals can be used to separate waves of different types from the total wave field, namely, the surface waves, the channel waves (of the Lamb type), the bulk waves (both longitudinal and transverse), and the non-ray-type waves (like head and critically refracted ones). This is possible, because each of the wave types produces its own hodograph curve or set of curves.

On the basis of the calculations performed, the hodographs were plotted on the range–arrival time plane for the waves that propagate over the entire spatial domain, up to distances of 10 km, and then are reflected toward the receivers. These hodographs are
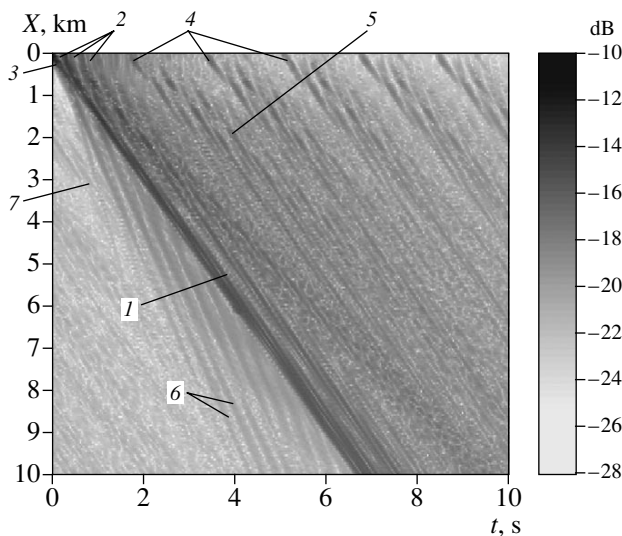
Fig. 2. Wave hodographs at the depth $Z = 246$ m. The velocity of transverse waves in the second bottom layer is $V_S^{(3)} = 1$ km/s.

presented in the following figures. The data of modeling correspond to the transmission of a pulsed tone signal with the carrier frequency $f = 30$ Hz and the bandwidth $\Delta f = 25$ Hz (the corresponding time resolution is 0.04 s). Let us begin with analyzing and interpreting the data of the calculations performed with the velocity of the transverse waves $V_S^{(3)} = 1$ km/s in the second bottom layer.

Figure 2 shows the section of the sound field 4 m above the bottom. The brightest strip (indicated by arrow *1* in the figure) is the set of curves produced by arrivals of the pulses propagating with the velocities 1.5 and 1.6 km/s. The latter is confirmed by the fact that the superposition of the arrivals leads to the periodic modulation of the entire bright area, whose width becomes somewhat larger as the distance increases. Averaging the slope of the curves over the entire path, which is nearly 10 km in length, yields an estimate of 1.5 km/s for the propagation velocity. The curves falling within this area (arrows *2*) are hyperbolas that deviate from straight lines in the vicinity of the epicentral point $X = 0$ and tend to some fixed value of the time delay Δt. The principal and reverberation waves corresponding to the hodographs are those reflected from the pressure-release water surface, and the principal wave has the delay $\Delta t = 0.333$ s at $X = 0$. The hodographs of multiply reflected waves produced by reverberation have the same period of repetition and the delay time that is a multiple of this value. There is also a hodograph of the satellite wave that has a delay of $\Delta t = 0.07$ s relative to the principal wave at $X = 0$. Hence, one can conclude that the principal wave is a longitudinal one with two reflections: at the pressure-release water surface and at the interface between the first and second bottom layers.

On the plane at hand, near the origin of coordinates, a straight hodograph line can be seen. It exists at distances shorter than 0.5 km and decays nearly to zero at a distance of 1 km from the source (arrow *3*). This hodograph may correspond to the direct wave propagating in the fluid ($V_P^{(1)} = 1.5$ km/s) near the interface between the fluid and the bottom.

A set of hodographs exists near the epicenter ($X = 0$), that is, at short distances from the source. These hodographs (arrows *4*) with large delay times ($\Delta t = 1.7$ s) and with an equal repetition period ($T = \Delta t$) correspond to multiply reflected waves. To explain the nature of such waves, one can suppose that the sound rays multiply penetrate from the fluid to the first bottom layer in the form of transverse waves and then return after being reflected from the next interface. They again transform to the sound wave when entering the fluid. The recurrence of such a process leads to a multiple interchange of waves at the fluid–bottom boundary. The required period of the interchange can be obtained by taking into account the abnormally low velocity of the transverse wave, $V_S^{(2)} = 60$ m/s, as compared to the velocity $V_P^{(1)} = 1.5$ km/s of the sound waves in the fluid, when the refraction occurs at angles close to 90°. Note that these reverberation waves are precisely the waves that produce the interfering noise in the detection of waves reflected from the deep interfaces and carrying the information about them.

Another set of parallel hodographs existing in the pattern at great delays (arrow *5*) has the repetition period $T = 0.333$ s. These hodographs can also be caused by the multiple reflections of longitudinal waves along with the aforementioned wave interchanges in the first bottom layer. However, the behavior of these curves is less regular.

There are hodographs corresponding to faster waves than those considered above. They exist at delay times preceding the arrivals of the direct and reflected waves travelling in the fluid. Among these waves, the head compression waves refracted at the interface between the first and second bottom layers are present. They propagate with the velocity $V_P^{(3)} = 2.5$ km/s and are also caused by multiple reflections (arrows *6*). At even earlier arrival times, i.e., at even steeper hodographs, multiply-reflected longitudinal waves can be found. They propagate with the velocity $V_P^{(4)} = 4$ km/s and are refracted at the basement boundary (arrow *7*).

Figure 3 shows the wave pattern corresponding to the signals received at a depth of 366 m, that is, in the second bottom layer, under the interface between the first and second layers. Here, the wave field consists of a greater number of wave types and the hodographs of longitudinal waves that are refracted at the interface of

the bottom layers and have high velocities ($V_P^{(3)}$ and $V_P^{(4)}$) are more pronounced (arrows *1* and *2*).

At the shortest distances (0–300 m), one can see a set of hodographs that corresponds to the longitudinal waves with the velocity $V \sim 1.5$ km/s (arrow *3*). The arrival times of these waves are multiples of 1.7 s. Another set of curves that alternates with the first set, has an additional time delay of 0.3 s and corresponds to the waves travelling with the velocity $V \sim 1$ km/s. The latter waves exist within a finite range of distances (0.5–0.9 km) from the source (arrows *4* in Fig. 3). The origin of these waves seems to be the same as that considered above.

According to the numerical modeling illustrated by Figs. 2 and 3, the signals received by the near-bottom array of hydrophones can be used to determine the velocities of the waves propagating in the layers that are close to the bottom. More representative and detailed data can be obtained by embedding the hydrophones under the fluid–bottom interface.

To analyze the effect of the shear rigidity of the second bottom layer, let us consider the aforementioned wave patterns for the lower velocity $V_S^{(3)} = 0.5$ km/s. Figure 4 shows the wave field received by the array of hydrophones at a depth of 246 m. The pattern shown is obtained by the numerical modeling with a new value of the shear rigidity of the second layer. In comparison with Fig. 2, the pattern is noticeably restructured at times exceeding the arrival times of the pulses scattered by the water surface. In addition to the bright strip caused by the weakly resolved hodographs of the waves with the velocities $V \sim 1.5$ and 1.6 km/s (arrow *1*), a broader area appears that contains the hodographs of the underwater sound waves multiply reflected from the pressure-release sea surface. These waves seem to penetrate into the first bottom layer and undergo reflection at the interface between the first and second layers (arrow *2*). The pulses of these waves are delayed with respect to those that are first in their arrival times, although they have nearly the same intensity. As above, multiply reflected longitudinal head waves (arrows *3* and *4*) exist in the range–time plane along the entire path. The latter waves are refracted at the interface between the first and second bottom layers (the propagation velocity $V \sim 2.5$ km/s) and at the interface between the second bottom layer and the basement (the propagation velocity $V \sim 4$ km/s). These waves arrive earlier than the hydroacoustic pulses.

Figure 5a illustrates the same case of a low shear rigidity of the second layer. Here, the pattern is presented for a depth of 366 m, that is, 66 m deeper than the boundary of the first bottom layer. The corresponding pattern on the range–delay time plane is bisected by the diagonal. The lower part of the pattern contains the hodographs of the longitudinal waves (arrows *1*) that are multiply reflected by the surface of the basement
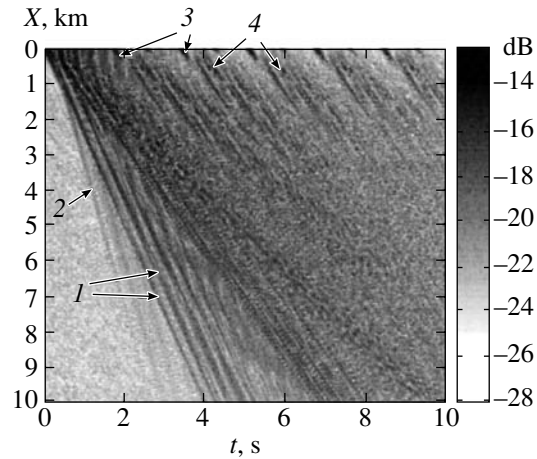
Fig. 3. Wave hodographs at the depth $Z = 366$ m. The velocity of transverse waves in the second bottom layer is $V_S^{(3)} = 1$ km/s.
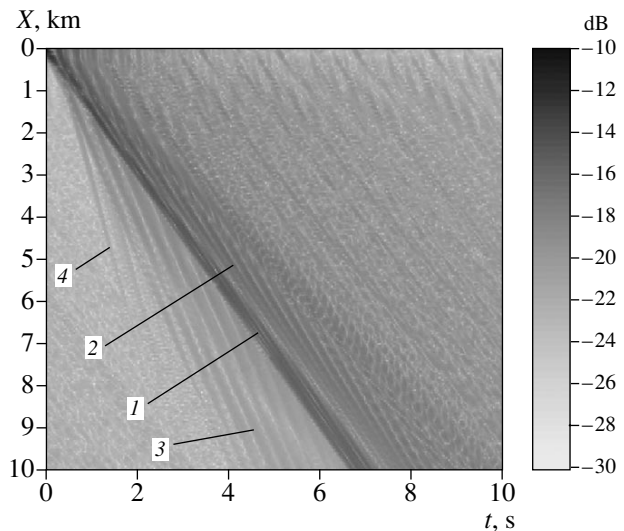
Fig. 4. Wave hodographs at the depth $Z = 246$ m. The velocity of transverse waves in the second bottom layer is $V_S^{(3)} = 0.5$ km/s.

(the repetition period $T = 0.25$ s) and travel with the velocity $V \sim 2.5$ km/s in the second layer. There are also the head waves propagating with the velocity $V \sim 4$ km/s (arrow *2*); they are refracted at the same boundary. The upper part of the pattern contains the hodographs of the longitudinal waves (arrow *3*) scattered by the pressure-release sea surface with the repetition period $T = 0.4$ s.

By analogy with the case of $V_S^{(3)} = 1$ km/s, two sets of hodographs exist at the distances of several hundreds of meters from the source with a delay of 2.5 s. These hodographs are presented in Fig. 5b, which is a magni-
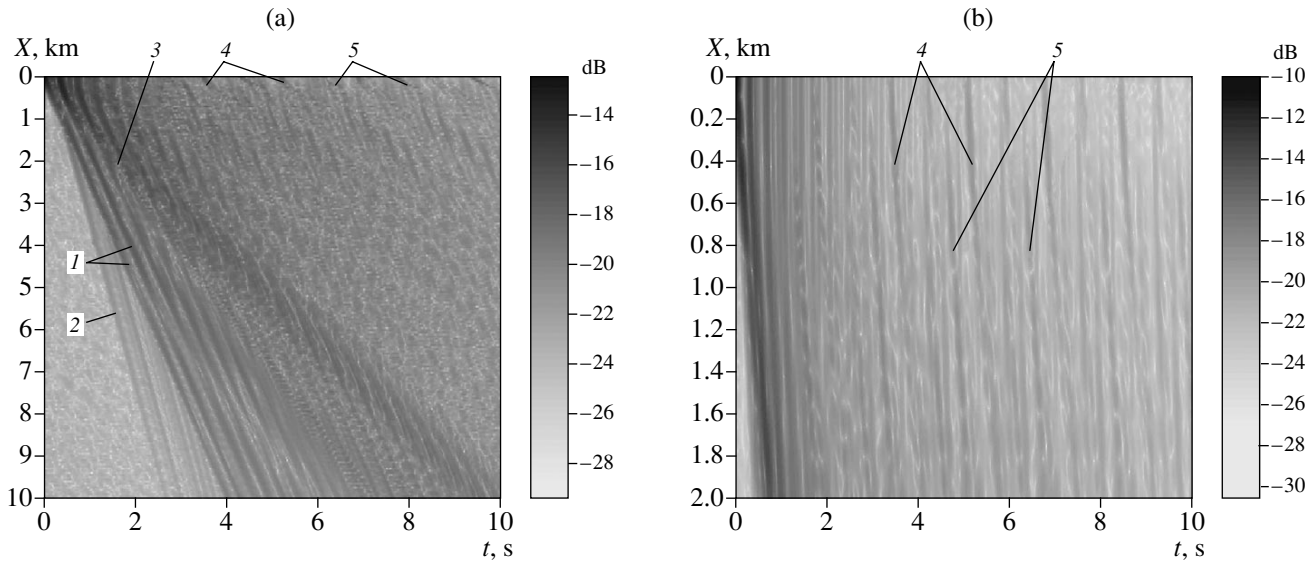
Fig. 5. (a) Wave hodographs at the depth $Z = 366$ m. The velocity of transverse waves in the second bottom layer is $V_S^{(3)} = 0.5$ km/s. (b) The same wave hodographs for the distances within 0–2 km.

fied image of the wave pattern of Fig. 5a for distances of 0–2 km.

Arrows *4* (Figs. 5a and 5b) indicate the hodographs of multiply reflected waves with velocities lower than $V \sim 1.5$ km/s. The existence of the slow wave in the developed wave structure is related to the reflection and refraction in the second bottom layer where the velocity of transverse waves is low. Arrows *5* (Figs. 5a and 5b) label the hodographs of the waves propagating with the velocity $V \sim 1.6$ km/s; those are the longitudinal waves

Fig. 6. Wave hodographs at the depth $Z = 366$ m. The velocity of transverse waves is $V_S^{(2, 3, 4)} = 0$ in all of the bottom layers.

refracted at the interface between the fluid and the first bottom layer.

Thus, the data of the wave field modeling corresponding to the seismic profiling lead to the conclusion that, for the pulsed signal with the adopted carrier frequency, the hodographs are primarily produced by the reflections of the longitudinal waves at the interfaces. However, in some cases, the hodographs are formed by the interchanging waves that change their types in passing through the boundaries of the bottom layers. The main information on the parameters of the deeper layers can be obtained from the slopes of the hodographs for the most intense waves and from the periodicity of these hodographs. In the experiment, these characteristics should be treated as preliminary information to be used in solving the inverse problem of reconstructing the structure of the medium and determining its parameters.

The results of numerical modeling offer a possibility to predict the presence of the fluid inclusions in the bottom layers, one of the manifestations of such inclusions being a decrease in the shear rigidity in the vicinity of the second layer. According to modeling, the decrease in the shear rigidity leads to an increase in the level of longitudinal waves in the total wave pattern. This is true for both the reflected waves and the head waves that are refracted at the critical angle. On the other hand, the decrease in the level of transverse waves takes place. Such a decrease can also be used as an indication of the fluid inclusions. This fact should presumably manifest itself in the experiments on seismic probing of natural deposits where the oil pools are mainly located in the near-bottom layers.

The validity of the aforementioned statements is confirmed by the wave pattern calculated for the limiting case of zero-valued velocity of the shear waves in all bottom layers, $V_S^{(2,3,4)} = 0$. Such a calculation is illustrated in Fig. 6. In this case, the wave pattern is formed by the more pronounced sound pulses that are multiply reflected and by the pulses of longitudinal waves that are refracted in the second layer and in the basement without any contribution of the transverse waves. The angular sector that is strongly "illuminated" on the range–time plane corresponds to the velocities from 0.5 to 2.5 km/s and even covers the velocity of 4 km/s, which coincides with the parameters specified in the calculations.

The results of the wave field modeling simulate the propagation of actual seismic and underwater sound signals. The representation of the data in the form of the oscillograms plotted one under another, like those presented above, is used in the in-sea experiments. By analyzing the experimentally obtained hodographs on the range-time plane, conclusions can be drawn about different types of waves propagating in the seafloor. In reconstructing the bottom strata for the sake of mineral exploration, the signals should be processed in view of the information extracted from the wave pattern, such an approach being traditional for applied geophysics.

The aforementioned data of the seismoacoustic wave field modeling serve to illustrate the possibilities offered by one of the newly developed approaches to the monitoring and seismoacoustic tomography of the seafloor. The results of modeling may contribute to updating the theoretical base of such methods. The data obtained for the simple layered model of the seafloor show that, in principle, one can estimate the acoustic parameters of the bottom, namely, the velocities of longitudinal and transverse waves, which are important for reconstructing the unknown structure of the layers. For the frequency band considered, the space–time distribution of the sound field in the water column and in the upper bottom layers are shown to be highly sensitive to changes in the velocity of the transverse waves. Future studies can be based on both simple and more complex models of layered structures, with different positions of the sound sources and receiving arrays, and with different algorithms of space–time signal processing. There are a number of promising directions in which further development of computer simulations of elastic waves will progress. Some of these directions are known from the publications cited here; others can be extensions of our work.

REFERENCES

1. A. A. Ostrovskiĭ, *Bottom Experiments* (Nauka, Moscow, 1998) [in Russian].

2. V. P. Antonov, V. V. Borodin, G. N. Kuznetsov, *et al.*, in *Proceedings of School–Seminar of Academician L.M. Brekhovskikh on Acoustics of the Ocean* (Moscow, 1998), p. 91.

3. A. N. Ivakin, in *Proceedings of School–Seminar of Academician L.M. Brekhovskikh on Acoustics of the Ocean* (Moscow, 1998), p. 84.

4. A. V. Il'in, in *Acoustic Waves in the Ocean* (Nauka, Moscow, 1987), pp. 130–137 [in Russian].

5. *Bottom-Interacting Ocean Acoustics*, Ed. by W. A. Kuperman and F. B. Jensen (Plenum, New York, 1980; Mir, Moscow, 1984).

6. L. Brian, in *Underwater Acoustics* (Mir, Moscow, 1970), pp. 449–462 [Russian translation].

7. Yu. M. Zaslavskiĭ, B. V. Kerzhakov, and V. V. Kulinich, in *Proceedings of XIV Session of the Russian Acoustical Society and X School–Seminar of Academician L.M. Brekhovskikh on Acoustics of the Ocean* (Moscow, 2004), p. 366.

Translated by E. Kopyl

Laser Optoacoustic Measurement of Paper Porosity

A. A. Karabutov, I. M. Pelivanov, and N. B. Podymova

International Laser Center, Moscow State University, Vorob'evy gory, Moscow, 119992 Russia
e-mail: ivan@sasha.phys.msu.su
Received September 9, 2004

Abstract—The propagation of broadband ultrasonic pulses in combined media that consist of printing paper of different porosity saturated with different liquids is studied. The experiments are performed with three types of paper, namely, Zoom Ultra (Stora Enso, Finland) with surface densities of 80 and 100 g/m^2 and Data Copy (Mo Do, Sweden) with a surface density of 160 g/cm^2, and with two types of saturating liquids: ethanol and transformer oil. To excite ultrasonic pulses and to detect them with a high time resolution, the laser optoacoustic spectroscopy method is used. For each type of liquid-saturated paper, the phase velocity of ultrasound is measured in the frequency range of 5–35 MHz. The absence of any noticeable frequency dispersion of the phase velocity is revealed. The possibility of measuring the porosity of printing paper on the basis of the theoretical model of a two-phase medium with the use of the corresponding experimental data is demonstrated. © 2005 Pleiades Publishing, Inc.

The development of methods for testing various properties of paper in the process of its production is an important problem in the printing industry. The main characteristics of printing paper include its whiteness, roughness, porosity, etc. The difficulty of quantitative measurements of these parameters is connected with their interdependence. Intensive studies had been carried out with the aim to apply various optical methods to the evaluation of paper properties [1–3]. In the majority of these studies, the measurements were based on the detection of laser radiation scattered by the medium under testing. The evaluation of the optical properties of printing and porous paper from the measurements of the backscattered signal of femtosecond laser radiation is described in [4]. The use of the Fourier-optics methods in monitoring the spatial variations of paper is described, e.g., in [5].

Ultrasonic methods also can be used to characterize porous media. In [6], a method for the determination of the gas content in bottom sediments is proposed on the basis of simulation results. The model uses the dependence of the velocity of sound on the porosity of the medium. The permeability of porous water-saturated media can be evaluated by the efficiency of electromagnetic-acoustic effect [7].

In this paper, we propose an ultrasonic method for measuring the porosity of paper. Probing ultrasonic pulses were excited in paper by laser radiation through the optoacoustic transformation [8]. Its advantage is the possibility to generate short high-power ultrasonic signals with a smooth time envelope and a broad frequency spectrum. The last fact is fundamentally important for attaining a high measurement accuracy in testing sound-absorbing objects with a thickness of tens to hundreds of micrometers. In addition, the use of optoa-

coustic signals provides an opportunity to investigate the ultrasonic frequency dispersion in media under study in a wide spectral range.

It seems most expedient to perform ultrasonic testing of dry paper during the production process. However, there are several fundamental difficulties, the first of which is caused by the necessity to provide an acoustic contact between the object and the receiver. The second difficulty is the absence of simple theoretical models for sound wave propagation in a porous medium with an unknown pore size distribution. Moreover, to use any of such models, it is necessary to know a priori the velocity and attenuation of sound in the solid phase of the object (paper with "zero" porosity), which is hardly possible in view of the technological features of manufacturing raw material for paper production.

The possibility of applying the optoacoustic method for a nondestructive local (within the diameter of the laser spot on the surface of the optoacoustic source of ultrasound) measurement of the porosity of silicon layers on a single-crystal substrate was demonstrated in [9]. Porous samples were saturated with ethanol, and the phase velocity of ultrasound was measured in them. Because the pore sizes and the sample thickness are much smaller than the acoustic wavelength, the acoustic signal is not separated into fast and slow components [10], and the phase velocity of sound in a combined two-phase medium can be expressed through the sound velocities in its individual components and the porosity of the medium. The silicon porosity was calculated with an error not worse than 5% according to the data of ultrasonic measurements. From the aspect of the problem formulation, the propagation of acoustic waves in paper saturated with a liquid filler must be of

Table 1

Paper sample	Trademark	Surface density, g/m^2	Density of dry paper $\rho_{paper} \times 10^3$, kg/m^3	Thickness $h \times 10^{-6}$, m
no. 1	Zoom Ultra (Stora Enso, Finland)	80	0.762	105
no. 2	Zoom Ultra (Stora Enso, Finland)	100	0.794	125–127
no. 3	Data Copy (Mo Do, Sweden)	160	0.914	170–175

a similar character and the theory of a two-phase medium can be used to calculate the porosity of paper.

The purpose of this work was to study the possibility of applying the optoacoustic method in measuring the porosity of printing paper.

Let us consider a theoretical model for propagation of longitudinal sound waves in a two-phase medium consisting of paper saturated with a liquid. We assume that the structure of the solid phase of paper (cellulose) does not change and that the liquid completely fills the pore volume. Let the bulk porosity of paper be P. Then, the density of the liquid-saturated paper ρ_0 can be expressed using the cellulose density ρ_{cel} and the liquid density ρ_{liq}:

$$\rho_0 = (1 - P)\rho_{cel} + P\rho_{liq}. \qquad (1)$$

If a plane acoustic wave propagates in a porous medium with a filler, its phase velocity can be expressed through increments of sound pressure and density in the medium [11]:

$$c^2 = \frac{\partial p}{\partial \rho_0} \approx \frac{\Delta p}{\Delta \rho_0}. \qquad (2)$$

The density increment for the two-phase medium under consideration is determined as

$$\frac{\Delta \rho_0}{\rho_0} = P\frac{\Delta \rho_{liq}}{\rho_{liq}} + (1 - P)\frac{\Delta \rho_{cel}}{\rho_{cel}}. \qquad (3)$$

Hence, the expression for the phase velocity of an acoustic wave in liquid-saturated paper can be written in the form

$$c^2 = \frac{1}{(\rho_{paper} + P\rho_{liq})(P/\rho_{liq}c_{liq}^2 + (1 - P)^2/\rho_{paper}c_{cel}^2)}, \qquad (4)$$

where c_{liq} and c_{cel} are the sound velocities in the filler and in cellulose, respectively. Formula (4) also takes into account that the density of air is negligible, and, therefore, $(1 - P)\rho_{cel} = \rho_{paper}$ is the density of dry paper, which can be determined by weighing or from the known surface density and thickness of dry paper. Assuming that the sound velocity c can be measured, the unknown quantity in Eq. (4) (apart from the paper porosity P) is only the sound velocity c_{cel} in cellulose. If one uses two different liquids as fillers, Eq. (4) yields two equations with two unknowns: P and c_{cel}. Hence,

the problem of the absence of a priori data on the cellulose properties is eliminated.

Thus, to determine the value of P, it is necessary and sufficient to measure the phase velocities of longitudinal sound waves in paper samples saturated with two different liquids.

In our experiments, we used the optoacoustic spectroscopy method with a laser source of ultrasound [12]. The basis of this method is the laser excitation of broadband ultrasonic signals due to the absorption of pulsed laser radiation in a medium specially selected as a source of ultrasound and the detection of these signals in a broad frequency band with a high time resolution.

Three types of printing paper samples (see Table 1) were taken for porosity measurements. Each sample was shaped as a circle 24 mm in diameter cut out of a paper sheet. The sample thickness h_i was measured using a micrometer gauge, by clamping the sample between two polished plane-parallel surfaces, with an accuracy of 1–2 μm. It is necessary to note that the paper thickness at different points of a sheet varied within several micrometers (see Table 1), and, therefore, the measurements were performed for each sample before the ultrasonic measurements. Liquids were chosen according to the criterion that paper should be well saturated with them without changing its structure. For example, distilled water distorts paper (in the course of saturation, its thickness increases), and therefore cannot be used as a filler. Furthermore, it is necessary to indicate an important feature of porosity calculation using Eq. (4): the stronger the liquids differ in their acoustic properties, the more accurately the porosity is determined. Taking into account the above factors, we chose ethanol (ethyl alcohol) and transformer oil as the fillers. Their densities ($\rho_{et} = 798$ kg/m^3 and $\rho_{oil} = 829$ kg/m^3) were measured gravimetrically, and the sound velocities in them ($c_{et} = 1170$ m/s and $c_{oil} = 1450$ m/s), using a standard optoacoustic technique (for example, see [9]). The relative error of measurements for the indicated quantities was not worse than 0.5%. After ultrasonic measurements, the paper thickness was measured for the second time and no deviations greater than 1–2 μm were revealed.

To excite probing acoustic pulses, we used a pulsed Nd³⁺YAG laser (the radiation wavelength was $\lambda =$
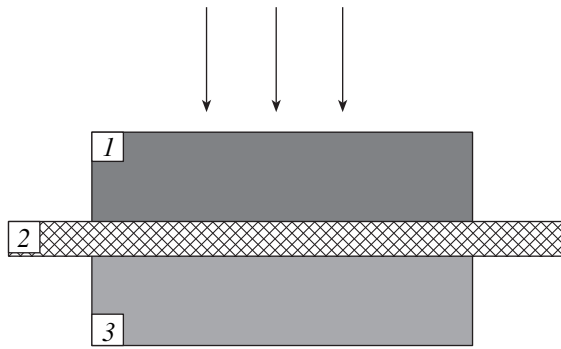
Fig. 1. Basic scheme of the immersion method with a laser source of ultrasound: (*1*) optoacoustic source, (*2*) liquid-saturated paper sample, and (*3*) broadband piezoelectric receiver of acoustic signals.

1.06 μm, the pulse length at the level of 1/*e* was 10–12 ns, the pulse energy was about 10–15 mJ, and the pulse repetition rate was 2 Hz). The laser radiation was directed through a light-diffuser at (*1*) the optoacoustic source of ultrasound (India ink in a quartz cell, see Fig. 1). In the presence of an impedance acoustic boundary between India ink and quartz glass, unidirectional acoustic pulses with exponential leading and trailing edges are excited. The transformation of the experimentally detected signal profile (Fig. 2a) at the trailing edge and the appearance of the rarefaction phase are connected with the ultrasonic pulse diffraction in the quartz glass and in the acoustic waveguide of the receiver. The characteristic frequency in the spectrum of the excited optoacoustic signal (Fig. 3) $f_h = \alpha c_{ink}/2\pi \approx 20$ MHz (at a level of 1/2) was provided by the coefficient of light absorption in India ink $\alpha \approx 1000\ \text{cm}^{-1}$. The sound velocity in India ink, $c_{ink} = (1.49 \pm 0.005) \times 10^3$ m/s, was measured experimentally. The lower operation frequency $f_{min} \approx 5$ MHz was determined by the diffraction of ultrasound in the acoustic waveguide of the receiver.

The detection of ultrasonic pulses was performed by (*3*) a calibrated broadband receiver based on LiNbO$_3$ (the operation frequency band was 1–100 MHz) (Fig. 1). The low-frequency sensitivity of the receiver was 15 mV/atm. For the demodulation of the probing ultrasonic signal, the rear surface of the optoacoustic source was pressed with the help of calibration screws and through a thin layer (~10 μm) of the corresponding filler to the face surface of the quartz acoustic waveguide of the receiver. All working surfaces of the source and the receiver were plane-parallel and initially polished. To detect ultrasonic signals transmitted through the liquid-saturated paper, (*2*) the samples were clamped between the source and the receiver (Fig. 1). Electric signals from the receiver were recorded by a Tektronix TDS-220 digital oscilloscope (an analog frequency band of 100 MHz).
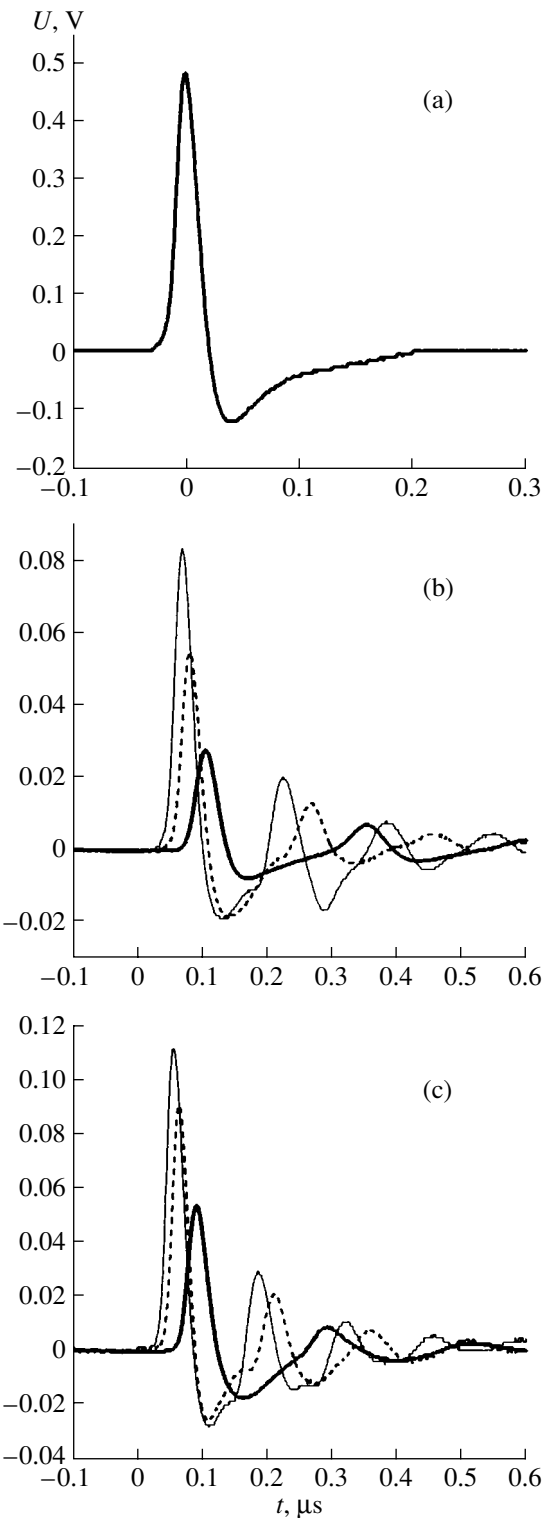
Fig. 2. (a) Temporal profile of the testing ultrasonic signal excited in the optoacoustic source and detected by the broadband piezoelectric receiver. The temporal profiles of ultrasonic signals transmitted through the samples of paper saturated with (b) ethanol and (c) transformer oil (the dashed line is for paper sample no.1; the thin solid line, for sample no. 2; and the thick solid line, for sample no. 3).
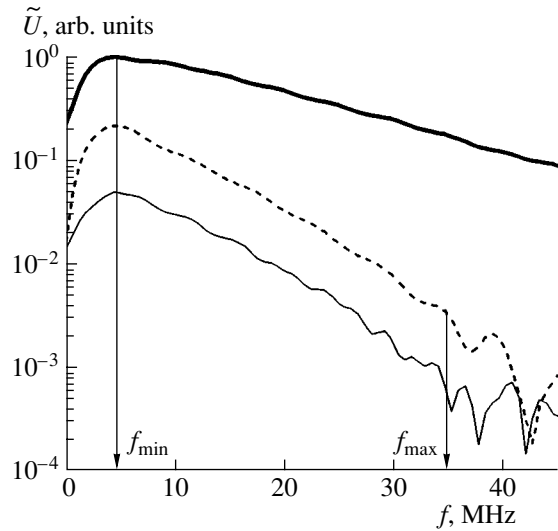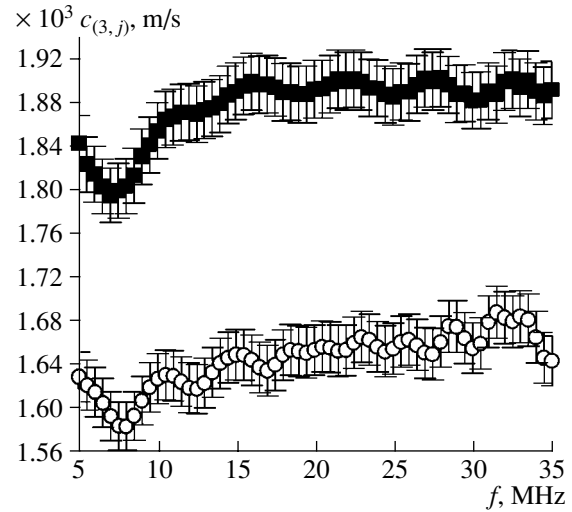
Fig. 3. Frequency spectra of the probe ultrasonic pulse excited in the optoacoustic source (the thick line) and of the ultrasonic signals transmitted through the paper sample no. 3 saturated with ethanol (the thin solid line) and with transformer oil (the dashed line).

Fig. 4. Frequency dependences of the phase velocity of ultrasound in the sample of printing paper no. 3 saturated with (■) transformer oil and with (○) ethanol.

After averaging over 128 realizations, the signals were processed by a personal computer.

Figure 2a shows the temporal profile of a probing ultrasonic pulse excited in India ink and detected by a broadband receiver. It is necessary to note that the liquid layer between the source and the receiver was thin and, therefore, irrespective of whether ethanol or transformer oil was used as the liquid, the form of the probing acoustic pulse was the same. The position of the signal maximum in Fig. 2a corresponds to the time instant $t = 0$ of the signal arrival at the receiver from the face surface of India ink irradiated by the laser pulse.

The profiles of the acoustic signals transmitted through the paper samples saturated with ethanol and transformer oil are presented in Figs. 2b and 2c, respectively. The thicker the paper sample, the farther from the reference time $t = 0$ the position of the signal transmitted through the sample is. The decrease in the pulse amplitudes is connected with damping of ultrasound in the samples. Figure 3 gives the spectrum of a probing pulse and the spectra of the signals transmitted through the paper sample no. 3 with different fillers. All curves are normalized to the maximum of the spectral amplitude of the probing pulse. One can see that the maximum frequency in the spectrum of signals under study is $f_{\max} \approx 35$ MHz (with the dynamic range of the receiving channel being equal to 35–40 dB). Higher-frequency harmonics cannot be discriminated against the noise background. Since the sound velocity in transformer oil is higher than that in ethanol, the signals transmitted through paper samples saturated with transformer oil have smaller time delays with respect to the

probing pulse in comparison with the samples saturated with ethanol. The time delay $\Delta t_{(i, j)} = t_{\max(i, j)} - t_{\max, (0)}$ between the maxima of these signals and the probing pulse can be used to calculate the group velocities of ultrasound $v_{g(i, j)}$ in the samples:

$$v_{g(i, j)} = h_i/\Delta t_{(i, j)}, \qquad (5)$$

where the index i indicates the number of the sample and the index j refers to the filler ($j = 1$ corresponds to ethanol, and $j = 2$, to transformer oil). However Eq. (4) involves the ultrasonic phase velocities that may depend on the frequency of the ultrasonic wave in the presence of a frequency dispersion. Since the paper porosity does not depend on the frequency of the ultrasonic pulse, the measurement accuracy is affected by the value of the frequency dispersion of ultrasonic phase velocities in the samples under investigation. The determination of the frequency dependences of ultrasonic phase velocities in all paper samples saturated with liquids is very difficult because of the reverberations of the probing acoustic pulse in paper samples clamped between the optoacoustic source and the receiver. The determination of the spectral phase is possible only for sample no. 3 in the case of sound propagation when the reverberations are practically separated in their arrival time at the receiver. Therefore, we have

$$c_{(3, j)} = 2\pi f h_3/\Delta\varphi_{(3, j)}, \qquad (6)$$

where $\Delta\varphi_{(3, j)}$ is the phase difference between the harmonics of the signals transmitted through the samples of paper no. 3 saturated with different liquids and the harmonics of the probing pulse corresponding to the filler.

Table 2

Paper sample	Surface density, g/m^2	$c_{(i,1)} \times 10^3$, m/s	$c_{(i,2)} \times 10^3$, m/s	P, %	$c_{cel} \times 10^3$, m/s	$\rho_{cel} \times 10^3$, kg/m^3
no. 1	80	1.52 ± 0.02	1.81 ± 0.03	36 ± 2	2.6 ± 0.2	1.20 ± 0.03
no. 2	100	1.60 ± 0.02	1.90 ± 0.03	32 ± 2	2.7 ± 0.2	1.17 ± 0.03
no. 3	160	1.64 ± 0.02	1.89 ± 0.03	25 ± 2	2.40 ± 0.14	1.21 ± 0.03

Figure 4 gives the phase velocities of ultrasound as functions of frequency for the sample of paper no. 3 that were calculated using Eq. (6) according to the experimental data. The frequency range of the phase velocity variation was limited by the values of f_{min} and f_{max}. In the case of ethanol used as the filler, the value of the standard deviation from the average velocity value $c_{(3,1)} = 1.64 \times 10^3$ m/s in the frequency range from f_{min} to f_{max} is $\sigma_c \approx 20$ m/s; in the case of transformer oil with $c_{(3,2)} = 1.89 \times 10^3$ m/s, it is $\sigma_c \approx 30$ m/s. These errors are caused by an inaccuracy in measuring the sample thickness (1–2 μm) and the time of signal detection by a receiver (≈ 1 ns). Thus, within an error of 1–2%, we can ignore the dependence of the ultrasonic phase velocity on frequency for the sample of paper no. 3. This allows us also to ignore the frequency dispersion of the phase velocity for two other paper samples despite the impossibility of direct measurements of spectral phases of signals. Therefore, the group velocities calculated from Eq. (5) by the delays of signal maxima in samples with respect to the probing pulse correspond to the values of the phase velocities within 1–2%. Thus, Eq. (4) can be used to calculate the porosity of printing paper from the data of ultrasonic measurements.

Table 2 presents the results of the ultrasonic studies described above. The time delays Δt between the maxima of the signals transmitted through a sample and the maximum of the probing signal were multiply measured for all types of paper. The error in their measurement was ~1–2 ns. The data of the sound velocity measurements in different samples show that the smallest relative error ($\Delta c_{(3,j)}/c_{(3,j)} = 1.3\%$) is obtained for the thickest paper. This is quite natural, because the absolute errors in measuring the sample thickness and arrival times of signals are equal for all samples. The lowest value of ultrasonic velocity is obtained for both fillers in the thinnest paper. For the samples of paper nos. 2 and 3, the velocity values are almost equal. An important specific feature of the method is the fact that the relative error in measuring the sound velocity, being $\Delta c_{(i,j)}/c_{(i,j)} = 1.3$–2%, does not lead to absolute errors greater than 2% in determining the porosity ΔP. In the fourth column of Table 2, the calculated porosity values for paper samples are given. The maximum value is obtained for paper sample no. 1 ($P = 36\%$), in which the sound velocity was minimum. The least porous paper was the thickest one, which had the maximum value of the bulk density (see the fourth column of Table 1).

Apart from the porosity, the proposed method provides an opportunity to determine the values of c_{cel} and ρ_{cel}. Their calculated values are given in the sixth and seventh columns of Table 2. Within the error, these quantities proved to be almost identical for different paper samples. Presumably, this is caused by the fact that raw materials used for the production of printing paper do not differ widely for different paper types. The absence of reference data on the density of cellulose, sound velocity in it, and porosity of paper does not allow us to state that the measured values correspond to the true ones for the samples studied. However, the reproducibility of the results in a series of experiments and the reasonable values of paper parameters obtained allow us to suggest the above-described method for measuring the paper porosity. A verification of this method requires measurements of porosity for the same paper samples by an independent technique.

Now, let us summarize the results. In this work, we studied the propagation of broadband acoustic pulses of longitudinal waves in printing paper saturated with liquids (ethanol and transformer oil). It was assumed that the liquids completely fill the volume of pores without changing the paper structure. An optoacoustic method was used to excite probing ultrasonic signals. The phase velocity of ultrasound was measured in the frequency range of 5–35 MHz in paper samples with different surface densities (80, 100, and 160 g/cm^2), and the absence of its noticeable frequency dispersion was demonstrated for all types of paper with any of the two fillers. The values of the paper porosity were calculated on the basis of a theoretical model of a two-phase medium using the data of ultrasonic measurements. It was found that the relative inaccuracy in measuring the sound velocity $\Delta c_{(i,j)}/c_{(i,j)} = 1.3$–2% leads to an absolute error in determining the porosity $\Delta P = 2\%$.

REFERENCES

1. M. C. Beland, Appl. Opt. **39**, 2719 (2000).

2. T. R. Letteri, E. Maex, J.-F. Song, and T. V. Vorburger, Appl. Opt. **30**, 4439 (1991).

3. J. Carlsson, P. Hellentin, L. Malmqvist, *et al.*, Appl. Opt. **34**, 1528 (1995).

4. K. P. Bestem'yanov, V. M. Gordienko, A. A. Ivanov, *et al.*, Kvantovaya Elektron. **34**, 666 (2004).

5. P. Hansson and G. Manneberg, Opt. Eng. **38**, 1683 (1999).

6. N. N. Komissarova and A. V. Furduev, Akust. Zh. **50**, 666 (2004) [Acoust. Phys. **50**, 571 (2004)].

7. A. A. Davydov and L. M. Lyamshev, Akust. Zh. **47**, 62 (2001) [Acoust. Phys. **47**, 50 (2001)].

8. V. É. Gusev and A. A. Karabutov, *Laser Optoacoustics* (Nauka, Moscow, 1991) [in Russian].

9. S. M. Zharkiĭ, A. A. Karabutov, I. M. Pelivanov, *et al.*, Fiz. Tekh. Poluprovodn. (St.-Petersburg) **37** (4), 485 (2003) [Semiconductors **37** (4), 468 (2003)].

10. M. A. Biot, J. Acoust. Soc. Am. **28**, 168 (1956).

11. L. F. Lependin, *Acoustics* (Vysshaya Shkola, Moscow, 1978) [in Russian].

12. A. A. Karabutov, M. P. Matrosov, N. B. Podymova, and V. A. Pyzh, Akust. Zh. **37**, 311 (1991) [Sov. Phys. Acoust. **37**, 157 (1991)].

Translated by M. Lyamshev

Velocity of Ultrasonic Waves in Ferrocomposites

I. S. Kol'tsova, E. N. Zinov'eva, and A. Yu. Mikhalev

Institute of Physics, St. Petersburg State University, ul. Ul'yanovskaya 1, St. Petersburg, 198904 Russia
e-mail: Dyatlova@rambler.ru, arcamy@yahoo.com
Received February 9, 2004

Abstract—The velocity of ultrasonic waves with a frequency of 3 MHz is experimentally studied in a wide range of volume concentrations (0.1–50%) of ferrite particles in the matrix. The mean size of particles is 6 μm. The results of the study show that the concentration dependence of the velocity of ultrasonic wave propagation in ferrocomposites has three specific regions, in which the concentration coefficient of velocity changes from negative to positive passing through a minimum in the percolation region. © *2005 Pleiades Publishing, Inc.*

With the progress in engineering and with the introduction of new technologies in industry, a steadily growing interest in composite materials has been observed, which is related to the possibility of producing materials with predetermined properties, the wide range of which makes them indispensable to microelectronics, space industry, civil engineering, etc.

The properties of composite materials are investigated using various methods, including acoustical ones. This paper presents an experimental study of the dependence of the velocity of ultrasonic wave propagation on the concentration of ferrite particles in ferrocomposites. Ferrocomposites, as well as magnetic fluids, are of great practical importance. In magnetic fluids, the matrix is water, oil, kerosene, etc. Possessing the property of fluidity, they are easily deformed but cannot hold their shape [1, 2]. The technology used for ferrocomposite preparation makes it possible to impart any shape to these materials and then fix it [3].

In the experimental study described in this paper, the composite matrix was a 10% solution of gelatin, into which Fe_3O_4 ferrite particles were introduced. It should be noted that, in the 10% solution of gelatin, at a temperature higher than the temperature of gelation, when the viscosity of the solution was relatively low, the ferrite particles exhibited magnetic properties. In particular, the particles were attracted by a magnet and the magnetic field changed their trajectories. In the absence of magnetic field, when the particles were randomly distributed over the sample volume, a decrease in the temperature of the solution below the gelation temperature resulted in the stabilization of the positions of randomly distributed particles in the matrix. In this case, the magnetic properties of the particles in the composite disappeared. Thus, the study of the concentration dependence of sound speed in such composites gives information on the general features of sound propagation in the solid particles–polymer composites. Afterwards, this problem can be complicated.

The samples under study had the form of rectangular parallelepipeds with edge dimensions of $6 \times 6 \times 2$ cm. The volume concentration of particles varied from 0.1 to 50%. The dimensions of 1000 particles were measured with a microscope, and the results were used to plot a histogram for determining the fractional composition. The mean size of particles was $r = 6$ μm, and the range of particle sizes was $r \in 3$–30 μm.

A simplified block diagram of the setup for measuring the velocity of ultrasonic waves is shown in Fig. 1. The sample (*2*) was placed in a container (*1*) filled with distilled water in such a way that the side planes of the sample were parallel to the planes of piezoelectric transducers (*3*, *4*) and its center of symmetry lay on the axis passing through the transducers' centers. A signal from an oscillator (*5*) was fed to radiating quartz (*3*),
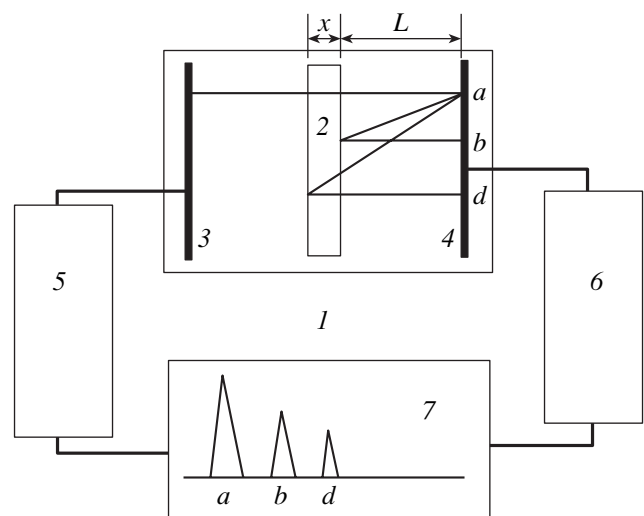
Fig. 1. Block diagram of the setup for measuring the velocity of ultrasonic waves with schematically represented beam trajectories and their image on the screen of the oscilloscope.

which excited ultrasonic waves. These waves, after passing through the sample (2), fell on the receiving quartz (4). Then, the signal was fed to an amplifier (6) and an oscilloscope (7) triggered by the oscillator. The measurements were performed at a frequency of 3 MHz. The velocity of ultrasonic wave propagation c in the sample was measured by the pulse method and calculated using the relationship $(2x/c) + (2L/c_w) = \tau$, where x is the sample thickness, L is the distance from the sample to the quartz, c_w is the sound velocity in water, and τ is the time between pulses a and d determined by the oscilloscope [4]. The pulse duration was 80 µs, and the delay time was 3 ms. The sound velocity measurement error determined by the errors in measuring x, L, and τ was about 1%.

In Fig. 2, curve 1 displays the results of measuring the dependence of the velocity of ultrasonic wave propagation in ferrocomposites on the volume concentration of particles, which varied from 0.1 to 10%. As is seen from the curve, the increase in the quantity of particles in the matrix leads to a decrease in the velocity of ultrasonic wave propagation in the ferrocomposite. In this range of concentrations, similar dependences of the velocity were observed for magnetic fluids and a suspension of glass particles [5, 6]. These data are shown in Fig. 2 by curves 2 and 3, respectively. Note that, in the suspension of glass spheres, after the concentration exceeds 16%, when the distance between the particles r_{mn} becomes comparable to or less than the particle size $r_{mn} \leq 2r$, the ultrasonic velocity begins to grow with the particle concentration (curve 3). In this region of concentrations, measurement of sound velocity in composites by the pulse method becomes impossible due to the strong absorption that leads to the disappearance of the third pulse d. For measuring the sound velocity in composites in the range of high particle concentrations, we used a new method.

As is well known, the coefficient of reflection from the boundary of two media K at normal incidence is determined by the formula $K = (Z_2 - Z_1)/(Z_2 + Z_1)$, where Z_2 and Z_1 are the characteristic impedances of the media [7]. Supposing that this relationship is valid for the reflection from the composite materials placed in water, we can write $K = (c\langle\rho\rangle - c_w\rho_w)/(c\langle\rho\rangle + c_w\rho_w)$, where $\langle\rho\rangle$ is the effective density of the composite and ρ_w is the water density. From this relation, it is possible to obtain the formula for calculating the sound velocity in the composite:

$$c = c_w\rho_w(K + 1)/(1 - K)\langle\rho\rangle. \qquad (1)$$

The measurements of the reflection coefficient were performed using the setup shown in Fig. 1 after some modification: one of the piezoelectric transducers (4) was used alternately as a radiator and as a receiver of ultrasonic waves. The results of measuring the coefficient of reflection from ferrocomposites are presented in Fig. 3. As is seen, in the region of low concentrations,
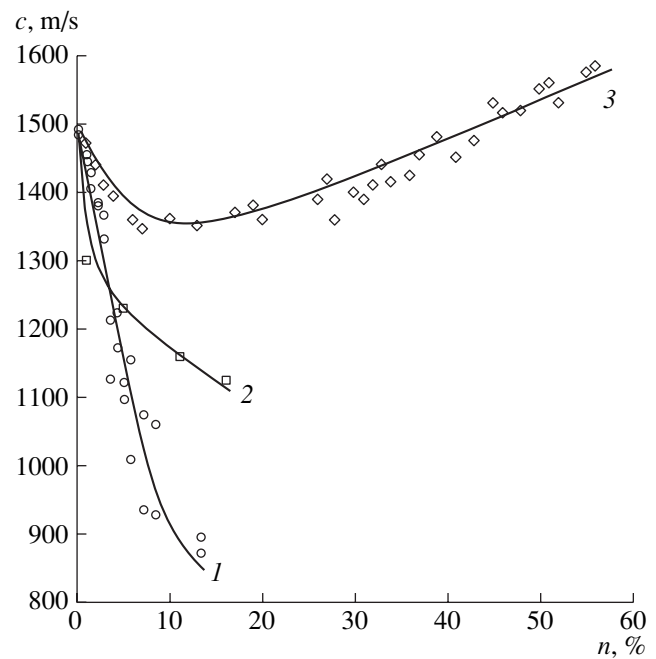
Fig. 2. Dependences of the velocity of ultrasonic waves on the concentration in (1) ferrocomposites, (2) magnetic fluids [6], and (3) a suspension of glass particles [5].
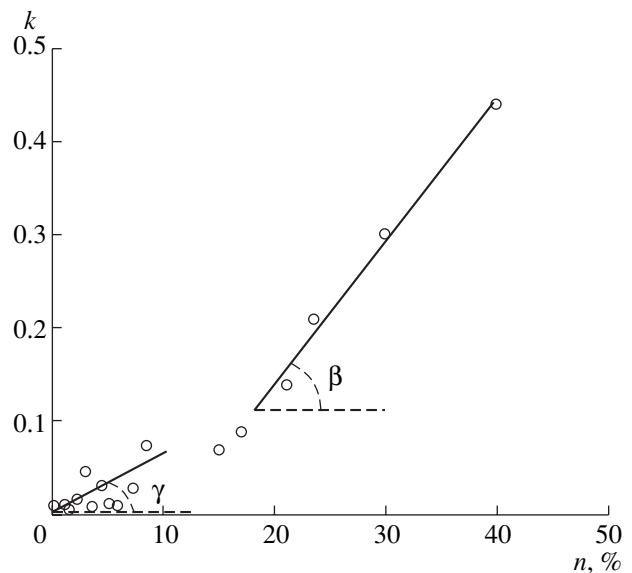
Fig. 3. Dependence of the reflection coefficient on the concentration of the ferrocomposite.

up to 7–10%, the reflection coefficient fluctuates, which hampers the determination of its dependence on the concentration. Numerous measurements, including measurements with the samples that had the same particles but differently distributed in the body of the sample, showed that the fluctuations of the reflection coefficient were connected with the ambiguity of the particle arrangement in the samples [8]. Statistical processing
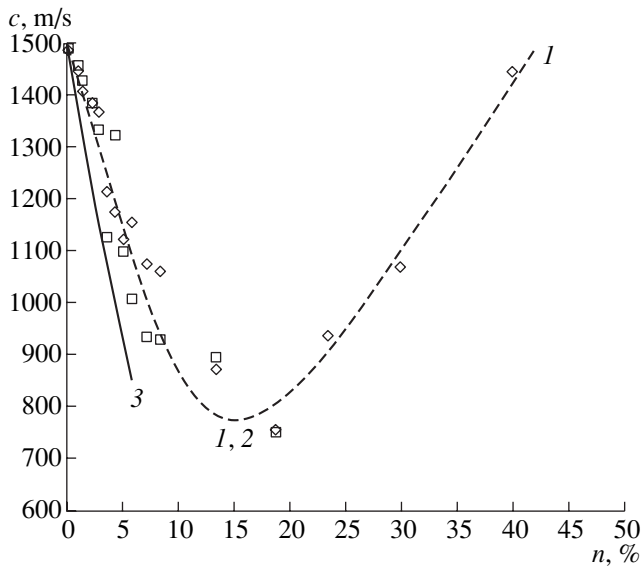
Fig. 4. Dependences of the velocity of ultrasonic wave propagation in ferrocomposites on the concentration: (*1*, ◇) data obtained from the reflection coefficient measurements, (*2*, □) measurements by the pulse method, and (*3*) the theoretical curve.

of a large body of measurement results made it possible to reveal the tendency for the growth of the reflection coefficient with an increase in concentration. The fluctuations of the reflection coefficient die out with the growth of concentration and, above 20%, the reflection coefficient becomes reproducible accurate to 10%. As is seen from Fig. 3, the concentration coefficient $\beta = \partial K/\partial n$ in the concentration region within 20–50% considerably exceeds the coefficient $\gamma = \partial K/\partial n$ in the region of 0.1–10%.

The effective density required for determining the velocity from the reflection coefficient was calculated theoretically and measured experimentally by weighing the samples and measuring their volumes. Experimental data were in satisfactory agreement with the theoretical ones.

The velocities of ultrasonic waves calculated by formula (1) are represented by curve *1* in Fig. 4 (diamonds). This figure also shows the velocities obtained by the pulse method (curve *2*, squares). It is seen that, in the concentration region 0.1–10%, the velocity values determined by the pulse method agree well with the velocities calculated from the measured reflection coefficient. Thus, the use of the two methods made it possible to measure the velocity of ultrasonic waves in ferrocomposites in a wide range of concentrations, from 0.1 to 50%.

As is seen from curves *1* and *2* in Fig. 4, the dependences of the velocity of ultrasonic waves on concentration have three distinctive regions. In the region of concentrations from 0.1 to 10%, in which the particles are discretely distributed in the matrix without touching

each other and the distance between them r_{mn} is greater than the particle size, the velocity of ultrasonic waves decreases with increasing concentration and the concentration coefficient of velocity is negative. In the percolation region of $n \in$ 16–20% [9], when infinite clusters begin to form and double and triple interparticle contacts appear, the concentration coefficient of velocity tends to zero. With a further growth of the particle concentration, the number of interparticle contacts increases [10], the velocity of ultrasonic waves grows, and the concentration coefficient of velocity becomes positive.

At present, there is no appropriate theory of acoustic wave propagation in composite materials. Specific models are considered for every class of materials [11–15]. For the composite materials under study, in which the matrix is a 10% solution of gelatin, the model of microinhomogeneous media proposed by Isakovich, Ratinskaya-Chaban, *et al.* [16–19] can be used, because, in these materials, the bound water comprises only 2% of the gelatin weight and the remaining 98% is in the free state [20]. The theories describing the propagation of acoustic waves in disperse systems assume the additivity of density $\langle\rho\rangle = (1 - n)\rho_1 + n\rho_2$, heat capacity at a constant pressure $\langle C_p\rangle = (1 - n)C_{p1} + nC_{p2}$, coefficient of thermal expansion $\langle\alpha\rangle = (1 - n)\alpha_1 + n\alpha_2$, and isothermal compressibility $\langle\beta\rangle = (1 - n)\beta_1 + n\beta_2$. Here, subscript 1 denotes the matrix medium and subscript 2, the disperse phase. The coefficient of adiabatic compressibility is also additive in the absence of exchange processes between the phases in the heterogeneous system: $\langle\beta_{ad}\rangle = (1-n)\beta_{ad1} + n\beta_{ad2}$. In this case, the Laplacian velocity of ultrasonic waves in the heterogeneous medium is determined as

$$c = \sqrt{\frac{1}{\langle\rho\rangle\langle\beta_{ad}\rangle}}. \qquad (2)$$

However, in the propagation of ultrasonic waves in heterogeneous systems, the energy exchange processes between the phases arise at the phase boundaries, which leads to an additional loss of acoustic energy and to corrections to the Laplacian sound velocity.

In the theoretical papers [16–19], under the condition that $r_{mn} \gg 2r$, the mechanisms of acoustic energy absorption in disperse systems due to the heat exchange, viscous stress, and scattering are considered and the corresponding corrections to the Laplacian velocity are calculated. Assuming that, in the composites under study, the exchange processes between the Fe_3O_4 particles and water play the dominant role in dissipative processes, we calculated the velocity and corrections to it for ferrocomposites in the concentration region $n \in$ 0.1–10%, where the condition $r_{mn} \gg 2r$ is satisfied. The values of the parameters required for calculating c, Δc_T, and Δc_η [21] are given in the table. In the calculations, we used the mean particle size $r = 6\ \mu m$ determined from the histogram. The choice of formulas

Table

Substance	Density ρ, kg/m^3	Heat capacity C_p, 10^{-2} J/kg K	Coefficient of compressibility β, 10^{-10} Pa^{-1}	Coefficient of thermal volumetric expansion α, 10^{-6} K^{-1}	Viscosity η, 10^{-3} Pa s
Water	0.998	41.9	4.61	182	1.01
Fe$_3$O$_4$ particles	7.87	4.6	0.062	35.571	–

for theoretical calculations was determined by the values of the parameters kr, $k_T r$, and $k_\eta r$, where k, k_T, and k_η are the wave numbers of acoustic, heat, and viscous waves, respectively. The correction to the velocity due to the heat exchange processes was calculated by the formula obtained for $k_T r \ll 1$:

$$\Delta c_T = -\frac{n}{2} T_0 c_{ll}^3 \langle \rho \rangle \rho_2 C_{p2} \left(\frac{\alpha_1}{\rho_1 C_{p1}} - \frac{\alpha_2}{\rho_2 C_{p2}} \right)^2. \quad (3)$$

The correction to the velocity connected with the excitation of viscous waves was calculated by the formula obtained for $k_\eta r \ll 1$:

$$\Delta c_\eta = \frac{c a \xi \sqrt{\xi} (1 + b\sqrt{\xi})}{(1 + \sqrt{\xi})^2 + \xi(1 + b\sqrt{\xi})^2 - a\xi\sqrt{\xi}(1 + b\sqrt{\xi})}, \quad (4)$$

where

$$\xi = \frac{\omega \rho}{\eta} r^2, \quad a = \frac{2n}{9}\left(\frac{\rho_2 - \rho_1}{\rho_1}\right)^2, \quad b = \frac{2}{9}\left(\frac{\rho_1 + 2\rho_2}{\rho_1}\right).$$

Note that the correction to the velocity connected with the heat exchange processes reduces the Laplacian velocity, and the correction owing to the viscous stresses increases the Laplacian velocity in the ferrocomposite.

In Fig. 4, where the experimental data are displayed (curve *1*), the results of theoretical calculations of the velocity by Eqs. (2)–(4) with allowance for the corrections $c + \Delta c_T + \Delta c_\eta$ are also presented (curve *3*). As is seen, theoretical curve *3* agrees well with the experimental curve in the concentration region 0.1–10%.

The above study of the concentration dependence of the velocity of ultrasonic waves propagating in ferrocomposites makes it possible, by using Eq. (2), to solve the inverse problem: to obtain information on the effective volume compressibility. Figure 5 shows the dependence of $\langle \beta_{\text{eff}} \rangle$ on the concentration of Fe$_3$O$_4$ particles in the matrix. The values of the coefficients of volume compressibility of a 10% solution of gelatin and Fe$_3$O$_4$ are also given in this figure.

As is seen from the plot, in the region of concentrations corresponding to a discrete particle distribution in the matrix, the coefficient of compressibility of the composite is on the order of the coefficient of compressibility of the matrix, and even slightly greater. The particles introduced into the matrix violate its homoge-

neity and cause an increase in compressibility. A reinforcement of the composite and a reduction of its compressibility takes place for the concentrations exceeding the concentration of the percolation region $n > 20\%$, when a globular network structure of particles develops in the matrix with the number of interparticle contacts greater than three; i.e., the strength of the composite grows with an increase in the number of interparticle contacts.

Thus, using the two methods of measuring the sound velocity, namely, the pulse method and the calculation from the reflection coefficient, we measured the concentration dependence of sound velocity in composite materials in a wide range of concentrations of the disperse phase, from 0.05 to 50 vol %.

The dependence of the velocity of ultrasonic waves on concentration has three specific regions: (i) the region of low concentrations within 0.05–10%, where the concentration coefficient of velocity is $\partial c / \partial n < 0$; (ii) the percolation region with concentrations of 10–
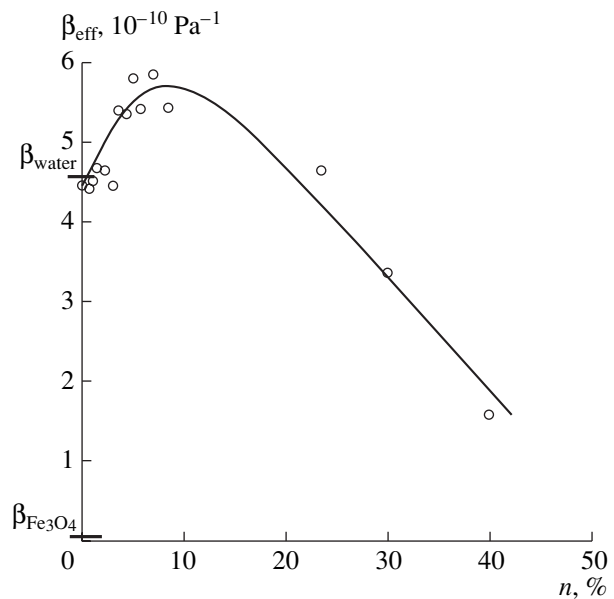
Fig. 5. Dependence of the coefficient of effective compressibility of ferrocomposites on the concentration of the disperse phase.

25%, where $\partial c/\partial n \approx 0$; and (iii) the region of high concentrations $n > 25\%$, where $\partial c/\partial n > 0$.

It is shown that, for the class of composite materials studied, in the region of low concentrations, the model of microinhomogeneous media developed by Isakovich, Rytov, Ratinskaya-Chaban *et al.* can be used.

REFERENCES

1. E. E. Bibik, Kolloidn. Zh. **35** (6), 1141 (1973).
2. V. M. Polunin, Magn. Gidrodin. **3**, 33 (1979).
3. I. S. Kol'tsova, Candidate's Dissertation in Physics and Mathematics (LGU, Leningrad, 1970).
4. H. J. McSkimin, in *Physical Acoustics: Principles and Methods*, Ed. by W. P. Mason (Academic, New York 1964; Mir, Moscow, 1966), Vol. 1, Part A, pp. 272–335.
5. E. N. Dyatlova and I. S. Kol'tsova, Akust. Zh. **48**, 52 (2002) [Acoust. Phys. **48**, 46 (2002)].
6. V. M. Polunin and N. M. Ignatenko, in *Ultrasound and Physical-Chemical Properties of Materials* (KGPI, Kursk, 1980), pp. 223–228.
7. V. A. Shutilov, *Fundamentals of the Physics of Ultrasound* (Leningr. Gos. Univ., Leningrad, 1980) [in Russian].
8. I. S. Koltzova and A. Y. Mikhalev, in *Proceedings of 17th International Congress on Acoustics* (Rome, 2001), p. 392.
9. A. L. Éfros, *Physics and Geometry of Disorder* (Nauka, Moscow, 1982) [in Russian].
10. S. I. Kol'tsov and N. G. Roslyakova, *Porous Materials* (Leningrad, 1987) [in Russian].
11. A. I. Potapov and V. M. Rodyushkin, Akust. Zh. **47**, 407 (2001) [Acoust. Phys. **47**, 347 (2001)].
12. S. A. Lisina, A. I. Potapov, and V. F. Nesterenko, Akust. Zh. **47**, 685 (2001) [Acoust. Phys. **47**, 598 (2001)].
13. R. A. Guyer and P. A. Johnson, Phys. Today, No. 4, 30 (1999).
14. C. S. Chang and Y. Gao, J. Eng. Mech. ASCE, No. 1, 52 (1997).
15. C. S. Chang and Y. Gao, Int. J. Nonlinear Mech., No. 2, 111 (1995).
16. I. A. Ratinskaya, Akust. Zh. **8**, 210 (1962) [Sov. Phys. Acoust. **8**, 160 (1962)].
17. S. M. Rytov, V. V. Vladimirskiĭ, and M. D. Galanin, Zh. Éksp. Teor. Fiz. **8** (5), 614 (1938).
18. M. A. Isakovich, Usp. Fiz. Nauk **129** (3), 531 (1979) [Sov. Phys. Usp. **22** (10), 928 (1979)].
19. Y. R. Allegra and S. A. Hawley, J. Acoust. Soc. Am. **51**, 1545 (1971).
20. V. N. Izmaĭlova and P. A. Rebinder, *Structure Formation in Protein Systems* (Khimiya, Moscow, 1976) [in Russian].
21. *Physical Quantities*, Ed. by I. S. Grigor'eva and E. Z. Meĭlikhova (Énergoatomizdat, Moscow, 1991), pp. 1232–1235 [in Russian].

Translated by A. Svechnikov

Nonlinear Elasticity in Structurally Inhomogeneous Materials: An Experimental Study

A. I. Korobov, Yu. A. Brazhkin, and Wang Ning

Faculty of Physics, Moscow State University, Vorob'evy gory, Moscow, 119992 Russia
e-mail: akor@acs465a.phys.msu.ru
Received January 31, 2005

Abstract—Experimental results on the propagation of longitudinal and torsional elastic waves in polycrystalline copper under elastoplastic strain are reported. The strain in the interval of 0–0.06 was created by applying heavy tensile loads to the samples. The Young and shear moduli, Poisson ratio, and nonlinear acoustic parameters of longitudinal and torsional elastic waves were measured as functions of the static strain. The nonlinear acoustic parameters were found to behave anomalously in loading–unloading cycles in the plastic strain region. The experimental results are discussed. The nonlinear properties of structurally inhomogeneous materials are explained in terms of the clapping nonlinearity and hysteretic nonlinearity mechanisms. © 2005 Pleiades Publishing, Inc.

The first milestone work on the effect of defect structure of metal polycrystals and single crystals on their nonlinear elastic properties was published by V.A. Krasil'nikov *et al.* in 1963 [1]. They experimentally showed that inhomogeneities (e.g., dislocations, microcracks, or local internal stresses) that occur in the internal structure of solids noticeably affect their nonlinear elastic properties. An experimental observation of the generation of the second shear harmonic in polycrystalline metals (aluminum and MA-8 magnesium–aluminum alloy) was also reported in [1]. It is well known that the second shear harmonic cannot be generated in perfect isotropic solids without defects [2, 3]. The results reported in [1] served as the basis for the development of new nondestructive testing methods for structural materials, as well as for the strength diagnostics of solids [4, 5]. An important result of these works is that, along with the nonlinearity associated with anharmonicity of the crystal lattice (classical nonlinearity), materials with defects exhibit structural (nonclassical) nonlinearity associated with the imperfection of material's internal structure. Nonclassical nonlinearity was found not only to be much stronger than classical nonlinearity, but also to change the symmetry of the nonlinear elastic properties of solids. Much later, other authors found that a strong nonclassical nonlinearity is also inherent in rock, construction materials, granular media, composite materials, and other media with irregular internal structure [6–9]. Possible mechanisms of the structural nonlinearity are considered in [10]. In recent years, two main phenomenological models have been used to describe the nonclassical nonlinearity of structurally inhomogeneous materials: the bilinear medium and the medium with hysteretic elastic properties [11, 12]. In the framework of these models, nonlin-

ear equations of state were proposed for rocks, fractured media, and oil-saturated granular media, which sufficiently well describe the experimental results [7, 13, 14].

The purpose of the present work is to experimentally study the propagation of torsional and longitudinal elastic waves in polycrystalline copper under elastoplastic strain with a continuous variation of its internal structure. The samples for the experiment were made of electrical copper wire, which acquired multiple structural defects and a texture in the course of sample preparation. The defect structure created in this manner can be modified by applying heavy static loads to the samples [15, 16].

EXPERIMENTAL TECHNIQUE AND RESULTS

Ultrasonic elastic waves propagating in thin metal rods (wires) are known to be noticeably different from waves that propagate in an unbounded medium. The presence of a dimensional parameter D (D is the rod diameter) comparable to the wavelength of the ultrasonic elastic wave, λ, leads to the situation where normal modes of three types can propagate in the rod: longitudinal, torsional, and flexural waves. As a rule, these waves exhibit a considerable dispersion. Rigorous analysis of these waves is associated with intricate and difficult mathematical calculations [17].

In the experiments, we used longitudinal and torsional normal modes. From the family of longitudinal waves, we used the lowest-order longitudinal mode. This mode exists at frequencies down to zero, whereas the higher-order longitudinal normal modes have cutoff frequencies. In the low-frequency limit, when the wire diameter is $D \ll \lambda$, the velocity of the longitudinal
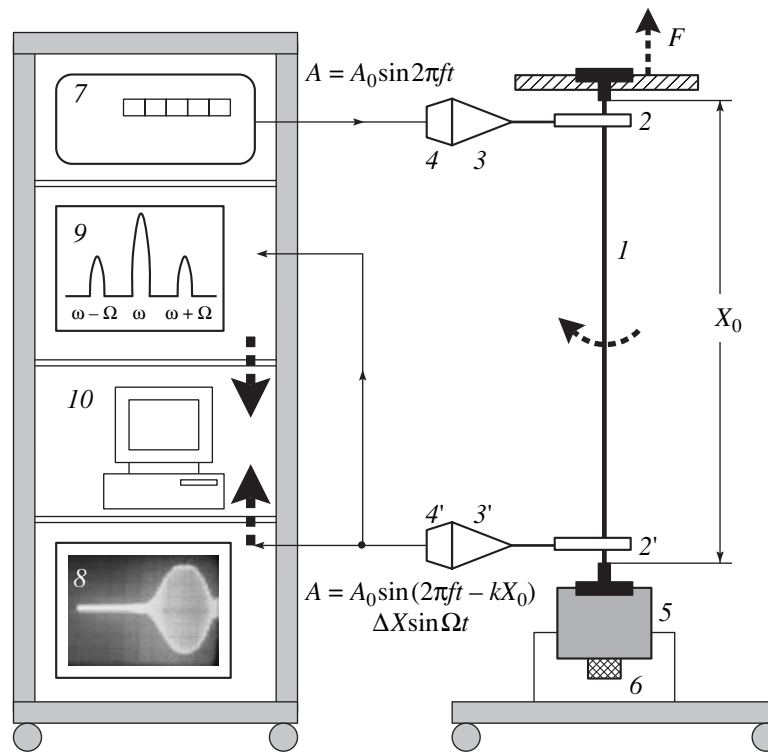
Fig. 1. Block diagram of the ultrasonic measurement system.

elastic wave, V_{long}, is determined by the simple expression

$$V_{\text{long}} = \sqrt{\frac{E}{\rho}}, \qquad (1)$$

where E is the dynamic Young modulus and ρ is the density of the material. From the family of torsional waves, the experiments employed the zero-order mode of the torsional wave, which is nondispersive. The phase velocity of this mode, V_{tors}, is equal to the velocity V_{trans} of the transverse (shear) elastic wave in an unbounded medium:

$$V_{\text{tors}} = V_{\text{trans}} = \sqrt{\frac{E}{2\rho(1+\nu)}} = \sqrt{\frac{\mu}{\rho}}, \qquad (2)$$

where μ is the dynamic shear modulus, ν is the Poisson ratio, and ρ is the density of the material.

The elastic properties of the samples, whose defect structure was changed due to the static strain, were studied with the help of an automated ultrasonic measurement system schematically represented in Fig. 1 [18]. The sample under study *1*, whose length was $L_0 \approx$ 1 m, was fixed between two movable plates. To the upper plate, a constant stretching force F was applied, which created a static strain ε_s in the sample. The lower plate could be vibrated with a shaking table *5* according to a harmonic law $\Delta X \sin(\Omega t)$ at a frequency Ω. The amplitude of these vibrations, ΔX, was measured with the help of an accelerometer *6* from Analog Devices. Simul-

taneously, a harmonic elastic wave $A = A_0 \sin(2\pi ft - \varphi)$ (where A_0 is the amplitude, $\varphi = kX$ is the phase, $k = 2\pi f/V$ is the wave number, f is the frequency, and V is the velocity of the elastic wave) was excited in the sample at a frequency $\omega \gg \Omega$ with the help of an oscillator *7* and transducer *2*. The output signal of the transducer *3'* was amplified and applied to an oscilloscope *8* and a spectrum analyzer *9* for recording. The information on the sample length L, length modulation amplitude ΔX, deviation of the sample length ΔL, the length modulation amplitude X, the sample length variation L, the force F, and the amplitude A_0 and phase φ of the elastic wave transmitted through the sample was fed into a personal computer *10* in order to store the results and to analyze them later. The measurement accuracy was $\sim 1 \times 10^{-6}$ m for the sample length, 0.02 radians for the phase φ, and (1–2)% for the wave amplitude A_0 and force F. The measurements could be performed in the pulsed or continuous mode of operation.

The methods for the excitation and detection of longitudinal elastic waves in thin rods were considered in [18]. To generate and receive torsional elastic waves in the wire, we used the setup whose diagram is shown in Fig. 1. A piezoelectric transducer *4* excited longitudinal oscillations in the conical concentrator *3*. These oscillations were guided to the plate *2* rigidly fixed on the wire *1*. The longitudinal oscillations of the concentrator created a variable torsional moment about the wire axis, which generated the torsional waves. To receive the tor-
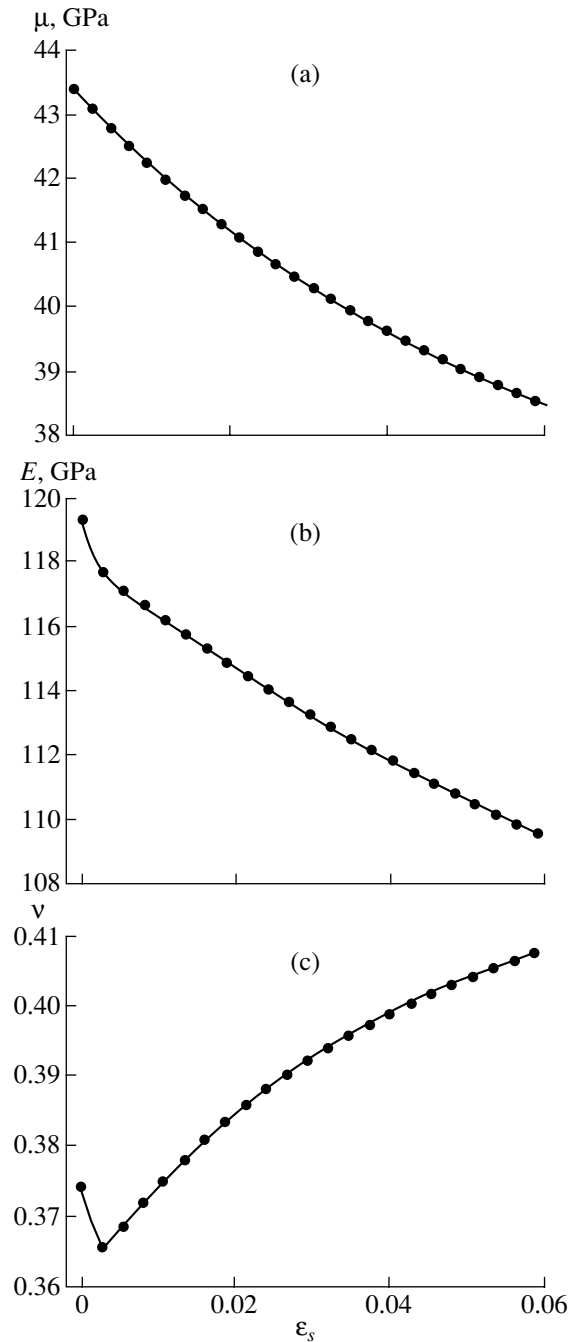
sional waves at the other end of the wire, the measuring system used a similar device.

The samples for the experiment were made from PÉV-1 electric copper wires of different diameters ($D = 0.75$ and 0.9 mm). The propagation velocity of torsional and longitudinal elastic waves in the samples was preliminarily measured by the echo-pulse method. The waveform of the elastic wave signal transmitted through the sample was shown on the oscilloscope 8 (Fig. 1). The velocities of the zero-order torsional and longitudinal modes were $V_{tors} = (2200 \pm 50)$ m/s and $V_{long} = (3650 \pm 50)$ m/s. The elastic constants of the copper samples in the initial state were calculated from these measurements by formulas (1) and (2): $E = (116 \pm 3)$ GPa, $\mu = (43 \pm 2)$ GPa, and $\nu = (0.38 \pm 0.02)$, which is in good agreement with reference data [19]. The elastic wave velocity was measured over the frequency range of $f = 50$–200 kHz. In this range, $D \ll \lambda$ and no dispersion of the elastic wave velocity was observed within the experimental error. After the initial elastic wave velocity was found, we simultaneously measured the stress σ_{st}–static strain ε_s curve ($\varepsilon_s = \Delta L/L_0$, where ΔL is the change in the wire length as a result of the stress σ_{st} caused in the sample by the external load) and the changes in the velocity and amplitude of the elastic wave. These measurements were performed in the automated mode at a constant rate of stress variation in the sample ($\partial\sigma_{st}/\partial t$) = const). The duration of one measurement cycle was no longer than 0.1 s. The interval between the measurement cycles was specified by the computer to be within 15 to 30 s. When the strain of the sample was as high as $\varepsilon_s \sim 0.06$, the experiment was terminated. The number of measurement cycles was 2000–3000. Based on the measured longitudinal $V_{long}(\varepsilon_s)$ and torsional $V_{tors}(\varepsilon_s)$ elastic wave velocities, the Young modulus ($E(\varepsilon_s)$), shear modulus $\mu(\varepsilon_s)$, and Poisson ratio $\nu(\varepsilon_s) = \{0.5[V_{long}(\varepsilon_s)/V_{tors}(\varepsilon_s)]^2 - 1\}$ were calculated as functions of the static strain. These functions are plotted in Figs. 2a–2c. An increase in the strain from 0 to 0.06 caused a monotonic decrease in $E(\varepsilon_s)$ and $\mu(\varepsilon_s)$ by approximately 9%. However, at small strains, the Young modulus $E(\varepsilon_s)$ decreased faster than the shear modulus $\mu(\varepsilon_s)$. With increasing strain, the Poisson ratio $\nu(\varepsilon_s)$ first decreases, reaches its minimum at $\varepsilon_s \cong 0.0022$, and then grows by ~11%.

The experimental dependencies of the moduli $E(\varepsilon_s)$ and $\mu(\varepsilon_s)$ were used to calculate the quasi-static nonlinear parameters G_{tors}^{qs} and G_{long}^{qs} of the torsional and longitudinal elastic waves, respectively:

$$G_{tors}^{qs} = \frac{\mu^n}{\mu}, \quad G_{long}^{qs} = \frac{E^n}{E},$$

where $\mu^n = \dfrac{\partial\mu}{\partial\varepsilon_s}$ and $E^n = \dfrac{\partial E}{\partial\varepsilon_s}$ are, respectively, the third-order quasi-static shear and Young's moduli [20]. It is impossible to directly differentiate the functions shown in Figs. 2a and 2b, because they are represented by discrete experimental points and are not continuous. Therefore, before differentiating, we approximated these functions by a sum of exponentials plotted in Figs. 2a and 2b by thin lines (to show these curves, in Figs. 2a and 2b we presented every 50th experimental point). Figures 3a and 3b show the quasi-static nonlinear acoustic parameters G_{tors}^{qs} and G_{long}^{qs} for the torsional

Fig. 2. (a) Shear modulus $\mu(\varepsilon_s)$, (b) Young modulus $E(\varepsilon_s)$, and (c) Poisson ratio $\nu(\varepsilon_s)$ of polycrystalline copper versus the static strain.
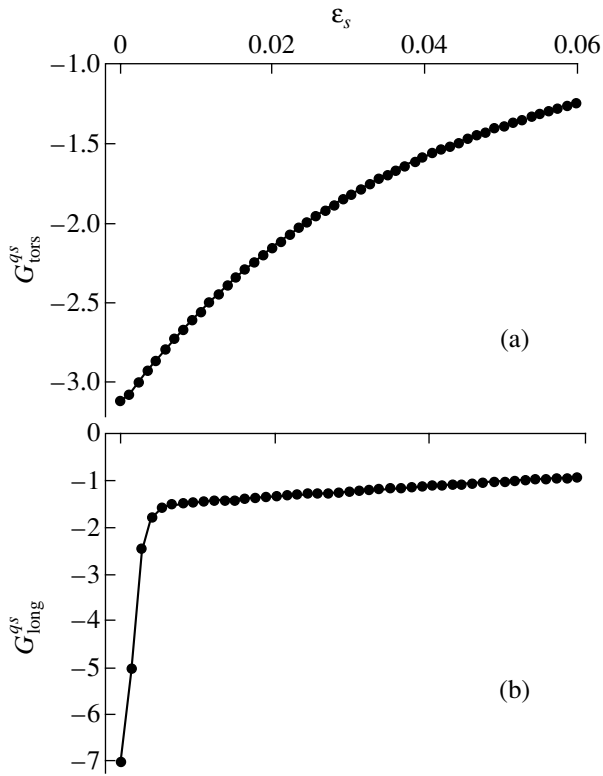
Fig. 3. Quasi-static nonlinear parameters of (a) torsional elastic waves, G_{tors}^{qs}, and (b) longitudinal elastic waves, G_{long}^{qs}, versus the static strain.

and longitudinal elastic waves, respectively, versus the strain ε_s. At small strains $\varepsilon_s \cong 0$, the nonlinear acoustic parameters G_{tors}^{qs} and G_{long}^{qs} within experimental errors agree well with those calculated from the second- and third-order moduli of elasticity of copper single crystals [21]. This fact indicates that, at these strains, the nonlinear acoustic parameters are predominantly determined by anharmonicity of interatomic forces. With increasing static strain, the absolute values of both parameters decrease and asymptotically tend to unity in the region of plastic strains.

The dynamic nonlinear acoustic parameter G was measured by the spectral method. The method measures the amplitudes $A(\omega)$, $A(\omega + \Omega)$, and $A(\omega - \Omega)$ of the fundamental and combination frequencies $(\omega + \Omega)$ and $(\omega - \Omega)$, which appear in the spectrum of the acoustic signal as a result of nonlinear interaction of elastic waves at the frequencies ω and Ω. Measuring the modulation depth

$$M(\varepsilon_s) = [A(\omega - \Omega) + A(\omega - \Omega)]/A(\omega)$$

of the acoustic signal for different static strains ε_s of the sample, it is possible to study the dependence of the dynamic nonlinear acoustic parameter on the strain ε_s:

$$G^{DN}(\varepsilon_s) = \{[2M(\varepsilon_s)/k\Delta X] - 2\}. \tag{3}$$

It should be noted that this method yields the absolute value of the acoustic parameter [20]. The dynamic nonlinear parameter for torsional and longitudinal elastic waves was measured in the continuous mode near the frequency of $f \sim 48$ kHz, which corresponds to one of the sample's standing wave resonances. Simultaneously, longitudinal oscillations at the frequency of $\Omega = 40$ Hz with the displacement amplitude $\Delta X = 1.7 \times 10^{-5}$ m were excited in the wire by the shaking table 5 (Fig. 1). The condition $((V/\Omega) \gg L$ was satisfied; i.e., the wavelength at the frequency Ω was much greater than the sample length. Therefore, the strain created in the sample by the oscillations at the frequency Ω could be considered to be uniform over its length. The screen of the spectrum analyzer 9 (Fig. 1) displayed a triplet with the fundamental frequency $A(\omega)$ and side frequencies $A(\omega - \Omega)$ and $A(\omega + \Omega)$. The measured triplet amplitudes were used to calculate the modulation index M and the parameter $G^{DN}(\varepsilon_s)$ from Eq. (3). The nonlinear parameters of the torsional and longitudinal elastic waves were determined by the following procedure. At the beginning of the experiment, the force applied to the sample was slowly increased until a plastic strain of $\varepsilon_s = (\Delta L/L_0) \sim 0.025$ (loading) was reached. After that, the force was slowly decreased to zero (unloading) and then increased again (repeated loading). Upon reaching the strain of $\varepsilon_s \sim 0.045$, the force applied to the sample was decreased to zero (repeated unloading) and then increased again (Figs. 4a and 5a). The measuring system was capable of creating static strains $\varepsilon_s \geq 0.4$ in the copper samples. However, as we noted above, upon reaching the static strain of $\varepsilon_s \sim 0.06$, the measurements were terminated for the following reasons. It was experimentally found that, for strains $\varepsilon_s \leq 0.06$, the static strain is uniform throughout the length of the sample and no anomalously high local strains (waists) are present. This circumstance simplifies the analysis of the experimental results. The nonlinear parameters of torsional and longitudinal waves, $G_{\text{tors}}^{DN}(\varepsilon_s)$ and $G_{\text{long}}^{DN}(\varepsilon_s)$, measured as functions of the static strain ε_s are shown in Figs. 4b and 5b. In these figures, curves *1–3* refer to loading of the sample; curves *1'* and *2'*, to unloading. At small values of ε_s, $G_{\text{tors}}^{DN}(\varepsilon_s) \approx 120$, which is four times as great as the parameter $G_{\text{long}}^{DN}(\varepsilon_s) \approx 30$. These values of the nonlinear parameters of torsional and longitudinal elastic waves in unstrained samples are several times higher than those for copper single crystals. The nonlinear acoustic parameter of copper single crystals is predominantly determined by the anharmonicity of the crystal lattice, and its value calculated from the data on the second- and third-order elastic coefficients borrowed from [21] is no greater than 10. The behavior of the nonlinear dynamic elastic parameters of torsional and longitudinal waves with increasing ε_s is noticeably different. The parameter
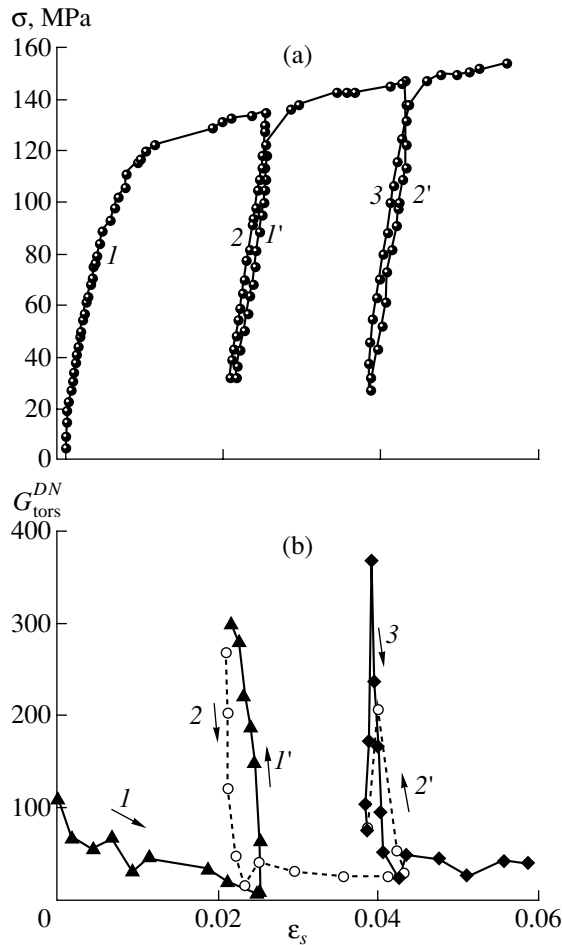
Fig. 4. (a) Stress–strain curve and (b) the nonlinear parameter of torsional elastic waves, $G_{\text{tors}}^{DN}(\varepsilon_s)$, versus the static strain.
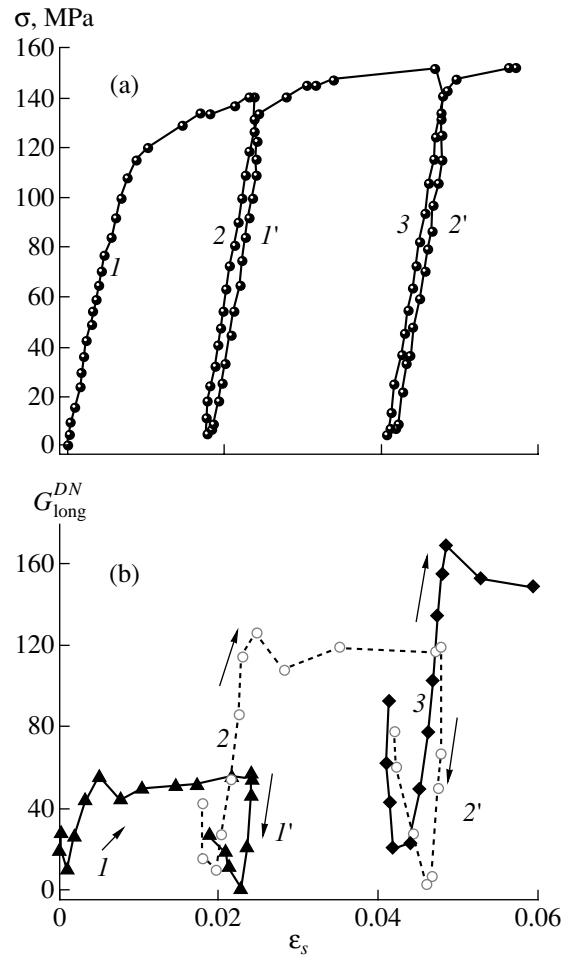
Fig. 5. (a) Stress–strain curve and (b) the nonlinear parameter of longitudinal elastic waves, $G_{\text{long}}^{DN}(\varepsilon_s)$, versus the static strain.

$G_{\text{tors}}^{DN}(\varepsilon_s)$ monotonically decreases whereas the longitudinal nonlinear parameter sharply increases reaching the value of $G_{\text{long}}^{DN}(\varepsilon_s) \sim 50$ at strains of $\varepsilon_s > 0.005$; with a further increase in strain, it remains constant within the measurement error. The behavior of the nonlinear parameters is also different in the unloading region. The nonlinear parameter of torsional waves sharply increases and reaches a value of $G_{\text{tors}}^{DN}(\varepsilon_s) \sim 300$, whereas $G_{\text{long}}^{DN}(\varepsilon_s)$ decreases. In the subsequent loading cycle, the nonlinear parameter $G_{\text{long}}^{DN}(\varepsilon_s)$ increases again, reaches a value of $G_{\text{long}}^{DN}(\varepsilon_s) \sim 120$ in the region of plastic strains, and remains constant until the subsequent unloading, in which the parameter $G_{\text{tors}}^{DN}(\varepsilon_s)$ increases and the parameter $G_{\text{long}}^{DN}(\varepsilon_s)$ decreases. In the region of the subsequent unloading–loading cycle, the situation is reproduced. This behavior of the nonlinear parame-

ters in the loading–unloading cycles indicates that the mechanisms of the dynamic nonlinearity of torsional and longitudinal elastic waves are different and are associated with changes in the samples' internal structure. As a result of plastic strain, dislocations and microcracks in the sample increase and microcrystalline grains fragmentize, which increases the area of intergrain boundaries. These effects are evidenced by microphotographs of the sample taken before and after it experienced the plastic strain (Fig. 6). As shown in Fig. 6a, the sample preparation process creates a columnar microstructure in the copper wire with ~10-μm grains in strips. After the plastic strain, the dimensions of the microcrystalline grains decreased to 5 μm (Fig. 6b). It should be noted that the crystallite dimensions are affected not only by the magnitude of the strain experienced by the sample but also by the number of unloading–loading cycles in the region of plastic strain, which increase the number of microcrystals and simultaneously reduce their dimensions [15, 16]. The loading–unloading cycle also changes the crack opening and the
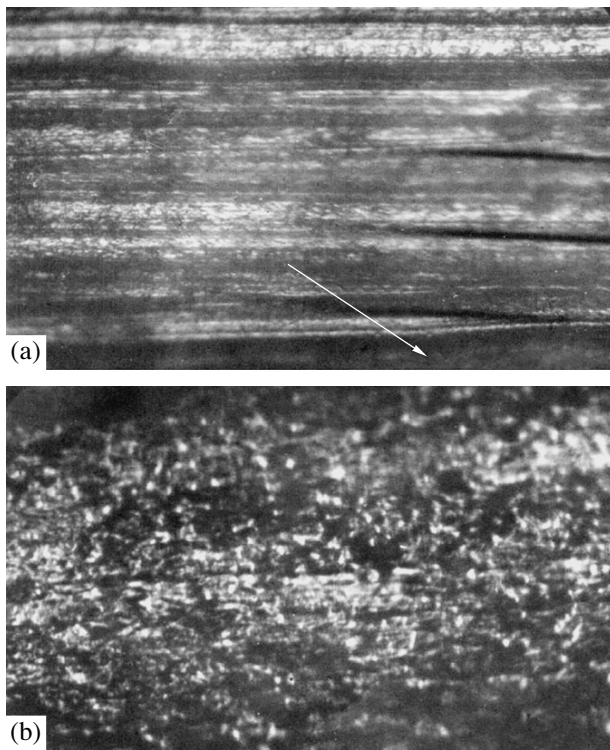
Fig. 6. Microphotographs of the samples under study (magnified by a factor of 140) (a) before and (b) after straining.

Fig. 7. Stress–strain curves $\sigma = \sigma(\varepsilon)$ for the (a) bilinear and (b) hysteretic media.

state of intergrain boundaries. These are the effects that change the nonlinear parameters $G_{\text{tors}}^{DN}(\varepsilon_s)$ and $G_{\text{long}}^{DN}(\varepsilon_s)$. A phenomenological description of the nonclassical nonlinearity in solids was proposed in [13, 22], where it was assumed that the equations of state for the normal and tangential (to the contacting boundaries) displacements in the elastic wave may be different. In the case under study, we consider the intergrain and microcrack boundaries as the contacting boundary. The strain normal to the interface was described in terms of the model of a bilinear medium, whose equation of state $\sigma = \sigma(\varepsilon)$ is a piecewise-linear function with a discontinuity at $\varepsilon = 0$ (Fig. 7a). As can be seen from this figure, when the strain amplitude ε_0 in the elastic wave is lower than the static strain ε_s at the boundary, i.e., the condition $\varepsilon_0 < |\varepsilon_s|$ is met, the medium is linear; when $\varepsilon_0 > |\varepsilon_s|$, the elastic properties of the medium are different for the loading and unloading phases, which causes the so-called clapping nonlinearity [13, 22]. At the strain $\varepsilon_s = 0$, the nonlinearity is maximal. For the shear elastic wave whose strain is parallel to the interface, a hysteretic equation of state $\sigma = \sigma(\varepsilon)$ (Fig. 7b) was proposed in [13, 22]. This equation was based on the fact that the friction force between the contacting surfaces caused by the shear strain does not exceed the static friction force $F_{\text{fric}} = kN$, where k is the friction coefficient and N is the normal pressure force that determines the pressure between the surfaces. In this situation, the motion of the

interfaces may consist of two phases. In the first phase, when, under the action of the elastic wave, the friction force between the contacting surfaces does not exceed the static friction force F_{fric}, the surfaces move together. In Fig. 7b, this phase corresponds to the sloping regions of the function $\sigma = \sigma(\varepsilon)$. In the second phase, when the friction force exceeds the static friction force F_{fric}, the contacting surfaces slide along each other, which corresponds to horizontal regions of the function $\sigma = \sigma(\varepsilon)$ (Fig. 7b). It is clear that, at a given strain amplitude $\varepsilon_0 > \varepsilon_i$ (ε_i is the strain at which the sliding phase begins), the area under the hysteresis curve $\sigma = \sigma(\varepsilon)$ depends on N, i.e., on the normal pressure force determining the pressure between the contacting surfaces σ_i in Fig. 7b and, hence, the magnitude of the hysteretic nonlinearity. When $\varepsilon_0 < \varepsilon_i$, the medium exhibits no hysteretic properties and remains linear. The equations of state $\sigma = \sigma(\varepsilon)$ (Fig. 7) qualitatively explain the behavior of the dynamic nonlinear parameters $G_{\text{tors}}^{DN}(\varepsilon_s)$ and $G_{\text{long}}^{DN}(\varepsilon_s)$ of the torsional and longitudinal elastic waves (Figs. 4b and 5b). With an increase in the static strain, the pressure between the contacting surfaces in the sample decreases, which enhances the clapping nonlinearity for the longitudinal elastic waves and suppresses the hysteretic nonlinearity of torsional elastic waves (Fig. 7). This effect increases $G_{\text{long}}^{DN}(\varepsilon_s)$ and reduces $G_{\text{tors}}^{DN}(\varepsilon_s)$. With a further strain increase in the sample's plastic strain region, the nonlinear acoustic parameters remain virtually unchanged (Figs. 4b and 5b), because the increase in the plastic strain does not noticeably

increase the stress in the samples (Figs. 4a and 4b); i.e., the pressure between the contacting surfaces remains virtually constant. Therefore, an increase in the static strain does not change the nonlinear parameters. The unloading increases the pressure between the contacting surfaces, which leads to a decrease in $G_{\text{tors}}^{DN}(\varepsilon_s)$ and an increase in $G_{\text{long}}^{DN}(\varepsilon_s)$. The unloading–loading cycles increase these parameters, because, as we noted above, an loading–unloading cycle reduces the crystallite dimensions and simultaneously increases the contacting area and, as a consequence, the number of elements that give rise to nonlinearity. In the next loading–unloading cycle, the above processes, which change the sample's internal structure, are repeated. As can be seen from Figs. 4b and 5b, there is an optimal pressure on the contacting boundaries at which the nonclassical nonlinearity is maximal. A similar effect was observed in [23, 24], where the amplitude of the second acoustic harmonic generated at the contacting boundary between two media was found to depend on the pressure across the contact. There, an optimum pressure at which the amplitude of this harmonic was maximal was also observed.

CONCLUSIONS

We presented an experimental study of the linear and nonlinear elastic properties of polycrystalline copper under elastoplastic strain with a continuous variation of internal structure caused by the external loading. The Young and shear moduli and the Poisson ratio were studied in the static strain interval of 0–0.06. The quasi-static and dynamic nonlinear acoustic parameters of the longitudinal and torsional elastic waves were measured. The dynamic nonlinear acoustic parameters were found to behave anomalously in the loading–unloading cycles in the plastic strain region. The experimental results were explained in terms of phenomenological equations of state for media with bimodular elasticity and media with hysteretic elasticity. It should be noted that the nonclassical nonlinearity is noticeably higher than the nonlinearity associated with dislocations in single crystals [21].

ACKNOWLEDGMENTS

REFERENCES

1. A. A. Gedroïts, L. K. Zarembo, and V. A. Krasil'nikov, Dokl. Akad. Nauk SSSR **150**, 515 (1963) [Sov. Phys. Dokl. **8**, 478 (1963)].

2. E. D. Murnaghan, *Finite Deformation of an Elastic Solid* (Wiley, New York, 1951).

3. L. K. Zarembo and V. A. Krasil'nikov, *Introduction to Nonlinear Acoustics* (Nauka, Moscow, 1966) [in Russian].

4. K. K. Ermilin, L. K. Zarembo, V. A. Krasil'nikov, *et al.*, Fiz. Met. Metalloved. **36** (3), 640 (1973).

5. L. K. Zarembo, V. A. Krasil'nikov, and I. É. Shkol'nik, Probl. Prochn., No. 11, 86 (1989).

6. K. A. Naugol'nykh and L. A. Ostrovskiĭ, *Nonlinear Wave Processes in Acoustics* (Nauka, Moscow, 1990) [in Russian].

7. R. Guyer and P. A. Johnston, Phys. Today, No. 4, 30 (1999).

8. I. B. Esipov, in *Proceedings of the Seminar of Scientific School by Professor S.A. Rybak, Moscow, 2001* (Moscow, 2001), p. 45.

9. L. K. Zarembo, V. A. Krasil'nikov, and I. É. Shkol'nik, Defektoskopiya **10**, 16 (1989).

10. O. V. Rudenko, Defektoskopiya, No. 8, 24 (1993).

11. S. A. Ambartsumyan, *Different-Modulus Theory of Elasticity* (Nauka, Moscow, 1982) [in Russian].

12. A. B. Lebedev, Fiz. Tverd. Tela **41** (7), 1214 (1999) [Phys. Solid State **41** (7), 1105 (1999)].

13. E. M. Ballad, B. A. Korshak, I. Yu. Solodov, *et al.*, in *Nonlinear Acoustics at the Beginning of the 21st Century,* Ed. by O. V. Rudenko and O. A. Sapozhnikov (Mosk. Gos. Univ., Moscow, 2002), Vol. 2, pp. 727–734.

14. I. B. Esipov, A. V. Fokin, and O. B. Ovchinnikov, in *Nonlinear Acoustics at the Beginning of the 21st Century,* Ed. by O. V. Rudenko and O. A. Sapozhnikov (Mosk. Gos. Univ., Moscow, 2002), Vol. 2, pp. 1189–1196.

15. O. A. Kaĭbashev and R. Z. Valiev, *Grain Boundaries and the Properties of Metals* (Metallurgiya, Moscow, 1987) [in Russian].

16. R. Z. Valiev and I. V. Aleksandrov, *Nanostructure Materials Obtained by Intense Plastic Deformation* (Logos, Moscow, 2000) [in Russian].

17. T. Meeker and A. Meitzler, in *Physical Acoustics: Principles and Methods*, Ed. by W. P. Mason (Academic, New York, 1964; Mir, Moscow, 1966), Vol. 1A.

18. A. I. Korobov, Yu. A. Brazhkin, and A. N. Ékonomov, Izmer. Tekh., No. 7, 48 (2000).

19. *Physical Quantities: A Handbook* (Énergoatomizdat, Moscow, 1991) [in Russian].

20. A. I. Korobov and A. N. Ékonomov, Akust. Zh. **48**, 640 (2002) [Acoust. Phys. **48**, 564 (2002)].

21. R. Truell, C. Elbaum, and B. B. Chick, *Ultrasonic Methods in Solid State Physics* (Academic, New York, 1969; Mir, Moscow, 1972).

22. N. Krohn, K. Prleider, R. Stoessel, *et al.*, in *Acoustical Imaging*, Ed. by W. Arnold and S. Hirsekorn (Kluver/Plenium, Dordrecht/New York, 2004), Vol. 27, pp. 91–98.

23. Ko Se Len, F. M. Severin, and I. Yu. Solodov, Akust. Zh. **37**, 1165 (1991) [Sov. Phys. Acoust. **37**, 610 (1991)].

24. O. V. Rudenko and Chin' An' Vu, Akust. Zh. **40**, 668 (1994) [Acoust. Phys. **40**, 593 (1994)].

Translated by A. Khzmalyan

Method for Solving the Problems of Multiple Scattering by Several Bodies in a Homogeneous Unbounded Medium

B. P. Sharfarets

Ul. Kubinskaya 14–70, St. Petersburg, 126128 Russia
e-mail: sharg@gmx.net
Received May 26, 2004

Abstract—A method is developed for solving problems of multiple scattering by an aggregate of bodies in a homogeneous unbounded medium. For this purpose, the problem on the multiple scattering produced by two bodies in the field of a plane wave is first considered under the assumption that the initial unperturbed scattering amplitudes of both scatterers are known. The solution is constructed by considering plane waves multiply rescattered by the scatterers. Integral equations are obtained that allow one to calculate the resulting scattering amplitude of each scatterer and the combined scattering amplitude of the system of two scatterers. It is shown that knowledge of the solution to this problem is sufficient to solve the problem on the scattering field of a system consisting of an arbitrary number of scatterers. Expressions for the scattering amplitude in the case of an arbitrary primary field are presented. The relationship between the integral equations describing the multiple scattering in a homogeneous space and the multiple scattering by a single scatterer located near an interface is demonstrated. Approximate expressions are given for calculating the scattering amplitude in the case of multiple scattering. © 2005 Pleiades Publishing, Inc.

Extensive literature is devoted to the problem of multiple scattering for the case of two or more scatterers illuminated by some primary field when the mutual effect of the scatterers (secondary rescattering effects) cannot be neglected. Some of these publications are included in the references [1–15]. Evidently, papers concerned with the problems of scattering caused by reflecting boundaries and inhomogeneities of the medium also refer to this subject. In this case, the presence of a single scatterer near an interface or an inhomogeneity of the medium is sufficient for the appearance of multiple scattering. Examples of such publications are papers [16–24].

In [1–15], a homogeneous space of two or three dimensions is considered with two or more scatterer illuminated by a certain primary wave. The solution is sought in the form of the sum of the primary wave and the fields produced by all of the scatterers under the assumption that all the required boundary conditions and the Sommerfeld radiation conditions at infinity are satisfied. The fields are represented as series expansions in spherical or cylindrical functions (depending on the dimension of the problem), and the unknown expansion coefficients in the expressions for the scattering fields are determined using either the *T*-matrix method [2, 6, 7, 10, 11, 13] or the addition theorems for spherical and cylindrical functions [4, 5, 8, 9]. From these coefficients, one can determine the individual scattering amplitudes of the scatterers. This approach automatically takes into account the effect of multiple scattering.

Interfaces also give rise to multiple scattering. For example, in [20], the problem on the scattering field of a sphere positioned near an acoustically soft plane boundary is considered. The problem is reduced to that of the multiple scattering by two spheres in a homogeneous space [8].

On the whole, despite the clarity of formalism, the above approach to the problem on multiple scattering by several bodies is not free of shortcomings. First, it generally requires calculating the countable set of unknown expansion coefficients of the scattered field. Second, the difficulty of this procedure drastically increases with the number of scatterers.

This paper suggests an alternative approach to the problem of multiple scattering by several bodies. The approach consists in considering the plane waves multiply reflected (rescattered) by the scatterers. The rescattered plane waves are taken into account using the unperturbed scattering amplitudes of each of the bodies, which yields the integral equations that allow calculating the perturbed scattering amplitudes from the unperturbed ones. A similar procedure was used earlier for calculating the fields scattered by distributed radiators and scatterers under the effect of interfaces and a layered inhomogeneity of the medium [25–27]. The sole limitation of this approach is the requirement that the unperturbed scattering amplitudes of the bodies must be known; however, this requirement is not excessive, because any scatterer is primarily characterized by its scattering amplitude in an unbounded medium in the absence of foreign bodies.

Let us consider the problem in the case of a three-dimensional unbounded medium. We begin with the simple special case of a single scatterer with its center at the point (x_0, y_0, z_0) in the primary field of a sound-transparent directional source located at the origin of coordinates. The field of the source is calculated by the formula [25]

$$u(\mathbf{x}) = \frac{i}{2\pi} \int_{R^2} \frac{D(\mathbf{k}_m)}{\alpha} \exp(i\mathbf{k}_m\mathbf{x}) dk_x dk_y, \quad m = 1, 2. \tag{1}$$

Here, $\mathbf{k}_1 = (k_x, k_y, \alpha)$ and $\mathbf{k}_2 = (k_x, k_y, -\alpha)$ are the conjugated wave vectors, $\alpha = (k^2 - k_x^2 - k_y^2)^{1/2}$, k is the wave number, $\mathbf{x} = (x, y, z)$, $m = 1$ corresponds to the field in the upper half-space $z \geq 0$ and $m = 2$ corresponds to the filed in the lower half-space $z \leq 0$, and $D(\mathbf{k}_m)$ is the directional pattern (DP) of the source in the whole (k_x, k_y) plane; this DP is related to the commonly used DP $\bar{D}(\theta, \varphi)$ in the circle $k_x^2 + k_y^2 \leq k^2$ (the visibility region) by the relationship (see, e.g., [25])

$$\left. \begin{array}{l} \bar{D}(\theta, \varphi) = D(\mathbf{k}_1) \\ \bar{D}(\pi - \theta, \varphi) = D(\mathbf{k}_2) \end{array} \right\} \quad \theta \in [0, \pi/2], \tag{2}$$

$$\varphi \in [0, 2\pi], \quad \alpha \in [k, 0].$$

Here, θ and φ are the angles of the spherical coordinate system, $\alpha = k\cos\theta$, $k_x = \xi\cos\varphi$, $k_y = \xi\sin\varphi$, $\xi = k\sin\theta$, and $\boldsymbol{\xi} = (k_x, k_y) = (\xi, \varphi)$ is the horizontal projection of the wave vector.

By analogy with the source, we characterize a scatterer by the function that describes its directional properties. This function $T_m^n(\mathbf{k}_l, \mathbf{k}_s)$, where $n, m = 1, 2$, of two vector variables $\mathbf{k}_l$ and $\mathbf{k}_s$, which are the wave vectors of the incident and scattered waves, respectively, is called the scattering amplitude (SA). Physically, this function describes the spectrum of plane waves $T_m^n(\mathbf{k}_l, \mathbf{k}_s)\exp(i\mathbf{k}_s\mathbf{x})$ excited by the scatterer centered at the origin of coordinates under the action of a unit-amplitude incident plane wave $\exp(i\mathbf{k}_l\mathbf{x})$ with a zero-valued phase at the scatterer's geometric center. The lower index $m = 1, 2$ specifies the propagation direction of the incident plane wave: $m = 1$ corresponds to the wave propagating in the direction of increasing z (i.e., upwards), and $m = 2$ corresponds to the wave propagating in the direction of decreasing z (i.e., downwards). The upper index n specifies the direction of scattering: $n = 1$ corresponds to the upward scattering $(+\alpha)$, and $n = 2$ corresponds to the downward scattering $(-\alpha)$. The domain of definition of this function includes the regions inside and outside the visibility region. Note that the scatterer centered at the point $\mathbf{x}_0 = (x_0, y_0, z_0)$ and driven by a plane incident wave $A\exp(i\mathbf{k}\mathbf{x})$, where $A = \text{const}$, generates a plane wave spectrum $A\exp(i\mathbf{k}_l\mathbf{x})T_m^n(\mathbf{k}_l, \mathbf{k}_s)\exp(i\mathbf{k}_s(\mathbf{x} - \mathbf{x}_0))$.

For a scatterer whose center is located at the point $\mathbf{x}_0$ and whose SA is known, the scattered field u_s is described by an expression similar to Eq. (1) [25]:

$$u_s(\mathbf{x}, \mathbf{k}_l) = \frac{i}{2\pi} \int_{R^2} \frac{T_m^n(\mathbf{k}_l, \mathbf{k}_s)}{\alpha_s} \tag{3}$$

$$\times \exp(i\mathbf{k}_s(\mathbf{x} - \mathbf{x}_0)) dk_{sx} dk_{sy}.$$

This expression can be used to determine the SA mathematically; namely, the SA of the scatterer centered at the point $\mathbf{x}_0$ and driven by the incident unit-amplitude plane wave $\exp(i\mathbf{k}_l(\mathbf{x} - \mathbf{x}_0))$ with zero-valued phase at the scatterer's center $\mathbf{x}_0$ is the corresponding spectrum of scattered plane waves with zero-valued phases at the scatterer's center, as given by the scattered field representation (3). As it will be seen from Eqs. (5)–(7), the SA in the spherical coordinate system coincides with the geometrical optics amplitude of the scattered field (3) calculated from the zero-order transfer equation.

If the primary field of the type given by Eq. (1) is created by a directional source (i.e., if it is representable as a set of plane waves) whose center falls at the origin of coordinates and the scatterer is located at the point (x_0, y_0, z_0), the resulting SA $\bar{T}_n(\mathbf{k}_s, \mathbf{x}_0)$ can be determined using the technique given in [25]. As a result, we obtain

$$\bar{T}_n(\mathbf{k}_s, \mathbf{x}_0) = \frac{i}{2\pi} \int_{R^2} \frac{D(\mathbf{k}_l)T_m^n(\mathbf{k}_l, \mathbf{k}_s)}{\alpha_l} \tag{4}$$

$$\times \exp(i\mathbf{k}_l\mathbf{x}_0) dk_{lx} dk_{ly}, \quad n = 1, 2.$$

The integral in Eq. (4) can be asymptotically evaluated as in [25]. This estimate has the form

$$\bar{T}'(R_0, \theta_0, \varphi_0, \theta_s, \varphi_s)$$

$$= \frac{\exp(ikR_0)}{R_0} \sum_{l=0}^{\infty} \frac{A_l(\theta_0, \varphi_0, \theta_s, \varphi_s)}{(kR_0)^l}, \tag{5}$$

$$A_{l+1}(\theta_0, \varphi_0, \theta_s, \varphi_s)$$

$$= L[A_l(\theta_0, \varphi_0, \theta_s, \varphi_s)](\theta_0, \varphi_0, l), \tag{6}$$

$$A_0(\theta_0, \varphi_0, \theta_s, \varphi_s)$$

$$= \bar{D}(\theta_0, \varphi_0)T'(\theta_0, \varphi_0, \theta_s, \varphi_s). \tag{7}$$

Here, L is the operator defined by the expression

$$L[\Psi](\theta, \varphi, l) = \left(\frac{\Delta_{\theta, \varphi} + l(l+1)}{2i(l+1)}\right)\Psi(\theta, \varphi); \tag{8}$$

$\bar{T}'$ and T' are the resulting and unperturbed SAs in the spherical coordinate system, respectively; $(R_0, \theta_0, \varphi_0)$ are the spherical coordinates of the point (x_0, y_0, z_0); $(R_s, \theta_s, \varphi_s)$ are the spherical coordinates in the spherical coordinate system with origin at the point (x_0, y_0, z_0)

(scatterer's center); and $\Delta_{\theta, \varphi}$ is the spherical Beltrami operator (the angular part of the Laplace operator).

Representations (5)–(8) offer a possibility to analyze the errors in calculating the actual SA in the form of a finite sum. In the Fraunhofer zone, it is sufficient to use the zero-order approximation:

$$\bar{T}'(R_0, \theta_0, \varphi_0, \theta_s, \varphi_s)$$
$$= \frac{\exp(ikR_0)}{R_0} \bar{D}(\theta_0, \varphi_0) T'(\theta_0, \varphi_0, \theta_s, \varphi_s) + O\left(\frac{1}{kR_0^2}\right), \quad (9)$$

which corresponds to the idea that the source field at the scatterer point is representable in the form of the weighted plane wave $\dfrac{\bar{D}(\theta_0, \varphi_0)}{R_0} \exp(ikR_0)$.

The combined field of a scatterer with SA in the form of Eq. (4) must be calculated by Eq. (3) after replacing SA $T_m^n(\mathbf{k}_l, \mathbf{k}_s)$ with SA (4) and fixing the origin at the scatterer's center. As a result, we obtain the geometrical optics representation similar to Eqs. (5)–(7). This procedure remains also valid for the zero-order approximation (9), for which the scattered field in the form of Eqs. (5)–(7) is given by the formulas

$$u_s(R_s, \theta_s, \varphi_s) = \frac{\exp(ikR_0)}{R_0}$$
$$\times \frac{\exp(ikR_s)}{R_s} \sum_{l=0}^{\infty} \frac{A_l(\theta_s, \varphi_s)}{(kR_s)^l}, \quad (10)$$

$$A_{l+1}(\theta_s, \varphi_s) = L[A_l(\theta_s, \varphi_s)](\theta_s, \varphi_s, l), \quad (11)$$

$$A_0(\theta_s, \varphi_s) = \bar{D}(\theta_0, \varphi_0) T'(\theta_0, \varphi_0, \theta_s, \varphi_s). \quad (12)$$

If we again restrict our consideration to the zero-order approximation in Eqs. (10)–(12), we arrive at the ray version of scattering. Namely, a ray launched from the directional source toward the scatterer at angles θ_0, φ_0 in the source coordinate system is weighted with its directional pattern $\bar{D}(\theta_0, \varphi_0)$; reaching the scatterer at the point $(R_0, \theta_0, \varphi_0)$, it is reflected at angles θ_s, φ_s relative to scatterer and weighted with its SA; when this ray reaches the point $(R_s, \theta_s, \varphi_s)$ in the scatterer coordinate system, the corresponding amplitude is given by the term of series (10) with index $l = 0$.

Consider now the case when two scatterers S_1 and S_2 characterized by the corresponding unperturbed (without the crosstalk effects) SAs, $^1T_m^n(\mathbf{k}_l, \mathbf{k}_s)$ and $^2T_m^n(\mathbf{k}_l, \mathbf{k}_s)$, are located in a homogeneous half-space. Let the center of the first scatterer be located at the point $\left(0, 0, -\dfrac{z_0}{2}\right)$ and the center of the second scatterer, at the point $\left(0, 0, \dfrac{z_0}{2}\right)$.

For definiteness, we consider the combined scattering field under the assumption that this pair of scatterers is illuminated by a plane wave $\exp(i\mathbf{k}_l\mathbf{x})$ propagating in the direction of increasing z, i.e., in the upward direction. We seek the field by summing multiply scattered plane waves (the superposition principle is appropriate here, because every plane wave generates its own set of scattered waves, which, being combined with the incident wave, ensure the fulfillment of the boundary conditions at every scatterer; this consideration holds for all pairs of plane waves and the corresponding scattered waves). In addition, we note that such a solution is unique by virtue of the uniqueness of all terms constituting the solution, beginning from primarily scattered fields, which is a consequence of the choice of appropriate Sommerfeld radiation conditions.

Let us denote the resulting SAs that take into account all multiple reflections by $^1\bar{T}_1^n(\mathbf{k}_l, \mathbf{k}_s)$ and $^2\bar{T}_1^n(\mathbf{k}_l, \mathbf{k}_s)$ and consider, for example, the formation of the resulting SA of scatterer S_1 in the upper hemisphere, i.e., $^1\bar{T}_1^1(\mathbf{k}_l, \mathbf{k}_s)$. The process is as follows. The plane wave $\exp(i\mathbf{k}_l\mathbf{x})$ traveling through scatterers S_1 and S_2 causes them to excite primary scattering fields with respective SAs $^1T_1^n(\mathbf{k}_l, \mathbf{k}_s)\exp\left(-i\alpha_l\dfrac{z_0}{2}\right)$ and $^2T_1^n(\mathbf{k}_l, \mathbf{k}_s)\exp\left(i\alpha_l\dfrac{z_0}{2}\right)$, and precisely these fields will affect the formation of the desired resulting SA $^1\bar{T}_1^1(\mathbf{k}_l, \mathbf{k}_s)$ (the factors $\exp\left(\pm i\alpha_l\dfrac{z_0}{2}\right)$ correspond to the plane wave phases at the sites of the scatterers S_2 and S_1, respectively). We explain this fact by the example of the primarily scattered field $^1T_1^1(\mathbf{k}_l, \mathbf{k}_s)\exp\left(-i\alpha_l\dfrac{z_0}{2}\right)$. This field is produced by the plane wave incident on scatterer S_1. It propagates in the upward direction, reaches scatterer S_2, where it is rereflected; then, the rereflected field propagates in the downward direction and is rereflected from scatterer S_1, thus generating the first correction to the SA; this rereflected field again propagates in the upward direction, and so forth to infinity. The result of this process is the component $^1_1\bar{T}_1^1(\mathbf{k}_l, \mathbf{k}_s)$ of the resulting SA $^1\bar{T}_1^1(\mathbf{k}_l, \mathbf{k}_s)$, which is caused by the field primarily scattered by scatterer S_1 with SA $^1T_1^1(\mathbf{k}_l, \mathbf{k}_s)\exp\left(-i\alpha_l\dfrac{z_0}{2}\right)$. The component $^1_2\bar{T}_1^1(\mathbf{k}_l, \mathbf{k}_s)$ of the resulting SA $^1\bar{T}_1^1(\mathbf{k}_l, \mathbf{k}_s)$ that is caused by the field $^2T_1^2(\mathbf{k}_l, \mathbf{k}_s)\exp\left(i\alpha_l\dfrac{z_0}{2}\right)$ primarily scattered by scatterer S_2 is formed in a similar way: the field $^2T_1^2(\mathbf{k}_l, \mathbf{k}_s)\exp\left(i\alpha_l\dfrac{z_0}{2}\right)$ primarily scattered by scatterer S_2 will propagate in the downward direction and will be

rereflected from scatterer S_1, thus generating the first correction to $_2^1\overline{T}_1^1(\mathbf{k}_l, \mathbf{k}_s)$; then, the rereflected field will propagate in the upward direction, will again be rereflected from S_2, and so forth to infinity. Thus, we have to calculate the sum

$$^1\overline{T}_1^1(\mathbf{k}_l, \mathbf{k}_s) = {}_1^1\overline{T}_1^1(\mathbf{k}_l, \mathbf{k}_s) + {}_2^1\overline{T}_1^1(\mathbf{k}_l, \mathbf{k}_s). \tag{13}$$

Calculating the secondary SAs by Eq. (4) and proceeding according to the procedure used in the case when the interface played the role of the second scatterer (in that case, the reflection coefficient served as the SA of the interface [25]), we obtain the following representations:

$$\frac{_1^1\overline{T}_1^1(\mathbf{k}_l, \mathbf{k}_s)}{\exp(-i\alpha_l z_0/2)} = \sum_{n=0}^{\infty} (A_1^1)^n [^1T_1^1](\mathbf{k}_l, \mathbf{k}_s) \tag{14}$$
$$= (I - A_1^1)^{-1} [^1T_1^1](\mathbf{k}_l, \mathbf{k}_s),$$

$$_2^1\overline{T}_1^1(\mathbf{k}_l, \mathbf{k}_s) = \sum_{n=0}^{\infty} (A_1^1)^n [^1\hat{T}_1^1](\mathbf{k}_l, \mathbf{k}_s) \tag{15}$$
$$= (I - A_1^1)^{-1} [^1\hat{T}_1^1](\mathbf{k}_l, \mathbf{k}_s),$$

where $^1\hat{T}_1^1(\mathbf{k}_l, \mathbf{k}_s)$ is determined by the expression

$$^1\hat{T}_1^1(\mathbf{k}_l, \mathbf{k}_s) = \exp\left(i\alpha_l\frac{z_0}{2}\right)\frac{i}{2\pi}$$
$$\times \int_{R^2} \frac{[^2T_1^1(\mathbf{k}_l, \mathbf{k}_n)][^1T_2^1(\mathbf{k}_n, \mathbf{k}_s)]}{\alpha_n} \exp(i\alpha_n z_0) dk_{nx}dk_{ny}, \tag{16}$$

and operator A_1^1 is defined as

$$A_1^1[T](\mathbf{k}_l, \mathbf{k}_s) = \left(\frac{i}{2\pi}\right)^2$$
$$\times \int_{R^2}\left(\int_{R^2} \frac{^2T_1^2(\mathbf{k}_n, \mathbf{k}_m)T(\mathbf{k}_l, \mathbf{k}_n)}{\alpha_n} \exp(i\alpha_n z_0) dk_{nx}dk_{ny}\right) \tag{17}$$
$$\times \frac{^1T_2^1(\mathbf{k}_m, \mathbf{k}_s)}{\alpha_m} \exp(i\alpha_m z_0) dk_{mx}dk_{my}.$$

As it is seen from Eq. (17), operator A_1^1 calculates the one-cycle correction to the SA $^1\overline{T}_1^1(\mathbf{k}_l, \mathbf{k}_s)$; namely, the wave scattered by scatterer S_1 reaches scatterer S_2, is rereflected in the backward direction, reaches scatterer S_1, and adds the next increment to the SA $^1\overline{T}_1^1(\mathbf{k}_l, \mathbf{k}_s)$. We note that series (14) and (15) truncated to a finite number of terms can be used to approximately calculate the components of the SA.

Formally, the Neumann series (14) and (15) converge if the norm of operator (17) is less then unity. However, physically, it is clear that the corresponding components of the resulting SA form precisely the series of type (14) and (15) according to the construction of the unique solution; indeed, these series reflect the physics of the formation of the resulting SA and represent the solution alternative to that described in [1–15]. This inference must hold even in the presence of resonance phenomena in single and multiple scattering [9, 13].

If series (14) and (15) converge, we can invert operator $(I - A_1^1)^{-1}$ according to the standard procedure. As a result, we obtain integral equations for the components of the resulting SA $^1\overline{T}_1^1(\mathbf{k}_l, \mathbf{k}_s)$:

$$(I - A_1^1)[^1_1\overline{T}_1^1](\mathbf{k}_l, \mathbf{k}_s) = {}^1T_1^1(\mathbf{k}_l, \mathbf{k}_s)\exp\left(-i\alpha_l\frac{z_0}{2}\right), \tag{18}$$

$$(I - A_1^1)[^1_2\overline{T}_1^1](\mathbf{k}_l, \mathbf{k}_s) = {}^1\hat{T}_1^1(\mathbf{k}_l, \mathbf{k}_s), \tag{19}$$

where operator A_1^1 is defined in Eq. (17).

Note that, having determined the resulting SA $^1\overline{T}_1^1(\mathbf{k}_l, \mathbf{k}_s)$ of scatterer S_1, we can easily obtain the resulting SA $^2\overline{T}_1^1(\mathbf{k}_l, \mathbf{k}_s)$ of scatterer S_2. It is easy to understand that this can be done by adding the primary component $^2T_1^1(\mathbf{k}_l, \mathbf{k}_s)\exp\left(i\alpha_l\frac{z_0}{2}\right)$ caused by the incidence of the primary plane wave with the component caused by the scattering of the combined scattering field of scatterer S_1 with the resulting SA $^1\overline{T}_1^1(\mathbf{k}_l, \mathbf{k}_s)$ by scatterer S_2. In the final form, we have

$$^2\overline{T}_1^1(\mathbf{k}_l, \mathbf{k}_s) = {}^2T_1^1(\mathbf{k}_l, \mathbf{k}_s)\exp\left(i\alpha_l\frac{z_0}{2}\right)$$
$$+ \frac{1}{2\pi}\int_{R^2} \frac{^2T_1^1(\mathbf{k}_m, \mathbf{k}_s)\,^1\overline{T}_1^1(\mathbf{k}_l, \mathbf{k}_n)}{\alpha_n} \exp(i\alpha_n z_0) dk_{nx}dk_{ny}. \tag{20}$$

Proceeding in a similar way, we find the corresponding integral equations for components $_1^2\overline{T}_1^2(\mathbf{k}_l, \mathbf{k}_s)$ and $_2^2\overline{T}_1^2(\mathbf{k}_l, \mathbf{k}_s)$ of the resulting SA,

$$^2\overline{T}_1^2(\mathbf{k}_l, \mathbf{k}_s) = {}_1^2\overline{T}_1^2(\mathbf{k}_l, \mathbf{k}_s) + {}_2^2\overline{T}_1^2(\mathbf{k}_l, \mathbf{k}_s), \tag{21}$$

of scatterer S_2 in the lower half-space. These equations have the form

$$(I - A_2^2)[^2_1\overline{T}_1^2](\mathbf{k}_l, \mathbf{k}_s) = {}^2T_1^2(\mathbf{k}_l, \mathbf{k}_s)\exp\left(i\alpha_l\frac{z_0}{2}\right), \tag{22}$$

$$(I - A_2^2)[^2_2\overline{T}_1^2](\mathbf{k}_l, \mathbf{k}_s) = {}^2\hat{T}_1^2(\mathbf{k}_l, \mathbf{k}_s), \tag{23}$$

where $^2\hat{T}_1^2(\mathbf{k}_l, \mathbf{k}_s)$ is defined by the expression

$$^2\hat{T}_1^2(\mathbf{k}_l, \mathbf{k}_s) = \exp\left(-i\alpha_l\frac{z_0}{2}\right)\frac{i}{2\pi}$$

$$\times \int\limits_{R^2}\frac{[^2T_1^2(\mathbf{k}_n, \mathbf{k}_s)][^1T_1^1(\mathbf{k}_l, \mathbf{k}_n)]}{\alpha_n}\exp(i\alpha_n z_0)dk_{nx}dk_{ny}$$

and operator $A_2^2[T](\mathbf{k}_l, \mathbf{k}_s)$ is given by the formula

$$A_2^2[T](\mathbf{k}_l, \mathbf{k}_s) = \left(\frac{i}{2\pi}\right)^2$$

$$\times \iint\limits_{R^2}\left(\int\limits_{R^2}\frac{^1T_2^1(\mathbf{k}_n, \mathbf{k}_m)T(\mathbf{k}_l, \mathbf{k}_n)}{\alpha_n}\exp(i\alpha_n z_0)dk_{nx}dk_{ny}\right) \quad (24)$$

$$\times \frac{^2T_1^2(\mathbf{k}_m, \mathbf{k}_s)}{\alpha_m}\exp(i\alpha_m z_0)dk_{mx}dk_{my}.$$

The resulting SA of scatterer S_1 in the lower half-space is determined by the expression

$$^1\overline{T}_1^2(\mathbf{k}_l, \mathbf{k}_s) = {}^1T_1^2(\mathbf{k}_l, \mathbf{k}_s)\exp\left(-i\alpha_l\frac{z_0}{2}\right)$$

$$+ \frac{i}{2\pi}\int\limits_{R^2}\frac{[^1T_2^2(\mathbf{k}_n, \mathbf{k}_s)][^2\overline{T}_1^2(\mathbf{k}_l, \mathbf{k}_n)]}{\alpha_n}\exp(i\alpha_n z_0)dk_{nx}dk_{ny}. \quad (25)$$

Now, let the primary wave propagate in the downward direction. In this case, Eqs. (13)–(25) remain valid with the following modifications. The primary fields will be $^1T_2^n(\mathbf{k}_l, \mathbf{k}_s)\exp\left(i\alpha_l\frac{z_0}{2}\right)$ and $^2T_2^n(\mathbf{k}_l, \mathbf{k}_s)\exp\left(-i\alpha_l\frac{z_0}{2}\right)$, respectively. In addition, in Eqs. (13)–(25), the right-hand subscript 1 should be replaced by 2 in all expressions for the SAs dependent on $\mathbf{k}_l$ and the sign of the exponents involving α_l should be changed. All other notations and expressions remain intact. As a result, Eqs. (22) and (23) take the form

$$(I - A_2^2)[^2_1\overline{T}_2^2](\mathbf{k}_l, \mathbf{k}_s) = {}^2T_2^2(\mathbf{k}_l, \mathbf{k}_s)\exp\left(-i\alpha_l\frac{z_0}{2}\right), \quad (22a)$$

$$(I - A_2^2)[^2_2\overline{T}_2^2](\mathbf{k}_l, \mathbf{k}_s) = {}^2\hat{T}_2^2(\mathbf{k}_l, \mathbf{k}_s). \quad (23a)$$

Thus, we obtained all expressions required for determining the resulting SAs of two scatterers $^1\overline{T}_l^n(\mathbf{k}_l, \mathbf{k}_s)$ and $^2\overline{T}_l^n(\mathbf{k}_l, \mathbf{k}_s)$, where $l, n = 1, 2$. These expressions are useful, for example, for estimating the degree of perturbation of the unperturbed SAs.

However, if perturbation of the SAs cannot be neglected, the combined SA of the system of a pair of scatterers may appear to be a more informative quantity. Such a quantity can be easily obtained from Eq. (3)

using the superposition principle. The corresponding final expression for the combined SA $\overline{T}_l^n(\mathbf{k}_l, \mathbf{k}_s)$ has the form

$$\left.\begin{aligned}\overline{T}_l^1(\mathbf{k}_l, \mathbf{k}_s) &= {}^1\overline{T}_l^1(\mathbf{k}_l, \mathbf{k}_s)\exp\left(i\alpha_s\frac{z_0}{2}\right)\\ &+ {}^2\overline{T}_l^1(\mathbf{k}_l, \mathbf{k}_s)\exp\left(-i\alpha_s\frac{z_0}{2}\right)\\ \overline{T}_l^2(\mathbf{k}_l, \mathbf{k}_s) &= {}^1\overline{T}_l^2(\mathbf{k}_l, \mathbf{k}_s)\exp\left(-i\alpha_s\frac{z_0}{2}\right)\\ &+ {}^2\overline{T}_l^2(\mathbf{k}_l, \mathbf{k}_s)\exp\left(i\alpha_s\frac{z_0}{2}\right)\end{aligned}\right\}, \quad l = 1, 2. \quad (26)$$

Substituting Eq. (26) either in Eq. (4) or in Eqs. (5)–(7), one can calculate the combined SA of the system of scatterers illuminated by the directional source generating the field given by Eq. (1). It is clear that the center of the system of scatterers is located at the center of the segment connecting the centers of both scatterers.

The ability to calculate the combined SA $\overline{T}_l^n(\mathbf{k}_l, \mathbf{k}_s)$ of the system of a pair of scatterers allows one to construct a solution to the problem with N scatterers. The process is as follows. First, we consider the system of two scatterers, determine their combined SA, and replace both scatterers with one fictitious scatterer characterized by the combined SA and the center lying at the center of the segment connecting the centers of both scatterers. Then, we consider the system consisting of the third scatterer and the above fictitious scatterer, determine their combined AP, and so forth until all scatterers are used and the combined SA of all N scatterers is determined. The validity of the above iterative procedure follows from the superposition principle.

Below, we consider several special cases. It is of interest to use the above expressions for deriving the results obtained earlier [25, 26] for the case when one of the scatterers is a reflecting plane (a plane interface) whose SA is calculated in Appendix 1. Substituting Eq. (A1) for the SA of the reflecting plane $T_1^2(\mathbf{k}_l, \mathbf{k}_s)$ into Eqs. (16)–(20), we obtain the integral equations given in [25, 26] for the case of a scatterer near a reflecting boundary.

Now, let us consider the case when the plane wave is incident on a system consisting, as before, of two scatterers. Here, we limit our consideration to the situation when the assumption is valid that every scatterer is located in the Fraunhofer zone of the other scatterer. In this case, we can use Eq. (9) to calculate the SA of the scatterer illuminated by the field scattered by the other scatterer and then calculate the resulting SAs. For generality, we assume that the centers of scatterers are located at points $\mathbf{r}_1$ and $\mathbf{r}_2$ relative to the origin of coordinates.

The plane primary wave traveling upward will cause scatterers S_1 and S_2 to excite two unperturbed scattered fields with respective SAs ${}^1T'(\theta_l, \varphi_l, \theta_{1s}, \varphi_{1s})\exp(i\mathbf{k}_1\mathbf{r}_1)$ and ${}^2T'(\theta_l, \varphi_l, \theta_{2s}, \varphi_{2s})\exp(i\mathbf{k}_1\mathbf{r}_2)$ (we use here spherical coordinates, and θ_{1s}, φ_{1s}, and θ_{2s}, φ_{2s} are the spherical angles measured relative to the scatterer's centers). As was shown earlier, both these initially scattered fields participate in the formation of the resulting field scattered by each of the scatterers. Let us derive the approximate expression for ${}^1\overline{T}'(\theta_l, \varphi_l, \theta_{1s}, \varphi_{1s})$, $\theta_{1s} \in \left[0, \dfrac{\pi}{2}\right]$, as an example. One can easily see that, in this case, such a calculation consists of summing two geometric progressions for the components ${}^1\overline{T}' = {}^1_1\overline{T}' + {}^1_2\overline{T}'$:

$$
{}^1_mT'(\theta_l, \varphi_l, \theta_{1s}, \varphi_{1s}) = \sum_{m=0}^{\infty} a_{0l}q^m, \quad l = 1, 2, \tag{27}
$$

$$
a_{01} = {}^1T'(\theta_l, \varphi_l, \theta_{1s}, \varphi_{1s})\exp(i\mathbf{k}_1\mathbf{r}_1);
$$

$$
a_{02} = \exp(i\mathbf{k}_1\mathbf{r}_2)[{}^2T'(\theta_1, \varphi_l, \theta_{(2-1)s}, \varphi_{(2-1)s})]
$$
$$
\times[{}^1T'(\theta_{1l} = \theta_{(2-1)s}, \varphi_{1l} = \varphi_{(2-1)s}, \theta_{1s}, \varphi_{1s})] \tag{28}
$$
$$
\times\frac{\exp(ik|\mathbf{r}_1 - \mathbf{r}_2|)}{|\mathbf{r}_1 - \mathbf{r}_2|};
$$

$$
q = \left(\frac{\exp(ik|\mathbf{r}_1 - \mathbf{r}_2|)}{|\mathbf{r}_1 - \mathbf{r}_2|}\right)^2
$$
$$
\times[{}^1T'(\theta_{1l} = \theta_{(2-1)s}, \varphi_{1l} = \varphi_{(2-1)s}, \theta_{1s}, \varphi_{1s})]
$$
$$
\times[{}^2T'(\theta_{2l} = \theta_{(1-2)s}, \varphi_{2l} = \varphi_{(1-2)s}, \tag{29}
$$
$$
\theta_{2s} = \theta_{(2-1)s}, \varphi_{2s} = \varphi_{(2-1)s})].
$$

Here, $(\theta_{(1-2)s}, \varphi_{(1-2)s})$ and $(\theta_{(2-1)s}, \varphi_{(2-1)s})$ are the angular coordinates of the center of the second scatterer relative to the center of the first scatterer and those of the center of the first scatterer relative to the center of the second one, respectively. Assuming that the condition $|q| < 1$ holds, we obtain the expression for the resulting SA:

$$
{}^1\overline{T}'(\theta_l, \varphi_l, \theta_{1s}, \varphi_{1s}) = \frac{a_{01} + a_{02}}{1 - q}, \quad \theta_{1s} \in \left[0, \frac{\pi}{2}\right]. \tag{30}
$$

Using Eq. (20), we obtain the expression for $\theta_{2s} \in \left[0, \dfrac{\pi}{2}\right]$:

$$
{}^2\overline{T}'(\theta_l, \varphi_l, \theta_{2s}, \varphi_{2s}) = {}^2T'(\theta_l, \varphi_l, \theta_{2s}, \varphi_{2s})\exp(i\mathbf{k}_1\mathbf{r}_2)
$$
$$
+ [{}^2T'(\theta_{2l} = \theta_{(1-2)s}, \varphi_{2l} = \varphi_{(1-2)s}, \theta_{2s}, \varphi_{2s})]
$$
$$
\times[{}^1\overline{T}'(\theta_l, \varphi_l, \theta_{1s} = \theta_{(1-2)s}, \varphi_{1s} = \varphi_{(1-2)s})] \tag{31}
$$
$$
\times\frac{\exp(ik|\mathbf{r}_1 - \mathbf{r}_2|)}{|\mathbf{r}_1 - \mathbf{r}_2|}.
$$

Expressions (30) and (31) assume that $\varphi_{1s}, \varphi_{2s} \in [0, 2\pi]$. The resulting SAs in the remainder of the domain of definition $\theta_s \in \left[\dfrac{\pi}{2}, \pi\right]$, $\varphi_s \in [0, 2\pi]$ are determined similarly:

$$
{}^2\overline{T}'(\theta_l, \varphi_l, \theta_{2s}, \varphi_{2s}) = \frac{\tilde{a}_{01} + \tilde{a}_{02}}{1 - \tilde{q}}, \tag{32}
$$

$$
{}^1\overline{T}'(\theta_l, \varphi_l, \theta_{1s}, \varphi_{1s}) = {}^1T'(\theta_l, \varphi_l, \theta_{1s}, \varphi_{1s})\exp(i\mathbf{k}_1\mathbf{r}_1)
$$
$$
+ [{}^1T'(\theta_{1l} = \theta_{(2-1)s}, \varphi_{1l} = \varphi_{(2-1)s}, \theta_{1s}, \varphi_s)] \tag{33}
$$
$$
\times[{}^2\overline{T}'(\theta_l, \varphi_l, \theta_{2s} = \theta_{(2-1)s}, \varphi_{2s} = \varphi_{(2-1)s})]
$$
$$
\times\frac{\exp(ik|\mathbf{r}_1 - \mathbf{r}_2|)}{|\mathbf{r}_1 - \mathbf{r}_2|}.
$$

Here,

$$
\tilde{q} = \left(\frac{\exp(ik|\mathbf{r}_1 - \mathbf{r}_2|)}{|\mathbf{r}_1 - \mathbf{r}_2|}\right)^2[{}^1T'(\theta_{1l} = \theta_{(2-1)s},
$$
$$
\varphi_{1l} = \varphi_{(2-1)s}, \theta_{1s} = \theta_{(1-2)s}, \varphi_{1s} = \varphi_{(1-2)s})] \tag{34}
$$
$$
\times[{}^2T'(\theta_{2l} = \theta_{(1-2)l}, \varphi_{2l} = \varphi_{(1-2)l}, \theta_{2s}, \varphi_{2s})];
$$

$$
\tilde{a}_{01} = {}^2T'(\theta_l, \varphi_l, \theta_{2s}, \varphi_{2s})\exp(i\mathbf{k}_1\mathbf{r}_2); \tag{35}
$$

$$
\tilde{a}_{02} = \exp(i\mathbf{k}_1\mathbf{r}_1)
$$
$$
\times[{}^2T'(\theta_{2l} = \theta_{(1-2)s}, \varphi_{2l} = \varphi_{(1-2)s}, \theta_{2s}, \varphi_{2s})]
$$
$$
\times[{}^1T'(\theta_l, \varphi_l, \theta_{1s} = \theta_{(1-2)s}, \varphi_{1s} = \varphi_{(1-2)s})] \tag{36}
$$
$$
\times\frac{\exp(ik|\mathbf{r}_1 - \mathbf{r}_2|)}{|\mathbf{r}_1 - \mathbf{r}_2|}.
$$

Note that the first terms in the numerators of Eqs. (30) and (32) are the corresponding unperturbed SAs weighted with phase factors. In the case of the plane wave incident on the scatterers in the downward direction, the corresponding expressions can be obtained from Eqs. (27)–(36) by replacing $\mathbf{k}_1$ with $\mathbf{k}_2$ in all exponential factors.

Let C be the center of the segment connecting the scatterer's centers and R_1, R_2, and R_C be the distances to the observation point measured from the centers of the first and second scatterers and from the point C, respectively. Then, under the condition that $R_1, R_2, R_C \gg |\mathbf{r}_2 - \mathbf{r}_1|$, we have $\theta_{1s} \approx \theta_{2s} \approx \theta_s$, $\varphi_{1s} \approx \varphi_{2s} \approx \varphi_s$, and the scattering field of the mth scatterer is given by the formula

$$
u_{ms} \approx ({}^m\overline{T}'(\theta_i, \varphi_i, \theta_s, \varphi_s)\exp(-ik\hat{\mathbf{R}}_C\overline{\mathbf{r}}_m)
$$
$$
\times\frac{\exp(ikR_C)}{R_C}, \quad m = 1, 2. \tag{37}
$$

Here, R_C, θ_s, and φ_s are the spherical coordinates of the observation point relative to the point C; $\mathbf{R}_C$ and $\hat{\mathbf{R}}_C = \dfrac{\mathbf{R}_C}{R_C}$ are the vector connecting the point C with the observation point and the collinear unit vector, respectively; and $\bar{\mathbf{r}}_1 = (\mathbf{r}_1 - \mathbf{r}_2)/2$ and $\bar{\mathbf{r}}_2 = (\mathbf{r}_2 - \mathbf{r}_1)/2$. Summing fields (37), we obtain the expression for the SA of the equivalent scatterer (combined of the two above scatterers) with the center at the point C:

$$\bar{T}'(\theta_i, \varphi_i, \theta_s, \varphi_s) = {}^1\bar{T}'(\theta_i, \varphi_i, \theta_s, \varphi_s)$$
$$\times \exp(-ik\hat{\mathbf{R}}_C\bar{\mathbf{r}}_1) + {}^2\bar{T}'(\theta_i, \varphi_i, \theta_s, \varphi_s)\exp(-ik\hat{\mathbf{R}}_C\bar{\mathbf{r}}_2), \quad (38)$$

which agrees with Eq. (26). It is clear that the procedure of including the third scatterer (and all other scatterers) can be easily realized with the known SA given by Eq. (38). In this procedure, the first pair of scatterers is characterized by SA (38) and the center at the point C, and so forth.

Thus, in this paper, we derived the exact expressions (integral equations) that allow one to calculate the resulting SAs of two scatterers under the conditions where each of the scatterers is driven by the primary wave and the perturbation field of the other scatterer while the unperturbed SAs of both scatterers are known. This, in turn, makes it possible to develop the procedure for considering multiple scattering by three and more bodies. In addition, we derived the zero-order geometrical optics approximations for the resulting SAs in the case when every scatterer is located in the Fraunhofer zone relative to all other scatterers. The expressions obtained appear to be useful for solving similar problems concerning the effect of interfaces and inhomogeneities on the resulting SAs.

The proposed method yields the same solutions to the problem of multiple scattering as those obtained by the methods given in [1–15], however, in other terms. It additionally emphasizes that the SA carries exhaustive information about the field at any point outside the scatterers, rather than characterizes the far field alone. Moreover, if a data bank of unperturbed SAs of scatterers is available, the proposed method makes it possible to construct the solutions to multiple scattering problems with arbitrary scatterer configurations, as distinct from alternative approaches that require obtaining a new solution for every new configuration.

APPENDIX 1

SCATTERING AMPLITUDE OF A PLANE INTERFACE

Let the plane $z = 0$ serve as an interface between the lower homogeneous half-space $z \leq 0$ and the upper inhomogeneous layered medium $z \geq 0$. When a plane wave $\exp(i(k_{lx}x + k_{ly}y + \alpha_l z))$ is incident on the interface from the lower half-space, the reflected plane wave $V(\alpha_l)\exp(i(k_{lx}x + k_{ly}y - \alpha_l z))$, where $V(\alpha_l)$ is the reflection coefficient, is formed in this half-space. To calculate the SA of the reflecting plane, we formally use Eq. (3). Taking into account that the scattered field is given in this case by the formula

$$u_s(\mathbf{x}, \mathbf{k}_l) = V(\alpha_l)\exp(i(k_{lx}x + k_{ly}y - \alpha_l z)),$$

we represent Eq. (3) in the form

$$V(\alpha_l)\exp(i(k_{lx}x + k_{ly}y - \alpha_l z))$$
$$= \frac{i}{2\pi}\int\limits_{R^2}\frac{T_1^2(\mathbf{k}_l, \mathbf{k}_s)}{\alpha_s}\exp(i(k_{sx}x + k_{sy}y - \alpha_s z))dk_{sx}dk_{sy}.$$

The analysis of this expression shows that the SA of the reflecting plane can be represented in the form

$$T_1^2(\mathbf{k}_l, \mathbf{k}_s) = \frac{2\pi}{i}V(\alpha_l)\alpha_l\delta(k_{lx} - k_{sx})\delta(k_{ly} - k_{sy})$$
$$= \frac{2\pi}{i}V(\alpha_s)\alpha_s\delta(k_{lx} - k_{sx})\delta(k_{ly} - k_{sy}). \quad (A1)$$

Here, we used the filtering property of the delta-function.

APPENDIX 2

SCATTERING AMPLITUDES OF THREE NEIGHBORING SPHERES CHARACTERIZED BY THE HOMOGENEOUS DIRICHLET BOUNDARY CONDITION

Let us have three identical spherical scatterers S_m, $m = 1, 2, 3$ of radius R_0 characterized by the homogeneous Dirichlet boundary conditions (perfectly soft boundaries). The centers of the spheres are located at the points $\left(0, 0, -\dfrac{z_0}{2}\right)$, $\left(0, 0, \dfrac{z_0}{2}\right)$, and $(x = z_0, 0, 0)$, respectively. The low-frequency approximation (to $O(k^3)$) of the unperturbed SA of such a sphere is given in [28, p. 86] and has the form

$$T(\theta_l, \varphi_l, \theta_s, \varphi_s)$$
$$= A + B(\cos\theta_l\cos\theta_s + \sin\theta_l\sin\theta_s\cos(\varphi_l - \varphi_s)), \quad (A2)$$

where

$$A = -R_0 + \frac{2}{3}k^2R_0^3 + ikR_0^2; \quad B = -k^2R_0^3.$$

On changing to the spherical coordinate system $dk_x dk_y = \xi d\xi d\varphi = k^2\sin\theta\cos\theta d\theta d\varphi = k\alpha\sin\theta d\theta d\varphi$, the integration limits of the integrals of type (17) are

changed as follows: k_x, $k_y \in R^2 \Rightarrow \theta \in \left[0, \frac{\pi}{2} - i\infty\right)$, $\varphi \in [0, 2\pi]$. Simple calculations yield [25]

$$T_1'^2(\theta_l, \varphi_l, \theta_s, \varphi_s) = T_2'^1(\theta_l, \varphi_l, \theta_s, \varphi_s)$$
$$= A + B(-\cos\theta_l\cos\theta_s + \sin\theta_l\sin\theta_s\cos(\varphi_l - \varphi_s))$$

$$T_1'^1(\theta_l, \varphi_l, \theta_s, \varphi_s) = T_2'^2(\theta_l, \varphi_l, \theta_s, \varphi_s)$$
$$= A + B(\cos\theta_l\cos\theta_s + \sin\theta_l\sin\theta_s\cos(\varphi_l - \varphi_s)) \quad (A3)$$

$$\varphi_l, \varphi_s \in [0, 2\pi]; \quad \theta_l, \theta_s \in \left[0, \frac{\pi}{2} - j\infty\right).$$

Here, θ_l, φ_l, and θ_s, φ_s are the respective spherical coordinates of vectors $\mathbf{k}_l$ and $\mathbf{k}_s$, respectively, on the sphere of radius k in (k_x, k_y, k_z) space for $\xi \in [0, \infty)$. Substituting Eqs. (A3) into integrals of type (16), (17), and so forth, one can exactly calculate the resulting SAs of the spheres. In calculating the SAs from approximate expressions (27)–(36), one should use the unperturbed expressions for the SAs.

Consider such a calculation for three spheres illuminated by a plane wave incident at the angles $\theta_l = \pi/2$, $\varphi_l = 0$. Estimate for example the combined SA $\bar{T}'$ in the direction $\theta_s = \pi/2$, $\varphi_s = 0$ coinciding with the direction of incidence of the primary wave. This direction is of

interest because of the fact that the relationship $Q = \frac{4\pi}{k}\operatorname{Im}\bar{T}'(\theta_l, \varphi_l, \theta_s = \theta_l, \varphi_s = \varphi_l)$, where Q is the total scattering cross section, holds in this case [28, p. 69]. First, we use Eqs. (30), (27)–(29), and (A2) to calculate the combined SAs $^{1,2}T\left(\frac{\pi}{2}, 0, \frac{\pi}{2}, 0\right)$ and $^{1,2}T\left(\frac{\pi}{2}, \pi, \frac{\pi}{2}, 0\right)$ of scatterers S_1 and S_2 for the scattering in the forward and backward directions. We have

$$^{1,2}T\left(\frac{\pi}{2}, 0, \frac{\pi}{2}, 0\right) = 2\frac{A + B + A^2\beta}{1 - \beta^2 A(A - B)},$$
$$^{1,2}T\left(\frac{\pi}{2}, \pi, \frac{\pi}{2}, 0\right) = 2\frac{A - B + A^2\beta}{1 - \beta^2 A(A - B)}, \quad (A4)$$

where $\beta = \dfrac{\exp(ikz_0)}{z_0}$. We replace the two first scatterers by the combined scatterer with center located at the origin of coordinates and the SA given by Eqs. (A4). Then, using again Eqs. (30), (27)–(29), and (A2) for calculating the unperturbed SAs of the combined and third scatterers, we determine the resulting SA $^{1,2}\bar{T}\left(\frac{\pi}{2}, 0, \frac{\pi}{2}, 0\right)$ of the combined scatterer:

$$^{1,2}\bar{T}'\left(\frac{\pi}{2}, 0, \frac{\pi}{2}, 0\right) = \frac{^{1,2}T'\left(\frac{\pi}{2}, 0, \frac{\pi}{2}, 0\right) + \exp(ikz_0)\beta(A - B)\left[^{1,2}T'\left(\frac{\pi}{2}, \pi, \frac{\pi}{2}, 0\right)\right]}{1 - \beta^2(A - B)\left[^{1,2}T'\left(\frac{\pi}{2}, \pi, \frac{\pi}{2}, 0\right)\right]}. \quad (A5)$$

In a similar way, using Eqs. (32), (34)–(36), (A4), and (A2), we determine the resulting SA of scatterer S_3:

$$^3\bar{T}'\left(\frac{\pi}{2}, 0, \frac{\pi}{2}, 0\right) \quad (A6)$$

$$= \frac{\exp(ikz_0)(A + B) + \beta(A + B)\left[^{1,2}T'\left(\frac{\pi}{2}, 0, \frac{\pi}{2}, 0\right)\right]}{1 - \beta^2(A + B)\left[^{1,2}T'\left(\frac{\pi}{2}, \pi, \frac{\pi}{2}, 0\right)\right]}.$$

With these results, the combined SA of the whole system of three scatterers with respect to the point $\left(x = \frac{z_0}{2}, 0, 0\right)$ can be found from Eq. (38):

$$\bar{T}'(\theta_i, \varphi_i, \theta_s, \varphi_s) = {}^{1,2}\bar{T}'\left(\frac{\pi}{2}, 0, \frac{\pi}{2}, 0\right)\exp\left(ik\frac{z_0}{2}\right)$$
$$+ {}^3\bar{T}'\left(\frac{\pi}{2}, 0, \frac{\pi}{2}, 0\right)\exp\left(-ik\frac{z_0}{2}\right). \quad (A7)$$

Note that, for $z_0 \longrightarrow \infty$, Eqs. (A5)–(A7) are reduced to the corresponding expressions derived without regard for the multiple scattering.

REFERENCES

1. V. Twersky, J. Acoust. Soc. Am. **24**, 42 (1952).
2. P. C. Waterman and R. Truell, J. Math. Phys. **2**, 512 (1961).
3. E. A. Ivanov, *Diffraction by Two Bodies* (Nauka i Tekhnika, Minsk, 1968) [in Russian].
4. L. A. Marnevskaya, Akust. Zh. **14**, 427 (1969) [Sov. Phys. Acoust. **14**, 356 (1969)].
5. L. A. Marnevskaya, Akust. Zh. **15**, 579 (1970) [Sov. Phys. Acoust. **15**, 499 (1970)].
6. B. Peterson and S. Strom, J. Acoust. Soc. Am. **56**, 771 (1974).
7. V. K. Varadan, in *Acoustic, Electromagnetic and Elastic Wave Scattering: Focus on the T-Matrix Approach* (Pergamon, Oxford, 1980), pp. 103–134.
8. J. C. Gaunaurd, H. Huang, and H. Strifors, J. Acoust. Soc. Am. **98**, 495 (1995).

9. H. Huang and J. C. Gaunaurd, J. Acoust. Soc. Am. **98**, 2149 (1995).

10. S. Koc and W. S. Chew, J. Acoust. Soc. Am. **103**, 721 (1998).

11. N. A. Gumerov and R. Duraiswami, J. Acoust. Soc. Am. **112**, 2688 (2002).

12. S. Sherer, J. Acoust. Soc. Am. **115**, 488 (2004).

13. P.-Y. Le Bas, F. Luppe, and J. Conoir, J. Acoust. Soc. Am. **115**, 1460 (2004).

14. V. A. Burov, S. N. Vecherin, and O. D. Rumyantseva, Akust. Zh. **50**, 14 (2004) [Acoust. Phys. **50**, 9 (2004)].

15. I. B. Andreeva and L. L. Tarasov, Akust. Zh. **49**, 156 (2003) [Acoust. Phys. **49**, 125 (2003)].

16. A. A. Kleshchev, Akust. Zh. **23**, 404 (1977) [Sov. Phys. Acoust. **23**, 225 (1977)].

17. Yu. A. Kravtsov, V. M. Kuz'kin, and V. G. Petnikov, Akust. Zh. **30**, 339 (1984) [Sov. Phys. Acoust. **30**, 199 (1984)].

18. S. M. Rao and B. S. Sridhara, J. Acoust. Soc. Am. **91**, 652 (1992).

19. V. E. Belov, S. M. Gorskiĭ, A. Yu. Zinov'ev, and A. I. Khil'ko, Akust. Zh. **40**, 548 (1994) [Acoust. Phys. **40**, 485 (1994)].

20. J. C. Gaunaurd and H. Huang, J. Acoust. Soc. Am. **96**, 2526 (1994).

21. G. C. Bishop and J. Smith, J. Acoust. Soc. Am. **105**, 130 (1999).

22. V. M. Kuz'kin, Akust. Zh. **49**, 77 (2003) [Acoust. Phys. **49**, 68 (2003)].

23. V. A. Grigor'ev, B. G. Katsnel'son, S. A. Pereselkov, and V. G. Petnikov, Akust. Zh. **49**, 43 (2003) [Acoust. Phys. **49**, 36 (2003)].

24. D. N. Ghosh Roy and G. J. Orris, J. Acoust. Soc. Am. **114**, 626 (2003).

25. A. V. Zatserkovnyĭ, V. S. Sergeev, and B. P. Sharfarets, Akust. Zh. **47**, 650 (2001) [Acoust. Phys. **47**, 565 (2001)].

26. B. P. Sharfarets, Akust. Zh. **48**, 547 (2002) [Acoust. Phys. **48**, 481 (2002)].

27. B. P. Sharfarets, Akust. Zh. **50**, 123 (2004) [Acoust. Phys. **50**, 107 (2004)].

28. P. M. Morse and H. Feshbach, *Methods of Theoretical Physics* (McGraw-Hill, New York, 1953; Inostrannaya Literatura, Moscow, 1960), Vol. 2.

Translated by A. Vinogradov

Amplification and Drift-Related Nonreciprocity of the Shear Wave Scattering by a Semiconductor Cylinder in a Piezoelectric

N. S. Shevyakhov

Institute of Radio Engineering and Electronics,
Ul'yanovsk Branch, Russian Academy of Sciences,
ul. Goncharova 48, Ul'yanovsk, 432011 Russia

e-mail: ufire@mv.ru

Received February 17, 2004

Abstract—The scattering of a plane monochromatic shear wave by a circular semiconductor cylinder soldered into a piezoelectric of class 6mm(4mm, ∞m) is considered for the case when an azimuth drift current occurs in the cylinder. It is found that the drift-related nonequivalence of scattering in opposite azimuth directions of wave propagation around the cylinder is the origin of the asymmetry of the polar scattering pattern while the effective (for the partial waves travelling around the cylinder in the drift direction with a sufficiently high angular velocity) acoustoelectronic amplification reduces the total scattering loss and can make it negative. A relatively strong contribution of the plasma and drift to the scattering is predicted for the case of acoustic matching between the materials of the cylinder and the surrounding piezoelectric. © 2005 Pleiades Publishing, Inc.

INTRODUCTION

Piezoelectric crystals and materials formed on their basis are used in radio electronics and adjacent technology as resonators, transducers, and filters [1, 2]. This is the main reason for the long-term interest in the propagation of acoustic waves in piezoelectrics. Recent years have been marked by an increased attention to the acoustic properties of heterophase polycrystalline materials of the piezoceramic type [3–5]. In the process of acoustic wave propagation in them, the conductivity and frequency dispersion of permittivity can manifest themselves due to the piezoelectric effect, for example, as a result of pores of piezoceramics being filled with an electrolyte (seawater) [6]. Analogous acoustoelectronic effects are possible if one of the phases of a material has semiconductor properties and the drift of charge carriers is generated in it to obtain the control effect.

The understanding of the essence of acoustic processes in composite piezoelectrics and piezoceramics with a conducting phase needs investigation of the particular features of wave scattering by single inhomogeneities. A number of aspects of this problem were considered earlier [7, 8]. However, in [7], the contribution of the piezoelectric effect, conductivity, and drift of charge carriers to the scattering of a shear wave by a conducting cylindrical region of a bulk piezoelectric crystal and a cylindrical cavity in a piezoelectric with a semiconductor cylinder separated by a thin vacuum gap

was not evaluated integrally but determined according to the variations of the amplitude coefficients of single partial waves of the scattered field. In that case, simplifying restrictions were used, such as a low level of coupling between the oscillations of the acoustic and plasma subsystems, a high diffusion frequency of plasma, and a small wave size of the cylindrical inhomogeneity.

Additional investigation [8] of the effects of acoustoelectronic amplification and damping of shear waves scattered by a cavity in a piezoelectric with a semiconductor cylinder in a noncontact position provided an opportunity to reveal the nonequivalence (nonreciprocity), induced by the drift of charge carriers in the semiconductor, for the scattering of partial waves in the opposite azimuth directions of propagation around the cavity. A consequence of the drift-related nonreciprocity of scattering is the visible asymmetry of the scattering pattern with respect to the angular coordinate. However the calculation of the scattering patterns in [8] was also restricted to the case of high diffusion frequencies of the semiconductor plasma and moderate cavity dimensions.

In the present paper, the results obtained in [7, 8] for the scattering of a shear wave by a circular cylindrical cavity with a noncontact semiconductor cylinder are generalized to the case of a piezoelectric and a cylinder brought into an acoustic contact. For several reasons, this situation provides, first, a unique opportunity to
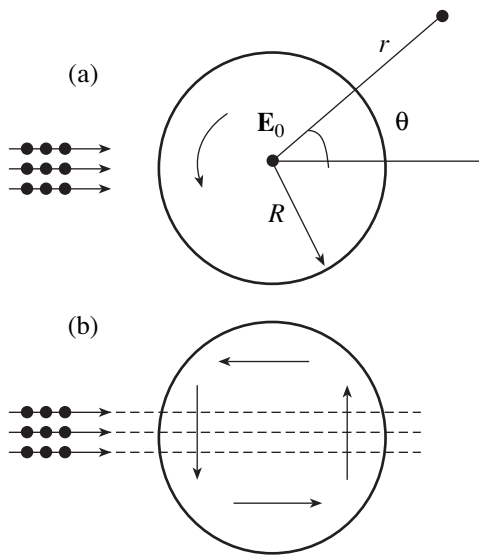
Fig. 1. (a) Geometry of the problem and (b) the pattern of paraxial rays in the semiconductor cylinder.

consider more exhaustively[1] the linear effects of acoustoelectronic interaction, including the control of acoustic scattering by the drift of charge carriers. This can be performed within the framework of the traditional continual approach and the hydrodynamic description of a semiconductor plasma without the restriction on a low level of oscillation coupling for the phonon and plasma subsystems in the whole available range of frequencies and wavelengths. Second, this situation is more adequate to the existing industrial technologies of manufacturing artificial composite media and allows one to separate the acoustoelectronic scattering of a shear wave that is induced by drift and the cylinder conductivity in the case of its acoustic matching with the piezoelectric. The acoustic matching of the materials, i.e., the piezoelectric and the semiconductor cylinder brought into contact with it, excludes common acoustic scattering caused by the cavity itself [7, 8]. The last plays the role of a masking background with respect to the acoustoelectronic effects of semiconductor current plasma. Therefore, there is an opportunity, in the approximation of a low repetition factor of scattering, to use the results on acoustoelectronic scattering by a single cylinder for a qualitative evaluation of the behavior of an artificial composite medium in the form of an aggregate of parallel and identical in all parameters

---

[1] It differs from the special case of scattering by a conducting region of a bulk piezoelectric crystal [7] in the absence of piezoelectric properties of the scattering cylinder. This fact provides an opportunity to avoid the difficulties in matching the elastic and electric fields in the scattering cylinder because of the presence of drift. However, the specific results, in particular, the spectral characteristics of such an important integral property of scattering as the extinction and scattering cross sections of a cylinder (which were not considered earlier), could be obtained without using the frequency limitations only by numerical calculation with the help of modern computing facilities.

semiconductor cylinders (fibers) distributed over a piezoelectric crystal with low density.

FORMULATION OF THE PROBLEM AND THE INITIAL EQUATIONS

Let, in the cylindrical coordinates r, θ, z, a piezoelectric of class 6mm(4mm, ∞m) with the highest-order symmetry axis $L_6(L_4, L_\infty) \parallel z$ occupy the region $r > R$, and the region $r < R$ be occupied by a nonpolar semiconductor also oriented with its crystallographic axis along the z axis. The consequence of this crystal positioning in the case of normal incidence of a plane monochromatic shear wave with amplitude U and axial polarization of displacements $\mathbf{u}_2^{in} = (0, 0, u_2^{in})$, $u_2^{in} = U\exp(i\psi)$, $\psi = k_2 r\cos\theta - \omega t$ on a semiconductor cylinder (Fig. 1), is the absence of boundary transformations of elastic oscillation modes. Therefore, in the quasistatic approximation [9], which is quite effective for scattering problems, we obtain a system of equations from the Maxwell equations and the equations for the piezoelectric effect [1, 2] owing to the harmonic character of oscillations of the resulting shear displacements $\mathbf{u}_2 = (0, 0, u_2)$ and the electric potential φ_2 of piezoelectric fields:

$$\nabla^2 u_2 + k_2^2 u_2 = 0, \quad \varphi_2 = \frac{4\pi e_{15}}{\varepsilon_2}u_2 + \Phi_2,$$
$$\nabla^2 \Phi_2 = 0. \tag{1}$$

Here and above, ∇^2 is the Laplacian in the plane of shear wave propagation, $k_2 = \omega(\rho_2/\lambda_2^*)^{1/2}$ is the wave number, ω is the frequency, $\lambda_2^* = \lambda_2 + 4\pi e_{15}^2/\varepsilon_2$, λ_2 is the shear modulus, e_{15} is the piezoelectric modulus, ε_2 is the dielectric constant, ρ_2 is the piezoelectric density, and t is time.

In the nonpiezoelectric semiconductor, the shear displacements u_1 are not connected directly with the electric field of the potential φ_1 and the equation of motion of the elastic medium leads to a common Helmholtz equation:

$$\nabla^2 u_1 + k_1^2 u_1 = 0, \tag{2}$$

where $k_1 = \omega(\rho_1/\lambda_1)^{1/2}$ is the wave number, ρ_1 is the density, and λ_1 is the shear modulus of the semiconductor. However, it is necessary to take into account the electric field penetrating from the piezoelectric crystal and perturbing the electronic plasma of charge carriers in the semiconductor. In the hydrodynamic approximation, the plasma is described by the equations

$$\nabla \cdot \mathbf{D}^{(1)} = -4\pi eN, \quad \nabla \cdot \mathbf{j} = e\frac{\partial N}{\partial t},$$
$$\mathbf{j} = \sigma\mathbf{E}_1 + efD_0\nabla N. \tag{3}$$

Here, $\mathbf{D}^{(1)}$ is the electric induction in the semiconductor, $\mathbf{j}$ is the current density, $\mathbf{E}_1 = \mathbf{E}_0 - \nabla\varphi_1$, $\mathbf{E}_0$ is the drift

field, $\sigma = \sigma_0 + ef\mu N$ is the semiconductor conductivity consisting of the static σ_0 and perturbed parts, N is the concentration of charge carriers, e is the elementary charge, μ is the mobility, f is the trapping factor, D_0 is the diffusion coefficient of charge carriers, and ∇ is the Hamilton operator in the plane orthogonal to the z axis.

For small perturbations of electronic plasma, we use the linearized current density $\mathbf{j} \approx efD_0\nabla N + \sigma\mathbf{E}_0 - \sigma_0\nabla\varphi_1$ and assume that the azimuth drift under the effect of the field $\mathbf{E}_0 = (0, E_0, 0)$, $E_0 = -\alpha r$ is reduced to the circular rotation of electrons with a constant angular velocity. The constant α is determined by the method of drift excitation. If one uses a nonstationary radially inhomogeneous magnetic field $\mathbf{H}_0 \parallel z$ ($H_0 \sim r^2$) [6] for these purposes, α has the meaning of the rate of magnetic field variation in time. Taking into account the relation $\mathbf{D}^{(1)} = \varepsilon_1\mathbf{E}_1$, we eliminate the quantities $\mathbf{j}$ and N from Eq. (3) and obtain an equation for the determination of φ_1:

$$\nabla^2\left[f\mu(\mathbf{E}_0 \cdot \nabla) + fD_0\nabla^2 - \frac{\partial}{\partial t} - \omega_c\right]\varphi_1 = 0, \quad (4)$$

where $\omega_c = 4\pi\sigma_0/\varepsilon_1$ is the Maxwell relaxation frequency.

We complement Eqs. (1), (2), and (4) with the boundary conditions of continuity at $r = R$ for shear displacements, components T_{rz} of the stress tensor, potentials, and radial components of the electric induction. Assuming that recombination and trapping of charge carriers at the surface levels is absent, we add the requirement of the absence of charge transfer from the semiconductor cylinder to the piezoelectric: $j_r|_{r=R} = 0$. Finally, using the equations for the piezoelectric effect [1, 2] and the linearized expression for the current density, we write

$$u_1|_{r=R} = u_2|_{r=R},$$

$$\left(\lambda_2\frac{\partial u_2}{\partial r} + e_{15}\frac{\partial\varphi_2}{\partial r}\right)\Big|_{r=R} = \lambda_1\frac{\partial u_1}{\partial r}\Big|_{r=R},$$

$$\varphi_1|_{r=R} = \varphi_2|_{r=R}, \quad (5)$$

$$\left(4\pi e_{15}\frac{\partial u_2}{\partial r} - \varepsilon_2\frac{\partial\varphi_2}{\partial r}\right)\Big|_{r=R} = -\varepsilon_1\frac{\partial\varphi_1}{\partial r}\Big|_{r=R},$$

$$\omega_c\frac{\partial\varphi_1}{\partial r}\Big|_{r=R} = fD_0\nabla^2\left(\frac{\partial\varphi_1}{\partial r}\right)\Big|_{r=R}.$$

SOLUTION OF THE BOUNDARY PROBLEM

The shear displacements $u_{1,2}$ as the solutions to homogeneous Helmholtz equations (1) and (2) can be formally represented by the Rayleigh series of the solution to the reference problem of the scalar theory

describing the diffraction of a plane monochromatic wave by a foreign cylinder [10, 11]:

$$u_1 = U\exp(-i\omega t)$$
$$\times \sum_{n=-\infty}^{\infty} i^n\exp(in\theta)J_n(k_1 r)b_n, \quad r < R, \quad (6)$$

$$u_2 = U\exp(-i\omega t)$$
$$\times \sum_{n=-\infty}^{\infty} i^n\exp(in\theta)[J_n(k_2 r) + H_n^{(1)}(k_2 r)a_n], \quad r > R. \quad (7)$$

Here, we use standard notations for the Bessel functions $J_n(x)$ and the Hankel functions of the first kind $H_n^{(1)}(x)$; the incident wave is taken into account in Eq. (7) by the first term in square brackets; the second term in them characterizes the partial contribution from the azimuth harmonic to the field scattered by the cylinder; and the coefficients a_n and b_n must be determined.

The determination of φ_2 is reduced to the determination of the potential Φ_2 of the field of boundary piezoelectric polarization oscillations, and, taking into account its limited character at $r > R$ along with the need to satisfy the boundary conditions given by Eqs. (5), we obtain, by virtue of Eq. (1),

$$\Phi_2 = \exp(-i\omega t)\sum_{n=-\infty}^{\infty} i^n\exp(in\theta)r^{-|n|}d_n. \quad (8)$$

From Eq. (4), it also follows that

$$\varphi_1 = \Phi_1 + \Phi, \quad \nabla^2\Phi_1 = 0,$$
$$\left[f\mu(\mathbf{E}_0 \cdot \nabla) + fD_0\nabla^2 - \frac{\partial}{\partial t} - \omega_c\right]\Phi = 0. \quad (9)$$

The potential Φ_1 of the piezoelectric polarization oscillations in the semiconductor cylinder is analogous in its structure to Eq. (8) with the exception of the fact that the powers of the radial coordinate are taken with the positive sign:

$$\Phi_1 = \exp(-i\omega t)\sum_{n=-\infty}^{\infty} i^n\exp(in\theta)r^{|n|}c_n. \quad (10)$$

In conformity with the adopted type of drift, for each azimuth harmonic, the effect of the operator $\mathbf{E}_0 \cdot \nabla$ in the last of Eqs. (9) is equivalent to multiplication by $-i\alpha n$. Taking into account the substitution of $\partial/\partial t$ for $-i\omega t$, this equation can be represented in the form $\nabla^2\Phi - \chi_n^2\Phi = 0$, which allows us to represent the potential Φ of the field response of the semiconductor plasma to piezoelectric polarization oscillations in the form

$$\Phi = \exp(-i\omega t)\sum_{n=-\infty}^{\infty} i^n\exp(in\theta)I_n(\chi_n)g_n. \quad (11)$$

Here, $I_n(x)$ is the modified Bessel function selected proceeding from the bounded character of the solution, $\chi_n = k_1(\omega_D/\omega)^{1/2}[\omega_c/\omega - i(1 - n\Omega/\omega)]^{1/2}$, $\omega/\omega_D = fD_0k_1^2/\omega$, ω_D is the diffusion frequency, and $\Omega = f\mu\alpha$ is the angular velocity of the azimuth drift of charge carriers.

The amplitude coefficients a_n, b_n, c_n, d_n, and g_n are obtained from the system of inhomogeneous algebraic equations, which are obtained from the substitution of the expressions for displacements (Eqs. (6) and (7)) and the summary potentials φ_1 and φ_2 following from Eqs. (1) and (8)–(11) into the boundary conditions (5). However, it should be noted that the indices of the scattering ability of the semiconductor cylinder are only characterized by the coefficients a_n, which have the form

$$
a_n = -\frac{J_n(\xi_2)}{H_n^{(1)}(\xi_2)}
$$

$$
\times \frac{\mathcal{K}^2|n|F_n(\tau, \xi_1) - m\xi_1[\ln J_n(\xi_1)]' + \xi_2[\ln J_n(\xi_2)]'}{\mathcal{K}^2|n|F_n(\tau, \xi_1) - m\xi_1[\ln J_n(\xi_1)]' + \xi_2[\ln H_n^{(1)}(\xi_2)]'}.
$$

(12)

Therefore, it is unnecessary to give here the equations for other amplitude coefficients. The latter are expressed finally by a chain of linked equations through the coefficients a_n. In Eq. (12), $\mathcal{K}^2 = 4\pi e_{15}^2(\varepsilon_2\lambda_2^*)^{-1}$ is the square of the electromechanical coupling coefficient of the piezoelectric, $\xi_1 = k_1R$, $\xi_2 = k_2R$, $m = \lambda_1/\lambda_2^*$, and

$$
F_n(\tau, \xi_1) = \frac{\dfrac{\varepsilon_1}{\varepsilon_2}\left(1 - n\dfrac{\Omega}{\omega}\right)\left[1 + \delta_n\left(1 + i\dfrac{\omega}{\omega_D}\right)\right]}{\left(1 - n\dfrac{\Omega}{\omega}\right)\left[1 + \dfrac{\varepsilon_1}{\varepsilon_2}(1 + \delta_n)\right] + i\dfrac{\omega}{\omega_D}\delta_n\dfrac{\varepsilon_1}{\varepsilon_2} + i\dfrac{\omega_c}{\omega}\dfrac{|n|}{\zeta}\dfrac{1}{[\ln I_n(\zeta)]'}}
$$

(13)

is the function of the generalized conductivity parameter τ and ξ_1, which contains the quantities $\delta_n = i[(1 - n\Omega/\omega) + i\omega/\omega_D]^{-1}\omega_c/\omega$ and $\zeta = \xi_1(\omega_D/\omega)^{1/2}[\omega_c/\omega - i(1 - n\Omega/\omega)]^{1/2}$. Equations (12) and (13), where the primes denote the derivatives of the logarithms of cylindrical functions, complete the representation of the solution to the boundary problem under consideration.

Let us verify that the result corresponds to previous data. For example, $m = 0$ means the absence of the acoustic contact of the semiconductor cylinder with the piezoelectric and Eq. (12), as it should be expected, transforms into Eq. (2) from [8]. If we additionally assume that $\omega_c = 0$, $\mu = 0$ ($\Omega = 0$), and $\varepsilon_1 = 1$, we obtain the case of scattering of a shear wave by a cylindrical air gap in a piezoelectric crystal, which was considered in [7, 8]. In the absence of the piezoelectric effect, when $\mathcal{K}^2 = 0$, Eq. (12) leads to the amplitude coefficients of the partial shear waves scattered by a foreign cylinder in an isotropic elastic medium [10]. The solution for the last case is mathematically equivalent to the solution to the problem of scattering of an H-polarized electromagnetic wave by a dielectric cylinder [11].

EFFECT OF THE CONDUCTIVITY AND DRIFT ON THE PARTIAL WAVES OF THE SCATTERED FIELD

In [8], the ratio $\Gamma_n = |a_n(\Omega)|/|a_n(0)|$ was taken as the measure of the amplitude variation of a partial scattered wave under the effect of conductivity and drift. This quantity was calculated for extremely low ultrasonic frequencies $\omega^2 \ll \omega_c\omega_D$ and a semiconductor plasma with a low conductivity ($\omega_c \ll \omega_D$). The resulting estimate for waves of low numbers $[\ln I_n(\zeta)]' \sim 1$ in the

asymptotic case of $|\zeta| \gg \xi_1$ allowed us to ignore the last term in the denominator of Eq. (12) and to solve the major problem connected with calculating the modified Bessel function of a complex argument. Along with this, we also ignored the terms proportional to ω/ω_D, and the function $F_n(\tau, \xi_1)$ acquired a relatively simple form $F_n(\tau, \xi_1) \approx \varepsilon_1(1 + \delta_n)[\varepsilon_2 + \varepsilon_1(1 + \delta_n)]^{-1}$. This description of the plasma response corresponds to its model representation as a medium with the effective dielectric constant $\varepsilon_1(1 + \delta_n)$, which is natural, since the boundary plasma effects under the aforementioned conditions (diffusion-free approximation) are negligibly small.

The approach adopted in [8] made it impossible to investigate the acoustoelectronic effects in the case of scattering of a shear wave by a cavity with a semiconductor ($m = 0$) in the most interesting frequency range $\omega^2 \sim \omega_c\omega_D$. The possibility of studying the azimuth drift with the angular velocities $\Omega = \omega/n$ or close to them was also excluded, since, in this case, it is unacceptable to ignore the "small" terms in Eq. (12) because of their growth with respect to the first term. The results of the present work are based on the data of an exact quantitative calculation according to Eqs. (12) and (13), and, therefore, they are free of the aforementioned drawbacks.

For the program module with the inaccuracy of calculation of Γ_n and other quantities no higher than 10^{-9} at $\xi_1 < 3 \times 10^2(\omega/\omega_D)^{1/2}$, when the characteristic range of variation of the ratio ω/ω_D was overly exceeded for cylinders with moderate ($\xi_1 \cong 10$) or higher wave dimensions, the basic procedure was the calculation of the cylindrical functions of integer order with a positive

argument according to Miller's algorithm [12, 13]. Its applicability to calculating the function $I_n(z)$ of a complex argument z together with the relations $I_n(z) = \exp(-in\pi/2)J_n(iz)$, $-\pi < \arg z \leq \pi/2$, $I_n(z) = \exp(i3n\pi/2) \times J_n(iz)$, $\pi/2 < \arg z \leq \pi$ is secured by the theorem of multiplication for the Bessel function [14]:

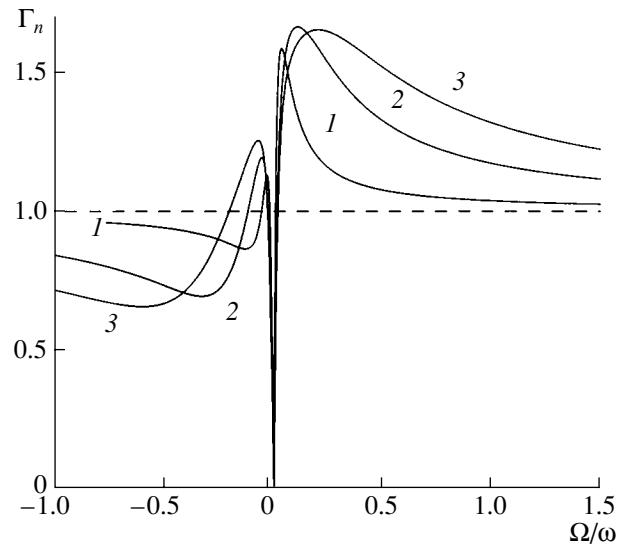$$J_n(az) = a^n \sum_{k=0}^{\infty} (-1)^k \frac{(a^2-1)^k(z/2)^k}{k!} J_{n+k}(z), \quad (14)$$

where a and z are any complex numbers. Assuming that, in Eq. (14), $az = w$ and $z = |w|$, we obtain the expansion of the Bessel function of a complex argument w into a series in the Bessel functions of a positive argument $|w|$.

The results of numerical calculation for the values of Γ_n qualitatively agree with the conclusions of [8]. For example, together with Eqs. (12) and (13), they point to the inequality $a_n \neq a_{-n}$ under the drift conditions for the amplitudes of the scattered field of the direct ($n > 0$) and inverse ($n < 0$) azimuth propagation of waves. The last means the drift-related nonreciprocity of scattering. The conclusion concerning the possibility of a noticeable acoustoelectronic amplification (attenuation) of partial scattered waves by the drift current, when the semiconductor cylinder has wave dimensions sufficient for the formation of plasma bunches $\xi_1 > 1$, was also confirmed.[2] However, together with the characteristic acoustoelectronic change of sign for the dependences $\Gamma_n(\Omega) - 1$ at the "critical" drift currents (Fig. 2), the presence of a drop in the value of Γ_n at an angular velocity of drift $\Omega = \omega/n$ was revealed, this drop being the deeper the closer to each other in acoustic properties the piezoelectric and the semiconductor were.

This is illustrated by the curves in Fig. 2. They are calculated for the case where the conditions of acoustic matching for the materials of the cylinder and the piezoelectric are assumed in Eq. (12): $m = 1$, $k_1 = k_2$ ($\xi_1 = \xi_2$). This case will be given special attention below. The largest depth of the dip, which reaches a value of $\Gamma_n = 0$, corresponds to this case. The horizontal dashed line in Fig. 2 indicates the level of zero variation for the amplitude of a partial wave $\Gamma_n = 1$.

As for the angular velocity of drift $\Omega = \omega/n$, it is necessary to note that it corresponds to the linear drift velocity $v_d = \Omega R$ of charge carriers, which coincides with the velocity of azimuth propagation of a partial wave around the cylinder boundary $v_n = \omega R/n$. To determine this fact, to the number n of an azimuth harmonic we assign the value $n = k_n R$, where $k_n = \omega/v_n$ is

Fig. 2. Drift dependences Γ_n for $n = 30$ in the case of $\xi_1 = 20$, $\mathcal{K}^2 = 0.01$, $\varepsilon_1/\varepsilon_2 = 1.4$, and $\omega_c/\omega = 1$ for different ratios ω/ω_D under the conditions of acoustic matching of the cylinder with the piezoelectric: $\omega/\omega_D = (1)$ 1, (2) 5, and (3) 10.

the azimuth wave number. According to Eq. (13), the dip in the dependence $\Gamma_n(\Omega)$ at the point of the "sonic" drift is caused by the termination of acoustoelectronic interaction: $F_n(\tau, \xi_1) = 0$, which is explained by the known [15] mechanism of phase synchronism of plasma bunches with a wave, which is supported by drift. The diffusion of charge carriers does not influence the position of the point of "sonic" drift. However, from the comparison of curves *1–3* (Fig. 2), one can see that, as it grows, a broadening of the peak observed in the dependence $\Gamma_n(\Omega)$ and cut through by the dip occurs. At $\Omega \longrightarrow 0$ ($\Omega > 0$, a direct azimuth drift), a sharp increase in the partial wave scattering, which occurs when $\Gamma_n \longrightarrow 1$ and may even exceed the zero level of scattering variation under the conditions $n/\xi_1 \leq 1$, $n \sim 1$, is caused by the fact that the acoustoelectronic mechanism is replaced by the screening action of the semiconductor plasma. The same circumstance ensures the validity of the inequality $\Gamma_n > 1$ at the initial sections of the inverse ($\Omega < 0$) drift and, together with the acoustoelectronic interaction, finally leads to the violation of the ideal asymmetry of the curves $\Gamma_n(\Omega)$ with respect to the zero level of scattering variation.

INTEGRAL CHARACTERISTICS OF THE ACOUSTOELECTRONIC SCATTERING OF A SHEAR WAVE BY A SEMICONDUCTOR CYLINDER

The analysis of variations of the amplitude coefficients for single partial waves scattered by a cylinder reveals the mechanisms of the control action by conductivity and drift upon the process of scattering but does not give the whole pattern of the phenomenon.

---

[2] At $\xi_1 \leq 1$, the semiconductor plasma has a polarization effect and, facilitating the "displacement" of the field of polarization oscillations to the external region, increases the acoustic scattering uniformly over all azimuths. This effect is analogous to the amplification of acoustic wave scattering by a cavity in a piezoelectric on account of boundary metallization [7, 9].

A complete picture of scattering is provided by the integral characteristics of scattering [10, 11, 13], i.e., the polar scattering pattern

$$F_S(\theta) = \left| \sum_{n=-\infty}^{+\infty} a_n \exp(in\theta) \right| \tag{15}$$

and the linear (per unit length of the cylinder) total scattering cross section σ_S. The first of these quantities characterizes the amplitude of the scattered field in the far wave zone, which is represented in the form of radiation from an effective linear source at the cylinder axis and shows in fact the azimuthal distribution of the scattered energy. The second quantity, which is usually expressed by the ratio of the time-averaged radially scattered power to the intensity of the incident wave, is taken as a measure for the energy efficiency of conversion of the incident wave into the scattered field.

This definition of σ_S leads to the expression [11, 13, 15]

$$\sigma_S = \frac{4}{k_2} \sum_{n=-\infty}^{+\infty} |a_n|^2. \tag{16}$$

It is evident that, in the presence of loss or in the case of wave amplification in the cylinder (negative loss), σ_S can be considered only with respect to a part of the incident power that remains in the cylinder minus the loss. The measure of the total conversion of the incident wave in the case of scattering is the quantity $\sigma_{ex} = \sigma_S + \sigma_A$ called the cross section of extinction by analogy with optics [13]. The addition σ_A to σ_S (now, it is sensible to exclude from the name of σ_S the prefix "total") determines the share of energy loss due to the scattering and can be called the absorption cross section of.

A convenient way to calculate σ_A is to follow the standard procedure for the determination of σ_S, but, in this case, the average radial flux of scattered energy is replaced by the difference of summary average radial energy fluxes converging to and diverging from the cylinder. A specific feature of this case is that the radial energy flux converging at the cylinder is formed by only part of the incident wave field. Its remaining part is added to the flux of the scattered field. The procedure of decomposition of the incident wave field into contributions to the radial energy fluxes converging to and diverging from the cylinder is described in [16].

In contrast to [10, 13], the determination of σ_A is performed in [16], as applied to the case of not only an absorbing but also an amplifying cylinder. However, this did not affect the final representation of σ_A by a series:

$$\sigma_A = -\frac{4}{k_2} \sum_{n=-\infty}^{+\infty} (|a_n|^2 + \mathrm{Re}\, a_n). \tag{17}$$

The minus sign in Eq. (17) reflects the fact of directivity of the absorbed energy flux towards the cylinder. Equations (16) and (17) yield the following expression for the extinction cross section:

$$\sigma_{ex} = -\frac{4}{k_2} \sum_{n=-\infty}^{+\infty} \mathrm{Re}\, a_n. \tag{18}$$

Since, according to [7, 8], the piezoelectric effect and, through it, the conductivity and drift manifest themselves weakly against the background of the acoustic scattering by the cavity in the piezoelectric and there are no grounds to expect something different in the case of a shear wave scattering by a foreign contacting cylinder, the above case of acoustically matched piezoelectric and semiconductor deserves some attention. In this case, because of the equations $\lambda_1 = \lambda_2^*$, $\rho_1 = \rho_2$, $\xi_1 = \xi_2 \equiv \xi$, and $m = 1$, from Eq. (12) we obtain

$$a_n = -\frac{\mathcal{H}^2 |n| F_n(\tau, \xi) J_n^2(\xi)}{\mathcal{H}^2 |n| F_n(\tau, \xi) J_n(\xi) H_n^{(1)}(\xi) + 2i/\pi}. \tag{19}$$

Equation (19) shows that now the scattering of a shear wave is completely determined by the piezoelectric effect ($\mathcal{H} \neq 0$) and the acoustoelectronic interaction ($F_n(\tau, \xi) \neq 0$) due to the appearance of piezoelectric polarization charges at the boundary under the effect of the incident wave. In its absolute value, this scattering effect (let us call it acoustoelectronic scattering) may be rather small, since most often $\mathcal{H}^2 \ll 1$, but it is very attractive, because it offers a possibility for the clear manifestation of the plasma properties of the semiconductor. Further, we will concentrate on the consideration of only the acoustoelectronic scattering.

It is necessary to note that the monopole contribution is absent in the acoustoelectronic scattering ($n = 0$), and, at low frequencies ($\xi \ll 1$), it is determined mainly by the dipole modes of oscillations of partial waves with the numbers $n = \pm 1$. This is the reason why the calculation of the normalized polar characteristics of scattering (below, simply polars) $g_S = F_S(\theta)/F_S(0)$ according to Eqs. (15) and (19) demonstrates that, in the Rayleigh region, the latter have a form differing little from the classical "figure eight." The conductivity enhances the thickening of its neck, and the drift, as in the case of scattering by a cavity with a semiconductor [8], causes a general azimuth rotation of polars.

As the wavelength shortens, the polarizing effect of the plasma charge carriers is replaced by the acoustoelectronic mechanism as the conditions for grouping of electronic bunches near the piezoelectric polarization field improve [15]. In this case, together with the rotational conversion of polars, their asymmetry with respect to the direction of location, as the general expression for the drift nonreciprocity of scattering, becomes more and more governed by the change of sidelobes and backscattering. Specific shapes of polars received at moderate and medium frequencies under the effect of conductivity and drift differ in greater variety. Figure 3 gives the polars of high-frequency scatter-

ing of a shear wave by a semiconductor cylinder in a piezoelectric of the $BaTiO_3$ type in the absence ($\Omega/\omega = 0$, the upper polar) and presence ($\Omega/\omega = 0.05$, the lower polar) of the azimuth drift. Their comparison illustrates the manifestation of the acoustoelectronic mechanism. The propagation direction of the incident shear wave is indicated by the arrow in Fig. 3.

The fact that the principal (in the location direction) shadow-forming side lobe with the length assumed to be equal to unity is not subjected to the effect of drift at high frequencies (see the scaling section in Fig. 3) is explained as follows. The bundles of paraxial rays forming it, these bundles being the narrower, the higher ξ is, cross the semiconductor cylinder in its central part, as is shown schematically in Fig. 1b by the dashed lines. Here, they are orthogonal to the drift current (shown by direct arrows at the cylinder periphery). The contribution of the drift current to the acoustoelectronic interaction in this case is absent [15]. At the same time, the amplification of scattering that can be seen in Fig. 3 in the angular sector $\pi/4 < \theta < \pi$ is evidence of the possibility for sufficiently effective control of the azimuth distribution of the scattered field with the help of drift.

The possibility of an acoustoelectronic absorption ($\sigma_A > 0$) and its change for the acoustoelectronic amplification of scattering ($\sigma_A < 0$, negative absorption) under the effect of drift is illustrated by the spectra of the absorption cross section, which are calculated according to Eqs. (17) and (19) for a piezoelectric of the $BaTiO_3$ type ($\mathcal{K}^2 = 0.38$, $\varepsilon_1/\varepsilon_2 = 1.4$) and a "dense" ($\omega^2 \ll \omega_c\omega_D$, $\omega/\omega_D = 0.001$, Fig. 4a) or "loose" ($\omega^2 \sim \omega_c\omega_D$, $\omega/\omega_D = 0.5$, Fig. 4b) plasma of the semiconductor with a conductivity $\omega_c/\omega = 1$. The corresponding spectral dependences in the absence of drift are plotted by dashed lines. The formation of the relaxation peak of absorption is observed for wave dimensions $\xi \leq 2$ (it is indicated by normal arrows), which corresponds to the peak of the Joule losses in the dipole oscillations of the cylinder plasma. The major difference is that, because of the strong diffusion damping under the conditions of a "loose" plasma, the effect of drift is extended to the long-wavelength part of the spectrum of the absorption cross section touching even upon the range of the Rayleigh scattering $\xi \ll 1$. One can see, for example, that, as the drift increases, the relaxation peak of absorption weakens and gradually transforms into the minimum of negative absorption that is indicated in curves 2 and 3 in Fig. 4b by light arrows.

Another characteristic detail of the absorption spectra is connected with the appearance (after the relaxation peak) of the plasma resonances of the cylinder. Since, in accordance with the nature of the drift, the waves of bulk charge in the cylinder are supported by the drift, the position of the plasma resonances is largely determined by the velocity of the azimuth drift. In Fig. 4a, as the result of the extremely high "density" of the plasma and considerable disproportion of acoustic wavelengths with respect to the Debye length, they
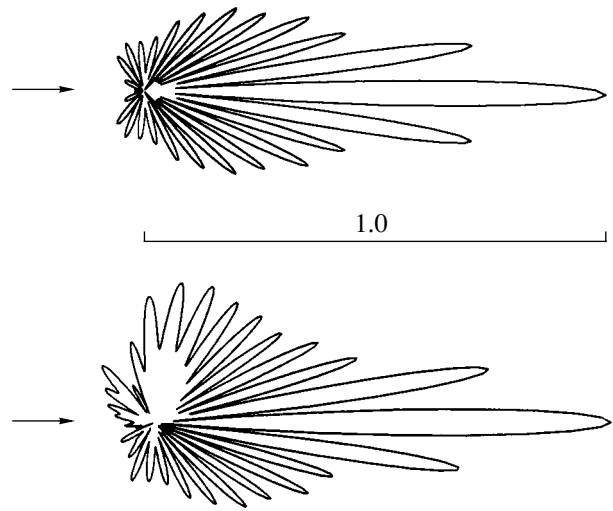
Fig. 3. Polar scattering patterns $g_S(\theta)$ of a semiconductor cylinder with the wave dimension $\xi = 20$ in the absence (the upper curve) and presence ($\Omega/\omega = 0.05$, the lower curve) of azimuth drift for $\omega_c/\omega = 1$, $\omega/\omega_D = 0.1$, $\mathcal{K}^2 = 0.38$, and $\varepsilon_1/\varepsilon_2 = 1.4$.

are expressed in the form of weak perturbations decreasing because of the transition to the regions of acoustoelectronic amplification of scattering in curves 1–3 of the dependences $\sigma_A(\xi)$. Under the conditions of a loose plasma, the degree of the boundary coupling of the acoustic and plasma subsystems, which, as the bulk modes of oscillations of a piezoelectric semiconductor [17], is determined by the value of $\mathcal{K}^2\omega_c/\omega_D$, is noticeably higher. Therefore, the plasma resonance peaks in curves 1 and 2 in Fig. 4b are well pronounced and considerably exceed the level of the absorption cross section in the absence of drift. At the same time, a high diffusion damping gives them such a large width that Fig. 4b contains just single peaks of the plasma resonance in the calculation range.

The serial character of plasma resonances in the spectrum of an absorption cross section is demonstrated graphically in Fig. 5a for the plasma less dense ($\omega/\omega_D = 0.04$) than in Fig. 4a but with a higher (by a factor of 40) degree of boundary coupling of acoustic and plasma modes. One can see that, in the absence of drift (the dashed curve), plasma resonances vanish and, as the cylinder curvature decreases, a gradual decrease in their peaks is observed. This is evidence that the peripheral plasma waves of the cylinder, i.e., the oscillations of charge carriers, which are carried away by the drift and on which plasma resonances develop, belong to the class of the boundary-curvature controlled "fast" (i.e., supersonic) waves of the type of whispering gallery modes [18]. This agrees well with the condition of supersonic drift for partial waves with the numbers $n > \omega/\Omega$, which make the decisive contribution to the formation of the plasma-resonance response of the cylinder in the case of the shear wave scattering. It is necessary to note that, according to the above consider-
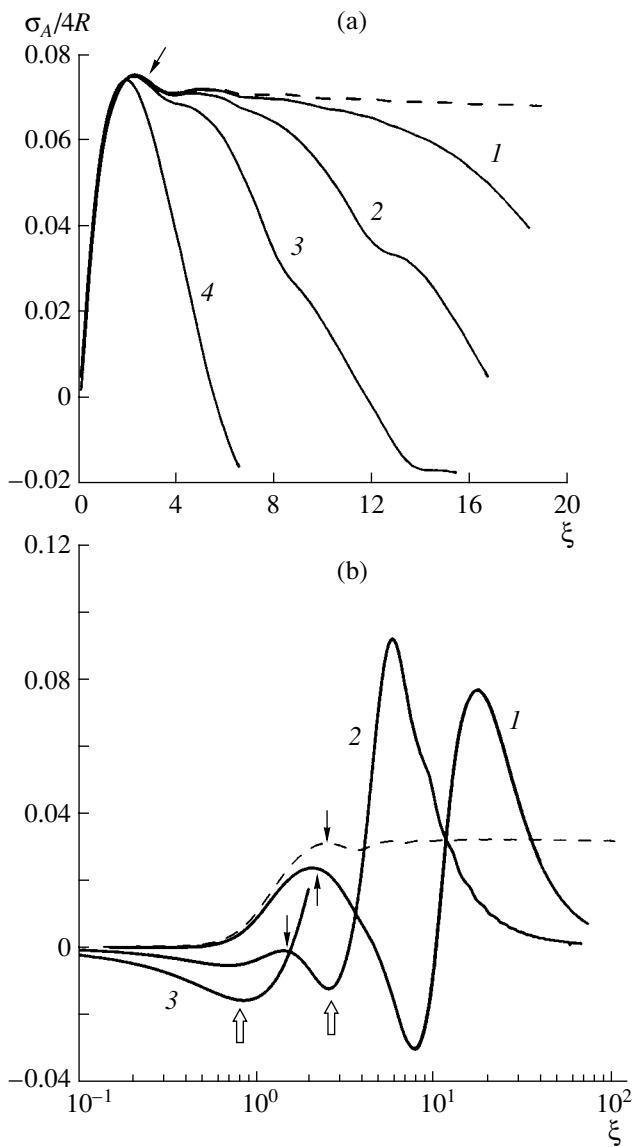
Fig. 4. (a) Spectra of the absorption cross section for the scattering of a shear wave by a semiconductor cylinder with a dense plasma: $\Omega/\omega =$ (*1*) 0.05, (*2*) 0.08, (*3*) 0.12, and (*4*) 0.25. (b) Spectra of the absorption cross section for the scattering of a shear wave by a semiconductor cylinder with a loose plasma: $\Omega/\omega =$ (*1*) 0.1, (*2*) 0.3, and (*3*) 0.5.

Fig. 5. (a) Spectra of the absorption cross section for $\omega/\omega_D =$ 0.04 and $\Omega/\omega =$ (*1*) 0.05 and (*2*) 0.15 (all other calculation parameters are the same as in Fig. 4a). (b) Spectra of the extinction cross section for $\omega/\omega_D = 1$ and $\Omega/\omega =$ (*1*) 0.4, (*2*) 0.54, (*3*) 0.7, and (*4*) 0.9 (all other parameters are the same as in Fig. 4b).

ations, the series of plasma resonances in curves *1* and *2* (Fig. 5a) is separated from the relaxation peak of absorption by the dip (indicated by arrows) of the acoustoelectronic interaction termination at $\Omega = n\omega$ for a partial wave with the corresponding number n. The possibility of its presence was discussed earlier and is illustrated in Fig. 2.

The value of σ_S, being always positive and numerically comparable to the absorption cross section, does not have an independent meaning as a characteristic of the scattering ability of the semiconductor cylinder.

However, the following feature of its spectral behavior deserves attention. In the Rayleigh region, σ_S is extremely small and, on the whole, the character of scattering is determined by the acoustoelectronic absorption. In the case of a loose plasma (Fig. 4b), this is fundamentally important, since it means the possibility of a negative extinction in the process of scattering, which is a result not indicated earlier in the theory of wave scattering by amplifying bodies [16, 19, 20]. Moreover, earlier [16], it was stated that the total energy gain of radiation on account of the amplification

by the scattering cylinder for only a part of partial waves is impossible. This conclusion was based on a series of approximations used in solving the problem of electromagnetic wave scattering by a rotating cylinder with a finite conductivity. In particular, the limitation by the nonrelativistic velocities of cylinder rotation seems to be essential, which automatically excluded the consideration of the conditions analogous to a strong drift in the loose ($\omega/\omega_D = 1$) plasma in Fig. 5b, where, in the region $\xi \leq 1$, curves 1–3 are located lower than the zero level of the extinction cross section indicated by the dashed line.

Typical spectra of an extinction cross section for a dense plasma with the calculation parameters of Fig. 5a are given in Fig. 6. The dashed line corresponds to the case of the absence of drift. The series of peaks of plasma resonances are also observed in them (they are especially pronounced in curve 1) together with the clear manifestation of the relaxation peak of absorption (indicated by arrows) only at sufficiently high angular velocities of drift. As one can see from the comparison of curves 1 in Figs. 5a and 6, the scattering itself, enhancing the monotonic growth of extinction with expansion into the short-wavelength part of the spectrum, ensures fulfillment of the condition $\sigma_{ex} > 0$ in this case.

ACOUSTIC PROPERTIES OF A HETEROPHASE PIEZOELECTRIC MEDIUM WITH FILAMENTOUS SEMICONDUCTOR INCLUSIONS

The negative character of extinction of a semiconductor cylinder with a loose plasma at $\xi \leq 1$ means that a piezoelectric with a large number of such inhomogeneities under the effect of drift should demonstrate the qualities of an active or, at least, quasi-transparent acoustic medium. The specificity of its effective acoustic properties can be connected, first of all, with the absence of a pronounced drift directivity characteristic of common acoustoelectronic interaction in homogeneous piezoelectric semiconductors and layered structures consisting of combinations of piezoelectric and semiconductor materials. Let us apply the results to the laws of shear wave propagation in a piezoelectric medium (matrix) with a multiplicity of identical randomly distributed parallel semiconductor cylinders each having identical azimuth drift currents.

The low scattering efficiency due to the acoustic matching of the cylinders and the matrix allows us to use the results of the theory of multiple scattering of waves in the approximation of low multiplicity of scattering [15]. The necessary restriction $kd \gg 1$, where d is the average distance between the cylinders, provides not only a sufficient weakness of acoustic rescattering but also allows us to ignore the mutual induction of piezoelectric polarization charges arising at the cylinder boundaries. Indeed, from the asymptotics of the scattered field at $kd \gg 1$, it follows that the field
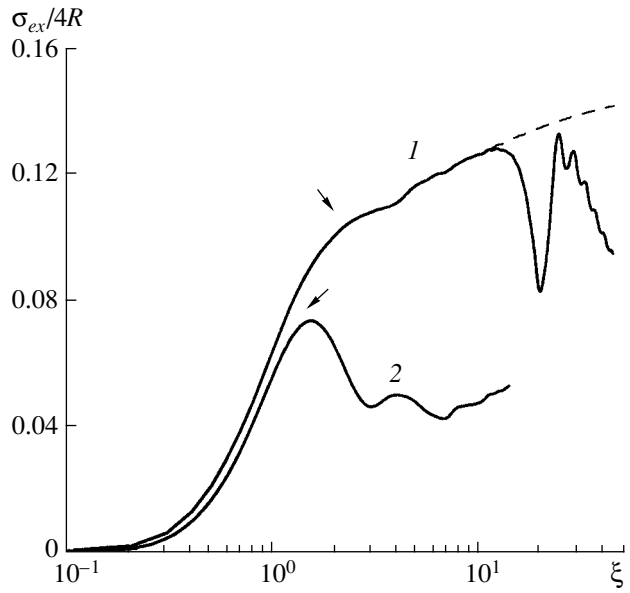
Fig. 6. Spectra of the extinction cross section for a semiconductor cylinder with a dense plasma: $\Omega/\omega = (1)$ 0.05 and (2) 0.5.

decreases by the law $(kr)^{-1/2}$, while, according to Eq. (8) and the evaluation of the main contribution of the dipole (at $|n| = 1$) terms to the field of piezoelectric polarization charges, we obtain a stronger decrease in the latter: $\Phi_2 \sim \xi/kr$, $kr \gg 1$. Under the aforementioned conditions of weak scattering and low concentration of cylinders n_0 (it indicates their number within a unit area of the sagittal plane, where the propagation of the shear wave occurs), one can satisfactorily predict the acoustic properties of the heterophase medium for $\xi \leq 1$.

If $f_S = \sum_{n=-\infty}^{n=+\infty} a_n \exp(in\theta)$ is the quotient function of scattering by a single cylinder and κ is the effective wave number of a shear wave in the heterophase piezoelectric, then, according to [15], we have

$$\kappa \approx k\sqrt{\left[1 + 2\frac{q}{\xi^2}f_S(0)\right]^2 - 4\frac{q^2}{\xi^4}f_S^2(\pi)}, \qquad (20)$$

where $q = \pi R^2 n_0$ is the specific volume of the semiconductor phase. The real part of $\kappa' = \mathrm{Re}(\kappa)$ determines the phase velocity $v = \omega/\kappa'$ and $\kappa'' = \mathrm{Im}(\kappa)$ is the absorption coefficient γ of the shear wave. Equation (20) is determined under the assumption of spherical shape of inclusions. However, it was noted repeatedly that the results obtained with it do not depend on the specific geometrical shape of the scatterers. The only point that is significant is their characteristic wave size.

Figure 7 presents the curves for the frequency dispersion of a shear wave in a piezoelectric of $BaTiO_3$ type ($\mathcal{K}^2 = 0.38$, $\varepsilon_1/\varepsilon_2 = 1.4$) with semiconductor cylinders. The curves are obtained by calculation according to Eqs. (19) and (20) at different angular velocities of drift for the most attractive (from the point of view of
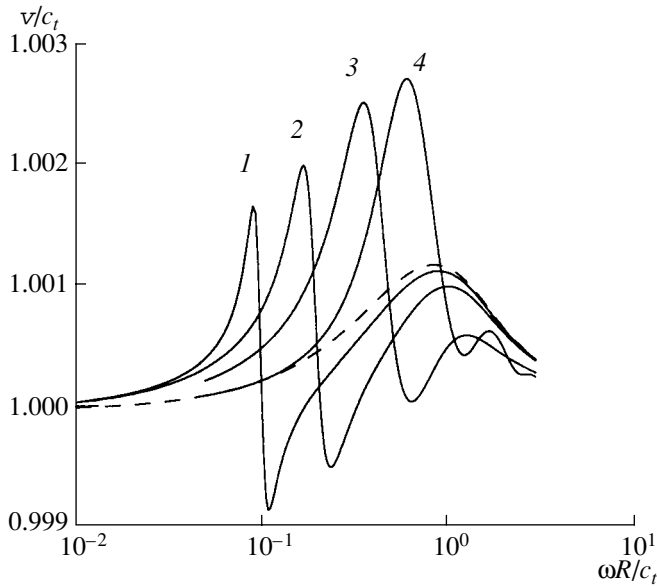
Fig. 7. Frequency dispersion of shear waves in a heterophase piezoelectric with semiconductor cylinders: $\Omega R/c_t =$ (1) 0.1, (2) 0.2, (3) 0.5, and (4) 1.
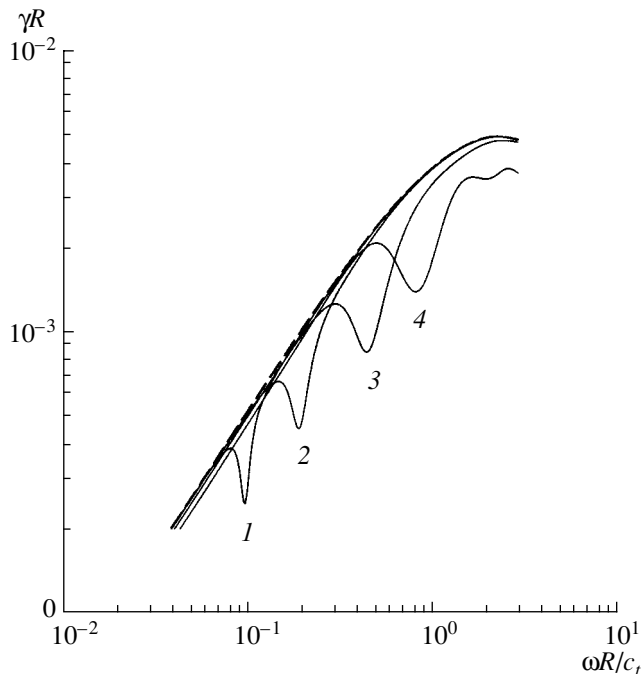
Fig. 8. Spectra of absorption for a shear wave in the heterophase piezoelectric; the spectra correspond to the dispersion spectra shown in Fig. 7.

control in the region $\xi \leq 1$) case of a loose plasma, $\omega_c R/c_t = 1$ and $c_t/\omega_D R = 1$. They resemble the curve of the frequency dependence of optical dispersion for the Drude–Lorentz medium near the absorption line [13], cross the dashed curve $v(\omega)$ for the case of the drift absence at the points $\omega = \Omega$, and, for the assumed small

value of the specific volume $q = 0.01$, demonstrate an insignificant (~0.1%) relative variation of the phase velocity, which indirectly confirms the reliability of calculation. The shifts of the curves towards shorter wavelengths with an increase in drift follow the frequency shift of the "sonic" velocity of drift for the dipole oscillations of number $n = 1$, which is reflected in the equality of these values due to the natural contrapositive of the angular velocity of drift with the cyclic frequency.

One can readily see that the reason for the agreement of the dependences $v(\omega)$ with the results of the electronic theory of dispersion lies in the aforementioned quasi-dipole character of the polars of cylinders at $\xi \leq 1$, which makes them similar to classical oscillators. The appearance of a hump in the drift-free dependence $v(\omega)$ at $\omega R/c_t = 1$ ($c_t = \omega/k$ is the velocity of shear waves) is apparently connected with the averaged manifestation of the relaxation peak of absorption by the system of randomly distributed cylinders. The dispersion dependences in Fig. 7 correspond to the absorption spectra in Fig. 8, which have the form of the characteristic loss minimum in the case of acoustoelectronic "clarification" of the medium under the conditions of sonic (for the dipole term of the scattered field) drift $\omega = \Omega$ manifesting itself against the background of monotonic growth of $\gamma(\omega)$ because of the general amplification of scattering with the increase in frequency. However, in calculations, it was impossible to obtain a full clarification of the medium $\gamma = 0$ and, especially, the absorption inversion, which is possible because of the negative extinction cross section. This is explained by both the low value of negative extinction of single scattering ($|\sigma_{ex}| \sim 10^{-3}$) and the multiple character of scattering, which bring the resulting extinction to the region of positive values.

In closing, it is necessary to note that, according to the set of properties determined above, a heterophase piezoelectric medium of parallel thin semiconductor cylinders randomly distributed over a piezoelectric crystal, where the transverse dimensions of the cylinders are slightly greater than the Debye radius, is a kind of analog to the Drude–Lorentz optical medium with the line of acoustoelectronic clarification controlled within the spectrum by azimuth drift.

CONCLUSIONS

The study of how the current plasma of a semiconductor cylinder in contact with a piezoelectric affects the scattering of a shear wave gave us the chance to determine that the most effective manifestation of conductivity and drift in acoustic wave scattering into the piezoelectric occurs in the case of acoustic matching of the materials of the cylinder and the external piezoelectric medium. The acoustoelectronic scattering that occurs under these conditions is characterized by the absence of the contribution of monopole sources; the presence of the drift-related nonreciprocity of scatter-

ing, which manifests itself by the nonequivalence of the scattering of partial waves with direct and inverse azimuth propagation; and the existence of plasma resonances and the relaxation peak in the spectra of the absorption cross section, where the peak is due to the optimal manifestation of the Joule loss in the dipole plasma oscillations. The essential feature of the effects of acoustoelectronic scattering also manifests itself in the fact that, as the frequency grows, the polarization effect of the semiconductor plasma in combination with the drift is replaced by the White mechanism of acoustoelectronic amplification (attenuation) of partial waves of the scattered field because of the grouping of charge carriers near the fields of boundary piezoelectric polarization oscillations penetrating in the semiconductor.

The general result is the conclusion on possible effective control of acoustoelectronic scattering by the azimuth drift and the presence of certain prerequisites for the development of special methods of acoustic spectroscopy of piezoelectric crystals with weak discrete electrical inhomogeneities. The prospects of a similar idea of using controlled acoustoelectronic scattering in the design of artificial heterophase piezoelectric materials with controlled acoustic parameters are demonstrated by the example of a composite piezoelectric medium consisting of parallel semiconductor filament cylinders randomly distributed over the piezoelectric. In particular, it is demonstrated that, under the effect of azimuth drift of charge carriers in filament cylinders, this composite piezoelectric is similar to the weakly absorbing Drude–Lorentz optical medium with a clarification line controlled within the spectrum.

REFERENCES

1. G. Kino, *Acoustic Waves: Devices, Imaging and Analog Signal Processing* (Prentice-Hall, Englewood-Cliffs, 1987; Mir, Moscow, 1990).

2. J. Zelenka, *Piezoelectric Resonators and Their Applications* (Elsevier, Amsterdam, 1986; Mir, Moscow, 1990).

3. Ce-Wen Nan, J. Appl. Phys. **76**, 1155 (1994).

4. Q. L. Fan, J. Takatsubo, and S. Yamamoto, J. Appl. Phys. **86**, 4023 (1999).

5. S.-H. Lee and T. J. Royston, J. Acoust. Soc. Am. **108**, 2843 (2000).

6. O. Lacour, M. Lagier, and D. Sornette, J. Acoust. Soc. Am. **96**, 3548 (1994).

7. N. S. Shevyakhov, Akust. Zh. **24** (2), 271 (1978) [Sov. Phys. Acoust. **24** (2), 150 (1978)].

8. N. S. Shevyakhov, Akust. Zh. **31**, 380 (1985) [Sov. Phys. Acoust. **31**, 223 (1985)].

9. N. S. Shevyakhov, Fiz. Voln. Proc. Radiotekh. Sys. **2** (1), 15 (1999).

10. N. Brauner and A. I. Beltzer, Ultrasonics **26** (6), 328 (1988).

11. R. B. Vaganov and B. Z. Katsenelenbaum, *Foundations of the Diffraction Theory* (Nauka, Moscow, 1982) [in Russian].

12. N. N. Lozinskiĭ, A. T. Makushkin, V. Ya. Rozenberg, and V. R. Érglis, *Handbook for a Programmer* (Sudostroenie, Leningrad, 1964), Vol. 2 [in Russian].

13. C. Boren and P. Hafmen, *Absorption and Scattering of Lihgt by Small Particles* (Wiley, New York, 1983; Mir, Moscow, 1986).

14. *Handbook of Mathematical Functions*, Ed. by M. Abramowitz and I. Stegun (Dover, New York, 1972; Nauka, Moscow, 1979).

15. R. Truell, C. Elbaum, and B. B. Chick, *Ultrasonic Methods in Solid State Physics* (Academic, New York, 1969; Mir, Moscow, 1972).

16. B. M. Bolotovskiĭ and S. N. Stolyarov, *Amplificaton of Electromagnetic Waves in the Presence of Moving Media* (Nauka, Moscow, 1980), p. 73 [in Russian].

17. N. S. Shevyakhov, Akust. Zh. **35**, 934 (1989) [Sov. Phys. Acoust. **35**, 541 (1989)].

18. L. M. Brekhovskikh, Akust. Zh. **13**, 541 (1967) [Sov. Phys. Acoust. **13**, 462 (1967)].

19. A. A. Starobinskiĭ and S. N. Churilov, Zh. Éksp. Teor. Fiz. **65** (1), 3 (1973) [Sov. Phys. JETP **65** (1), 1 (1973)].

20. A. L. Fabrikant, Akust. Zh. **28**, 694 (1982) [Sov. Phys. Acoust. **28**, 410 (1982)].

Translated by M. Lyamshev

===== **SHORT COMMUNICATIONS** =====

Magnetohydrodynamic Generator of Pseudosound

A. V. Danilyan, D. L. Dorofeev, V. I. Naskidashvili, G. V. Pakhomov, and B. A. Zon

Voronezh State University, Universitetskaya pl. 1, Voronezh, 394893 Russia
e-mail: zon@niif.vsu.ru
Received June 23, 2004

Abstract—The theory of a periodic flow of a conducting magnetized liquid in the presence of an ac current passing through it is described. It is shown that the flow arising under these conditions is of pseudosound character rather than sonic, as stated in some publications. Experimental data demonstrating the transformation of pseudosound flow into sound waves are presented. © *2005 Pleiades Publishing, Inc.*

The magnetohydrodynamic (MHD) effect in hydroacoustics was first considered by Anderson [1], who calculated the influence of the terrestrial magnetic field on the attenuation of sound in seawater. This effect is characterized by a quadratic dependence on magnetic induction, and its magnitude proves to be significant for infrasonic frequencies.

An observation of sound waves arising in a conducting liquid (salt water) because of the MHD effect of an ac electric field was reported in [2]. The potential difference between the electrodes, between which the sound waves propagated in the liquid, was found to depend linearly on magnetic induction, as the potential difference in the Hall effect.

In [3] (see also [4, 5]), the excitation of a periodic motion of a conducting liquid was observed under the combined effect of a constant magnetic field and an ac current passing through the liquid. The periodic motion of the liquid was interpreted in [3] as a sound wave, and the effect itself, as an MHD analog of the Hall effect.

In the present paper, we show that the sound waves observed in [3] arise as a result of the reflection of the pseudosound flows produced by the MHD generator from the boundaries of the tank containing the liquid. In other words, the MHD generator excites pseudosound, which is then transformed to ordinary sound at the walls of the tank.

Remember that the notion of pseudosound as a periodic liquid flow unrelated to density variations in the liquid was introduced by L.D. Blokhintsev [6] in describing turbulent flows around rigid objects. Recent publications devoted to pseudosound include [7–10].

Figure 1 schematically represents the experimental setup. The magnetic field and the electrodes fed by an ac voltage are oriented perpendicular to each other and placed in a conducting liquid. The pseudosound flow generated in this setup has a directional pattern whose maximum is oriented in the third orthogonal direction.

The hydrodynamics equations for an ideal liquid in a force field $\mathbf{f}(\mathbf{r}, t)$ have the form [11]

$$\frac{\partial \mathbf{v}}{\partial t} + (\mathbf{v}\nabla)\mathbf{v} = -\frac{1}{\rho}\nabla p + \frac{1}{\rho}\mathbf{f}(\mathbf{r}, t),$$

$$\frac{\partial \rho}{\partial t} + \nabla(\rho\mathbf{v}) = 0. \tag{1}$$

Here, $\rho(\mathbf{r}, t)$ is the density of the liquid and $\mathbf{v}(\mathbf{r}, t)$ is its velocity.

Linearizing Eqs. (1), we obtain an equation for the deviation of the density ρ of the liquid from the equilibrium value ρ_0 ($\rho' = \rho - \rho_0$):

$$\frac{\partial^2 \rho'}{\partial t^2} - u^2 \Delta\rho' = -\mathrm{div}\mathbf{f}(\mathbf{r}, t), \tag{2}$$

where u is the velocity of sound.

The boundary condition for Eq. (2) can be obtained as follows. We proceed from the boundary condition for the velocity. For a liquid bounded by a rigid surface Γ, the normal velocity component v_n should be equal to zero, i.e.,

$$v_n|_\Gamma = 0, \tag{3}$$
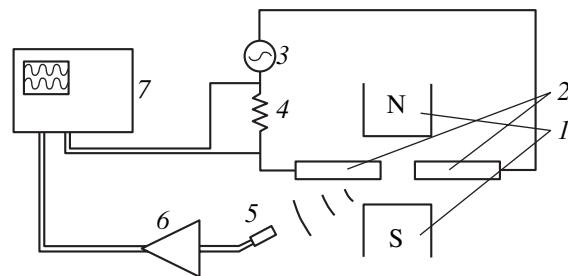
Fig. 1. Schematic representation of the experimental setup: (*1*) permanent magnet, (*2*) electrodes, (*3*) source of ac current, (*4*) current-measuring resistor, (*5*) hydrophone, (*6*) amplifier, and (*7*) oscilloscope.

and $\mathbf{v}(\mathbf{r}, t)$ should satisfy the linearized Euler equation

$$\frac{\partial \mathbf{v}}{\partial t} = -\frac{u^2}{\rho_0}\nabla\rho' + \frac{1}{\rho_0}\mathbf{f}(\mathbf{r}, t). \qquad (4)$$

Differentiating boundary condition (3) with respect to time and taking into account Eq. (4), we obtain a boundary condition for ρ':

$$\left.\frac{\partial\rho'}{\partial n}\right|_\Gamma = \left.\frac{1}{u^2}f_n\right|_\Gamma. \qquad (5)$$

Let us show that, in the case under consideration, both Eq. (2) and boundary condition (5) are homogeneous. Assume that two electrodes are placed in an unbounded liquid in a constant homogeneous magnetic field $\mathbf{H}$ and that each of the electrodes has the form of a closed surface made of a perfectly rigid and perfectly conducting material. In this case, the surface of each of the electrodes is equipotential and a current with density $\mathbf{j}(\mathbf{r}, t)$ generating a Lorentz force $\mathbf{f} = [\mathbf{j}, \mathbf{H}]$ passes through the liquid. In the quasi-stationary case, $\text{curl}\,\mathbf{j} = 0$. Then, at the surfaces of the electrodes, the current density vector is perpendicular to these surfaces. Therefore, $\text{div}\,\mathbf{f} = (\mathbf{H}, \text{curl}\,\mathbf{j}) = 0$ and $f_n|_\Gamma = 0$. Hence, $\rho'(\mathbf{r}, t) \equiv 0$. In other words, in the given case, the effect of the force field $\mathbf{f}(\mathbf{r}, t)$ does not lead to a compression or rarefaction of the liquid and, hence, no sound wave is formed in the liquid.

However, under the effect of such a force field, a liquid flow whose nature is different from that of a sound wave may arise. In particular, if the force field $\mathbf{f}(\mathbf{r}, t)$ harmonically depends on time as $\mathbf{f}(\mathbf{r}, t) = \mathbf{f}(\mathbf{r})e^{-i\omega t}$, the liquid flow will also be of a harmonic character. Such periodic liquid flows of nonsound nature are called pseudosound [6].

To study the velocity distribution in the given pseudosound flow, we consider Eq. (4). Substituting $\rho' = 0$ and integrating with respect to time, we finally obtain

$$\mathbf{v}(\mathbf{r}, t) = \frac{i}{\omega\rho}\mathbf{f}(\mathbf{r})e^{-i\omega t}. \qquad (6)$$

Let the electrodes have the form of spheres of radius a with their centers at the points $\pm\mathbf{l}$. Assume that $r \gg l \gg a$. Then, the current density in the quasistationary case is determined by the expression

$$\mathbf{j}(\mathbf{r}, t) = \frac{I(t)l}{2\pi r^3}(\mathbf{l}_0 - 3\mathbf{r}_0(\mathbf{r}_0, \mathbf{l}_0)),$$
$$\mathbf{r}_0 = \mathbf{r}/r, \quad \mathbf{l}_0 = \mathbf{l}/l, \qquad (7)$$

where $I(t) = Ie^{-i\omega t}$ is the total current between the electrodes. Substituting the corresponding expression for the Lorentz force $\mathbf{f} = [\mathbf{j}, \mathbf{H}]$ into Eq. (6), we obtain $v \sim r^{-3}$. Hence, for the pseudosound field, the rate of decrease with distance from the source is much greater than that for the ordinary sound field, for which $v \sim r^{-1}$.

Naturally, any object placed in a pseudosound flow represents a source of sound waves [6], and this fact should be taken into account in interpreting experimen-

tal data. In the experiment described in [3], such objects could be the walls of the tank and the membrane separating the volume of the conducting liquid, in which pseudosound flows were generated, from the volume of the nonconducting liquid, in which the hydrophone was placed.

The theory described above was developed with the aim to interpret the results of our experiments. As the conducting liquid, we used a 3.5% aqueous solution of NaCl, which corresponds to the salinity of seawater. The tank containing the liquid was made of stainless steel with the dimensions $162 \times 77 \times 10$ cm^3. The source of magnetic field was a permanent magnet, which, with the use of pole concentrators with an outer diameter of 30 mm, provided a magnetic field of about 0.5 T in a 15-mm-wide gap. Bronze cylindrical electrodes 9 mm in diameter were coaxially positioned at a distance of 10 mm from each other in the region of the maximal magnetic field in such a way that their common axis was normal to the field. The output voltage of the master oscillator was supplied via a power amplifier to a series-connected current-measuring resistor and to the electrodes. The sound pressure receiver was represented by calibrated piezoelectric transducers in the form of cylinders 19 mm in diameter and 22 mm in length. The transducers were positioned on the axis perpendicular to both magnetic field and electrode current directions, at a distance of 40 cm from the electrodes. The signal from the receiver was preamplified and supplied to one of the oscilloscope channels. The second oscilloscope signal served for controlling the magnitude and form of the electrode current.

Figure 2 shows the experimental dependences of the receiver signal amplitude on the amplitude of the electrode current for several frequencies. One can see that the amplitude of the detected sound signal linearly depends on the current strength, according to Eqs. (6) and (7). As for the spatial distribution of sound, its parameters could not be explained in terms of the standing sound wave pattern produced by the source of fairly simple geometry used in the experiment. This fact has stimulated us in analyzing theoretically the phenomenon described above. Presumably, under our experimental conditions, the transformation of the pseudosound flow into acoustic oscillations mainly occurred at the metal electrodes and at the poles of the magnet. This conclusion can be made in view of the fast attenuation of pseudosound with distance that is predicted by Eq. (7). Such a fast attenuation of the signal with increasing source–hydrophone distance was not observed in the experiment.

In addition to the sound signal at the frequency of the exciting current, in some cases we observed a double-frequency signal, as in [3]. This signal is associated with the periodic heat release in the gap between the electrodes: the heat release does not depend on the polarity of the electrodes and, therefore, varies with time at a double frequency. Indirect evidence of the

p, Pa
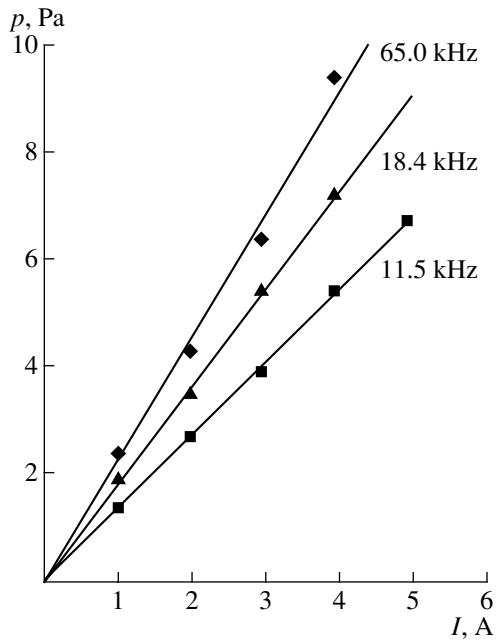
Fig. 2. Dependence of the hydrophone signal amplitude on the amplitude of the electrode current.

thermal nature of the double-frequency signal is the fact that this signal was only observed within a time after the beginning of the oscillator operation, because, in the course of its operation, the electrodes become oxidized and the heat release in the metal–electrolyte boundary layer increases.

REFERENCES

1. N. S. Anderson, J. Acoust. Soc. Am. **25**, 529 (1953).
2. P. H. Moose and R. F. Klaus, J. Acoust. Soc. Am. **74**, 1066 (1983).
3. A. J. Campanella, J. Acoust. Soc. Am. **111**, 2087 (2002).
4. A. B. Dobrucki, J. Acoust. Soc. Am. **113**, 1207 (2003).
5. A. J. Campanella, J. Acoust. Soc. Am. **113**, 1209 (2003).
6. D. I. Blokhintsev, *Acoustics of an Inhomogeneous Mooving Medium* (Nauka, Moscow, 1981) [in Russian].
7. A. V. Smol'yakov, Akust. Zh. **46**, 401 (2000) [Acoust. Phys. **46**, 342 (2000)].
8. V. M. Tkachenko, Akust. Zh. **46**, 408 (2000) [Acoust. Phys. **46**, 342 (2000)].
9. S. A. Rybak, Akust. Zh. **47**, 717 (2001) [Acoust. Phys. **47**, 629 (2001)].
10. S. Timouchev and J. Tourret, in *Proceedings of 19th International Pump User's Simposium* (2002), pp. 85–105.
11. L. D. Landau and E. M. Lifshitz, *Fluid Mechanics*, 2nd ed. (Nauka, Moscow, 1986; Pergamon, Oxford, 1987).

Translated by E. Golyamina

════════════════════ **CHRONICLE** ════════════════════

In Memory of Yuriĭ Mikhaĭlovich Sukharevskiĭ
(September 8, 1906–September 17, 2004)

On September 17, 2004, one of the prominent acousticians of Russia, Professor Yuriĭ Mikhaĭlovich Sukharevskiĭ—the founder of the Russian school of hydroacoustics, a doctor of engineering, a laureate of the USSR State Award, and a person of manifold gifts—passed away at the age of 98.

In 1925–1930, Sukharevskiĭ was a student of the Faculty of Electrical Engineering of the Moscow Power Engineering Institute. There, he simultaneously specialized in electrical engineering, local power stations, factory electrical instruments, electrical machine building, and safety means for high-voltage power lines. In total, during the years of his studies at the institute, he passed 115 examinations in different branches of engineering. Sukharevskiĭ carried out his first research project as a student, and his first scientific publication appeared in 1929.

In 1927–1931, Sukharevskiĭ also studied at the Piano Faculty of the Moscow Conservatory. After receiving his master's degree in music, he continued his education at the Conservatory as a postgraduate student until 1935. In those years, Sukharevskiĭ gave many concerts with the symphony orchestras of the Moscow Conservatory and Moscow Radio.

The aforementioned activities did not exhaust his versatile talents. He was keen on sports, being a figure-skater and a mountain-climber.

The variety of occupations and creative abilities formed the life of young Sukharevskiĭ—the future prominent scientist.

After his graduation from the Moscow Power Engineering Institute, within 1930 to 1938, Sukharevskiĭ worked at the Acoustical Laboratory of the Central Research Institute of the People's Commissariat of Communication.

In late 1938, Sukharevskiĭ was invited to work at the Academy of Sciences of the USSR as a senior researcher in the Group of Applied Physics at the Engineering Science Division of the Academy of Sciences of the USSR. Simultaneously, he worked as a scientist-secretary of the Acoustical Commission of this division (the chair of the commission was N.N. Andreev), which was later transformed into the Scientific Council on Acoustics of the Academy of Sciences of the USSR.

In the same period of time, Sukharevskiĭ was a member of the commission established by the Presidium of the Academy of Sciences to supervise the acoustic design of the large halls of the Palace of Soviets in Moscow. The commission was headed by N.N. Andreev.

In 1939, Sukharevskiĭ became a senior researcher at the Acoustical Laboratory of the Lebedev Physical Institute of the Academy of Sciences of the USSR. In the same year, he received his candidate degree, and, in 1940, at the age of 33, he became a doctor of engineering.

From the beginning of the German invasion of the USSR in World War II until the end of the war, Sukharevskiĭ, together with his colleagues, worked on military problems.

In 1945, Sukharevskiĭ became the head of the Sector of Hydroacoustics of the Acoustical Laboratory of the Lebedev Physical Institute and also the head of the Sukhumi Marine Research Expedition, which ran until 1954. At the same time, he was involved in the problems of construction and equipment of the future marine research station.

Supervising research in underwater acoustics, he recruited young scientists for this field: he visited universities and institutes of Moscow and other cities, gave lectures on his own studies, and invited graduate and postgraduate students to work at his Hydroacoustic Research Sector in Moscow and at the permanent Sukhumi Expedition. Within a short period of time, Sukharevskiǐ formed two teams of young researchers—his future students and colleagues.

In 1954, after the Acoustical Laboratory of the Lebedev Physical Institute was transformed into the Acoustics Institute of the Academy of Sciences of the USSR and the Sukhumi Expedition was transformed into the Sukhumi Marine Research Station, Sukharevskiǐ became the head of a laboratory and then the head of a department of the Acoustics Institute and, simultaneously, the head of the Sukhumi Marine Research Station.

In 1959–1960, Sukharevskiǐ supervised the work of the joint Soviet–China expedition on hydroacoustics that was organized by the Academy of Sciences of the USSR and the Academy of Sciences of the People's Republic of China.

In 1961–1966, Sukharevskiǐ was a Deputy Director of the Acoustics Institute and, simultaneously, remained the head of the Hydroacoustics Department.

In 1970, Sukharevskiǐ received the title of Professor. In his final years, he was a principal researcher of the Acoustics Institute, an active member of the Scientific Council of the Institute, and the chairman of the regular seminar on hydroacoustics. He continued his active work in research and published a number of papers devoted to the generalization of his previous studies and to the development of certain new lines of research in hydroacoustics.

At the age of 90, Sukharevskiǐ earned the Prize for the Best Publication in Academic Editions.

In 2004, approaching the age of 98, Sukharevskiǐ wrote three articles for the book devoted to the 50th anniversary of the Acoustics Institute. He also prepared a brief paper outlining the main contents of his future monograph that should be entitled *Several New Aspects of the Sonar Problem*. However, he had not enough time to realize this project.

Sukharevskiǐ left a rich scientific heritage. He is the author of 165 scientific works, including three monographs.

He was not only a prominent scientist but also a talented teacher of young scientists. The scientific school formed by Sukharevskiǐ is well known as a school of excellent specialists in hydroacoustics. Sukharevskiǐ educated 11 doctors of science and 26 candidates of science. His former students have become full and corresponding members of the Academy of Sciences, honored scientists and engineers, and honored inventors.

The name of the prominent practical scientist Sukharevskiǐ is respected among broad circles of civil and military specialists in hydroacoustics.

For his services to the country, Sukharevskiǐ was awarded two Orders of the Red Banner of Labor, an Order of the October Revolution, a Badge of Honor, a Valiant Labor during the Patriotic War Medal, and other medals; he also received the title of the Laureate of the USSR State Award. In the last years of his life, Sukharevskiǐ received a special grant from the President of the Russian Federation as "a Prominent Scientist of Russia."

THE MAIN RESULTS OF SUKHAREVSKIǏ'S SCIENTIFIC AND ENGINEERING ACTIVITIES

In 1930–1942, Sukharevskiǐ carried out research and design in electroacoustics, acoustic metrology, and architectural acoustics.

He developed metrological test benches for the calibration and testing of electroacoustic transducers—transmitters and receivers of sound—under the conditions of an acoustic chamber and under field conditions.

He designed Russia's first test bench for the absolute calibration of loudspeakers and microphones and for measuring their frequency characteristics and nonlinear distortions. This test bench was used for testing the quality of the electroacoustic equipment produced by the enterprises of the People's Commissariat of Communication and by local industry.

Sukharevskiǐ developed the theory of insonification of large halls and open spaces with the use of electroacoustic horn systems.

He planned and realized Russia's first outdoor acoustic test site (near Balashikha, Moscow region) for full-scale measurements of the characteristics of powerful sound sources, including horn loudspeakers for outdoor broadcasting.

On the basis of the results obtained from studying the directional characteristics of acoustic horns at the test site, Sukharevskiǐ proposed and designed a fundamentally new high-quality horn loudspeaker with a uniform response and directional characteristic in a broad frequency band.

He studied electroacoustic horn systems for insonifying large halls and outdoor spaces. He developed a method for calculating the parameters of these systems.

He performed theoretical and experimental studies of the acoustic feedback that restricted the possibilities of sound amplification in both indoor and outdoor sound amplifying systems.

He developed and substantiated Russia's first system of distributed loudspeakers for insonifying large open spaces, which simulated the effect of boominess of a large hall without echo interference (reverberation). Such a system was installed under his supervision at the All-Union Agricultural Exhibition in Moscow.

Sukharevskiĭ designed and organized the manufacture of Russia's first low-frequency directional loudspeaker with a very large horn. To test the characteristics of the new powerful loudspeaker, he organized an expedition to the region of Mount Elbrus. The loudspeaker and a microphone (with the transmission of the received signal through radio) were positioned on the two ridges of Elbrus (3000–3500 m in height) separated by a deep valley. There, Sukharevskiĭ studied the sound propagation range without the acoustic effect of the earth's surface; he also studied the fluctuations of the signal in amplitude and phase due to the inhomogeneity and dynamics of the medium.

Sukharevskiĭ put forward the original idea of installing a set of loudspeakers on the giant airplane *Maksim Gor'kiĭ* for insonifying large areas with intelligible speech.

He carried out research in architectural acoustics and electroacoustics in application to broadcasting. He performed full-scale measurements of the acoustical characteristics of broadcasting studios and the characteristics of microphones. He implemented his original idea of controlling the directivity of vector microphones used in broadcasting.

In application to the problems of architectural acoustics, he developed a new impulse method for an objective evaluation of the acoustics of concert halls and large auditoriums by the criterion of the nonstationary "process of sound formation" instead of the previously known reverberation time criterion. The impulse method of excitation with an analysis of a recording of the sound formation process allows the determination of the instant of the first reflection arrivals and the spatial identification of these reflections. A similar method was mastered by architectural acousticians in the United States 10 years later.

Sukharevskiĭ used the aforementioned method to reveal the acoustic defects of the Tchaikovsky Concert Hall, which was newly built at that time. As a result, the acoustic drawbacks of this hall were explained from the scientific point of view. The discussion of the defects along with the possible measures for their improvement was planned for July of 1941, but the outbreak of World War II on the territory of the USSR prevented the fulfillment of these peaceful plans.

Sukharevskiĭ began working on military problems together with other scientists. He worked at the improvement of sound-detecting horns used in anti-aircraft artillery. The first full-scale experimental studies of the characteristics of these horns were performed near Moscow, 15 km away from the front. It was found that the main disadvantage of sound-detecting horns is their high sensitivity to wind noise, which considerably reduces the detection range. To suppress wind noise, Sukharevskiĭ developed a wind-protecting screen in the form of a multilayer fairing made of a thin metal net, which protected the horn throat. Full-scale tests of sound-detecting horns with wind protection showed a considerable increase in the detection range. The improved sound-detecting horns were accepted for use in air defense in 1942, and the commander of the air-defense forces officially expressed his gratitude to Sukharevskiĭ.

From 1943 to 2004, Sukharevskiĭ mainly worked in underwater acoustics.

In 1943–1944, he organized and carried out the first hydroacoustic expedition on the vessels belonging to the Pacific part of the navy. He studied the characteristics of hydroacoustic armaments used by Russian and foreign naval vessels, as well as the acoustic characteristics of the armed vessels and underwater targets. He carried out comprehensive studies of the conditions of sound propagation in the ocean and reverberation as the main interference arising in underwater detection and ranging.

Sukharevskiĭ used the results of the Pacific expedition to develop proposals concerning the improvement of sonar and recommendations for their optimum application in different tactical situations and under varying acoustical conditions of the ocean. For his contribution to the defense potential of the USSR, Sukharevskiĭ was awarded an Order of the Red Banner of Labor in 1945.

Based on the results of the Pacific expedition, Sukharevskiĭ justified the necessity of establishing a permanent experimental hydroacoustic base and put forward the relevant proposals. The latter were supported by Director of the Lebedev Physical Institute, President of the Academy of Sciences of the USSR S.I. Vavilov, and their implementation began in 1945.

Sukharevskiĭ supervised the construction, the equipment, and the formation of the research group of the Sukhumi Marine Research Station, which was later transformed into the Sukhumi Branch of the Acoustics Institute. The Sukhumi Marine Research Station created by Sukharevskiĭ was the most-advanced stationary hydroacoustic base of the USSR at that time.

Sukharevskiĭ formed and educated teams of specialists in underwater acoustics, who first worked at his research sector of the Lebedev Physical Institute and, then, at the laboratory and the department of the Acoustics Institute.

Sukharevskiĭ supervised experimental studies of fundamental importance in physical and applied underwater acoustics at the Sukhumi Marine Research Station and the Sukhumi Branch. One of the results of these studies was the discovery of the secondary zones of acoustic illumination and focusing of sound.

He supervised the hydroacoustic research groups working at the Acoustics Institute and other related organizations involved in comprehensive experimental studies that were carried out during oceanic expeditions on research vessels, submarines, and naval vessels, including field tests of newly designed hydroacoustic armaments.

Sukharevskiĭ supervised the studies of noise radiation and reflectivity of submarines and the development of acoustic protection means for them.

He carried out basic and applied research and supervised the development of a series of noise-suppressing, antisonar, and vibration-damping coatings, which were put into mass production and used in the construction of Russian submarines.

He developed a statistical approach and criteria for evaluating the probability of acoustic security of submarines under a variety of conditions of motion, which allowed a submarine to maintain security at a given level.

He developed the principles of the frequency optimization of sonars with allowance for the whole set of spectral characteristics of sounding signals and noise, the parameters of the acoustic waveguide, and the methods of data processing.

He developed a method of using the coefficients of variation or decrease in the detection range of a frequency-optimized sonar under the variation of its own parameters or the acoustic characteristics of the targets and the waveguide.

He proposed a statistical approach to the main criterion of the quality of hydroacoustic systems, namely, their detection range, by introducing the probable detection range of a sonar under the set of physical oceanic conditions as a statistical quantity with a given integral probability.

On the basis of the results of comprehensive studies and with the use of the effect of far zones of acoustic illumination and focusing of sound, he developed the foundations for designing a new generation of ship-borne hydroacoustic armaments.

Sukharevskiĭ made a radically new proposal concerning the development of hydroacoustic systems for nuclear-powered submarines with a detection range an order of magnitude greater than that existing at the time and calculated the parameters of such systems.

He supervised the design of the first long-range hydroacoustic system, which was accepted for use by the navy. This work was honored by a USSR State Award.

Sukharevskiĭ developed a scientific basis for the design of the future, more advanced ship-borne hydroacoustic armaments.

He initiated and supervised the development of three generations of sonar systems for nuclear-powered submarines. These systems were approved by the Navy, put to mass production, and installed on submarines of six different types.

Sukharevskiĭ never restricted the scope of his interests to professional occupation. He gave concerts as a pianist with the Symphony Orchestra of the House of Scientists of the Russian Academy of Sciences. His repertoire included more than 15 concerts for piano and orchestra by Beethoven, Liszt, Tchaikovsky, Rachmaninov, and Gershwin. He gave us the pleasure of listening to his musical performances at parties held at the Acoustics Institute and during the expeditions.

The memory of Yuriĭ Mikhaĭlovich Sukharevskiĭ will forever remain in the hearts of his friends and colleagues.

V.I. Mazepov,
a former student
and a comrade of Sukharevskiĭ

Translated by E. Golyamina

=========== **INFORMATION** ===========

Information on the Activities of the St. Petersburg Seminar on Computational and Theoretical Acoustics of the Scientific Council on Acoustics of the Russian Academy of Sciences in 2004

In 2004, the St. Petersburg Seminar on Computational and Theoretical Acoustics proceeded with its regular activities. As usual, the seminar consisted of a series of spring sessions (March to May) and a series of autumn sessions (October to December). In total, sixteen sessions were held. The scope of the seminar can be divided into three main topics: wave processes in an acoustic (i.e., nonresistant to shear) medium, wave processes in a solid elastic medium, and wave processes in thin-walled structures (isolated or placed in an external acoustic medium).

The first topic was represented by the papers by D.P. Kouzov, S.V. Bobyshev, and S.G. Kadyrov.

Kouzov introduced refined acoustic equations that take into account the presence of the gravitational field. This approach, in particular, allows one to consider sound waves in a medium and gravity waves on a liquid surface from a single point of view.

Bobyshev analyzed the formation of a steady-state self-oscillation mode due to the interaction of a jet issuing from a Laval nozzle with resonators of cylindrical and conical shapes.

Kadyrov studied the diffraction field caused by the incidence of a discontinuous nonstationary wave on a rigid convex body. Using boundary integral equations, he derived both "early" and "late" asymptotics.

The second topic was represented by the papers by P.V. Tkachev, A.P. Kiselev, A.V. Osetrov, A.M. Lin'kov, A.V. Teplyakova, and R.G. L'vov.

The purpose of the study carried out by Tkachev was to estimate the effect of the microstructure of a material on the wave processes that occur in it. The study was based on the microstructure equations of a medium modeled by a set of pairwise interacting concentrated elements that formed an infinite perfect crystal lattice. Tkachev derived the dispersion relations for a plane uniform deformation of the lattice and determined the stability conditions for its deformed state.

In the paper coauthored by E. Becache and A.P. Kiselev, the field of a planar source of elastic waves was considered and the asymptotic and numerical method of its determination were compared.

Kiselev together with G. Huet and M. Deschamps investigated the forms of the transverse component of a nonstationary P-wave field.

Osetrov proposed an analytical method for the determination of the surface waves propagating along a randomly rough boundary. The medium was assumed to be piezoelectric and belonging to an arbitrary symmetry class. The roughness was described by a correlation function. The boundary conditions at the rough surface of the medium were formulated using the Rayleigh hypothesis.

Lin'kov discussed a new effect: amplification of waves at a softening surface between elastic media. He considered the connection with the problem of rock bursts in deep mines. He also proposed an interpretation of the seismic data recorded along the fault produced by the earthquake in Taiwan in 1999.

The papers presented by Teplyakova and L'vov were concerned with the development of the theory of nondestructive testing methods. Teplyakova studied the field scattered by rigid cylindrical inclusions of infinite length with a disruption of the adhesion bond on part of the surface. The disruption of adhesion was quantitatively characterized by introducing the moduli of the contact stiffness responsible for the transfer of elastic displacements in the directions normal and tangential to the boundary. L'vov considered a scatterer in the form of a sphere that contained a nonconcentric empty sphere inside it. The purpose of the studies was to determine the scattering coefficients.

The papers concerned with the third topic were presented by I.P. Babaĭlov, G.V. Filippenko, and I.V. Andronov.

Babaĭlov considered the oscillations of an elastic spherical segment rigidly fixed along its contour. The initial equations were the Goldenveiser equations for a spherical shell. The eigenfrequencies were calculated.

Filippenko, on the basis of an exact analytical solution, calculated the eigenfrequencies of a plate partially submerged in a water basin. The water basin was assumed to have a finite depth and an infinite length (an acoustic waveguide), and the plate was assumed to be

rigidly fixed to the bottom. The upper edge of the plate was assumed to be free.

The papers presented by Andronov were concerned with generalized point models in boundary-contact problems of acoustics. He described the theoretical foundations of the proposed approach (the theory of zero-radius potentials) and two its applications for calculating the wave field in a liquid covered with a plate: the diffraction of an acoustic wave by a crack of a finite width and by a prominent stiffening rib. The dimensions of the obstacles (the crack width and the height of the rib) were assumed to be small compared to the wavelength. The advantage of the proposed approach is that, after the necessary characteristics of the field are determined for a single obstacle, the diffraction field of a finite number of such obstacles can be calculated by solving a system of linear algebraic equations.

The sessions of the seminar are held in the assembly hall of the Institute for Problems of Mechanical Engineering, Russian Academy of Sciences (Vasil'evskiĭ Ostrov, Bol'shoĭ pr. 61, St. Petersburg), Tuesdays at 18:30.

More detailed authors' abstracts of papers and other information on the seminar can be obtained on the web site:

http:/mph.phys.spb.ru/~george/seminar.html

Applications for papers can be forwarded by e-mail: kouzov@alfa.ipme.ru or george@GF4663.spb.edu

and also by phone to the seminar head D.P. Kouzov (812)312-3530 or the seminar secretary G.V. Filippenko (812)143-2323.

D.P. Kouzov

Translated by E. Golyamina

==================== **INFORMATION** ====================

Scientific–Engineering Conference
"Ship Acoustics—2005"

The scientific–engineering conference "Ship Acoustics 2005" was held April 12–14, 2005, in St. Petersburg. The conference was organized by the Krylov Central Research Institute, the East-European Acoustical Association, and the Council on Acoustics of the Russian Academy of Sciences.

The participants of the conference included scientists from St. Petersburg and Moscow, specifically, from the Krylov Central Research Institute, Institute of Mechanical Engineering of the Russian Academy of Sciences, Research Institute of Physicotechnical and Radio Engineering Measurements, Aurora Central Research Institute, Central Research Institute of Shipbuilding Technology, and Central Research Institute of Military Shipbuilding, as well as representatives from different design offices.

In total, 42 papers were presented at the conference. Some of them caused much discussion, for example, the problem of self-testing for the external acoustic parameters of a vessel. Fundamentally different solutions to this problem were proposed by A.K. Novikov and V.I. Popkov. The way of using on board measuring means, the choice of the number and positions of the test points, the algorithms of data processing, and the calculated control parameter—all of these aspects of the problem were considered by the two authors and new original solutions were proposed, which, however, were criticized by the opponents because of the difficulties in their realization. Nevertheless, the possibility of developing an on board self-testing system is beyond question, and the need for an experimental study of the basic solutions with the use of models and actual vessels is evident. Many papers were concerned with the problem of reliability of underwater noise level measurements in the course of the motion of an object. This problem was discussed by Yu.F. Shlemov, V.A. Kal'yu, and V.Yu. Garin from the Krylov Central Research Institute and by O.A. Shiryak, A.F. Kurchanov, and V.B. Bychkov from the Research Institute of Physicotechnical and Radio Engineering Measurements.

Some of the noise control problems encountered in certifying a frigate built for export were considered by M.Ya. Moshchuk and N.V. Vasil'ev. Nontypical noise sources, such as a defect supporting bearing of the shaft line or a cavitation flow around the stock of the ship stabilizer, made it impossible to reach the specified ship noise levels, which required special investigation to elaborate appropriate engineering solutions.

The paper presented by Yu.I. Bobrovnitskiǐ (Institute of Mechanical Engineering, Russian Academy of Sciences) attracted considerable interest. It was entitled "How to Make a Body Transparent to Sound." The problem of developing an active system for reducing the radiation and scattering of sound by an underwater object had been considered years ago (G.D. Malyuzhinets), but a technical implementation of such a system had been impossible until this day. The new approach proposed by Bobrovnitskiǐ was approved by the audience as being much more realizable from the technical point of view but still calling for experimental verification.

The calculation of oscillations and radiation and scattering of sound by elastic bodies was the subject of papers presented by M.Ya. Pekel'nyi, T.M. Tomilina, I.V. Grushetskii, and A.V. Smol'nikov. A number of papers were concerned with the development of acoustic protection means for ships. The papers by Yu.N. Popov, N.V. Volkova, V.I. Kuz'menko, Yu.I. Kotsarev, and V.S. Konevalov reported on the results of recent studies aimed at increasing the efficiency of hydroacoustic and vibration-absorbing coatings and at the design of new types of composite vibration dampers.

In the course of discussions, the participants of the conference gave some interesting comments and put forward some new ideas concerning the topical problems of measuring and reducing noise produced by different ships and vessels.

The participants of the conference estimated the latter as quite successful. The next conference, "Ship Acoustics 2007," is planned for April of 2007.

É.L. Myshinskiǐ

Translated by E. Golyamina